TRINITY COLLEGE DUBLIN
COLÁISTE NA TRÍONÓIDE, BAILE ÁTHA CLIATH
THE UNIVERSITY OF DUBLIN

Applying geogenic methods and decision-making tools to model radon at local and regional scales.

A thesis submitted to the University of Dublin for the degree of Doctorate of Philosophy

Department of Geology, University of Dublin, Trinity College.

2023.

Author:

Méabh Hughes Banríon

Declaration

I declare that this thesis has not been submitted as an exercise for a degree at this or any other university and it is entirely my own work.

I agree to deposit this thesis in the University's open access institutional repository or allow the library to do so on my behalf, subject to Irish Copyright Legislation and Trinity College Library conditions of use and acknowledgement.

Méabh H Banríon

To Aisling

Summary

Radon is an environmental health hazard for indoor environments, caves and underground mines exposure to which is related to an increased probability of developing lung cancer. Globally, radon is the second leading cause of lung cancer after tobacco smoking, and the leading cause of lung cancer in non-smokers. Radon is geogenic, in that it primarily originates from beneath the Earth's surface. Specifically, radon has several isotopes which form intermediate decay products from the radioactive decay of uranium and thorium (^{238}U, ^{235}U and ^{232}Th). From a radiological protection perspective ^{222}Rn is the main isotope of interest, given its relatively longer half-life compared to the other radon isotopes. Ireland has a geographically weighted average indoor radon concentration (77 Bq m^{-3}) and population weighted average indoor radon (98 Bq m^{-3}) which is over twice that of the global average (39 Bq m^{-3}), and a disproportionally high number of radon-related lung cancer cases occur here (ca. 300 - 350 cases per year, which equates to 14% of the total lung cancer cases, compared to the global range of between 3% to 15%) (Elío et al., 2018, p. 20; Fuente et al., 2020; Long, 2018; Murphy et al., 2021; World Health Organization, 2009). The high average radon concentrations, geological diversity, and availability of open access data relating to natural and built environments make Ireland an ideal case study to better understand the factors contributing to the concentration and spatial variation of radon.

Although the connection between local geology and radon is widely known, radon maps seldom utilise information relating to the radon source or pathway through the natural environment; both factors govern the distribution of indoor radon. For instance, the first national radon map of Ireland (S.G Fennell et al., 2002) although a major achievement in that it estimated the probability of indoor radon exceeding a threshold value from 10 x 10 km grids, it had several

shortcomings in that it utilised a limited number of indoor radon measurements, and did not contain any geological data.

Not only does Ireland have a high average indoor radon concentration, some exceptionally high indoor radon concentrations have also been found here. In 2003, the highest single measurement of indoor radon (65,000 Bq m^{-3}) was reported in a house in Castleisland Co. Kerry after several occupants tragically died of lung cancer, despite being non-smokers. No previous geological studies have been implemented to investigate the cause of high radon occurring in the area.

This research sets out to investigate the use of geological datasets to map radon. This thesis also aims to provide decision-making tools that will aid with efficiently choosing appropriate methods for mapping radon depending on the intended purpose. The primary data collected in this thesis includes (a) subsoil radon gas concentration, (b) subsoil permeability and (c) topsoil geochemistry. A number of additional pre-existing data types have been used as part of this research (e.g. geological maps, geophysical data, geochemical data, indoor radon data).

The work presented here utilizes a background knowledge of geological processes and applies it to model radon distribution.

Within this thesis, a range of case studies are presented for different spatial scales, and utilising a range of different datasets. Castleisland in Co. Kerry was chosen as a case study due to the geologically unexplained high indoor radon occurring in the area. More than one hundred soil-gas radon and subsoil permeability measurements were collected in a systematic and representative manner over several geology types. Analysis of major and trace elements is completed for 92 topsoil samples and compared with soil-gas radon samples collected from the same locations. In addition, the geochemical data from the topsoils are investigated for covariance and correlation to determine if certain elements are commonly associated with geogenic radon. The general geostatistical methodology developed for Castleisland is scaled and repeated for the Irish Midlands. In this instance various modelling approaches are applied to 4,131 topsoil samples obtained from the Geological Survey Ireland TELLUS Midlands, and combined with a previously published national radon potential map, which was derived from TELLUS radiometric data, and a national subsoil permeability model (Elío et al., 2020).

The main findings demonstrate that geology and geological attributes can offer useful insights to the distribution and expected concentration of radon. From this research, it is apparent that different spatial scales of sampling and modelling can result in significantly different radon risk maps even if the same dataset is used. Soil-gas radon and soil permeability mapping can act as a rapid method for quantifying the radon risk in relatively small (i.e. 10 km^2) areas, but are not practical for considerably larger areas.

Regardless of spatial scale, integration of topsoil geochemistry into radon models shows covariance occurring between elements correlated with geogenic radon, thus demonstrating that chemistry of soils can be indicative of radon prone areas. In this way legacy soil geochemistry data and geological map data can be utilised to assist efforts to highlight radon prone areas, without the need to directly measure radon indoors or in soil gas.

Publications

Published

1. Hughes, M.B., Elío, J. and Crowley, Q.G., 2022. A user's guide to radon priority areas, examples from Ireland. *Journal of the European Radon Association*. DOI: https://doi.org/10.35815/radon.v3.7586
2. Banríon, M.H., Elío, J. and Crowley, Q.G., 2022. Using geogenic radon potential to assess radon priority area designation, a case study around Castleisland, Co. Kerry, Ireland. *Journal of Environmental Radioactivity*, *251*, p.106956. DOI: https://doi.org/10.1016/j.jenvrad.2022.106956

Submitted

3. Banríon, M.H., Cobelli, M. and Crowley, Q.G., *under revision*. Investigating topsoil geochemistry in relation to geogenic radon using multivariate geo-statistics, examples from local and regional scale data in Ireland. *Submitted Journal of Applied Geochemistry*. *March 2023*

Acknowledgements

My paramount acknowledgement goes to my supervisor Prof. Quentin Crowley. I have major appreciation and gratitude for you accepting me to manage, implement and complete this project. There is no doubt I wouldn't be at this stage of submitting this thesis if you didn't encourage me to transfer the project to a Ph.D. The project has evolved a lot since initially starting; it's been an engaging and intriguing process exploring the different aspects and angles that can be focused on when implementing a single research project. I'm grateful for the scientific discussion, support and direction you provided over the years. I will never see soils, geology, research and radon in the same way again.

After spending almost eight years in Trinity College Dublin and the Department of Geology, there are simply too many people to thank; many lecturers have instilled enthusiasm for learning more about geology, and if it weren't for the help of staff Francis, Sarah, Maura, Cora, Frances, James and Noel I wouldn't have completed this research. And I appreciate all the research/technical staff from various departments for all the helpful conversations of efficient survey design and implementation. A special thanks to Dr. Vincent Gallagher who provided a lot of technical support regarding the TELLUS protocols for soil sampling in the early days. I'm also very appreciative of Dr. Javier Elío who thankfully sent on resources and tips for self-learning 'R' at the beginning, and for being a discussion partner on many aspects of geogenic radon over the years. Immense gratitude goes to the Association of Applied geochemists and BV labs CA, who helped sponsor the ICPMS analysis of the soil samples as well as ESRL.

When I started my undergraduate degree in 2014, I never expected to graduate as a geologist. Frankly, I applied to Trinity to become a neuroscientist through the general science degree. In

September 2014, I chose geology as a random extra credit module. Yet it was an environmental science module that spurred me to moderate with geology. Having learned that freshwater was a diminishing resource for many countries, I asked various departments which degree would most equip me with the knowledge and tools for managing freshwater, to which Dr. Dave Chew corresponded Geology was the right degree considering much of freshwater is stored in aquifers.

After graduating as a geologist in June 2018, I couldn't wait to start a research masters on the topic environmental geochemistry; and in July 2018 I embarked on the first field trip. I'd like to thank Ryan O'Toole, Patricia McGuire, Mirela Dardac for helping with that field survey during a rare drought and heatwave. Particular thanks to Ryan and Patricia for the enthusiasm, craic and unforgettable memories on this field trip while we camped in a field near the highest known radon in Ireland. With the lack of a car, we used a wheel burrow to transport our equipment, at times the terrain was rough yet they never backed down and stuck it through to get the data. A special thanks to Andrew and Angela Kelleher who let us camp in their field, letting us borrow a wheel burrow on multiple occasions and for taking us up Carrauntoohil.

In October 2018, I returned to the field alone to collect physical soil samples. I'd like to thank so many of the locals who were interested in the research and, like me, wanted to know the results already. I'd like to thank all of the locals, strangers and fellow post-grads who helped get the heavy samples from Castleisland Co. Kerry, from the field area back to the Museum building. In March 2019, another soil sample collection survey was scheduled which happened to coincide with Storm Gareth. It wouldn't have been as enjoyable without the help of Freya Bartels and Dr. Maxime Savieter. Even in blizzard like snow (which was beautiful) we still pushed our shovels 50 cm deep into the ground to retrieve those samples. Much gratitude is given to Winifred Duncan who not only assisted on multiple field surveys but also contributed as a lab assistant during the sample preparation for analysis.

A special thanks to my brothers for advice on managing a Ph.D. and my sister Aisling for always reassuring and encouraging me! Also Lily and Klara, their enthusiasm for rocks, even the gravel containing calcareous fossils on the road, their interest in how mountains form and where soil comes from; their questions always reminded me the significance of understanding geology and how awesome it really is. Mum and Dad, you already know I wouldn't have reached this point without your support and encouragement. Thanks fam!

I can't conclude these acknowledgements without mentioning the support of Trinity Access Programmes (TAP), who encouraged me to not drop out in my first year in 2014. The support I received from my tutor Ronan Smith, and many people at TAP allowed me to find the joys in education despite the difficulties financing tuition/expenses. These thanks are extended to the Student Union, Senior Tutor, SUSI and SCS who have helped me in the more challenging times.

I am grateful for the support of my friends who have helped me avoid endlessly working on the project without breaks. I've much appreciation for Matteo, who undoubtedly helped keep me sane, especially during the Pandemic lockdowns; our conversations on many aspects of science have kept me motivated and excited to keep learning.

For everyone who played a part in this journey, my gratitude is immense. I aimed to achieve a doctorate not to eventually become a professor, but to be able to contribute to society in a way that excites me, through helping with environmental issues on the ground. Thanks to everyone who encouraged and supported me throughout the past eight years, I'm getting closer to achieving that goal.

“*There is no end to education. It is not that you read a book, pass an examination, and finish with education. The whole of life, from the moment you are born to the moment you die, is a process of learning.”* — **Jiddu Krishnamurti**

Table of contents

List of Figures

List of Tables

Thesis motivation and structure

1.1.1 Research objectives

The primary research objectives of this thesis are to:

(a) Develop a decision matrix for radon mapping and modelling for the non-specialist, which takes into account different possible available datasets, and the possible intended purposes of mitigation measures.

(b) Investigate the use of radon potential and soil geochemistry in determining the radon risk of a small area (Castleisland, Co. Kerry). Secondary objectives are to assess the assigned legislative radon risk designation, and investigate the source of radon anomalies in the area.

(c) Develop novel statistical and modelling methodologies to utilise legacy soil geochemistry and geological map datasets for regional or national scale radon mapping or modelling.

1.1.2 Research questions

Using subsurface geogenic properties, this thesis aims to understand the spatial distribution of radon in natural and built environments. Research questions are developed in each of the research chapters as follows:

For chapter 3 – (a) does the spatial resolution of radon risk maps significantly impact the designation of radon risk for an area? (b) what are the common methods for mapping radon? (c) does a specific method for mapping radon risk exceed efficiency and performance than alternative methods? (d) does integrating geological parameters improve radon mapping? (e) does a radon model exist that addresses both aims of the EU Basic Safety Standards directive

59 of 2013; to inform/protect both (1) individuals and (2) the collective from the harmful effects of ionising radiation? and (f) can decision making tools be developed to aid policy makers/radon risk researchers in choosing the most efficient and effective model, taking into account available datasets in a given country and incorporating variables including (i) cost-efficiency, (ii) time-efficiency, (iii) protecting individuals, (iv) protecting the collective, and (v) capturing spatial variability of radon at local scales (<10 km^2) and large scales (>10 km^2)?

For chapter 4 – (a) does soil-gas radon and indoor radon vary above different bedrock geologies? (b) is there a significant behavioural trend between soil-gas radon and indoor radon variance above different bedrock geologies? (c) does the geogenic radon potential (GRP) method effectively map the naturally available radon in a local area (<10 km^2)? and (d) can geological methods (incorporating bedrock geology maps, soil-gas radon and soil permeability survey's) be used to indicate if an area is susceptible to higher risk of indoor radon concentrations at local scales?

The main research questions of chapter 5 are (a) to what extent does the geochemistry of soil impact geogenic radon? and (b) are there a combination of specific elements which are associated with geogenic radon i.e. do 'radon-prone' elements exist? (c) to what extent are radon-prone elements associated with the underlying geology of an area? and (c) can soil geochemistry be utilized to model geogenic radon risk at local and regional scales?

1.2 Research rationale and motivation

Geology is intrinsically linked with understanding natural environments, and geological expertise is gaining traction for actively mitigating environmental issues ranging from developing geothermal energy to carbon capture storage, soil contamination, landslide and flood risk management (Elders and Moore, 2016; Highland, 2018; House, 2005; McIlwaine et al., 2014; McKinley et al., 2013; Raza et al., 2019). However, geological expertise has seldom been integrated to tackling the environmental issue of radon gas exposure. This thesis utilises geological knowledge to investigate and validate how geogenic data can be a powerful tool when combatting radon risk.

Long term exposure to radon gas is recognised as the leading cause of lung cancer in non-smokers and is a primary motivation underpinning the importance of mapping radon (World Health Organization, 2009). Considering radon is colourless, tasteless and odourless, specialised technology is required to detect radon, and individuals are unaware of the levels they are being exposed to; which is the reason behind radon colloquially referred to as the ‘silent killer’. The study area focused on in this thesis was partially chosen due to several individuals in the area dying of lung-cancer; with their house subsequently measured to have extremely high radon (65,000 Bq m^{-3}) (Organo et al., 2004).

Additionally, the area around the highest indoor radon measurement in Ireland is designated as having a low probability of containing radon values over the reference level (200 Bq m^{-3}) on the Environmental Protection Agency of Irelands national radon maps (S.G Fennell et al., 2002b). As such, there is a need to verify the EPA designation of this specific small-scale area. Since the study area is rural with spatially sparse indoor radon measurements, it is more feasible to adopt geological methods, such as soil-gas radon surveys, to investigate the radon variation. Furthermore, geogenic methods can not only monitor and map radon but if planned correctly, can be used to understand the underlying processes causing radon in the area to be produced and transported. To add, this research also aims to demonstrate the efficiency geogenic radon potential surveys for assessing the designation of radon priority areas at a local-scale.

The link between radon and geology has been established for many decades. Initially, the mining industry utilised soil-gas radon surveys for uranium ore and hydrocarbon exploration (Castillo et al., 2015; Cvetković et al., 2021; McCarthy Jr and Reimer, 1986). Also, soil-gas radon surveys have been used to detect faults and have been adopted to monitor seismic and volcanic activity (Ioannides et al., 2003; Padilla et al., 2013; Sun et al., 2018; Zmazek et al., 2005). Moreover, an international report by the World Health Organisation concludes that soil-gas radon is the major contributor of indoor radon (World Health Organization, 2007). However, methods commonly used to map indoor radon don’t typically integrate geological knowledge despite spatially dense geological datasets being available. As such, the field case-study area was designed to include multiple samples collected above the bedrock lithology underlaying the region with the anomalous indoor radon measurement, as well as samples collected above several different bedrock lithologies and structural geological features. The inclusion of a range of geology types in the study area is aimed at investigating the variation of radon with respect to geology.

Consequently, investigating the geochemistry of physical soil samples collected in the same locations as soil-gas radon measurements may verify the influence of earth surface parameters on the availability of geogenic radon to become indoor radon. Samples were strategically collected following the Geological Survey Ireland TELLUS protocol to allow results to be comparable. Moreover, the midlands TELLUS topsoil geochemistry dataset is studied to evaluate the feasibility of adopting regional soil surveys to model radon prone areas.

The overall aim of this thesis is to contribute to the existing understanding of radon and how geological expertise can be integrated to assessing radon riskareas. Whilst the data demonstrated in this thesis are obtained from specific geological areas in Ireland, the methodologies are applicable to different geological regions and can be utilised by other countries evaluating their national radon action plans. By providing rigorous research regarding methods to model radon, geological approaches could contribute more to understanding where and how radon occurs naturally in an area, assisting the interpretation of which municipalities may require prioritised mitigation efforts, and aid in the reduction of radon induced lung cancer cases.

1.2.1 Chapter 3: A user's guide to radon priority areas, examples from Ireland

There is an important need for research in Ireland to validate the geogenic parameters contributing to radon distribution. To elaborate, the average indoor radon concentration in Ireland is 77 Bq/m^3, which is almost double the European average of 39 Bq/m^3 (Environmental Protection Agency Ireland, 2020; World Health Organization, 2009). Despite geogenic radon being recognized as the main contributor to indoor radon, geological methods are seldom used to mitigate radon (World Health Organization, 2007).

The first published paper included in this thesis (chapter 3) focuses on demonstrating different methodologies and outputs for radon mapping as well as developing a workflow for choosing the most appropriate methodology for specific aspects of radon mitigation measures. Chapter 3 summarises the various common ways in which radon risk can be mapped, highlighting different maps may be needed depending on the exact purpose of mapping radon (for workplaces, building regulation, homes etc). Chapter 3 also introduces the integration of geospatial and geological expertise into combatting the environmental risk of radon. Additionally, a tabulation and figures are produced which can aid in the decision-making process for determining the more appropriate approach for mapping radon under different circumstances.

The first published paper (chapter 3) is a valuable and novel contribution to the field of environmental radon mitigation. The outcome of chapter 3 (a) adds to the efficiency of choosing the most appropriate type of radon map for effectively mitigating radon in various settings, (b) highlights the advantages of integrating geological data into radon models, and (c) demonstrates the effect of spatial resolution when producing a radon map.

1.2.2 Chapter 4: Using geogenic radon potential to assess radon risk area designation, a case study around Castleisland, Co. Kerry, Ireland.

A national-scale legislative radon-risk map, based exclusively on indoor radon measurements was published in 2002 (Fennell et al., 2002). The lack of geological data being used to create the map as well as its 10 x 10 km spatial resolution limit its use in defining radon prone areas at local (< 10 km^2) resolution, and in areas that lack indoor radon measurements. An objective of the second published paper in this thesis is to demonstrate the spatial variation of radon at a local scale. For this chapter, the radon prone area of Castleisland, Co. Kerry was chosen as a case study.

Previous research from the study area reports the highest indoor radon concentrations recorded in Ireland and Europe (Organo et al., 2004). In 2003, a dwelling named the "Castleisland House" was discovered to contain radon values up to 65,000 Bq m^{-3}, despite the fact that Castleisland is not designated as a high radon area on the legislative national radon risk map (RPII 2002). To add, no geological studies have previously been implemented to investigate the highest known radon area in Ireland.

The main research questions of chapter 4 are (a) can geogenic data constrain the understanding of radon soil-gas source and distribution at local scales, and (b) can geological data be used as a proxy to predict indoor radon. The main outcomes are (a) high-spatial resolution radon risk maps produced for the Castleisland study area, (b) statistical correlation of soil-gas radon and geology, (c) a research approach that is proven appropriate for testing radon prone areas and (d) results that are relevant to other regions with similar geology.

The individual datasets used in chapter 4 include: (1) soil-gas radon concentration, (2) soil permeability, (3) indoor radon (supplied by the Environmental Protection Agency), and (4)

Geological Survey Ireland geological maps. All of the data was collected in the same 6 km^2 study area (figure 2 chapter 4). The soil-gas and soil permeability data were collected in short (less than ten days) field trips during the summer months (July/August) to minimise any possible temporal affects. The resolution of the soil-gas, soil permeability as well as physical soil samples are exactly the same as these datasets were collected from the same locations.

1.2.3 Chapter 5: Investigating topsoil geochemical relation to geogenic radon using multivariate geo-statistics, examples from local and regional scale data.

There are very few published studies which investigate variation of geogenic radon in relation to a wide range of elements in the topsoil. The research presented in chapter 5 examines the possibility that certain soil geochemical signatures can be used to delineate radon prone areas. As such, topsoil geochemical data may be useful in areas which lack indoor radon data to accurately model radon risk.

The research rationale of chapter 5 is a continuation from that of chapter 4; investigating the value of geogenic data in delineating radon prone areas. Considering soil-gas radon is the main contributor to indoor radon, the main research questions of chapter 5 are (a) to what extent does the geochemistry of soil impact soil-gas radon concentrations and (b) are there a combination of specific elements which are associated with geogenic radon and (c) can soil geochemistry be utilized to model geogenic radon.

Chapter 5 contributes a robust and novel analytical approach for extracting useful information from topsoil geochemical data; the results demonstrate that soil geochemistry is an important factor in determining radon risk. Furthermore, the modelling approach used for the high-resolution case study area around Castleisland Co. Kerry is repeated and validated using a regional scale dataset from the Geological Survey Ireland TELLUS Midlands dataset. The methodology and results of chapter 5 demonstrate the value that local and regional topsoil geochemical surveys can have in the management of radon prone areas.

1.3 Thesis structure

This thesis has been constructed following the thesis submission guidelines published by graduate studies in Trinity College Dublin. There are 5 main chapters, firstly an introduction (chapter 2), three manuscripts (chapters 3 to 5), followed by a concluding section with future research recommendations (chapter 6). Each of the manuscripts presented are standalone research outputs. The format of the two published papers (chapter 3 and 4) have been reformatted to be consistent with the thesis structure, however their content and layout remains unchanged from the published versions (see Appendix C). In line with paper format, references are presented at the end of each chapter. Supplementary material for each manuscript is presented in Appendix A. Additional data not included in the thesis, but collected and processed during the project is presented in Appendix B.

1.4 References

Castillo, P.I., Townley, B.K., Emery, X., Puig, Á.F., Deckart, K., 2015. Soil gas geochemical exploration in covered terrains of northern Chile: data processing techniques and interpretation of contrast anomalies. Geochemistry: Exploration, Environment, Analysis 15, 222–233.

Cvetković, M., Kapuralić, J., Pejić, M., Kolenković Močilac, I., Rukavina, D., Smirčić, D., Kamenski, A., Matoš, B., Špelić, M., 2021. Soil gas measurements of radon, CO2 and hydrocarbon concentrations as indicators of subsurface hydrocarbon accumulation and hydrocarbon seepage. Sustainability 13, 3840.

Elders, W., Moore, J., 2016. Geology of geothermal resources. Geothermal Power Generation 7–32.

Environmental Protection Agency Ireland, 2020. Radon Map :: Environmental Protection Agency, Ireland [WWW Document]. URL https://www.epa.ie/radiation/radonmap/

Fennell, S.G., Mackin, G.M., McGarry, A.T., Pollard, D., 2002. Radon exposure in Ireland. International Congress Series 1225, 71–77. https://doi.org/10.1016/S0531-5131(01)00549-0

Highland, L.M., 2018. Landslide hazard and risk: Current and future directions for the United States Geological Survey’s Landslide Program, in: Landslide Risk Assessment. Routledge, pp. 207–213.

House, P.K., 2005. Using geology to improve flood hazard management on alluvial fans-an example from laughlin, Nevada. JAWRA Journal of the American Water Resources Association 41, 1431–1447.

Ioannides, K., Papachristodoulou, C., Stamoulis, K., Karamanis, D., Pavlides, S., Chatzipetros, A., Karakala, E., 2003. Soil gas radon: a tool for exploring active fault zones. Applied Radiation and Isotopes 59, 205–213.

McCarthy Jr, J.H., Reimer, G.M., 1986. Advances in soil gas geochemical exploration for natural resources: Some current examples and practices. Journal of Geophysical Research: Solid Earth 91, 12327–12338.

McIlwaine, R., Cox, S.F., Doherty, R., Palmer, S., Ofterdinger, U., McKinley, J.M., 2014. Comparison of methods used to calculate typical threshold values for potentially toxic elements in soil. Environmental Geochemistry and Health 36, 953–971. https://doi.org/10.1007/s10653-014-9611-x

McKinley, J.M., Ofterdinger, U., Young, M., Barsby, A., Gavin, A., 2013. Investigating local relationships between trace elements in soils and cancer data. Spatial Statistics 5, 25–41. https://doi.org/10.1016/j.spasta.2013.05.001

Organo, C., Ellard, A., Fenton, D., Synnott, H., O'Colmáin, M., Prenter, S., O'Reilly, S., Colgan, P.A., 2004. High radon concentrations in a house near Castleisland, County Kerry (Ireland)—identification, remediation and post-remediation. Journal of Radiological Protection 24.

Padilla, G.D., Hernández, P.A., Padrón, E., Barrancos, J., Pérez, N.M., Melián, G., Nolasco, D., Dionis, S., Rodríguez, F., Calvo, D., 2013. Soil gas radon emissions and volcanic activity at El Hierro (Canary Islands): The 2011-2012 submarine eruption. Geochemistry, Geophysics, Geosystems 14, 432–447.

Raza, A., Gholami, R., Rezaee, R., Rasouli, V., Rabiei, M., 2019. Significant aspects of carbon capture and storage–A review. Petroleum 5, 335–340.

Sun, X., Yang, P., Xiang, Y., Si, X., Liu, D., 2018. Across-fault distributions of radon concentrations in soil gas for different tectonic environments. Geosciences Journal 22, 227–239.

World Health Organization (Ed.), 2009. WHO handbook on indoor radon: a public health perspective. World Health Organization.

World Health Organization, 2007. International radon project: survey on radon guidelines, programmes and activities (No. WHO/HSE/RAD/07.01). World Health Organization.

Zmazek, B., Živčić, M., Todorovski, L., Džeroski, S., Vaupotič, J., Kobal, I., 2005. Radon in soil gas: how to identify anomalies caused by earthquakes. Applied geochemistry 20, 1106–1119.

Chapter 2

Introduction

2.1 Radon: An Overview

There are several key events that occurred in the early 20th century which lay the foundation for understanding radon (Rn). In 1896 Henri Becquerel discovered radioactivity, resulting in the SI unit of measurement of radioactivity being named the Becquerel (Bq). The Bq corresponds to the activity of a quantity of radioactive material in which one nucleus decays per second. Marie Curie coined the term 'radioactivity', and discovered Radium (Ra) in 1898. In 1900 Friedrich Ernst Dorn discovered radon, which was one of the first radioactive elements to be discovered after uranium, thorium, polonium and radium (Radvanyi and Villain, 2017). Friedrich Ernst Dorn reported radioactive gas emanating from a radium source, which was later named radon (Dorn, 1901).

Radon is a naturally occurring radioactive noble gas which is tasteless, odourless, and colourless. Radon forms as a result of uranium decay and its daughter products emitting alpha and/or beta particles in order to become more stable (fig.2.1). Uranium has several isotopes occurring in different abundances, ^{238}U (99.274%), ^{235}U (0.72%) and ^{234}U (0.005%). The most abundant isotope ^{238}U forms ^{222}Rn (radon) as an intermediate decay product. The isotopes of ^{235}U and ^{232}Th form ^{219}Rn (actinon) and ^{220}Rn (Thoron) as intermediate decay products, respectively. The half-life of ^{238}U, ^{235}U and ^{232}Th is 4.5 Byr, 700 Myr and 250 kyr. It takes a few hundred thousand years for ^{238}U to be transformed into ^{222}Rn gas. The ^{222}Rn isotope has a half-life of 3.823 days. The isotopes of actinon and thoron have half-lives of 3.96 seconds and 55.6 seconds, respectively.

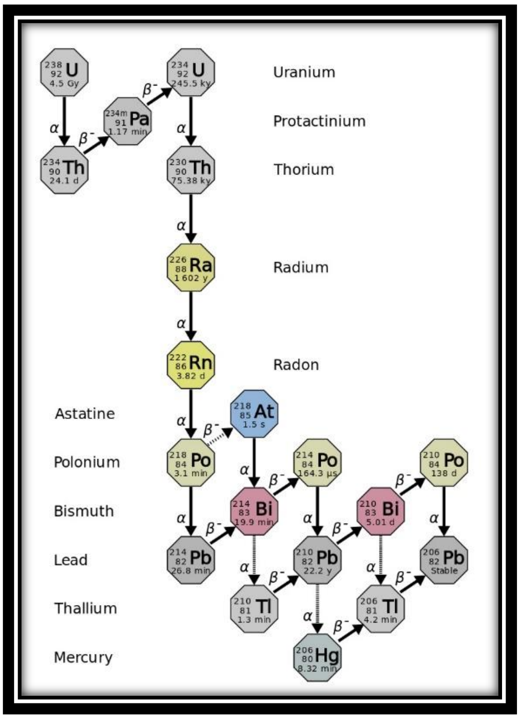

Figure 2.1 238-Uranium decay chain; 'This chart shows the decay chain of the 238U series and the half-lives of each isotope (y = year, d = day, m = minute and s = second). Alpha decays are represented by vertical arrows and beta decays by diagonal arrows' (Sutton et al., 1993). Image sourced from Wikipedia (shorturl.at/dmxKU).

The radioactivity of uranium can be attributed to its unstable nucleus. For instance, ^{238}U has a large number of neutrons (146) compared to protons (92), resulting in uranium having a low binding energy (i.e., energy holding the nucleus of the atom together) making it unstable. Similar to other radioactive elements, uranium becomes more stable by losing excess energy. Energy is lost by stochastic emission of radioactive particles which converts the initial uranium element into elements with lower mass and higher binding energies. ^{238}U and its daughter products go through a series of alpha and/or beta decay processes until it is converted to a stable state in the form of ^{206}Pb (figure 2.1). During the series of decay processes uranium is transformed into radium (^{226}Ra). The ^{226}Ra isotope is the immediate predecessor of radon gas.

Exposure to radon gas indoors is considered an environmental risk and categorized as a class 1 carcinogen for causing lung cancer (world Health Organisation, 2009). Concisely, when radon is inhaled while it decays, it can transform into metal isotopes of ^{218}polonium and/or

^{214}polonium. Alpha particles emitted from the polonium isotopes can cause damage to lung tissue and contribute to the development of lung cancer (Bowie and Bowie, 1991; Degu Belete and Alemu Anteneh, 2021).

The primary initiative of the International Commission on Radiological Protection (ICRP) is to protect against ionising radiation. The ICRP recommends the maximum occupational radiation dose received by a person each year to be in the range of 3 milli Sieverts (mSv) to 10 mSv, which is in line with the World Health Organisation's (WHO) recommendation of 10 mSv (ICRP, 2019; World Health Organisation, 2009). The associated higher limits for indoor radon concentration (IRC) is 300 Bq m^{-3} in workplaces and 200 Bq m^{-3} in homes, although the WHO recommends that IRC levels in homes should not exceed 100 Bq m^{-3} (World Health Organization, 2009). A house in the main study area of this thesis measured an IRC (average 49,000 Bq m^{-3}) ca. 250 times greater than the 200 Bq m^{-3} reference level. The resulting annual radiation dose received by the occupants was estimated to be approximately 1200 mSv (Organo et al., 2004).

The variation in terrestrial natural radiation is largely dependent on geology (Hamideen et al., 2020; Tzortzis et al., 2003); as the amount of natural radioactivity in distinct rocks varies in the earth subsurface (Abed et al., 2022; Al-Khawlany et al., 2018; Alshahrani, 2021; Gaafar et al., 2021). Radionuclide concentration is generally higher in granitic, gneiss and granulites whereas sedimentary rocks contain lower concentrations of radionuclides, with the exception of some phosphatic rocks and shales (table 2.1). Additionally, soils above different lithologies are characterised by distinct ranges of natural radioactivity (table 2.2). As such, geochemical analysis of soils can give insight to underlying geological influences impacting natural radioactivity in soils (Faanu et al., 2011; Ribeiro et al., 2018; United Nations Scientific Committee on the Effects of Atomic Radiation and Annex, 2000).

Table 2.1 Range of natural radioactivity levels in various rock types.

Region	Rock type	Associated natural radioactivity Bq kg-1	Reference
Wadi El- Mashash, El Mahamid mines - Egypt	Phosphates Shales	^{226}Ra : 665.8 +/- 33.4 ^{232}Th : 329.4 +/- 17 ^{40}K : 587.6 +/- 29.4 ^{226}Ra : 85.2 +/- 5.7 ^{232}Th : 93.3 +/- 5.6 ^{40}K : 303.1 +/- 15.2	(Abbady et al., 2005)
Jeronym Mine – Czech Republic	Granite	^{238}U : 907 ^{232}Th : 33 ^{40}K : 166	(Kim et al., 2021) (Malczewski et al., 2021)
Egypt	Gneiss Granite Basalt	^{226}Ra: 28.4 +/- 3 ^{232}Th : 37.7 +/- 4 ^{40}K : 1167.6 +/- 42 ^{226} Ra: 118 +/- 7 ^{232}Th : 90.5 +/- 7 ^{40}K :2208 +/- 91 ^{226}Ra: 59.5 +/- 4 ^{232}Th : 67.7 +/- 6 ^{40}K :718 +/- 42	(Harb et al., 2012)

	Sandstone Siltstone	^{226}Ra: 7.5 +/- 1.5 ^{232}Th : 12.5+/-3 ^{40}K :263+/-11 ^{226}Ra: 113 +/- 7 ^{232}Th : 148.5+/- 12 ^{40}K :1672 +/- 55	
Larsemann Hills region – East Antarctica	Granulite	^{238}U : 118 +/- 6.8 ^{226}Ra : 56 +/- 5.5 ^{232}Th : 451 +/- 13.5 ^{40}K : 1210 +/- 9.9	(Pal et al., 2021)
Aussois – Modane region SE France	Quartzite Marble Dolomite Limestone dolomite Calcschist	^{226}Ra : 9.5 +/- 16 ^{40}K : 572 +/- 11 ^{226}Ra : 23.7 +/- 25 ^{40}K : 78 +/- 2 ^{226}Ra : 27.4 +/- 23 ^{40}K : 129 +/- 3 ^{226}Ra : 24.2 +/- 25 ^{40}K : 18 +/- 1 ^{226}Ra : 15.1 +/- 17 ^{40}K : 392 +/- 8	(Malczewski and Żaba, 2012)

Table 2.2 Natural radioactivity of soils from various geological regions.

Region	Soil type above:	Associated natural radioactivity Bq kg-1	Reference
Ashanti Beslt – SW Ghana	Conglomerate and pebbly quartzite, gold mineralisation	^{226}Ra : 13.61 +/- 5.39 ^{232}Th : 24.22 +/- 17.15 ^{40}K : 162.08 +/- 63.69	(Faanu et al., 2011)
Rio de Janeiro - Brazil	Holocene/Tertiary sediments	^{226}Ra : 31 ^{232}Th : 69 ^{40}K : 161	(Ribeiro et al., 2018)
	Migmatite	^{226}Ra : 37 ^{232}Th : 69 ^{40}K : 100	
	Granite, Granitoid	^{226}Ra : 34 ^{232}Th : 59 ^{40}K : 112	
	Gneiss, Granulite	^{226}Ra : 30 ^{232}Th : 75 ^{40}K : 109	
Global – UNSEAR	-	^{226}Ra : 35 ^{232}Th : 30 ^{40}K : 400	(United Nations Scientific Committee on the Effects of Atomic Radiation and Annex, 2000)

Volcanic region of La Garrotxa - Spain	Basaltic and basanitic	^{226}Ra : 30 ^{232}Th : 22 ^{40}K : 377	(Moreno et al., 2014)
Gaborone Granite Complex – SE Botswana	Primarily granites with minor dolomite-sandstone-shale	^{6}Ra : 34.8 ^{232}Th : 41.8 ^{40}K : 432.7	(Murty and Karunakara, 2008)

^{220}Radon (thoron) also impacts indoor radon levels although ^{222}Radon is the main contributor (Chen et al., 2015; Vuckovic et al., 2016). The research of thoron contributing to indoor radon is increasing in recent decades (Bineng et al., 2020; Chen et al., 2010; Ramola and Prasad, 2020). Considering the short half-life of thoron, it may be more of an issue in houses built with building materials containing thoron parent isotopes or houses located above certain geology types (Baptista et al., 2022; Chen, 2022). However, the primary focus of this thesis is on ^{222}Radon considering it generally accounts for the most significant portion of indoor radon.

2.2 Geochemical association of radon

In order to determine where radon gas may be geologically located, the geochemical properties of its parent isotope uranium must be considered. Uranium is an actinide and lithophile element which reflects its large atomic and ionic radii as well as its radioactive nature. The large atomic size of uranium makes it incompatible, meaning that it is prone to remaining in the liquid phase during magmatic activity. Consequentially, uranium typically resides in late-stage evolved igneous melts such as granite, with concentrations ranging from dozens to hundreds of parts per million (ppm) (Bute et al., 2020; Ibrahim et al., 2001). Uranium can also be found in significantly high quantities (hundreds ppm) in other rocks such as shales and phosphorites (Cuney, 2008; Liu et al., 2020; Romer and Cuney, 2018). The occurrence of uranium in shales and phosphorites may be explained by the hexavalent uranium (UO_4^{2-}) substituting for PO_4^{3-}, or tetravalent uranium (U^{4+}) substituting for Ca^{2+} in shales and phosphorites (Abed et al., 2016; Al-Bassam, 2007; McKelvey et al., 1955; Swanson and Swanson, 1961)

It may be possible to indicate the likelihood of a mineral being a point source of radon by examining the presence of radon precursor elements (i.e. uranium and radium) being present in the mineral. Uranium can occur as the minerals uraninite (UO_2) and autunite ($Ca(UO_2)_2(PO_4)_{2*10\text{-}12}H_2O$). Although, uranium can substitute for elements in other minerals that share the same valency; such as in zircon where isomorphous replacements occurs (Holliday et al., 2009). Uranium is more abundant in rock-forming and accessory minerals such as zircon ($ZrSiO_4$), apatite ($Ca_5(PO_5)_3(F, Cl, OH)$), Sphene ($CaTiSiO_5$) and allanite ($Ca(Ce,La,Y,Ca)Al_2(Fe_{2+},Fe_{3+})(SiO_4)(Si_2O_7)O(OH)$) (Gallagher, et al., 2016). As a decay product of uranium, radium is also found in association with uranium bearing minerals (Fabritius et al., 2022). Assuming radon precursor elements within the soil are derived from minerals that contain them, it is expected that other elements unique to these minerals will also demonstrate correlation with geogenic radon.

Geochemical soil samples containing elements associated with uranium accessory minerals could give insight into the geological and environmental processes causing uranium or radium accumulation. Such elements include Mo, Si, Ba, Se, As, Au, Zr, V, Ti and Y (Bute et al., 2020; Chen et al., 2022; Mingxing et al., 2006). Consequently, a soil sample correlated to geogenic radon that also has a statistical correlation with elements derived from uranium accessory minerals, may be indicating that the soil geochemistry is acting as a point source of radon due to the likelihood of uranium accessory minerals being present.

Uranium is reported to be leached from topsoil and redeposited in deeper horizons (Taboada et al., 2006). Primary mechanisms for uranium redistribution are adsorption to organic matter and precipitation in secondary mineral phases (Braun et al., 2017). The extent of depletion also depends on the degree of oxidation which is controlled by the depth of the water table, porosity of the soil, the rainfall and the absorption capacity of the soils themselves. The absorption capacity is controlled by the concentration of iron oxides, organics, clays and certain complexing anions such as phosphates and arsenates (Cumberland et al., 2016).

2.3 Overview of Pedogenesis

In order to comprehend the natural distribution of radon in soils, it is paramount to understand how soils are formed; and thus how radon precursor elements may naturally vary in concentration beneath the earth surface. Soil formation can be conceptualised as the balance between the production of soil (transformation of parent material or bedrock to soil) and denudation (chemical and physical loss of soil material).

$$Fsoil = Psoil - Dsoil \qquad (1)$$

where F_{soil} refers to the rate of soil formation, P_{soil} is the rate of soil production and D_{soil} is the rate of soil denudation.

$$Psoil = TPsoil + A + (O - G) \qquad (2)$$

The P_{soil} represents the transformed sum of parent material to soil (TP_{soil}). Input from the atmosphere (i.e. dust) is represented as A, whereas the organic matter net input and decay of organic matter are characterized by O and G respectively.

$$\mathrm{Dsoil} = \mathrm{Wsoil} + \mathrm{Esoil} \qquad (3)$$

Denudation (D_{soil}) symbolises the sum of erosion (E_{soil}) and chemical weathering (W_{soil}) (Dosseto et al., 2011; Heimsath et al., 1997). In this manner, the formation of soil is an intricately dynamic process whereby its present state is a result of integrating past phases of progressive pedogenesis and regressive pedogenetic phases (Johnson and Watson-Stegner, 1987; Musso et al., 2022).

The theory that provides the foundation for understanding the geochemical component of soil is researched in the discipline of pedogenesis; particularly in the pedogenesis studies that investigate the impact of parent material and weathering processes on soil composition. For example, granite or gneisses contain many micas and feldspars, thus soils derived from these parent materials would be expected to contain iron, aluminium, sodium, calcium and silicon (Egli et al., 2001; Kiczka et al., 2011; Perri et al., 2015). In contrast, soils containing parent material derived from limestone may be enriched with calcium and magnesium from aragonite and dolomite minerals (Zupančič et al., 2018). Additionally, ironstone and serpentinite parent material may add iron, magnesium, nickel and manganese to a soil profile from minerals such as hematite and chrysotile (Zinn et al., 2020). The parent material composition is intrinsically linked with the physical and chemical weathering rates (Goodfellow et al., 2009; Riebe et al., 2003). The processes integrating lithological material into soil form the foundation for applying soil geochemical data to study environmental radon risk and source distribution. Illustrations of typical soil profiles can be seen in figure 2.2.

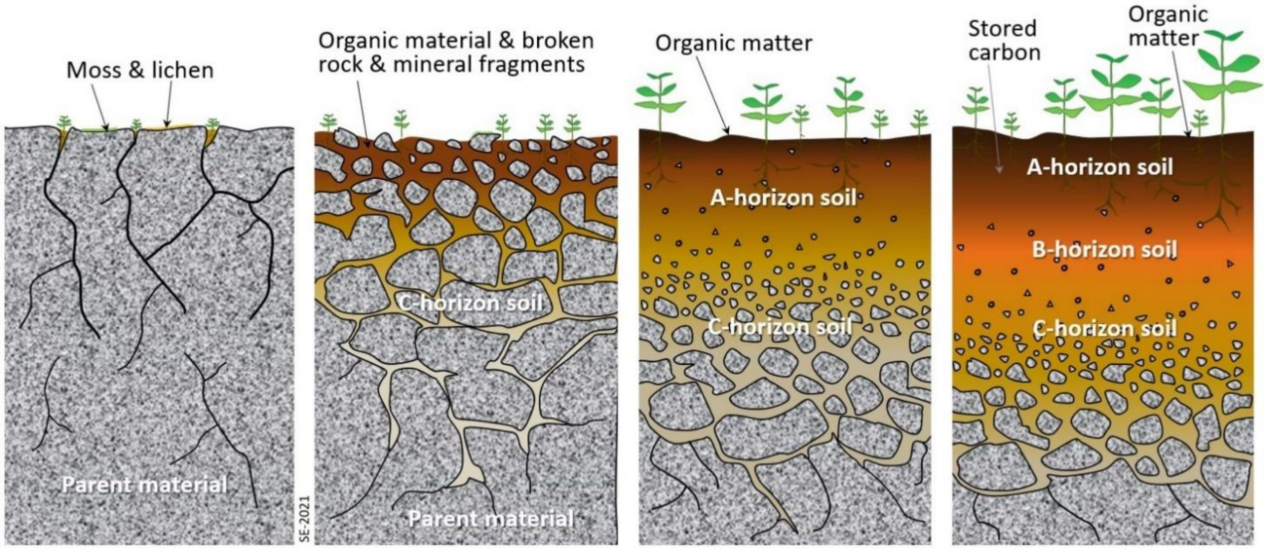

Figure 2.2 Sourced from Steven Earle, Environmental Geology, chapter 10.3 soil formation (book still under development) Thompson rivers university

2.4 Subsurface transport routes exploited by radon gas

2.4.1 Soil permeability

Soil permeability is the rate at which a gas or liquid can pass through the soil profile; and dictates the mobility which radon gas can rise from beneath the earth surface and become indoor radon. The permeability of soil is governed by natural geological processes i.e. weathering of rock, transportation and deposition by paleo-environments and modern climate/weather (as well as anthropogenic activities i.e. ploughing) and is intrinsically linked to soil physiology (Dungca and Galupino, 2017; Moldrup et al., 2001; Safari et al., 2021; Shepherd, 1989). Soil physiology refers to physical constituencies of the soil (i.e. soil grains size, sorting, the sphericity of the grains as well as the level of roundedness of the soil grains).

The physical constituencies of the soil dictate its permeability. Explicitly, if the soil grains form interconnected pore spaces, then the soil will have effective porosity. High effective porosity enables liquid and/or gas to move easily in the soil, making it highly permeable. Whereas low effective porosity inhibits liquid or/and gas from moving with ease throughout the soil profile. In that capacity, the underlying mechanism of soil permeability is a principal parameter for understanding geogenic radon risk in an area.

2.4.2 Structural geology

There are a range of structural geology features that gases including radon can exploit to reach the surface. For instance, eruptive fissures in igneous settings (Neri et al., 2016; Shimoike et al., 2002)(Padrón et al., 2013), karstification in limestone regions (Cucoș et al., 2021; Sukanya et al., 2022), and non-mineralised faults (Ioannides et al., 2003; Mahajan et al., 2010; Sun et al., 2018). The underlying characteristics of the structural geology in an area can be a significant factor increasing radon levels in an area. For example, there are reports of elevated indoor radon occurring in karst regions which are naturally low in radon precursor elements; the increased levels of geogenic radon can be caused by elevated permeability in the subsurface due to underlying karst bedrock (Long et al., 2016).

2.5 Geology of study area

2.5.1 Geology of primary study area Castleisland Co. Kerry

The study area is 6 km^2 and located in the south-west of Ireland, around a town named Castleisland in Co. Kerry (fig.4.1). The Castleisland and surrounding areas are underlain by Dinantian (359 Ma – 326 Ma) limestones which formed on a continental shelf in a subtidal open water zone (Sleeman et al., 2004). Geologically, the Castleisland study area is situated between the Shannon Basin and South Munster Basin which formed after the closure of the Iapetus Ocean. Specifically, the study area is located several kilometres north to the axial plane of an anticlinal E—W trending fold (Pracht, 1997).

The Rockfield limestones, Waulsortian limestones, Cracoean reef member and Dirtoge limestones form the bedrock beneath the study area, mainly in the south. Two other lithologies, the Namurian (326 Ma – 313 Ma) Clare Shales and Carboniferous (358.9 Ma – 298.9 Ma) Cloone flagstones are located in the north of the study area. The bedrock is overlain by two main Quaternary geologies; glacial till derived from limestone is mainly present in the south of the study area, with alluvium occurring in a narrow east-west trend. Whereas, the north of the study area is largely composed of glacial till derived from Namurian sandstones, siltstones and shales.

It is commonly accepted that the geology around Castleisland town was deformed at the northern edge of the Variscan front; resulting in large amplitude anticlines, reverse, normal and wrench faulting as well as minor parasitic folds and minor faulting associated with buckling (Brennand, 1965; Pracht, 1997). Extensive karstification features are present in the limestones, including Crag cave, the Carrignafeela and Potaley underground stream system and the Tobermaing sink and rising (Organo and Murphy, 2007).

2.5.2 Geology of TELLUS midlands area.

The TELLUS midlands dataset includes samples collected from counties Galway, Mayo, Offaly, Roscommon, Longford, Westmeath, Wicklow, Meath, Kildare and Dublin. The geology of the area consists mainly of a range of limestones that formed during the Carboniferous (Beck, 2010). Specifically, a northward shallow marine transgression caused by tectonic subsidence coupled with sea-level rise resulted in sea-shelf facies (including dark limestone and shale, dark cherty limestone, pale grey packstones and wackstones, massive lime-mudstones, cherty and undifferentiated limestones) to be deposited across the midlands during the Dinantian (Beck, 2010; Hitzman, 1995; Pracht et al., 2015).

The Dublin basin is located to the east of the Midlands dataset and is fault-bounded on its southern and northern margins (Sevastopulo and Wyse Jackson, 2009). During the lower Carboniferous, Caledonian structures were reactivated resulting in the development of deeper water carbonate turbidite facies in the Dublin basin; (Phillips and Sevastopulo, 1986; Somerville et al., 1992; Strogen et al., 1996).

The Galway porphyritic-megacrystic granites were emplaced in the late Caledonian (~400 Ma) into Grampian metamorphic rocks (~470 Ma metagabbro-gneiss suite in the north and Ordovician greenschist-facies rocks in the south) (Baxter et al., 2005). Samples from north of the Leinster granite in Co. Wicklow are included in the TELLUS midlands dataset. The Leinster granite formed after en-echelon intrusion of five plutons into lower Palaeozoic host rocks during the Caledonian orogeny (McArdle and Kennedy, 1986; McConnell and Philcox, 1994; Reavy, 2001).

2.6 Co-author statement

As the first author on all three papers (chapters 2, 3 and 4), I completed the vast majority of the work involved; including sample collection, sample processing and preparing for analysis. I produced most of the tables, figures, statistical and analysis results and led the interpretation and writing of the manuscripts.

The roles of each co-author to the manuscripts forming chapters 3, 4 and 5 are as follows:

Prof. Quentin Crowley – my supervisor at Trinity College Dublin. Prof. Crowley has many years of experience and expertise in researching radon which helped ensure each manuscript was designed to bring novelty and value to the geogenic radon community. Additionally, Prof. Crowley provided feedback, encouragement and direction over the past 4 years that ensured quality manuscripts were submitted for publication. Quentin has been the main discussion partner for this project over the past four years, stimulating many learning perspectives.

Dr. Javier Elío – Post-doctorate researcher at Aalborg University Denmark. Dr. Elío is an expert in modelling radon. Dr. Elío contributed a figure and provided direction and feedback for the first manuscript (chapter 3). Dr. Elío also reviewed and provided feedback for the second manuscript (chapter 4). Dr. Elío has been an important discussion partner regarding many aspects of modelling radon.

Mr. Matteo Cobelli – Ph.D. researcher Centre for Research on Adaptive Nanostructures and Nanodevices (CRANN), Trinity College Dublin. Mr. Cobelli has many years' experience in computational physics. Mr. Cobelli played an important role in overseeing the code used for the machine learning models in chapter 5. Without Mr. Cobelli's contribution, the results of the machine learning models would not be as rigorous. Mr. Cobelli has been an important discussion partner for refining the models. Many different models were tested before deciding the models presented in chapter 5.

2.7 References

Abbady, A.G.E., Uosif, M.A.M., El-Taher, A., 2005. Natural radioactivity and dose assessment for phosphate rocks from Wadi El-Mashash and El-Mahamid Mines, Egypt. Journal of Environmental Radioactivity 84, 65–78. https://doi.org/10.1016/j.jenvrad.2005.04.003

Abed, A.M., Jaber, O., Alkuisi, M., Sadaqah, R., 2016. Rare earth elements and uranium geochemistry in the Al-Kora phosphorite province, Late Cretaceous, northwestern Jordan. Arabian Journal of Geosciences 9, 1–19.

Abed, N.S., Monsif, M.A., Zakaly, H.M., Awad, H.A., Hessien, M.M., Yap, C.K., 2022. Assessing the radiological risks associated with high natural radioactivity of microgranitic rocks: A case study in a northeastern desert of Egypt. International Journal of Environmental Research and Public Health 19, 473.

Al-Bassam, K.S., 2007. Uranium in the Iraqi phosphorites. Iraqi Bulletin of Geology and Mining 3, 13–31.

Al-Khawlany, A., Khan, A., Pathan, J., 2018. Review on studies in natural background radiation. Radiation Protection and Environment.

Alshahrani, B.E., 2021. Natural radioactivity level in pumice rock, in Saudi Arabia and effect on human health. null 1–12. https://doi.org/10.1080/03067319.2021.1907363

Baptista, E., Pereira, A.J.S.C., Domingos, F.P., Sêco, S.L.R., 2022. Radon and thoron concentrations in the southwest region of Angola: dose assessment and implications for risk mapping. Environmental Geochemistry and Health. https://doi.org/10.1007/s10653-022-01226-8

Baxter, S., Graham, N.T., Feely, M., Reavy, R.J., Dewey, J.F., 2005. A microstructural and fabric study of the Galway Granite, Connemara, western Ireland. Geological Magazine 142, 81–95. https://doi.org/10.1017/S0016756804000378

Beck, B.F., 2010. CH Holland, IS Sanders (eds): The Geology of Ireland, 2nd edn.

Bineng, G.S., Tokonami, S., Hosoda, M., Tchuente Siaka, Y.F., Issa, H., Suzuki, T., Kudo, H., Bouba, O., 2020. The importance of direct progeny measurements for correct estimation of effective dose due to radon and thoron. Frontiers in Public Health 8, 17.

Bowie, C., Bowie, S.H.U., 1991. Radon and health. The Lancet 337, 409–413.

Braun, J., Riotte, J., Battacharya, S., Violette, A., Prunier, J., Bouvier, V., Candaudap, F., Maréchal, J., Ruiz, L., Panda, S.R., 2017. REY-Th-U solute dynamics in the critical zone: Combined influence of chemical weathering, atmospheric deposit leaching, and vegetation cycling (Mule Hole Watershed, South India). Geochemistry, Geophysics, Geosystems 18, 4409–4425.

Brennand, T.P., 1962. The Carboniferous geology of the Castleisland area. Unpublished PhD thesis, University of Dublin.

Bute, S.I., Yang, X., Suh, C.E., Girei, M.B., Usman, M.B., 2020. Mineralogy, geochemistry and ore genesis of Kanawa uranium mineralization, Hawal Massif, eastern Nigeria terrane: Implications for uranium prospecting in Nigeria and Cameroon. Ore Geology Reviews 120, 103381. https://doi.org/10.1016/j.oregeorev.2020.103381

Chen, J., 2022. Assessment of thoron contribution to indoor radon exposure in Canada. Radiation and Environmental Biophysics 61, 161–167. https://doi.org/10.1007/s00411-021-00956-0

Chen, J., Bergman, L., Falcomer, R., Whyte, J., 2015. Results of simultaneous radon and thoron measurements in 33 metropolitan areas of Canada. Radiation Protection Dosimetry 163, 210–216. https://doi.org/10.1093/rpd/ncu141

Chen, J., Dessau, J.C., Frenette, E., Moir, D., Cornett, R.J., 2010. Preliminary assessment of thoron exposure in Canada. Radiation Protection Dosimetry 141, 322–327. https://doi.org/10.1093/rpd/ncq226

Chen, X., Wen, C., Meng, D., Li, B., Jiang, B., Qin, J., 2022. Implications of Major and Trace Element Migration in Altered Granites for Hydrothermal Alteration and Granite-Related Uranium Mineralization in the Sanjiu Ore Field, South China. Minerals 12. https://doi.org/10.3390/min12020144

Cucoş Dinu, A., Călugăr, M.I., Burghele, B.D., Dumitru, O.A., Cosma, C., Onac, B.P., 2017. Radon levels in Romanian caves: an occupational exposure survey. Environmental Geochemistry and Health 39, 1085–1099. https://doi.org/10.1007/s10653-016-9878-1

Cumberland, S., Grice, K., Douglas, G., Moreau, J.W., 2016. Uranium mobility in organic matter-rich sediments: A review of geological and geochemical processes. Earth-Science Reviews Volume 159, pp. 160-185. https://doi.org/10.1016/j.earscirev.2016.05.010}

Cuney, M., 2008. The extreme diversity of uranium deposits. Mineralium Deposita 44, 3. https://doi.org/10.1007/s00126-008-0223-1

Degu Belete, G., Alemu Anteneh, Y., 2021. General Overview of Radon Studies in Health Hazard Perspectives. Journal of Oncology 2021.

Dorn, F.E., 1901. "Ueber die von radioaktiven Substanzen ausgesandte Emanation.

Dosseto, A., Buss, H., Suresh, P.O., 2011. The delicate balance between soil production and erosion, and its role on landscape evolution. Applied Geochemistry 26, S24–S27. https://doi.org/10.1016/j.apgeochem.2011.03.020

Dungca, J., Galupino, J., 2017. Artificial neural network permeability modeling of soil blended with fly ash. GEOMATE 12, 77–82. https://doi.org/10.21660/2017.31.6549

Egli, M., Mirabella, A., Fitze, P., 2001. Clay mineral formation in soils of two different chronosequences in the Swiss Alps. Geoderma 104, 145–175. https://doi.org/10.1016/S0016-7061(01)00079-9

Faanu, A., Darko, E., Ephraim, J., 2011. Determination of natural radioactivity and hazard in soil and rock samples in a mining area in Ghana. West African Journal of Applied Ecology 19.

Fabritius, O., Puhakka, E., Li, X., Nurminen, A., Siitari-Kauppi, M., 2022. Radium sorption on biotite; surface complexation modeling study. Applied Geochemistry 140, 105289.

Gaafar, I., Hanfi, M., El-Ahll, L.S., Zeidan, I., 2021. Assessment of radiation hazards from phosphate rocks, Sibaiya area, central eastern desert, Egypt. Applied Radiation and Isotopes 173, 109734. https://doi.org/10.1016/j.apradiso.2021.109734

Gallagher, V., Knights, K.V., Carey, S., Glennon, M., Scanlon, R., 2016. Atlas of topsoil geochemistry of the Northern Counties of Ireland: Data from the Tellus and Tellus border projects. Geological Survey of Ireland.

Goodfellow, B.W., Fredin, O., Derron, M.-H., Stroeven, A.P., 2009. Weathering processes and Quaternary origin of an alpine blockfield in Arctic Sweden. Boreas 38, 379–398. https://doi.org/10.1111/j.1502-3885.2008.00061.x

Hamideen, M.S., Bdair, O.M., Chandrasekaran, A., Saleh, H., Elimat, Z., 2020. Multivariate statistical investigations of natural radioactivity and radiological hazards in building materials mainly used in Amman Province, Jordan. International Journal of Environmental Analytical Chemistry 100, 189–203.

Harb, S., Abbady, A.E.-B., El-Kamel, A.E.-H., Saleh, I.I., Abd El-Mageed, A.I., 2012. Natural radioactivity and their radiological effects for different types of rocks from Egypt. Radiation Physics and Chemistry 81, 221–225. https://doi.org/10.1016/j.radphyschem.2011.11.005

Heimsath, A.M., Dietrich, W.E., Nishiizumi, K., Finkel, R.C., 1997. The soil production function and landscape equilibrium. Nature 388, 358–361. https://doi.org/10.1038/41056

Hitzman, M., 1995. Geological setting of the Irish Zn-Pb-(Ba-Ag) orefield.

Holliday, K., Hartmann, T., Poineau, F., Rory Kennedy, J., Czerwinski, K., 2009. Synthesis and characterization of zirconia–magnesia inert matrix fuel: Uranium homolog studies. Journal of Nuclear Materials 393, 224–229. https://doi.org/10.1016/j.jnucmat.2009.06.007

Ibrahim, M.E., Saleh, G.M., Abd El-Naby, H.H., 2001. Uranium mineralization in the two mica granite of Gabal Ribdab area, South Eastern Desert, Egypt. Applied Radiation and Isotopes 55, 861–872. https://doi.org/10.1016/S0969-8043(01)00122-1

ICRP, 2019. Radiological protection from naturally occuring radioactive material (NORM) in industrial processes. 142.

Ioannides, K., Papachristodoulou, C., Stamoulis, K., Karamanis, D., Pavlides, S., Chatzipetros, A., Karakala, E., 2003. Soil gas radon: a tool for exploring active fault zones. Applied Radiation and Isotopes 59, 205–213.

Johnson, D.L., Watson-Stegner, D., 1987. Evolution model of pedogenesis. Soil Science 143, 349–366.

Kiczka, M., Wiederhold, J.G., Frommer, J., Voegelin, A., Kraemer, S.M., Bourdon, B., Kretzschmar, R., 2011. Iron speciation and isotope fractionation during silicate weathering and soil formation in an alpine glacier forefield chronosequence. Geochimica et Cosmochimica Acta 75, 5559–5573. https://doi.org/10.1016/j.gca.2011.07.008

Kim, S.W., Kee, W.-S., Lee, S., Lee, B.C., Byun, U.H., 2021. Tracking and Evaluating the Concentrations of Natural Radioactivity According to Chemical Composition in the Precambrian and Mesozoic Granitic Rocks in the Jangsu-gun Area, Central Southwestern South Korea. Minerals 11. https://doi.org/10.3390/min11070684

Liu, B., Mastalerz, M., Schieber, J., Teng, J., 2020. Association of uranium with macerals in marine black shales: Insights from the Upper Devonian New Albany Shale, Illinois Basin. International Journal of Coal Geology 217, 103351. https://doi.org/10.1016/j.coal.2019.103351

Long, S.C., Fenton, D., Scivyer, C., Monahan, E., 2016. Factors underlying persistently high radon levels in a house located in a karst limestone region of Ireland – lessons learned about remediation. Nukleonika 61, 327–332. https://doi.org/10.1515/nuka-2016-0054

Mahajan, S., Walia, V., Bajwa, B., Kumar, A., Singh, S., Seth, N., Dhar, S., Gill, G., Yang, T., 2010. Soil-gas radon/helium surveys in some neotectonic areas of NW Himalayan foothills, India. Natural Hazards and Earth System Sciences 10, 1221–1227.

Malczewski, D., Dziurowicz, M., Kalab, Z., Rösnerová, M., 2021. Natural radioactivity of rocks from the historic Jeroným Mine in the Czech Republic. Environmental Earth Sciences 80, 650. https://doi.org/10.1007/s12665-021-09944-5

Malczewski, D., Żaba, J., 2012. Natural radioactivity in rocks of the Modane–Aussois region (SE France). Journal of Radioanalytical and Nuclear Chemistry 292, 123–130. https://doi.org/10.1007/s10967-011-1428-9

McArdle, P., Kennedy, M., 1986. The east Carlow deformation zone and its regional implications.

McConnell, B., Philcox, M., 1994. Geology of Kildare-Wicklow: a geological description to accompany the bedrock geology 1: 100,000 Map Series, Sheet 16, Kildare-Wicklow. Published under the authority of the Director of the Geological Survey of ….

McKelvey, V.E., Everhart, D.L., Garrels, R.M., 1955. Origin of uranium deposits.

Mingxing, L., Xiaoyong, Y., Wei, S., Jianyu, M., Chiyang, L., 2006. REE/trace element characteristics of sandstone-type uranium deposits in the Ordos basin.

Moldrup, P., Olesen, T., Komatsu, T., Schjønning, P., Rolston, D., 2001. Tortuosity, diffusivity, and permeability in the soil liquid and gaseous phases. Soil Science Society of America Journal 65, 613–623.

Moreno, V., Bach, J., Baixeras, C., Font, Ll., 2014. Radon levels in groundwaters and natural radioactivity in soils of the volcanic region of La Garrotxa, Spain. Journal of Environmental Radioactivity 128, 1–8. https://doi.org/10.1016/j.jenvrad.2013.10.021

Murty, V.R.K., Karunakara, N., 2008. Natural radioactivity in the soil samples of Botswana. Radiation Measurements 43, 1541–1545. https://doi.org/10.1016/j.radmeas.2008.10.004

Musso, A., Tikhomirov, D., Plötze, M.L., Greinwald, K., Hartmann, A., Geitner, C., Maier, F., Petibon, F., Egli, M., 2022. Soil Formation and Mass Redistribution during the Holocene Using

Meteoric 10Be, Soil Chemistry and Mineralogy. Geosciences 12. https://doi.org/10.3390/geosciences12020099

Neri, M., Ferrera, E., Giammanco, S., Currenti, G., Cirrincione, R., Patanè, G., Zanon, V., 2016. Soil radon measurements as a potential tracer of tectonic and volcanic activity. Scientific Reports 6, 24581. https://doi.org/10.1038/srep24581

Organo, C., Ellard, A., Fenton, D., Synnott, H., O'Colmáin, M., Prenter, S., O'Reilly, S., Colgan, P., 2004. High radon concentrations in a house near Castleisland, County Kerry (Ireland)—identification, remediation and post-remediation. Journal of Radiological Protection 24, 107. https://doi.org/10.1088/0952-4746/24/2/001

Organo, C., Murphy, P., 2007. The Castleisland Radon Survey—follow-up to the discovery of a house with extremely high radon concentrations in County Kerry (SW Ireland). Journal of Radiological Protection 27. https://doi.org/10.1088/0952-4746/27/3/002

Padrón, E., Padilla, G., Hernández, P.A., Pérez, N.M., Calvo, D., Nolasco, D., Barrancos, J., Melián, G.V., Dionis, S., Rodríguez, F., 2013. Soil gas geochemistry in relation to eruptive fissures on Timanfaya volcano, Lanzarote Island (Canary Islands, Spain). Journal of Volcanology and Geothermal Research 250, 91–99. https://doi.org/10.1016/j.jvolgeores.2012.10.013

Pal, R., Patra, A.C., Bakshi, A.K., Dhabekar, B., Reddy, P.J., Sengupta, P., Sapra, B.K., 2021. Investigations on baseline levels for natural radioactivity in soils, rocks, and lakes of Larsemann Hills in East Antarctica. Environmental Monitoring and Assessment 193, 822. https://doi.org/10.1007/s10661-021-09446-8

Perri, F., Scarciglia, F., Apollaro, C., Marini, L., 2015. Characterization of granitoid profiles in the Sila Massif (Calabria, southern Italy) and reconstruction of weathering processes by mineralogy, chemistry, and reaction path modeling. Journal of Soils and Sediments 15, 1351–1372. https://doi.org/10.1007/s11368-014-0856-x

Phillips, W., Sevastopulo, G., 1986. The stratigraphic and structural setting of Irish mineral deposits. Presented at the Geology and genesis of mineral deposits in Ireland, pp. 1–30.

Pracht, M., 1997. Geology of Kerry - Cork: A geological description to accompany the bedrock geology 1:100,000 scale map series, sheet 21, Kerry-Cork.

Pracht, M., Somerville, I.D., Wang, Y., 2015. A revised Mississippian lithostratigraphy of County Galway (western Ireland) with an analysis of carbonate lithofacies, biostratigraphy, depositional environments and palaeogeographic reconstructions utilising new borehole data. Journal of Palaeogeography 4, 1–26. https://doi.org/10.3724/SP.J.1261.2015.00065

Radvanyi, P., Villain, J., 2017. The discovery of radioactivity. Comptes Rendus Physique 18, 544–550. https://doi.org/10.1016/j.crhy.2017.10.008

Ramola, R.C., Prasad, M., 2020. Significance of thoron measurements in indoor environment. Journal of Environmental Radioactivity 225, 106453. https://doi.org/10.1016/j.jenvrad.2020.106453

Reavy, R.J., 2001. Caledonian granites–emplacement. Open University Geological Society Journal 22.

Ribeiro, F.C.A., Silva, J.I.R., Lima, E.S.A., do Amaral Sobrinho, N.M.B., Perez, D.V., Lauria, D.C., 2018. Natural radioactivity in soils of the state of Rio de Janeiro (Brazil): Radiological characterization and relationships to geological formation, soil types and soil properties. Journal of Environmental Radioactivity 182, 34–43. https://doi.org/10.1016/j.jenvrad.2017.11.017

Riebe, C.S., Kirchner, J.W., Finkel, R.C., 2003. Long-term rates of chemical weathering and physical erosion from cosmogenic nuclides and geochemical mass balance. Geochimica et Cosmochimica Acta 67, 4411–4427. https://doi.org/10.1016/S0016-7037(03)00382-X

Romer, R.L., Cuney, M., 2018. Phanerozoic uranium mineralization in Variscan Europe – More than 400 Ma of tectonic, supergene, and climate-controlled uranium redistribution. Ore Geology Reviews 102, 474–504. https://doi.org/10.1016/j.oregeorev.2018.09.013

Safari, M., Gholami, R., Jami, M., Ananthan, M.A., Rahimi, A., Khur, W.S., 2021. Developing a porosity-permeability relationship for ellipsoidal grains: A correction shape factor for Kozeny-Carman's equation. Journal of Petroleum Science and Engineering 205, 108896.

Sevastopulo, G.D., Wyse Jackson, P., 2009. Carboniferous: Mississippian (Tournaisian and Viséan). The geology of Ireland 215–268.

Shepherd, R.G., 1989. Correlations of permeability and grain size. Groundwater 27, 633–638.

Shimoike, Y., Kazahaya, K., Shinohara, H., 2002. Soil gas emission of volcanic CO2 at Satsuma-Iwojima volcano, Japan. Earth, planets and space 54, 239–247.

Somerville, I.D., Strogen, P., Jones, G.Ll., 1992. Mid-Dinantian Waulsortian buildups in the Dublin Basin, Ireland. Sedimentary Geology 79, 91–116. https://doi.org/10.1016/0037-0738(92)90006-D

Strogen, P., Somerville, I., Pickard, N., Jones, G.L., Fleming, M., 1996. Controls on ramp, platform and basinal sedimentation in the Dinantian of the Dublin Basin and Shannon Trough, Ireland. Geological Society, London, Special Publications 107, 263–279.

Sukanya, S., Noble, J., Joseph, S., 2022. Application of radon (222Rn) as an environmental tracer in hydrogeological and geological investigations: An overview. Chemosphere 303, 135141. https://doi.org/10.1016/j.chemosphere.2022.135141

Sun, X., Yang, P., Xiang, Y., Si, X., Liu, D., 2018. Across-fault distributions of radon concentrations in soil gas for different tectonic environments. Geosciences Journal 22, 227–239.

Sutton, G.A., Napier, S.T., John, M., Taylor, A., 1993. Uranium-238 decay chain data. Science of The Total Environment 130–131, 393–401. https://doi.org/10.1016/0048-9697(93)90094-M

Swanson, Vernon E, Swanson, Vernon Emanuel, 1961. Geology and geochemistry of uranium in marine black shales: a review. US Government Printing Office Washington, DC.

Taboada, T., Cortizas, A.M., García, C., García-Rodeja, E., 2006. Uranium and thorium in weathering and pedogenetic profiles developed on granitic rocks from NW Spain. Science of the Total Environment 356, 192–206.

Tzortzis, M., Tsertos, H., Christofides, S., Christodoulides, G., 2003. Gamma-ray measurements of naturally occurring radioactive samples from Cyprus characteristic geological rocks. Radiation Measurements 37, 221–229. https://doi.org/10.1016/S1350-4487(03)00028-3

United Nations Scientific Committee on the Effects of Atomic Radiation, Annex, B., 2000. Exposures from natural radiation sources. New york, United Nation 9, 11.

Vuckovic, B., Gulan, L., Milenkovic, B., Stajic, J.M., Milic, G., 2016. Indoor radon and thoron concentrations in some towns of central and South Serbia. Journal of Environmental Management 183, 938–944. https://doi.org/10.1016/j.jenvman.2016.09.053

World Health Organization (Ed.), 2009. WHO handbook on indoor radon: a public health perspective. World Health Organization.

Zinn, Y.L., Faria, J.A. de, Araujo, M.A. de, Skorupa, A.L.A., 2020. Soil parent material is the main control on heavy metal concentrations in tropical highlands of Brazil. CATENA 185, 104319. https://doi.org/10.1016/j.catena.2019.104319

Zupančič, N., Turniški, R., Miler, M., Grčman, H., 2018. Geochemical fingerprint of insoluble material in soil on different limestone formations. CATENA 170, 10–24. https://doi.org/10.1016/j.catena.2018.05.040

Chapter 3

A user's guide to radon priority areas, examples from Ireland

Published in Journal of European Radon Association 2022

Banríon M.H. [(1)], Elío J. [(2)], Crowley Q.G. [(1)]

(1) Geology department, School of Natural Sciences, Trinity College, Dublin 2, Ireland

(2) Department of Planning, Aalborg University Copenhagen, Copenhagen, Denmark

*Corresponding author, email: crowleyq@tcd.ie

Abstract

Exposure to radon over time has significant detrimental effects on human health. Approximately 226,000 annual radon-related deaths have been reported from 66 countries (Gaskin et al., 2018). Many countries have a radon action plan, in order to reduce the harmful effects of radon exposure on the general public. Maps are routinely used to assist with mitigation strategies and delineate areas of priority regulation. Standard regulations in the European Union include the requirement for workplaces to test and the requirement to have reduction methods in newly built homes. Such laws are assigned systematically to areas that are understood to have high values of indoor radon. This article demonstrates that the boundaries of radon priority areas may vary, depending on the data set and methods used. We propose a table and a decision matrix to assist in choosing the most appropriate visual aid according to the purpose for which the map is to be used. We conclude that no single radon map is suitable to fit all objectives, and some maps are more suitable than others depending on the purpose.

Keywords:

Indoor radon; radon maps; radon mapping objectives; spatial resolution; geogenic data.

Abbreviations:

InRn: Indoor radon; RPA: Radon priority area; HRA: High radon area; RL: Reference level; GRP: Geogenic radon potential.

3.1 Introduction

Mitigating the level of radioactive exposure to citizens has been the task of many countries for decades (European Commission, 2013; United Nations, 1958; World Health Organization, 2007). The radioactive exposure mitigated against includes natural (e.g. radon) and anthropogenic (e.g. nuclear energy and medical x-rays) sources. This article focuses on the mapping and modelling of radon gas and its possible negative health effects on the general public, which accounts for approximately 50% of a person's radiation dose (Monty, 2000). Radon is a natural gas that poses a negligible health risk when outdoors, with radon concentrations in the order of 10's of Bq m^{-3} (Gunning, 2016). However, radon can accumulate inside dwellings and caves, typically from 100's of Bq m^{-3} to 1,000's of Bq m^{-3}, respectively (Darby et al., 2005; Duffy et al., 1996). Exposure to higher radon concentrations is linked to the development of health ailments, the most commonly recognized of which is lung cancer (Kreuzer et al., 2015; Lorenzo-González et al., 2019; Ludewig and Lorenser, 1924; Vahakangas et al., 1992; World Health Organization, 2009; Yarmoshenko and Malinovsky, 2016). Other diseases (e.g. skin cancer, non-Hodgkin's lymphoma, stomach cancer and brain cancer) may be correlated with radon exposure, and any causative links are still under investigation (Ha et al., 2017; López-Abente et al., 2018; Monastero and Meliker, 2020; Ruano-Ravina et al., 2018).

Radon (Rn) is the largest contributor of natural radioactivity to the general public. The ^{222}Rn isotope is considered the primary radon risk source indoors (Rosario and Wichmann, 2006; Schwela, 2014; Tommasino, 2005) due to its relatively long half-life (i.e. 3.8 days). ^{222}Rn is commonly used indistinctly in the legislation, and the definitions of radon priority areas (RPAs) are based on this isotope. Therefore, we use this criterion in the text; however, another natural radon isotope that may pose a risk in particular circumstances is thoron (i.e. ^{220}Rn; half-life of 55.6 s), and it is attracting more attention with the development of the first thoron maps

(Lucchetti et al., 2019; Pandurang et al., 2014; Vuckovic et al., 2016). ^{222}Rn, ^{220}Rn and their daughter products emit alpha particles, damaging lung tissue if inhaled (Krewski et al., 2019; Lorenzo-González et al., 2019; Samet, 1989; Taylor et al., 1994). ^{222}Rn and ^{220}Rn concentrations naturally vary geo-spatially, influenced by soil geochemistry, soil permeability and underlying geogenic factors (Elío et al., 2017; Ferreira et al., 2018; Gallagher et al., 2016; Je et al., 1999; Young et al., 2016). Furthermore, indoor radon (hereafter referred to as InRn) accumulation is also influenced by weather/climate, housing and occupancy characteristics (Akbari et al., 2013; Casal-Mouriño et al., 2020; Lantz et al., 2013; Muntean et al., 2014; Rigby and La Pointe, 1993).

The issue of radioactivity, including radon, is recognized by the European Union (EU), which has resulted in the development of an EU Directive (Basic Safety Standards, BSS) that obliges member states to assign Radon Priority Area's (hereafter referred to as RPAs). The EU Directive aims to protect both individuals and the collective from radiation exposure (European Commission, 2013). The aforementioned directive requires a National Radon Action Plan (NRAP) to be established, which addresses radon risk in water, domestic dwellings, public buildings and workplaces from radon ingress, whether from the soil, water or building materials. Furthermore, this directive requires that effective radon mitigation and prevention measures are established for new buildings. It legally binds the member states to identify areas where 'the radon concentration in a significant number of buildings is expected to exceed the relevant national reference level'. However, the definitions of 'a significant amount of buildings' and 'the reference level' are not clarified, allowing for different methods to be used. In turn, this can lead to radon risk maps, which are not directly comparable, and different evaluations needed to assess the success of each Action Plan (Tollefsen et al., 2014).

Therefore, the Directive obligates EU member states to create radon maps where the spatial distribution of indoor radon levels is presented. The radon maps are consequently useful for: (1) predicting regions with non-acceptable levels at home/workplace, (2) targeting public awareness, (3) estimating radiation dose from radon and (4) studying the health effects of radon. The tools needed to achieve each objective may be different, and thus, different maps would be required simultaneously (Elío et al., 2018). The different types of radon hazard index maps should be distinguished to avoid confusion (Bossew et al., 2020).

In Ireland, the 1997 Building Regulations state that high radon can occur in any part of the country (Building Regulations, 1997). However, only buildings in high radon areas (HRA) are legally obliged to include mitigation measures in their construction, for example, a membrane and a subsurface radon extraction device (i.e. sump) should be provided. In other areas, a subsurface radon extraction device should be installed in case it needs to be activated at a future time. Other buildings do not have specific guidance in the 1997 regulations. In relation to gamma radiation for building materials, the Radiological Protection Act 1991 (Radiological Protection Act 1991 (Ionising Radiation) Regulations, 2019) states, in Regulation 67, that building materials should not emit more than 1 mSv of gamma radiation per year. Schedule 10 gives an indicative list of building materials with the potential to emit gamma radiation (Radiological Protection Act 1991 (Ionising Radiation) Regulations, 2019).

Building developers and employers in High Radon Area’s (hereafter referred to as HRA) are legally obliged to prevent, remediate and ensure that their buildings/workplaces are below the radon Reference Level (hereafter referred to as RL). HRA receive priority regulation, which is necessary to reduce the harmful effects of natural radiation cost-effectively. The most recently established national RL decided by the EPA in Ireland should not exceed 300 Bq m^{-3} in homes as well as workplaces (Radiological Protection Act 1991 (Ionising Radiation) Regulations, 2019). Currently, the EPA decided a more conservative value, which, keeping with legislation, is 200 Bq m^{-3} for homes and 300 Bq m^{-3} for workplaces. As such, in Ireland, HRA for dwellings are defined as ‘any area where it is predicted that 10% or more of homes will exceed the reference level of 200 Becquerels per cubic meter (Bq m^{-3})’ (Environmental Protection Agency Ireland, 2020). The initiatives to reduce radon from accumulating in a building could be considered a primary prevention method, whereas targeting public awareness and mitigation in HRA could be regarded as secondary and tertiary prevention measures.

3.2 Radon priority areas and mapping

RPAs signify areas that may have a higher radon risk than others. Such sites are prioritised for public awareness initiatives and are specially protected through the building regulations. RPAs are legally defined and can be determined using different data and criteria, which can lead to differing RPA boundaries in the same location (Bossew, 2018). Without appropriate strategy and communication, such discrepancies can lead to loss in fidelity of information, loss of credibility, and diminished public trust and interest. Numerous methods have been used by different countries in Europe (Table 3.1). An in-depth report of natural radiation and the various techniques can be read in the European Atlas of Natural Radiation (Cinelli et al., 2020). The studies referred to in Table 3.1 utilize different concepts of radon risk, but all are valid. These concepts range from an area having a probability of Indoor Radon (InRn) over the RL to the likelihood of developing lung cancer in a given region. In the following sections, we discuss the most relevant approaches.

Table 3.1 Average indoor radon values have been grouped to administrative levels, as seen for Austria and Ireland. Grids of 1 km^2 have been utilized in Belgium, the UK and Ireland. Austria and Norway used geological units. Several reference levels operate across the member states. These range from 100 Bq m–3 in Malta, 200 Bq m^{-3} in Ireland, Norway and the UK, and 400 Bq m^{-3} in Belgium. Adapted from Ref. (57).

Country	Reference Level	Objectives	Methods	Resolution	Reference
Austria	200 and 400 Bq m^{-3}	Divide the country in three classes: i.e. average annual concentration <200, 200 - 400, and > 400 Bq m^{-3}	Annual mean radon concentration in a standard situation	Administrative Level (i.e. municipality)	(Friedmann, 2005)
			Bayesian statistics, combining indoor radon measurements (standard situation) and geology	Geological classes (scale 1:500.000)	(Friedmann and Gröller, 2010)
Belgium (Wallon region)	400 Bq m^{-3}	Percentage of dwellings above the R.L. taking into account geological information	Moving average between geological units	1 km x 1 km	(Cinelli et al., 2011)
United Kingdom	200 Bq m^{-3}	Percentage of houses above the R.L., taking into account geological information. RPA when P[InRn > RL]≥1%	Lognormal model, corrections to account for year-to-year and random variations (i.e., Bayesian statistics)	Grids 1km×1km	(Daraktchieva et al., 2015; Miles, 1997; Miles et al., 2007)
Norway	200 Bq m^{-3}	Percentage of houses above the R.L. based on indoor radon and geological information (bedrock and Quaternary geology). RPA when P[InRn > RL]≥20%.	Classify geological polygons according to local (polygon) statistics or national (class) statistics	Geological polygons	Watson et al. (2017) (Watson et al., 2017)
Ireland	200 Bq m^{-3}	Percentage of houses above the R.L. based solely on indoor	Lognormal model	Grids 10km×10km	Fennell et al. (2002)

Country	Reference Level	Objectives	Methods	Resolution	Reference
		radon measurements R.P.A. when P[InRn > R.L.]≥10%			
	200 Bq m^{-3}	Percentage of houses above the R.L. based on indoor radon and geological information (i.e., bedrock geology, Quaternary geology, deeper topsoil permeability, and soil permeability). RPA when P[InRn > RL]≥10%	Logistic regression model	Grids 1 km x 1 km	Elío et al. (2017)
	-	Estimation of radon-related lung cancer cases	Dose estimation based on average concentrations (i.e., block averages after ordinary kriging)	Administrative level (i.e., electoral division)	Elío et al. (2018)
Malta	100 Bq m^{-3}	Display the indoor radon concentration values	Average of geometric mean annual indoor radon gas concentration values for each sampling point	Grids 5km×5km	(Baluci et al., 2013)

3.3 Maps based on indoor radon measurements

Probabilistic map

This method uses the concept that a percentage of houses in a certain area does/does not exceed a RL. If more than a certain number (i.e. a threshold) of homes in the area are above the RL, then the site is deemed an RPA (Bossew, 2018). For example, an InRn map of Switzerland assigned areas a percentage representing the probability of exceeding the RL of 300 Bq m^{-3}, and the regions allocated with a higher rate are the RPAs (Kropat et al., 2014).

Average concentration map

The concept of this method is that an area will have an average InRn value resulting from all of the InRn values for the zone. For example, Estonia averaged the InRn per administrative unit of communes to visualize the spatial distribution of InRn (Petersell et al., 2004). Another example is Italy's map (Bochicchio et al., 2005), which has determined the average InRn according to region. Austria and Switzerland have other examples where areas with a mean indoor value above the RL are deemed an RPA (Bossew, 2018).

Radioactive dose map

This technique aims to map the distribution of the radioactive dose received by people in a zone. Furthermore, this approach seeks to correlate InRn exposure to the amount of radioactive exposure available to be received in an area. For example, the Slovak Republic deployed the method of converting the population-weighted arithmetic mean of the InRn measurements into an estimated radioactive dose for each district (Ministry of Environment of the Slovak Republic, 2003) and considered the different types of houses in this process.

3.4 Maps based solely on geogenic factors

Information on geogenic characteristics, such as geology, Quaternary geology, soil type, permeability, structural geology (faults and fractures) and aquifer type, has been utilized to improve the predictions of radon mapping (Friedmann et al., 2017; Watson et al., 2017). Considering that radon arising from the earth is the primary source of InRn (World Health Organization, 2007), understanding the spatial distribution and variation of geological factors is useful when mapping radon. Two main concepts are defined regarding the mapping of naturally available radon. The first concept is the Geogenic Radon Hazard Index (GRHI), which incorporates data of available geogenic entities. The second concept is the Geogenic Radon Potential (GRP), which is radon that is naturally available in an area and is mainly influenced by the soil properties, hydrology and geology (Bossew et al., 2020). However, the use of GRP for radon mapping is more limited due to the availability of the necessary data; these concepts are discussed in detail in (Bossew et al., 2020).

Radon potential maps

GRP mapping aims to define boundaries according to the availability of radon entering a building. The most commonly adopted method is the 'Czech method' (Neznal et al., 2004), which collects in situ soil-gas radon and soil permeability measurements. The combination of soil-gas radon information and soil permeability values results in a GRP, giving an index which represents the potential of finding elevated radon levels in a building on the surveyed site.

3.5 Spatial resolution of radon maps

Many different resolutions of radon maps have been used, each of which have their pros and cons.

Regular grids

Regular grids are used, for example 500 m^2 and 5 km^2 in Montenegro and 10 km^2 in Albania (Antovic et al., 2007; Tushe et al., 2016). Many factors may be considered when deciding which size of a grid to use. For example, if creating a map using InRn data, the number of samples in a given area is incredibly relevant. Grids for rural areas may need to be larger to have a sufficient data set, whereas urban areas inherently have more InRn measurements, allowing for smaller grids to be used (Antovic et al., 2007). Smaller grids are better at representing the high spatial variation of radon and should be preferentially used when the size of a data set allows it.

Administrative boundaries

In other cases, radon is mapped according to municipalities, counties or even electoral divisions (Andersen et al., 2001; Bochicchio et al., 2005; Ministry of Environment of the Slovak Republic, 2003; Petersell et al., 2004). In each case, the data for mapping radon risk are grouped within each boundary type. The chosen boundary type influences each map's outcome in a similar way that different grid sizes dictate the outcome. An advantage of this approach is that it is easier to engage the public to identify with an area. However, difficulties arise in mapping according to administrative boundaries, especially if using geogenic data. Using administrative boundaries for mapping makes it arduous to compare neighbouring countries when different methods and concepts are used, as is the case for all European countries (Tollefsen et al., 2014).

3.6 Ireland as a case study

Maps based on indoor radon values

Probabilistic map

The legislative radon risk map in Ireland is a probabilistic map (Stephen G. Fennell et al., 2002). It defines an area as radon prone if 10% or more of houses are above the RL (Fig. 3.1a). The probabilistic radon risk method is useful for defining areas that are generally more prone to radon. Since InRn measurements from private dwellings were used, it may be unsuitable for workplaces and other building types due to the differences in radon behaviour in different building types (Cinelli et al., 2019). The advantage of using this mapping style is that measurements of InRn are used, allowing for a direct representation of an area's radon category status.

The Irish Environmental Protection Agency (EPA) protocol for measuring indoor radon includes taking at least two measurements in two separate rooms of a house using a CR-39 detector over a 3-month measurement period. The results are then seasonally corrected to an annual average (Environmental Protection Agency, 2019).

Average concentration map

The average concentration map illustrates the mean InRn level for an area (Fig. 3.1b (Elío et al., 2018)), allowing the map user to identify zones with higher radon levels. This helps to get an estimate of the typical InRn value for a specific area. Furthermore, this map is convenient for linking with health effects and epidemiological studies of lung cancer. An advantage of this map type is that it uses direct measurements of InRn, which allows for a true and accurate representation of the radon value in a given area. The mean InRn concentrations were collected from homes using the EPA protocol (Environmental Protection Agency, 2019). Furthermore, the measurements were performed mainly from the ground floor of houses, and it is assumed that the results are representative of multistorey buildings (Elío et al., 2018).

Radon-related lung cancer cases

Maps made to include the radioactive dose due to radon allow for distinguishing areas based on the expected lung cancer incidence (Elío et al., 2018). In Elío et al. (2018), two models were analysed, the first being a linear no-threshold model and the second being a dose-effect model, both of which resulted in similar numbers of estimated lung cancer cases (216– 246, 257–249, 220–251 and 316–317 cases for the linear model and dose effect model, respectively). Comparably, approximately 300 annual radon-related lung cancer cases were reported by presenters at Ireland’s 14th and 15th National Radon Forum (Hickey, 2019; Walsh et al., 2017). This mapping procedure targets the concept that lung cancer incident rates differ between areas. A map made using this method incorporated information on the population size and distribution (Fig. 3.1e (Elío et al., 2018)). The resulting map may be useful for initiatives to reduce the long-term adverse health effects of radon exposure. Specifically, it could delineate areas designated as possessing a higher lung cancer incidence rate, therefore identifying where the collective population at a higher risk are situated. The main advantage is that the long-term aim of the radon action plan is targeted, which is to reduce the number of lung diseases resulting from Rn exposure. However, a disadvantage arises: high population areas are more likely to be designated as an RPA. As a result, this method would only be appropriate for identifying larger populations at risk and is inappropriate for detecting individuals at high radon risk.

The radon-related lung cancer incidence was estimated over a lifetime of 70 years, and it is assumed that a person lives in the same place. Furthermore, the effect on smokers and non-smokers is assumed to be the same (Elío et al., 2018).

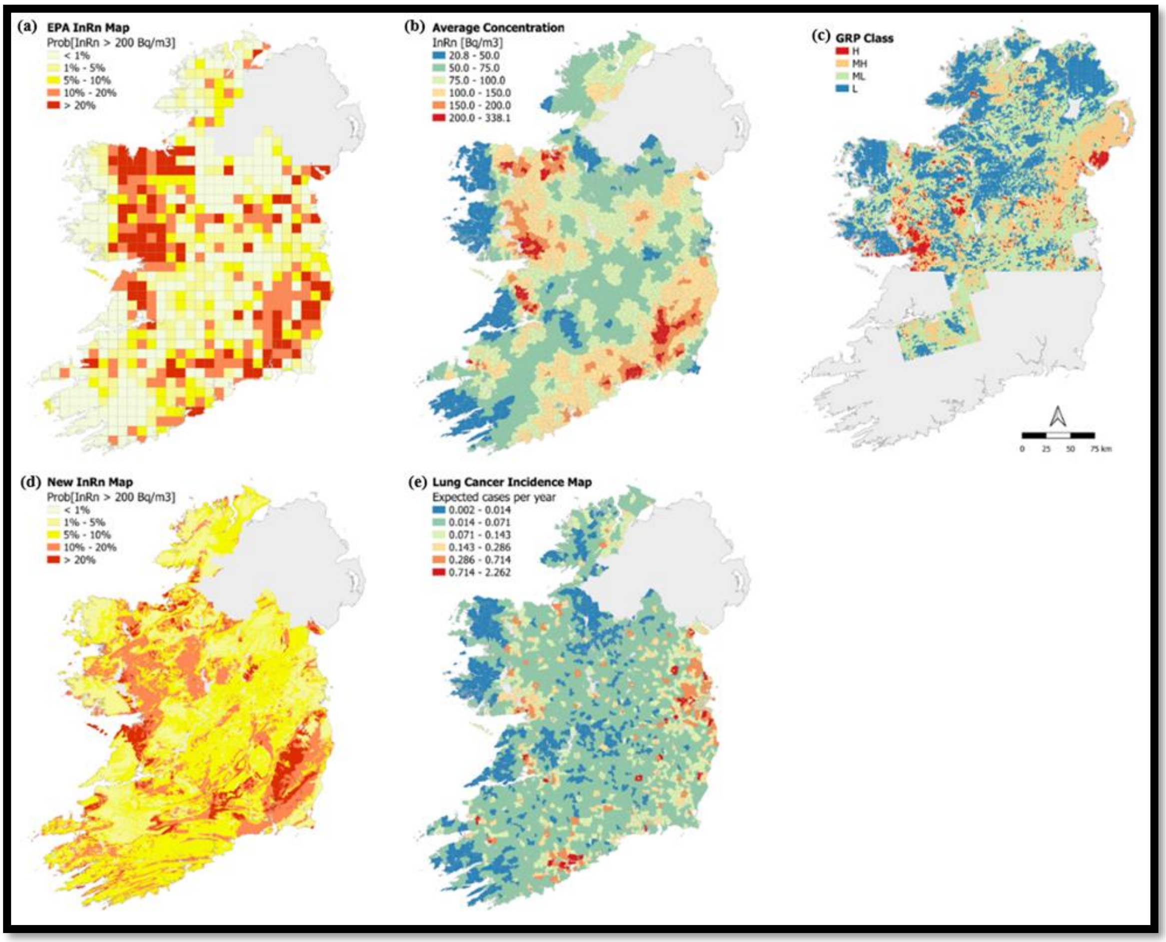

Figure 3.1 (a) Legislative indoor radon probability map (Stephen G. Fennell et al., 2002) (b) Indoor radon average concentration map (Elío et al., 2018). (c) Radon potential map (Elío et al., 2020). (d) Indoor radon probability map (Elío et al., 2017). (e) Radon-related modelled lung cancer incidence map (Elío et al., 2018).

Adding geogenic data

Maps that integrate geological information utilize the fact that geology impacts radon values (Fig. 3.1d (Elío et al., 2017)). Radon maps, which include geogenic data, are useful for improving mapping, especially in areas with a low amount of InRn data. Visual aids made using this methodology could also be practical for land redesignation in low populated areas. An advantage of this map type is that it employs information on the radon source and its pathway into a building. A drawback of using geogenic maps for radon mapping is that the geological maps scale may cause deviations of radon designation boundaries.

Maps based solely on geogenic factors

Radon potential map

The concept targeted by GRP maps is that the source and the pathway of radon gas determine the InRn risk. Such maps are useful for understanding the radon risk in any area. Advantages include that they are appropriate for any building type: workplace, public and domestic dwellings. These visual aids are also useful in low populated areas where there may be a lack of InRn data to make other radon risk map types. An example is shown in Fig. 3.1c (Elío et al., 2020).

Furthermore, in situ GRP surveys can be done rapidly at a local scale despite being a costly and arduous task to implement at a national level (Elío et al., 2019). It is important to note that the GRP map shown in Fig. 3.1c used a method that was created for a local scale and applied it to a regional/national scale, that is, the method was used differently from how it was designed. In theory, these maps are independent of building characteristics. However, the building characteristics do have an influence on the infiltration rate and behaviour of radon within a house (Bossew, 2014; Cinelli et al., 2019).

3.7 Spatial resolution

The boundaries of the radon risk categories on a map can change significantly depending on the spatial resolution used. Figure 3.2 demonstrates several probabilistic radon risk maps, with the only variable for sub-figures (a) to (f) being the spatial resolution. The probabilistic map is shown on the left side of Fig. 3.2 [sourced from (Elío et al., 2017)]; it was created using InRn data and several geogenic data sets. Distinctly, the addition of geogenic data reveals areas with higher radon, particularly in the southeast of County Dublin. The sub-figures (a) to (c) on Fig. 3.2 illustrate how different grid sizes (i.e. 1 km^2, 5 km^2 and 10 km^2, respectively) impact the radon categories despite the same input data InRn being used. Noticeably, the 1 km^2 grid shows that there are areas in the north of County Dublin which have high InRn values. The sub-figures (d) to (f) on Fig. 3.2 illustrate how radon categories for zones change according to spatial resolution (i.e. small areas, electoral divisions and county regions) despite the same input data (i.e. InRn) being used. Importantly, smaller units allow for the spatial variability of radon to be represented, which is essential for protecting individuals against high radon exposure.

Regular boundaries

The benefit of using a 10 km^2 grid is that InRn data can be grouped, allowing for a more significant sample set, which is favourable for statistics. To elaborate, using larger grid sizes permits smaller areas with low-density data sets to be aggregated and assigned a category as opposed to being left blank. However, lower-resolution grids do not represent the high variability of radon within the area, that is, some parts of the grid may be more prone to radon. Even within a 10 km^2 area, radon concentrations can vary due to radon source variability and subsurface transportation routes (faults, fractures and soil permeability).

The use of smaller grids (i.e. 1 km^2) permits radon variability in any area to be represented more accurately. However, a high number of data points would be needed. This would be an issue in areas with a low population density. However, the need for large amounts of InRn data can be overcome by using alternative data sets, such as geogenic factors, for the models.

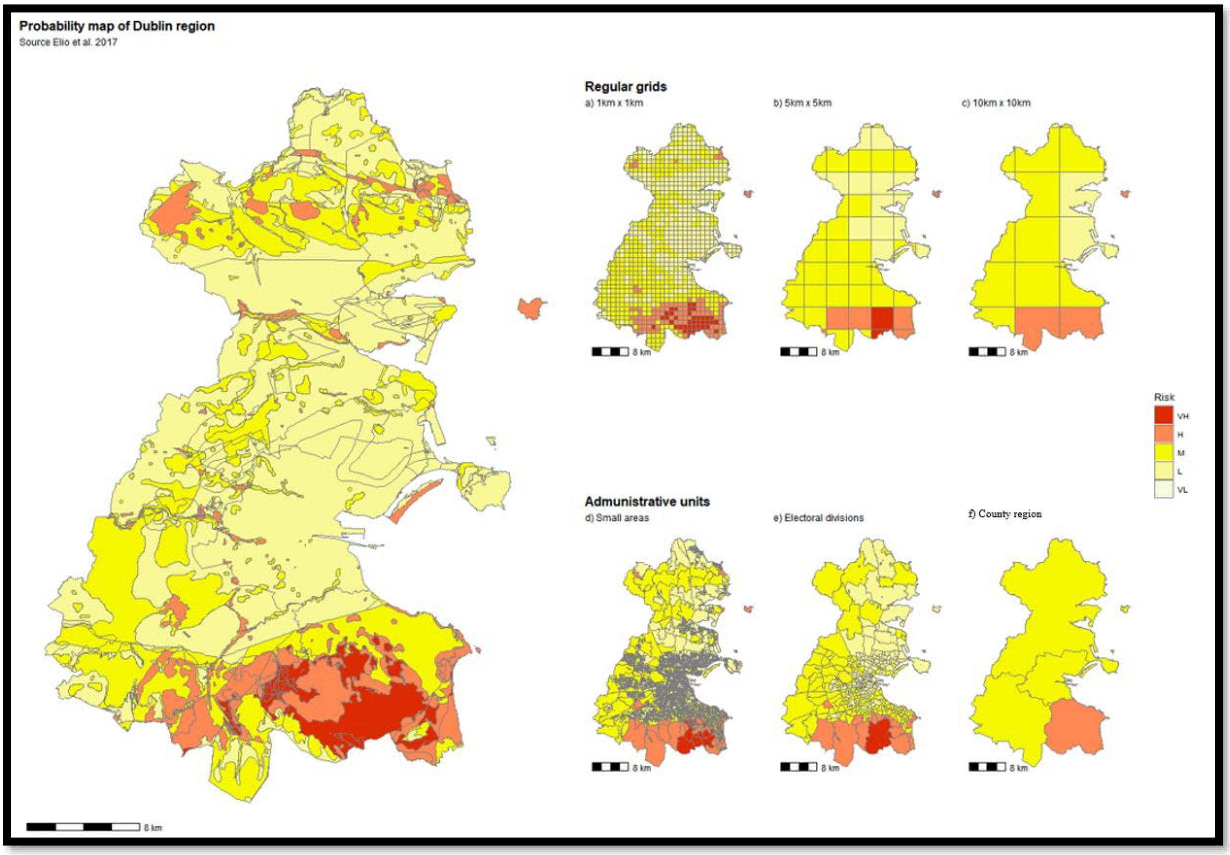

Figure 3.2. Radon probabilistic map of County Dublin, Ireland. The various maps (a) to (f) in this figure have been made using the same input data. The spatial resolution varies between the maps. Maps (a) to (c) show how the radon probability boundaries change from grid sizes of 1 km^2, 5 km^2 and 10 km^2. Maps (d) to (f) show how the boundaries change depending on which administrative boundary is used, that is, small areas, electoral division and county region. For comparison, the large map of Dublin on the left is sourced from (Elío et al., 2017) and was created using both indoor radon data and several geogenic data types.

Administrative boundaries

Choosing to use administrative units for radon mapping makes it easier to link with other statistics (e.g. cancer registry and population density). This also allows for better public awareness initiatives as it is easier to identify areas where people live.

As for the case with the gridded areas, larger administrative boundaries, such as municipalities or counties, make it easier to have a bigger sample set, which is more statistically favourable. In contrast, smaller areas (areas generally comprising between 80 and 120 dwellings) or

Electoral Divisions in Ireland are better at representing the spatial variability of radon concentrations. However, in the latter, a higher density of data would be needed.

Overall, maps based on InRn data are useful for targeting domestic dwellings that may be over the RL. Although the InRn measurements taken decades ago may not still be representative of InRn measures today, especially when the building style has changed, which impacts how radon accumulates inside. In contrast, radon maps based solely on geogenic data are more consistent through time because the geology in an area does not change for extended periods, although Geological Surveys may upgrade the geological maps when more information is available.

3.8 Discussion

It is important to mitigate against radon exposure, given that it accounts for the highest proportion of natural radioactivity to which the general public are exposed (Monty, 2000; World Health Organization, 2009). Maps as visual aids are a valuable resource and planning tool to prioritise certain areas to reduce radon exposure to citizens. However, choosing the most appropriate map is a complicated procedure that reflects the issues intricate nature. There are many factors to consider when deciding on a national or local radon mitigation strategy. These include if the purpose is to reduce Rn in workplaces, homes or public spaces, or if the aim is to reduce the resulting lung cancer incidence from Rn exposure. As well as considering the purpose of the strategy, the ease of using available data sets may be a determining factor on which map to use. Considering this intricacy, we attempt to make the decision process simpler by proposing a table (Table 3.2) and a decision matrix (Fig.3.3) below.

We propose a process, or method, to approach the task of deciding which visual aid to use based on (a) the purpose and (b) the available data.

In Table 3.2, the different Rn maps are tabulated according to time and cost-efficiency. We have indicated if each map type is representative at a local and large scale. Additionally, the suitability of the maps for protecting the collective or the individual is shown. The last column of Table 3.2 outlines the suggested use of each map type. The decision matrix (Fig. 3.3) simplifies the EU and national Rn mitigation objectives. These objectives are rationalized into several initiatives, available data sets and sources. Finally, considering the above counterparts, the output options are indicated for the data available.

The decision matrix, however, does not indicate the time and cost-efficiency of each option, although this is indicated in Table 3.2. Further difficulties are outlined in the decision matrix. Figure 3.3 does not capture that any data used may be updated over time, which could lead to discrepancies in the resulting maps. This issue could be accounted for by automating the process where the data set could be updated every few years or over a set amount of time. Another disadvantage not depicted in Fig. 3.3 is that the accessibility to building characteristics may be difficult. The amount of time spent indoors and in different Rn areas has not been integrated into most of the reviewed maps. The exception is Fig. 3.1e, which assumes that the time spent indoors is 80% (Elío et al., 2018).

There is compelling evidence of a synergetic effect between radon and smoking in contributing to lung cancer development (Leuraud et al., 2011; Meenakshi and Mohankumar, 2013). Smokers in high radon risk areas are more likely to develop lung cancer than smokers in low radon exposure areas (Li et al., 2020; Park et al., 2020). Furthermore, Li et al., (2020) reported an 11% increase in lung cancer, with InRn increasing by 100 Bq m^{-3}. Hampson et al., (1998) surveyed people regarding radon risk perception, noting that 32% of people knew little or nothing about radon. Butler et al., (2018) suggested that people may perceive a higher risk of lung cancer when exposure to smoking and radon is combined. Such information (Butler et al.,

2018) could prove vital in strategising more effective public outreach, engagement and respiratory health awareness programmes. Explicitly, it may be a practical approach to combine the public health initiative of smoking awareness with radon awareness.

Both smoking and radon exposure are systematic problems in respiratory health. However, the approaches for managing these two issues are compartmentalised. Public awareness regarding the risks related to tobacco smoking is extensive, whereas the risk awareness related to radon is relatively low. Considering that radon is the leading cause of lung cancer after smoking and the synergistic effect of developing lung cancer when smoking and radon exposure is combined, it may be beneficial to amalgamate these campaigns. Conceptualising smoking demographics onto a map may be challenging. However, it may be better to simultaneously communicate the effect of these two issues on respiratory health. Our lungs can be affected by radon as well as smoking. As such, incorporating this information would allow for a more holistic approach to combating respiratory health issues.

Map type	Cost-effective	Time-Effective	Captures Rn variability at a large scale (≥10km²)	Captures Rn variability at a local scale (<10km²)	Considers Lung Cancer incidence	Considers various lifestyles and building characteristics	Accurate individual measurements of Indoor radon	Useful for protecting individuals	Useful for protecting collective	Best suggested use
Indoor radon (Probability Reference level). E.g., Fig.3.1a	N	N	Y	N	N	N	Y	Y depends on spatial resolution/data density	Y	(a) Identifying people living with high InRn risk. (b) Assessment of remediation effectiveness for homes. (c) Public communication initiatives.
Indoor radon (Annual Average). E.g., Fig.3.1b	N	N	Y	Y depends on the dataset density	N	N	Y	Y	Y	(a) Evaluate health effects (e.g., lung cancer) and detect potential areas with high collective doses. (b) Assessment of remediation effectiveness for homes. (c) Public communication initiatives.
Radon potential. E.g., Fig.3.1c	Y at a local scale	Y at a local scale	Y if data available	Y	N	N	N	Y depends on spatial resolution	Y	(a) For Building regulations reference. (b) Radon risk mapping regardless of building type. (c) Assessment of maps derived from InRn data.

InRn and geogenic factors (bedrock geology, aquifer types, eU Airborne data – etc.). E.g., Fig.3.1d	**Y if data available**	**Y**	**Y**	**Y/N depends on the geological scale used.**	**N**	**N**	**Y**	**Y depends on spatial resolution**	**Y**	**(a) For Building regulations reference. (b) Increase resolution of maps derived from InRn (i.e., probability and average InRn maps).**
Lung cancer incidence. E.g., Fig.3.1e	**N**	**N**	**Y**	**Y**	**Y**	**N**	**Y**	**N**	**Y**	**(a) Long-term radon action measures for reducing adverse health effects (i.e., lung cancer). (b) Public communication initiatives.**

Table 3.2. Summary of radon maps tabulated against several categories, including the cost-effectiveness and time efficiency, whether the variability of radon is captured at a local (<10 km^2) or large (≥10 km^2) scale, and if the radon map type considered the radon-induced lung-cancer incidence. Furthermore, the maps are tabulated to highlight if building characteristics are considered and if indoor radon measurements are used to create the maps. The last several columns delineate if the maps are useful for protecting the collective. Lastly, the best-suggested use of each map is given in the final column. To clarify, the reference to 'spatial resolution' brings attention to how radon risk boundaries can change even if the grid size of the map changes. Reference to 'data density' highlights that there may be a lack of data for indoor radon at small scales, that is, in rural areas. Disclaimer: An example is given for each of the map types; however, the tabulation extends to other maps made with a similar process.

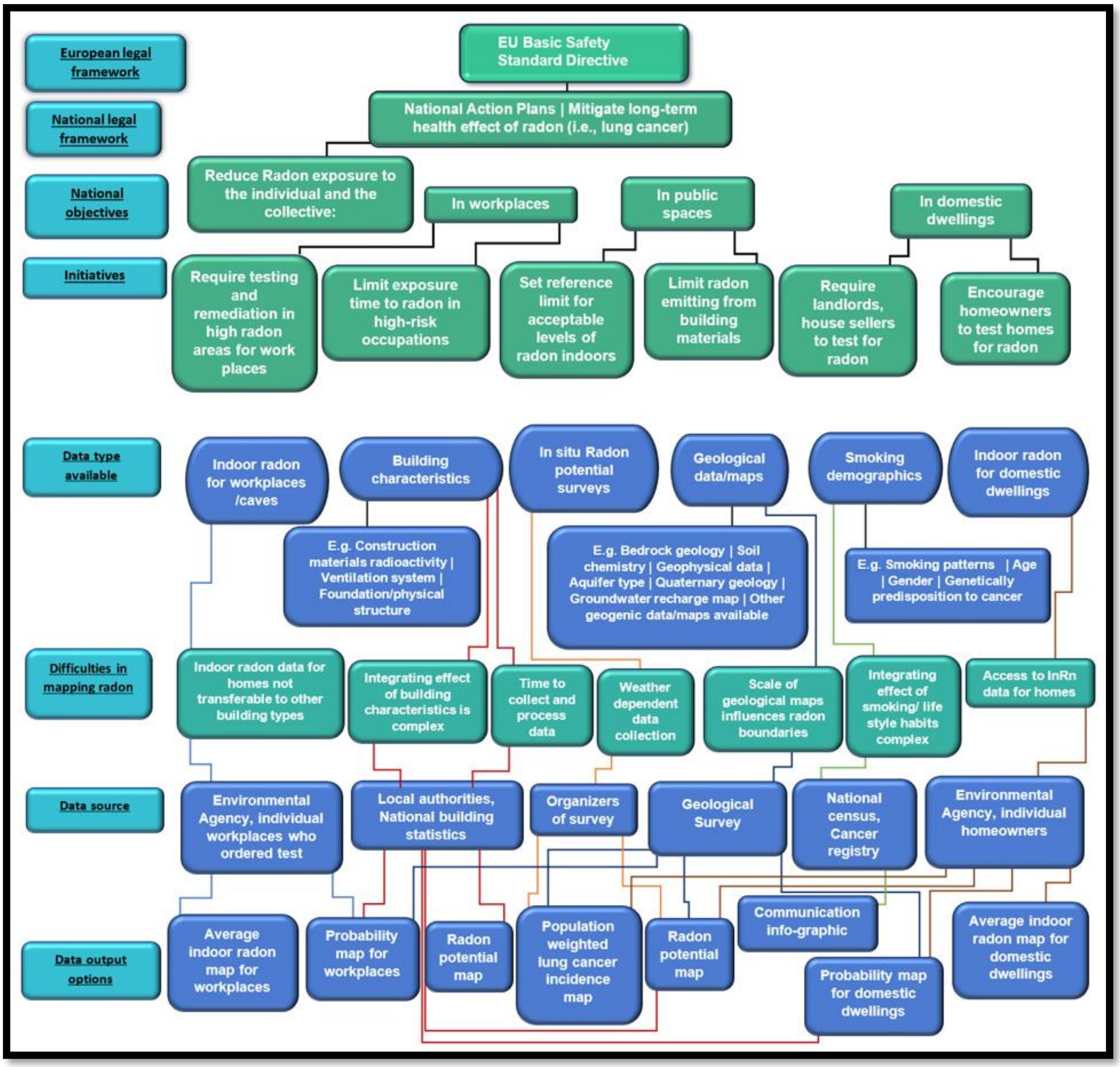

Figure 3.3 Decision matrix to aid in choosing an appropriate radon map best suited to its purpose. Several frameworks and objectives, as well as initiatives, are indicated in the top half of the decision key. The bottom half gathers the range of data types available and how they are linked to the various data output options. Difficulties associated with some potential sources of each data group are given. The different coloured lines are simply to make the connections between categories easier to observe.

In some cases, this is starting to be done. For example, the World Health Organisation's International Agency for Research on Cancer (IARC) has developed an initiative implemented by the European Commission to inform people how to reduce cancer risk, which includes reducing exposure to radon (World Health Organization, 2016). As part of the IARC initiative, the Irish Cancer Society has included radon on a public communication list of 12 ways to reduce cancer risk (Irish Cancer Society, 2016).

3.9 Conclusion

In this article, a review of some potential visual aids for radon mapping is made, focusing on Ireland's various radon maps already published. We have assumed that the indoor radon data were representative for mapping the target estimate (e.g. probability, average and collective dose) and that the maps were properly developed. In this sense, we do not discuss the methods of how maps are devised, but in how they are used.

Visual aids can make the decision process more manageable, considering where to target regulations or public awareness initiatives. The resources available and the radon map's purpose should be at the core of the decision process when deciding on a plan. Firstly, the spatial resolution can influence the map's outcome even if the same input data are used (Fig. 3.2). When considering spatial resolutions, a large scale is good for national-level initiatives, such as delineating RPAs for requiring workplaces to have radon barriers/sumps. A small/local spatial resolution would be useful for building developers or homeowners who want to remediate their homes.

Secondly, the different methods used do not map the same thing concerning radon exposure. For example, probabilistic maps aim to identify areas that are more prone to InRn, while the average concentration radon maps aim to distinguish regions according to their mean concentration. These maps would help target radon awareness campaigns for individual homeowners. If the aim is to protect the collective and rank citizens' risk of developing radon-induced lung cancer, then choosing a lung cancer incidence map would be appropriate.

Finally, the GRP maps aim to provide information on the amount of soil-gas radon available to become InRn in the area, which is particularly useful for redesignating land or when constructing a new building. Depending on the purpose of which one wants a radon risk map to be used, one map type may be more favourable than the other, and one visual aid will not be appropriately suitable to fit all strategies.

3.10 Conflict of interest and funding

The authors declare no potential conflicts of interest. This work has been financed by the Student Universal Support Ireland (SUSI) to MHB.

3.11 References

Abbady, A.G.E., Uosif, M.A.M., El-Taher, A., 2005. Natural radioactivity and dose assessment for phosphate rocks from Wadi El-Mashash and El-Mahamid Mines, Egypt. Journal of Environmental Radioactivity 84, 65–78. https://doi.org/10.1016/j.jenvrad.2005.04.003

Abed, N.S., Monsif, M.A., Zakaly, H.M., Awad, H.A., Hessien, M.M., Yap, C.K., 2022. Assessing the radiological risks associated with high natural radioactivity of microgranitic rocks: A case study in a northeastern desert of Egypt. International Journal of Environmental Research and Public Health 19, 473.

Akbari, K., Mahmoudi, J., Ghanbari, M., 2013. Influence of indoor air conditions on radon concentration in a detached house. 116. https://doi.org/10.1016/j.jenvrad.2012.08.013

Al-Khawlany, A., Khan, A., Pathan, J., 2018. Review on studies in natural background radiation. Radiation Protection and Environment.

Alshahrani, B.E., 2021. Natural radioactivity level in pumice rock, in Saudi Arabia and effect on human health. null 1–12. https://doi.org/10.1080/03067319.2021.1907363

Andersen, C.E., Ulbak, K., Damkjær, A., Gravesen, P., 2001. Radon i danske boliger. Kortlægning af lands-, amts-og kommuneværdier.

Antovic, N., Vukotic, P., Zekic, R., Svrkota, R., Ilic, R., 2007. Indoor radon concentrations in urban settlements on the Montenegrin Coast. Radiation Measurements 42, 1573–1579. https://doi.org/10.1016/j.radmeas.2007.06.003

Artugyan, L., Urdea, P., 2015. A complex approach in the interdisciplinary field of karst geomorphology. The case study of Anina karst area (Banat Mountains, Romania). Forum geografic XV.

Baluci, C., Vincenti, K., Tilluck, B., Conchin, S., Formosa, S., Grech, D., 2013. National mapping survey of indoor radon levels in the Maltese Islands (2010-2011).

Baptista, E., Pereira, A.J.S.C., Domingos, F.P., Sêco, S.L.R., 2022. Radon and thoron concentrations in the southwest region of Angola: dose assessment and implications for risk mapping. Environmental Geochemistry and Health. https://doi.org/10.1007/s10653-022-01226-8

Baxter, S., Graham, N.T., Feely, M., Reavy, R.J., Dewey, J.F., 2005. A microstructural and fabric study of the Galway Granite, Connemara, western Ireland. Geological Magazine 142, 81–95. https://doi.org/10.1017/S0016756804000378

Beck, B.F., 2010. CH Holland, IS Sanders (eds): The Geology of Ireland, 2nd edn.

Bineng, G.S., Tokonami, S., Hosoda, M., Tchuente Siaka, Y.F., Issa, H., Suzuki, T., Kudo, H., Bouba, O., 2020. The importance of direct progeny measurements for correct estimation of effective dose due to radon and thoron. Frontiers in Public Health 8, 17.

Bochicchio, F., Campos-Venuti, G., Piermattei, S., Nuccetelli, C., Risica, S., Tommasino, L., Torri, G., Magnoni, M., Agnesod, G., Sgorbati, G., Bonomi, M., Minach, L., Trotti, F., Malisan, M.R., Maggiolo, S., Gaidolfi, L., Giannardi, C., Rongoni, A., Lombardi, M., Cherubini, G., D'Ostilio, S., Cristofaro, C., Pugliese, M., Martucci, V., Crispino, A., Cuzzocrea, P., Santamaria, A.S., Cappai, M., 2005. Annual average and seasonal variations of residential radon concentration for all the Italian Regions. Radiation Measurements 686–694. https://doi.org/10.1016/j.radmeas.2004.12.023

Bossew, P., 2018. Radon Priority Areas - Definition, estimation and uncertainty. Nuclear Technology and Radiation Protection 33, 11–11. https://doi.org/10.2298/NTRP180515011B

Bossew, P., 2014. Determination of radon prone areas by optimized binary classification. Journal of Environmental Radioactivity 129, 121–132. https://doi.org/10.1016/j.jenvrad.2013.12.015

Bossew, P., Cinelli, G., Ciotoli, G., Crowley, Q., Cort, M., Elío, J., Gruber, V., Petermann, E., Tollefsen, T., 2020. Development of a Geogenic Radon Hazard Index—Concept, History, Experiences. International Journal of Environmental Research and Public Health 17, 4134. https://doi.org/10.3390/ijerph17114134

Bowie, C., Bowie, S.H.U., 1991. Radon and health. The Lancet 337, 409–413.

Braun, J., Riotte, J., Battacharya, S., Violette, A., Prunier, J., Bouvier, V., Candaudap, F., Maréchal, J., Ruiz, L., Panda, S.R., 2017. REY-Th-U solute dynamics in the critical zone: Combined influence of chemical weathering, atmospheric deposit leaching, and vegetation cycling (Mule Hole Watershed, South India). Geochemistry, Geophysics, Geosystems 18, 4409–4425.

Brennand, T.P., 1965. The Upper Carboniferous (Namurian) stratigraphy north-east of Castleisland, Co. Kerry, Ireland. Proceedings of the Royal Irish Academy.

Building Regulations, 1997. Building Regulations. Statutory Instruments No. 497 of 1997.

Bute, S.I., Yang, X., Suh, C.E., Girei, M.B., Usman, M.B., 2020. Mineralogy, geochemistry and ore genesis of Kanawa uranium mineralization, Hawal Massif, eastern Nigeria terrane: Implications for uranium prospecting in Nigeria and Cameroon. Ore Geology Reviews 120, 103381. https://doi.org/10.1016/j.oregeorev.2020.103381

Butler, K.M., Huntington-Moskos, L., Rayens, M.K., Wiggins, A.T., Hahn, E.J., 2018. Perceived Synergistic Risk for Lung Cancer After Environmental Report-Back Study on Home

Exposure to Tobacco Smoke and Radon. Am J Health Promot 33, 597–600. https://doi.org/10.1177/0890117118793886

Casal-Mouriño, A., Ruano-Ravina, A., Torres-Durán, M., Parente-Lamelas, I., Provencio-Pulla, M., Castro-Añón, O., Vidal-García, I., Pena-Álvarez, C., Abal-Arca, J., Piñeiro-Lamas, M., Fuente-Merino, I., Fernández-Villar, A., Abdulkader, I., Valdés-Cuadrado, L., Barros-Dios, J.M., Pérez-Ríos, M., 2020. Lung cancer survival in never-smokers and exposure to residential radon: Results of the LCRINS study. Cancer Letters 487, 21–26. https://doi.org/10.1016/j.canlet.2020.05.022

Castillo, P.I., Townley, B.K., Emery, X., Puig, Á.F., Deckart, K., 2015. Soil gas geochemical exploration in covered terrains of northern Chile: data processing techniques and interpretation of contrast anomalies. Geochemistry: Exploration, Environment, Analysis 15, 222–233.

Chen, J., 2022. Assessment of thoron contribution to indoor radon exposure in Canada. Radiation and Environmental Biophysics 61, 161–167. https://doi.org/10.1007/s00411-021-00956-0

Chen, J., Bergman, L., Falcomer, R., Whyte, J., 2015. Results of simultaneous radon and thoron measurements in 33 metropolitan areas of Canada. Radiation Protection Dosimetry 163, 210–216. https://doi.org/10.1093/rpd/ncu141

Chen, J., Dessau, J.C., Frenette, E., Moir, D., Cornett, R.J., 2010. Preliminary assessment of thoron exposure in Canada. Radiation Protection Dosimetry 141, 322–327. https://doi.org/10.1093/rpd/ncq226

Chen, X., Wen, C., Meng, D., Li, B., Jiang, B., Qin, J., 2022. Implications of Major and Trace Element Migration in Altered Granites for Hydrothermal Alteration and Granite-Related Uranium Mineralization in the Sanjiu Ore Field, South China. Minerals 12. https://doi.org/10.3390/min12020144

Cinelli, G., de, C., Tollefsen, T., Achatz, M., Ajtic, J., Ballabio, C., Barnet, I., Bochicchio, F., Borrelli, P., Bossew, P., Braga, R., Brattich, E., Briganti, A., Carpentieri, C., Castellani, C.-M., Castelluccio, M., Chiaberto, E., Ciotoli, G., Coletti, C., Cucchi, A., Daraktchieva, Z., Di Carlo, C., De France, J., Dehandschutter, B., Domingos, F., Dudar, T., Elio, J., Falletti, P., Ferreira, A., Finne, I.E., 2020. European atlas of natural radiation. https://doi.org/10.2760/46388

Cinelli, G., Tollefsen, T., Bossew, P., Gruber, V., Bogucarskis, K., De Felice, L., De Cort, M., 2019. Digital version of the European Atlas of natural radiation. Journal of Environmental Radioactivity 196, 240–252. https://doi.org/10.1016/j.jenvrad.2018.02.008

Cinelli, G., Tondeur, F., Dehandschutter, B., 2011. Development of an indoor radon risk map of the Walloon region of Belgium, integrating geological information. Environmental Earth Sciences 62, 809–819. https://doi.org/10.1007/s12665-010-0568-5

Clark, R.N., Roush, T.L., 1984. Reflectance spectroscopy: Quantitative analysis techniques for remote sensing applications. Journal of Geophysical Research: Solid Earth 89, 6329–6340.

Coblinski, J.A., Inda, A.V., Demattê, J.A.M., Dotto, A.C., Gholizadeh, A., Giasson, É., 2021. Identification of minerals in subtropical soils with different textural classes by VIS–NIR–SWIR reflectance spectroscopy. CATENA 203, 105334. https://doi.org/10.1016/j.catena.2021.105334

Crandall, C.A., Katz, B.G., Hirten, J.J., 1999. Hydrochemical evidence for mixing of river water and groundwater during high-flow conditions, lower Suwannee River basin, Florida, USA. Hydrogeology Journal.

Cucoș, A.L., Moldovan, M.C., Burghele, B.D., Dicu, T., Moldovan, O.T., 2021. Radiological Risk Assessment for Karstic Springs Used as Drinking Water in Rural Romania. Atmosphere 12. https://doi.org/10.3390/atmos12091207

Cumberland, S., Grice, K., Douglas, G., Moreau, J.W., 2016. Uranium mobility in organic matter-rich sediments: A review of geological and geochemical processes. Earth-Science Reviews Volume 159, pp. 160-185. https://doi.org/10.1016/j.earscirev.2016.05.010}

Cuney, M., 2008. The extreme diversity of uranium deposits. Mineralium Deposita 44, 3. https://doi.org/10.1007/s00126-008-0223-1

Cvetković, M., Kapuralić, J., Pejić, M., Kolenković Močilac, I., Rukavina, D., Smirčić, D., Kamenski, A., Matoš, B., Špelić, M., 2021. Soil gas measurements of radon, CO2 and hydrocarbon concentrations as indicators of subsurface hydrocarbon accumulation and hydrocarbon seepage. Sustainability 13, 3840.

Daraktchieva, Z., Appleton, J., Reese, D., 2015. Radon in Northern Ireland: Indicative Atlas. Centre for Radiation, Chemical and Environmental Hazards, Public Health England.

Darby, S., Hill, D., Auvinen, A., Barros-Dios, J.M., Baysson, H., Bochicchio, F., Deo, H., Falk, R., Forastiere, F., Hakama, M., Heid, I., Kreienbrock, L., Kreuzer, M., Lagarde, F., Mäkeläinen, I., Muirhead, C., Oberaigner, W., Pershagen, G., Ruano-Ravina, A., Ruosteenoja, E., Schaffrath Rosario, v, Tirmarche, M., Tomáscaron;ek, L., Whitley, E., Wichmann, H.-E., Doll, R., 2005. Radon in homes and risk of lung cancer: collaborative analysis of individual data from 13 European case-control studies. BMJ 2005;330:223. https://doi.org/10.1136/bmj.38308.477650.63

Degu Belete, G., Alemu Anteneh, Y., 2021. General Overview of Radon Studies in Health Hazard Perspectives. Journal of Oncology 2021.

Dorn, F.E., 1901. "Ueber die von radioaktiven Substanzen ausgesandte Emanation.

Dosseto, A., Buss, H., Suresh, P.O., 2011. The delicate balance between soil production and erosion, and its role on landscape evolution. Applied Geochemistry 26, S24–S27. https://doi.org/10.1016/j.apgeochem.2011.03.020

Duffy, J.T., Madden, J.S., Mackin, G.M., McGarry, A.T., Colgan, P.A., 1996. A reconnaissance survey of radon in show caves in Ireland. Environment International 22, 415–423. https://doi.org/10.1016/S0160-4120(96)00140-7

Dungca, J., Galupino, J., 2017. Artificial neural network permeability modeling of soil blended with fly ash. GEOMATE 12, 77–82. https://doi.org/10.21660/2017.31.6549

Egli, M., Mirabella, A., Fitze, P., 2001. Clay mineral formation in soils of two different chronosequences in the Swiss Alps. Geoderma 104, 145–175. https://doi.org/10.1016/S0016-7061(01)00079-9

Elders, W., Moore, J., 2016. Geology of geothermal resources. Geothermal Power Generation 7–32.

Elío, J., Crowley, Q., Scanlon, R., Hodgson, J., Long, S., 2019. Rapid radon potential classification using soil-gas radon measurements in the Cooley Peninsula, County Louth, Ireland. Environmental Earth Sciences 78, 359. https://doi.org/10.1007/s12665-019-8339-4

Elío, J., Crowley, Q., Scanlon, R., Hodgson, J., Long, S., 2017. Logistic regression model for detecting radon prone areas in Ireland. Science of The Total Environment 599–600. https://doi.org/10.1016/j.scitotenv.2017.05.071

Elío, J., Crowley, Q., Scanlon, R., Hodgson, J., Long, S., Cooper, M., Gallagher, V., 2020. Application of airborne radiometric surveys for large-scale geogenic radon potential classification. Journal of the European Radon Association.

Elío, J., Crowley, Q., Scanlon, R., Hodgson, J., Zgaga, L., 2018. Estimation of residential radon exposure and definition of Radon Priority Areas based on expected lung cancer incidence. Environment International 114, 69–76. https://doi.org/10.1016/j.envint.2018.02.025

Environmental Protection Agency, 2019. EPA protocol for the measurement of radon in homes and workplaces.

Environmental Protection Agency Ireland, 2020. Radon Map :: Environmental Protection Agency, Ireland [WWW Document]. URL https://www.epa.ie/radiation/radonmap/

European Commission, 2013. Council directive 2013/59/Euratom. Official Journal of the European Union 2013/59/EURATOM.

Faanu, A., Darko, E., Ephraim, J., 2011. Determination of natural radioactivity and hazard in soil and rock samples in a mining area in Ghana. West African Journal of Applied Ecology 19.

Fabritius, O., Puhakka, E., Li, X., Nurminen, A., Siitari-Kauppi, M., 2022. Radium sorption on biotite; surface complexation modeling study. Applied Geochemistry 140, 105289.

Fang, Q., Hong, H., Zhao, L., Furnes, H., Lu, H., Han, W., Liu, Y., Jia, Z., Wang, C., Yin, K., 2017. Tectonic uplift-influenced monsoonal changes promoted hominin occupation of the Luonan Basin: insights from a loess-paleosol sequence, eastern Qinling Mountains, central China. Quaternary Science Reviews 169, 312–329.

Fennell, Stephen G., Mackin, G.M., Madden, J.S., McGarry, A.T., Duffy, J.T., O'colmain, M., Colgan, P.A., Pollard, D., 2002. Radon in dwellings: the Irish National Radon survey. Radiological Protection Institute of Ireland Dublin.

Fennell, S.G, Mackin, G.M., McGarry, A.T., Pollard, D., 2002a. Radon exposure in Ireland. International Congress Series 1225, 71–77. https://doi.org/10.1016/S0531-5131(01)00549-0

Fennell, S.G, Mackin, G.M., McGarry, A.T., Pollard, D., 2002b. Radon exposure in Ireland. International Congress Series 1225, 71–77. https://doi.org/10.1016/S0531-5131(01)00549-0

Ferreira, A., Daraktchieva, Z., Beamish, D., Kirkwood, C., Lister, T.R., Cave, M., Wragg, J., Lee, K., 2018. Indoor radon measurements in south west England explained by topsoil and stream sediment geochemistry, airborne gamma-ray spectroscopy and geology. Journal of Environmental Radioactivity 181, 152–171. https://doi.org/10.1016/j.jenvrad.2016.05.007

Friedmann, H., 2005. Final results of the Austrian Radon Project. Health Physics 89, 339–348. https://doi.org/10.1097/01.HP.0000167228.18113.27

Friedmann, H., Baumgartner, A., Bernreiter, M., Gräser, J., Gruber, V., Kabrt, F., Kaineder, H., Maringer, F.J., Ringer, W., Seidel, C., Wurm, G., 2017. Indoor radon, geogenic radon surrogates and geology – Investigations on their correlation. Journal of Environmental Radioactivity 166, 382–389. https://doi.org/10.1016/j.jenvrad.2016.04.028

Friedmann, H., Gröller, J., 2010. An approach to improve the Austrian Radon Potential Map by Bayesian statistics. Journal of Environmental Radioactivity 101, 804–808. https://doi.org/10.1016/j. jenvrad.2009.11.008

Fuente, M., Long, S., Fenton, D., Hung, L.C., Goggins, J., Foley, M., 2020. Review of recent radon research in Ireland, OPTI-SDS project and its impact on the National Radon Control Strategy. Applied Radiation and Isotopes 163, 109210. https://doi.org/10.1016/j.apradiso.2020.109210

Gaafar, I., Hanfi, M., El-Ahll, L.S., Zeidan, I., 2021. Assessment of radiation hazards from phosphate rocks, Sibaiya area, central eastern desert, Egypt. Applied Radiation and Isotopes 173, 109734. https://doi.org/10.1016/j.apradiso.2021.109734

Gallagher, V., Glennon, M., Scanlon, R., Knights, K., 2016. Atlas of Topsoil Geochemistry of the Northern Counties of Ireland.

Gallagher, V., Knights, K.V., Carey, S., Glennon, M., Scanlon, R., 2016. Atlas of topsoil geochemistry of the Northern Counties of Ireland: Data from the Tellus and Tellus border projects. Geological Survey of Ireland.

Gaskin, J., Coyle, D., Whyte, J., Krewksi, D., 2018. Global Estimate of Lung Cancer Mortality Attributable to Residential Radon. Environmental Health Perspectives 126, 057009. https://doi.org/10.1289/EHP2503

Gomez, C., Lagacherie, P., Coulouma, G., 2008. Continuum removal versus PLSR method for clay and calcium carbonate content estimation from laboratory and airborne hyperspectral measurements. Geoderma 148, 141–148.

Goodfellow, B.W., Fredin, O., Derron, M.-H., Stroeven, A.P., 2009. Weathering processes and Quaternary origin of an alpine blockfield in Arctic Sweden. Boreas 38, 379–398. https://doi.org/10.1111/j.1502-3885.2008.00061.x

Gregory, D.D., Large, R.R., Halpin, J.A., Baturina, E.L., Lyons, T.W., Wu, S., Danyushevsky, L., Sack, P.J., Chappaz, A., Maslennikov, V.V., 2015. Trace element content of sedimentary pyrite in black shales. Economic Geology 110, 1389–1410.

Gunning, G.A., 2016. Studies of radon in Ireland: Outdoor levels, detector intercomparison and school remediation methods. Trinity College (Dublin, Ireland). School of Physics.

Ha, M., Hwang, S., Kang, S., Park, N.-W., Chang, B.-U., Kim, Y., 2017. Geographical Correlations between Indoor Radon Concentration and Risks of Lung Cancer, Non-Hodgkin's Lymphoma, and Leukemia during 1999–2008 in Korea. International Journal of Environmental Research and Public Health 14, 344. https://doi.org/10.3390/ijerph14040344

Hamideen, M.S., Bdair, O.M., Chandrasekaran, A., Saleh, H., Elimat, Z., 2020. Multivariate statistical investigations of natural radioactivity and radiological hazards in building materials mainly used in Amman Province, Jordan. International Journal of Environmental Analytical Chemistry 100, 189–203.

Hampson, S.E., Andrews, J.A., Lee, M.E., Foster, L.S., Glasgow, R.E., Liechtenstein, E., 1998. Lay Understanding of Synergistic Risk: The Case of Radon and Cigarette Smoking. Risk Analysis 18, 343–350. https://doi.org/10.1111/j.1539-6924.1998.tb01300.x

Harb, S., Abbady, A.E.-B., El-Kamel, A.E.-H., Saleh, I.I., Abd El-Mageed, A.I., 2012. Natural radioactivity and their radiological effects for different types of rocks from Egypt. Radiation Physics and Chemistry 81, 221–225. https://doi.org/10.1016/j.radphyschem.2011.11.005

Heimsath, A.M., Dietrich, W.E., Nishiizumi, K., Finkel, R.C., 1997. The soil production function and landscape equilibrium. Nature 388, 358–361. https://doi.org/10.1038/41056

Hickey, C., 2019. Setting the Scene.

Highland, L.M., 2018. Landslide hazard and risk: Current and future directions for the United States Geological Survey's Landslide Program, in: Landslide Risk Assessment. Routledge, pp. 207–213.

Hitzman, M., 1995. Geological setting of the Irish Zn-Pb-(Ba-Ag) orefield.

Holliday, K., Hartmann, T., Poineau, F., Rory Kennedy, J., Czerwinski, K., 2009. Synthesis and characterization of zirconia–magnesia inert matrix fuel: Uranium homolog studies. Journal of Nuclear Materials 393, 224–229. https://doi.org/10.1016/j.jnucmat.2009.06.007

Hong, H., Churchman, G.J., Yin, K., Li, R., Li, Z., 2014. Randomly interstratified illite–vermiculite from weathering of illite in red earth sediments in Xuancheng, southeastern China. Geoderma 214, 42–49.

House, P.K., 2005. Using geology to improve flood hazard management on alluvial fans-an example from laughlin, Nevada. JAWRA Journal of the American Water Resources Association 41, 1431–1447.

Ibrahim, M.E., Saleh, G.M., Abd El-Naby, H.H., 2001. Uranium mineralization in the two mica granite of Gabal Ribdab area, South Eastern Desert, Egypt. Applied Radiation and Isotopes 55, 861–872. https://doi.org/10.1016/S0969-8043(01)00122-1

ICRP, 2019. Radiological protection from naturally occuring radioactive material (NORM) in industrial processes. 142.

Ioannides, K., Papachristodoulou, C., Stamoulis, K., Karamanis, D., Pavlides, S., Chatzipetros, A., Karakala, E., 2003. Soil gas radon: a tool for exploring active fault zones. Applied Radiation and Isotopes 59, 205–213.

Irish Cancer Society, 2016. 12 ways to reduce your risk of getting cancer.

Je, H., Kang, C., Chon, H., 1999. A Preliminary Study on Soil–Gas Radon Geochemistry According to Different Bedrock Geology in Korea. Environmental Geochemistry and Health 21, 117–131. https://doi.org/10.1023/A:1006613016217

Johnson, D.L., Watson-Stegner, D., 1987. Evolution model of pedogenesis. Soil Science 143, 349–366.

Kiczka, M., Wiederhold, J.G., Frommer, J., Voegelin, A., Kraemer, S.M., Bourdon, B., Kretzschmar, R., 2011. Iron speciation and isotope fractionation during silicate weathering and soil formation in an alpine glacier forefield chronosequence. Geochimica et Cosmochimica Acta 75, 5559–5573. https://doi.org/10.1016/j.gca.2011.07.008

Kikaj, D., Jeran, Z., Bahtijari, M., Stegnar, P., 2016. Radon in soil gas in Kosovo. Journal of Environmental Radioactivity 164, 245–252. https://doi.org/10.1016/j.jenvrad.2016.07.037

Kim, S.W., Kee, W.-S., Lee, S., Lee, B.C., Byun, U.H., 2021. Tracking and Evaluating the Concentrations of Natural Radioactivity According to Chemical Composition in the Precambrian and Mesozoic Granitic Rocks in the Jangsu-gun Area, Central Southwestern South Korea. Minerals 11. https://doi.org/10.3390/min11070684

Koglin, N., Frimmel, H.E., Lawrie Minter, W.E., Brätz, H., 2010. Trace-element characteristics of different pyrite types in Mesoarchaean to Palaeoproterozoic placer deposits. Mineralium Deposita 45, 259–280. https://doi.org/10.1007/s00126-009-0272-0

Kreuzer, M., Fenske, N., Schnelzer, M., Walsh, L., 2015. Lung cancer risk at low radon exposure rates in German uranium miners. British journal of cancer 113, 1367–1369.

Krewski, D., Lubin, J.H., Zielinsk, J.M., Alavanja, M., Catalan, V.S., Field, R.W., Klot, J.B., Letournea, E.G., Lynch, C.F., Lyon, J.I., Sandler, D.P., Schoenberg, J.B., Steck, D.J., Stolwijk, J.A., Weinberg, C., Wilcox, H.B., 2019. Residential Radon and Risk of Lung Cancer A Combined Analysis of 7 North American Case-Control Studies. Epidemiology 16. https://doi.org/0.1097/01.ede.0000152522.80261.e3

Kropat, G., Bochud, F., Jaboyedoff, M., Laedermann, J.-P., Murith, C., Palacios, M., Baechler, S., 2014. Major influencing factors of indoor radon concentrations in Switzerland. Journal of environmental radioactivity 129, 7–22.

Lantz, P.M., Mendez, D., Philbert, M.A., 2013. Radon, smoking, and lung cancer: the need to refocus radon control policy. American journal of public health 103, 443–447.

Leuraud, K., Schnelzer, M., Tomasek, L., Hunter, N., Timarche, M., Grosche, B., Kreuzer, M., Laurier, D., 2011. Radon, Smoking and Lung Cancer Risk: Results of a Joint Analysis of Three European Case-Control Studies Among Uranium Miners. Radiation research 176, 375–87. https://doi.org/10.2307/41318201

Li, C., Wang, C., Yu, J., Fan, Y., Liu, D., Zhou, W., Shi, 2020. Residential Radon and Histological Types of Lung Cancer: A Meta-Analysis of Case–Control Studies. Int. J. Environ. Res. Public Health 17. https://doi.org/10.3390/ijerph17041457

Liu, B., Mastalerz, M., Schieber, J., Teng, J., 2020. Association of uranium with macerals in marine black shales: Insights from the Upper Devonian New Albany Shale, Illinois Basin. International Journal of Coal Geology 217, 103351. https://doi.org/10.1016/j.coal.2019.103351

Long, S., 2018. Ireland's National Radon Control Strategy and Supporting Research. Radiation environment and medicine: covering a broad scope of topics relevant to environmental and medical radiation research 7, 80–85.

Long, S.C., Fenton, D., Scivyer, C., Monahan, E., 2016. Factors underlying persistently high radon levels in a house located in a karst limestone region of Ireland – lessons learned about remediation. Nukleonika 61, 327–332. https://doi.org/10.1515/nuka-2016-0054

López-Abente, G., Núñez, O., Fernández-Navarro, P., Barros-Dios, J.M., Martín-Méndez, I., Bel-Lan, A., Locutura, J., Quindós, L., Sainz, C., Ruano-Ravina, A., 2018. Residential radon and cancer mortality in Galicia, Spain. Science of The Total Environment 610–611, 1125–1132. https://doi.org/10.1016/j.scitotenv.2017.08.144

Lorenzo-González, M., Torres-Durán, M., Barbosa-Lorenzo, R., Provencio-Pulla, M., Barros-Dios, J.M., Ruano-Ravina, A., 2019. Radon exposure: a major cause of lung cancer. Expert Rev. Respir. Med 13, 839–850. https://doi.org/10.1080/17476348.2019.1645599

Lucchetti, C., Briganti, A., Castelluccio, M., Galli, G., Santilli, S., Soligo, M., Tuccimei, P., 2019. Integrating radon and thoron flux data with gamma radiation mapping in radon-prone areas. The case of volcanic outcrops in a highly-urbanized city (Roma, Italy). Journal of Environmental Radioactivity 202, 41–50. https://doi.org/10.1016/j.jenvrad.2019.02.004

Ludewig, P., Lorenser, E., 1924. Untersuchung der Grubenluft in den Schneeberger Gruben auf den Gehalt an Radiumemanation. Zeitschrift für Physik 22, 178–185.

Mahajan, S., Walia, V., Bajwa, B., Kumar, A., Singh, S., Seth, N., Dhar, S., Gill, G., Yang, T., 2010. Soil-gas radon/helium surveys in some neotectonic areas of NW Himalayan foothills, India. Natural Hazards and Earth System Sciences 10, 1221–1227.

Malczewski, D., Dziurowicz, M., Kalab, Z., Rösnerová, M., 2021. Natural radioactivity of rocks from the historic Jeroným Mine in the Czech Republic. Environmental Earth Sciences 80, 650. https://doi.org/10.1007/s12665-021-09944-5

Malczewski, D., Żaba, J., 2012. Natural radioactivity in rocks of the Modane–Aussois region (SE France). Journal of Radioanalytical and Nuclear Chemistry 292, 123–130. https://doi.org/10.1007/s10967-011-1428-9

McArdle, P., Kennedy, M., 1986. The east Carlow deformation zone and its regional implications.

McCarthy Jr, J.H., Reimer, G.M., 1986. Advances in soil gas geochemical exploration for natural resources: Some current examples and practices. Journal of Geophysical Research: Solid Earth 91, 12327–12338.

McConnell, B., Philcox, M., 1994. Geology of Kildare-Wicklow: a geological description to accompany the bedrock geology 1: 100,000 Map Series, Sheet 16, Kildare-Wicklow. Published under the authority of the Director of the Geological Survey of ….

McIlwaine, R., Cox, S.F., Doherty, R., Palmer, S., Ofterdinger, U., McKinley, J.M., 2014. Comparison of methods used to calculate typical threshold values for potentially toxic elements in soil. Environmental Geochemistry and Health 36, 953–971. https://doi.org/10.1007/s10653-014-9611-x

McKinley, J.M., Ofterdinger, U., Young, M., Barsby, A., Gavin, A., 2013. Investigating local relationships between trace elements in soils and cancer data. Spatial Statistics 5, 25–41. https://doi.org/10.1016/j.spasta.2013.05.001

Meenakshi, C., Mohankumar, M.N., 2013. Synergistic effect of radon in blood cells of smokers – An in vitro study. Mutation Research/Genetic Toxicology and Environmental Mutagenesis 757, 79–82. https://doi.org/10.1016/j.mrgentox.2013.06.018

Miles, J., 1997. Calibration and standardisation of etched track detectors, in: Radon Measurements By Etched Track Detectors: Applications in Radiation Protection, Earth Sciences and the Environment. World Scientific, pp. 143–154.

Miles, J., Appleton, J., Rees, D., Green, B., Adlam, K., Myers, A., 2007. Indicative Atlas of Radon in England and Wales (Chilton). Health Protection Agency.

Mingxing, L., Xiaoyong, Y., Wei, S., Jianyu, M., Chiyang, L., 2006. REE/trace element characteristics of sandstone-type uranium deposits in the Ordos basin.

Ministry of Environment of the Slovak Republic, 81102 Bratislava (Slovakia), 2003. Report on state of the environment of the Slovak Republic 2002. Ministry of Environment of the Slovak Republic, Slovakia.

Moldrup, P., Olesen, T., Komatsu, T., Schjønning, P., Rolston, D., 2001. Tortuosity, diffusivity, and permeability in the soil liquid and gaseous phases. Soil Science Society of America Journal 65, 613–623.

Monastero, R.N., Meliker, J.R., 2020. Incidence of brain and spinal cord cancer and county-level radon levels in New Jersey, Wisconsin, Minnesota, Pennsylvania, and Iowa, USA. Environmental Geochemistry and Health 42, 389–395. https://doi.org/10.1007/s10653-019-00368-6

Monty, C., 2000. UNSCEAR Report 2000: Sources and Effects of Ionizing Radiation. Journal of Radiological Protection 21. https://doi.org/10.1088/0952-4746/21/1/609

Moreno, V., Bach, J., Baixeras, C., Font, Ll., 2014. Radon levels in groundwaters and natural radioactivity in soils of the volcanic region of La Garrotxa, Spain. Journal of Environmental Radioactivity 128, 1–8. https://doi.org/10.1016/j.jenvrad.2013.10.021

Muntean, L., Cosma, C., Cucos, A., Dicu, T., Moldovan, D., 2014. Assessment of annual and seasonal variation of indoor radon levels in dwelling houses from Alba County, Romania. Rom Journ Phys 59, 163–71.

Murphy, P., Dowdall, A., Long, S., Curtin, B., Fenton, D., 2021. Estimating population lung cancer risk from radon using a resource efficient stratified population weighted sample survey protocol – Lessons and results from Ireland. Journal of Environmental Radioactivity 233, 106582. https://doi.org/10.1016/j.jenvrad.2021.106582

Murty, V.R.K., Karunakara, N., 2008. Natural radioactivity in the soil samples of Botswana. Radiation Measurements 43, 1541–1545. https://doi.org/10.1016/j.radmeas.2008.10.004

Musso, A., Tikhomirov, D., Plötze, M.L., Greinwald, K., Hartmann, A., Geitner, C., Maier, F., Petibon, F., Egli, M., 2022. Soil Formation and Mass Redistribution during the Holocene Using Meteoric 10Be, Soil Chemistry and Mineralogy. Geosciences 12. https://doi.org/10.3390/geosciences12020099

Nelson, D. a, Sommers, L., 1983. Total carbon, organic carbon, and organic matter. Methods of soil analysis: Part 2 chemical and microbiological properties 9, 539–579.

Neri, M., Ferrera, E., Giammanco, S., Currenti, G., Cirrincione, R., Patanè, G., Zanon, V., 2016. Soil radon measurements as a potential tracer of tectonic and volcanic activity. Scientific Reports 6, 24581. https://doi.org/10.1038/srep24581

Neznal, Matěj, Neznal, Martin, Matolin, M., Barnet, I., Miksova, J., 2004. The new method for assessing the radon risk of building sites. Czech Geological Survey Prague.

Norris, K., Williams, P., 1984. Optimization of mathematical treatments of raw near-infrared signal in the. Cereal Chem 61, 158–165.

Organo, C., Ellard, A., Fenton, D., Synnott, H., O'Colmáin, M., Prenter, S., O'Reilly, S., Colgan, P.A., 2004. High radon concentrations in a house near Castleisland, County Kerry (Ireland)—identification, remediation and post-remediation. Journal of Radiological Protection 24.

Organo, C., Murphy, P., 2007. The Castleisland Radon Survey—follow-up to the discovery of a house with extremely high radon concentrations in County Kerry (SW Ireland). Journal of Radiological Protection 27. https://doi.org/10.1088/0952-4746/27/3/002

Padilla, G.D., Hernández, P.A., Padrón, E., Barrancos, J., Pérez, N.M., Melián, G., Nolasco, D., Dionis, S., Rodríguez, F., Calvo, D., 2013. Soil gas radon emissions and volcanic activity at El Hierro (Canary Islands): The 2011-2012 submarine eruption. Geochemistry, Geophysics, Geosystems 14, 432–447.

Padrón, E., Padilla, G., Hernández, P.A., Pérez, N.M., Calvo, D., Nolasco, D., Barrancos, J., Melián, G.V., Dionis, S., Rodríguez, F., 2013. Soil gas geochemistry in relation to eruptive fissures on Timanfaya volcano, Lanzarote Island (Canary Islands, Spain). Journal of Volcanology and Geothermal Research 250, 91–99. https://doi.org/10.1016/j.jvolgeores.2012.10.013

Pal, R., Patra, A.C., Bakshi, A.K., Dhabekar, B., Reddy, P.J., Sengupta, P., Sapra, B.K., 2021. Investigations on baseline levels for natural radioactivity in soils, rocks, and lakes of Larsemann Hills in East Antarctica. Environmental Monitoring and Assessment 193, 822. https://doi.org/10.1007/s10661-021-09446-8

Pandurang, A., Kerur, B., Siddanna, R., Mishra, R., 2014. Radon, thoron and their progeny concentration variations in dwellings of Gogi region, Yadgir district of Karnataka, India. Journal of Radioanalytical and Nuclear Chemistry 302, 1321–1326. https://doi.org/10.1007/s10967-014-3608-x

Park, E.J., Lee, H., Kim, H.C., Sheen, S.S., Koh, S.B., Park, K.S., Cho, N.H., Lee, C.-M., Kang, D.R., 2020. Residential Radon Exposure and Cigarette Smoking in Association with Lung Cancer: A Matched Case-Control Study in Korea. International journal of environmental research and public health 17, 2946.

Perri, F., Scarciglia, F., Apollaro, C., Marini, L., 2015. Characterization of granitoid profiles in the Sila Massif (Calabria, southern Italy) and reconstruction of weathering processes by mineralogy, chemistry, and reaction path modeling. Journal of Soils and Sediments 15, 1351–1372. https://doi.org/10.1007/s11368-014-0856-x

Petersell, V., Åkerblom, G., Ek, B.-M., Enel, M., Mõttus, V., Täht, K., 2004. The radon risk map of Estonia. Tallinn-Stockholm.

Phillips, W., Sevastopulo, G., 1986. The stratigraphic and structural setting of Irish mineral deposits. Presented at the Geology and genesis of mineral deposits in Ireland, pp. 1–30.

Pracht, M., 1997. Geology of Kerry - Cork: A geological description to accompany the bedrock geology 1:100,000 scale map series, sheet 21, Kerry-Cork.

Pracht, M., Somerville, I.D., Wang, Y., 2015. A revised Mississippian lithostratigraphy of County Galway (western Ireland) with an analysis of carbonate lithofacies, biostratigraphy, depositional environments and palaeogeographic reconstructions utilising new borehole data. Journal of Palaeogeography 4, 1–26. https://doi.org/10.3724/SP.J.1261.2015.00065

Radiological Protection Act 1991 (Ionising Radiation) Regulations, 2019. Statutory Instruments Ireland, S.I. No. 30 of 2019.

Radvanyi, P., Villain, J., 2017. The discovery of radioactivity. Comptes Rendus Physique 18, 544–550. https://doi.org/10.1016/j.crhy.2017.10.008

Ramola, R.C., Prasad, M., 2020. Significance of thoron measurements in indoor environment. Journal of Environmental Radioactivity 225, 106453. https://doi.org/10.1016/j.jenvrad.2020.106453

Raza, A., Gholami, R., Rezaee, R., Rasouli, V., Rabiei, M., 2019. Significant aspects of carbon capture and storage–A review. Petroleum 5, 335–340.

Reavy, R.J., 2001. Caledonian granites–emplacement. Open University Geological Society Journal 22.

Ribeiro, F.C.A., Silva, J.I.R., Lima, E.S.A., do Amaral Sobrinho, N.M.B., Perez, D.V., Lauria, D.C., 2018. Natural radioactivity in soils of the state of Rio de Janeiro (Brazil): Radiological characterization and relationships to geological formation, soil types and soil properties. Journal of Environmental Radioactivity 182, 34–43. https://doi.org/10.1016/j.jenvrad.2017.11.017

Riebe, C.S., Kirchner, J.W., Finkel, R.C., 2003. Long-term rates of chemical weathering and physical erosion from cosmogenic nuclides and geochemical mass balance. Geochimica et Cosmochimica Acta 67, 4411–4427. https://doi.org/10.1016/S0016-7037(03)00382-X

Rigby, J.G., La Pointe, D.D., 1993. Wind and barometric pressure effects on radon in two mitigated houses, in: The 1993 International Radon Conference. pp. 61–68.

Romer, R.L., Cuney, M., 2018. Phanerozoic uranium mineralization in Variscan Europe – More than 400 Ma of tectonic, supergene, and climate-controlled uranium redistribution. Ore Geology Reviews 102, 474–504. https://doi.org/10.1016/j.oregeorev.2018.09.013

Rosario, A.S., Wichmann, H.-E., 2006. ENVIRONMENTAL POLLUTANTS | Radon, in: Laurent, G.J., Shapiro, S.D. (Eds.), Encyclopedia of Respiratory Medicine. Academic Press, Oxford, pp. 120–125. https://doi.org/10.1016/B0-12-370879-6/00135-6

Ruano-Ravina, A., Dacosta-Urbieta, A., Miguel Barros-Dios, J., T Kelsey, K., 2018. Radon exposure and tumors of the central nervous system. Gaceta Sanitaria 32. https://doi.org/10.1016/j.gaceta.2017.01.002

Safari, M., Gholami, R., Jami, M., Ananthan, M.A., Rahimi, A., Khur, W.S., 2021. Developing a porosity-permeability relationship for ellipsoidal grains: A correction shape factor for Kozeny-Carman's equation. Journal of Petroleum Science and Engineering 205, 108896.

Samet, J.M., 1989. Radon and lung cancer. JNCI: Journal of the National Cancer Institute 81, 745–758.

Savitzky, A., Golay, M.J., 1964. Smoothing and differentiation of data by simplified least squares procedures. Analytical chemistry 36, 1627–1639.

Schwela, D., 2014. Pollution, Indoor Air, in: Wexler, P. (Ed.), Encyclopedia of Toxicology (Third Edition). Academic Press, Oxford, pp. 1003–1017. https://doi.org/10.1016/B978-0-12-386454-3.01028-9

Sevastopulo, G.D., Wyse Jackson, P., 2009. Carboniferous: Mississippian (Tournaisian and Viséan). The geology of Ireland 215–268.

Shepherd, R.G., 1989. Correlations of permeability and grain size. Groundwater 27, 633–638.

Shimoike, Y., Kazahaya, K., Shinohara, H., 2002. Soil gas emission of volcanic CO2 at Satsuma-Iwojima volcano, Japan. Earth, planets and space 54, 239–247.

Skupio, R., Kowalska, S., Jankowski, L., 2018. Analysis of influence of environmental conditions and natural gamma radiation for radon concentration measurements. Nafta-Gaz 74.

Somerville, I.D., Strogen, P., Jones, G.Ll., 1992. Mid-Dinantian Waulsortian buildups in the Dublin Basin, Ireland. Sedimentary Geology 79, 91–116. https://doi.org/10.1016/0037-0738(92)90006-D

Stenberg, B., Rossel, R.A.V., Mouazen, A.M., Wetterlind, J., 2010. Visible and near infrared spectroscopy in soil science. Advances in agronomy 107, 163–215.

Strogen, P., Somerville, I., Pickard, N., Jones, G.L., Fleming, M., 1996. Controls on ramp, platform and basinal sedimentation in the Dinantian of the Dublin Basin and Shannon Trough, Ireland. Geological Society, London, Special Publications 107, 263–279.

Sukanya, S., Noble, J., Joseph, S., 2022. Application of radon (222Rn) as an environmental tracer in hydrogeological and geological investigations: An overview. Chemosphere 303, 135141. https://doi.org/10.1016/j.chemosphere.2022.135141

Sun, X., Yang, P., Xiang, Y., Si, X., Liu, D., 2018. Across-fault distributions of radon concentrations in soil gas for different tectonic environments. Geosciences Journal 22, 227–239.

Sutton, G.A., Napier, S.T., John, M., Taylor, A., 1993. Uranium-238 decay chain data. Science of The Total Environment 130–131, 393–401. https://doi.org/10.1016/0048-9697(93)90094-M

Swakoń, J., Kozak, K., Paszkowski, M., Gradziński, R., Łoskiewicz, J., Mazur, J., Janik, M., Bogacz, J., Horwacik, T., Olko, P., 2005. Radon concentration in soil gas around local disjunctive tectonic zones in the Krakow area. Journal of Environmental Radioactivity 78, 137–149. https://doi.org/10.1016/j.jenvrad.2004.04.004

Taboada, T., Cortizas, A.M., García, C., García-Rodeja, E., 2006. Uranium and thorium in weathering and pedogenetic profiles developed on granitic rocks from NW Spain. Science of the Total Environment 356, 192–206.

Taylor, J.A., Watson, M.A., Devereux, T.R., Michels, R.Y., Saccomanno, G., Anderson, M., Devereux, T.R., 1994. p53 mutation hotspot in radon-associated lung cancer. The Lancet 343, 86–87. https://doi.org/10.1016/S0140-6736(94)90818-4

Tollefsen, T., Cinelli, G., Bossew, P., Gruber, V., De Cort, M., 2014. From the European indoor radon map towards an atlas of natural radiation. Radiation Protection Dosimetry 162, 129–134. https://doi.org/10.1093/rpd/ncu244

Tommasino, L., 2005. Radiochemical Methods | Radon., in: Worsfold, P., Townshend, A., Poole, C. (Eds.), Encyclopedia of Analytical Science (Second Edition). Elsevier, Oxford, pp. 32–44. https://doi.org/10.1016/B0-12-369397-7/00520-3

Tushe, K.B., Bylyku, E., Xhixha, G., Dhoqina, P., Daci, B., Cfarku, F., Xhixha, M.K., Strati, V., 2016. FIRST STEP TOWARDS THE GEOGRAPHICAL DISTRIBUTION OF INDOOR RADON IN DWELLINGS IN ALBANIA. Radiation Protection Dosimetry 172, 488–495. https://doi.org/10.1093/rpd/ncv494

Tzortzis, M., Tsertos, H., Christofides, S., Christodoulides, G., 2003. Gamma-ray measurements of naturally occurring radioactive samples from Cyprus characteristic geological rocks. Radiation Measurements 37, 221–229. https://doi.org/10.1016/S1350-4487(03)00028-3

United Nations Scientific Committee on the Effects of Atomic Radiation, Annex, B., 2000. Exposures from natural radiation sources. New york, United Nation 9, 11.

United Nations, U.N.S.C. on the E. of A.Radiation., 1958. Report of the United Nations Scientific Committee on the Effects of Atomic Radiation (UNSCEAR) 1958: Report to the General Assembly, with Scientific Annexes. 229. https://doi.org/10.18356/0b0b1bc1-en

Vahakangas, K.H., Metcalf, R.A., Welsh, J.A., Bennett, W.P., Harris, C.C., Samet, J.M., Lane, D.P., 1992. Mutations of p53 and ras genes in radon-associated lung cancer from uranium miners. The Lancet 339, 576–580. https://doi.org/10.1016/0140-6736(92)90866-2

Vuckovic, B., Gulan, L., Milenkovic, B., Stajic, J.M., Milic, G., 2016. Indoor radon and thoron concentrations in some towns of central and South Serbia. Journal of Environmental Management 183, 938–944. https://doi.org/10.1016/j.jenvman.2016.09.053

Walsh, P.M., National Cancer Registry, EPA, 2017. A revision of the number of radon-related lung cancers in Ireland: preliminary results.

Watson, R.J., Smethurst, M.A., Ganerød, G.V., Finne, I., Rudjord, A.L., 2017. The use of mapped geology as a predictor of radon potential in Norway. Journal of Environmental Radioactivity 166, 341–354. https://doi.org/10.1016/j.jenvrad.2016.05.031

World Health Organisation, 2009. W.H.O Handbook on indoor radon: apublic health perspective.

World Health Organization, 2016. Radon and health. World Health Organization.

World Health Organization (Ed.), 2009. WHO handbook on indoor radon: a public health perspective. World Health Organization.

World Health Organization, 2007. International radon project: survey on radon guidelines, programmes and activities (No. WHO/HSE/RAD/07.01). World Health Organization.

Yarmoshenko, I.V., Malinovsky, G.P., 2016. Lung cancer mortality and radon exposure in Russia. Nukleonika 61, 263–268. https://doi.org/10.1515/nuka-2016-0044

Yin, K., Hong, H., Churchman, G.J., Li, Z., Fang, Q., 2018. Mixed-layer illite-vermiculite as a paleoclimatic indicator in the Pleistocene red soil sediments in Jiujiang, southern China. Palaeogeography, Palaeoclimatology, Palaeoecology 510, 140–151.

Young, M.E., Knights, K.V., Smyth, D., Glennon, M.M., Scanlon, R.P., Gallagher, V., 2016. The Tellus geochemical surveys, results and applications. Unearthed: impacts of the Tellus surveys of the north of Ireland. Dublin. Royal Irish Academy. https://doi.org/10.3318/ 978-1-908996-88-6.ch3

Zhao, L., Hong, H., Liu, J., Fang, Q., Yao, Y., Tan, W., Yin, K., Wang, C., Chen, M., Algeo, T.J., 2018. Assessing the utility of visible-to-shortwave infrared reflectance spectroscopy for analysis of soil weathering intensity and paleoclimate reconstruction. Palaeogeography, Palaeoclimatology, Palaeoecology 512, 80–94.

Zinn, Y.L., Faria, J.A. de, Araujo, M.A. de, Skorupa, A.L.A., 2020. Soil parent material is the main control on heavy metal concentrations in tropical highlands of Brazil. CATENA 185, 104319. https://doi.org/10.1016/j.catena.2019.104319

Zmazek, B., Živčić, M., Todorovski, L., Džeroski, S., Vaupotič, J., Kobal, I., 2005. Radon in soil gas: how to identify anomalies caused by earthquakes. Applied geochemistry 20, 1106–1119.

Zupančič, N., Turniški, R., Miler, M., Grčman, H., 2018. Geochemical fingerprint of insoluble material in soil on different limestone formations. CATENA 170, 10–24. https://doi.org/10.1016/j.catena.2018.05.040

Chapter 4

Using geogenic radon potential to assess radon risk area designation, a case study around Castleisland, Co. Kerry, Ireland.

Published in Journal of Environmental Radioactivity 2022

Banríon M.H. (1)*, Elío J. (2), Crowley Q.G. (1)

Abstract

Globally, indoor radon exposure is the leading cause of lung cancer in non-smokers and second most common cause after tobacco smoking. Soil-gas radon is the main contributor to indoor radon, but its spatial distribution is highly variable, which poses certain challenges for mapping and predicting radon anomalies. Measurement of indoor radon typically takes place over long periods of time (e.g. 3 months) and is seasonally adjusted to an annual average concentration. In this article we investigate the suitability of using soil-gas radon and soil-permeability measurements for rapid radon risk assessments at local scale. The area of Castleisland, Co. Kerry was chosen as a case study due to availability of indoor radon data and the presence of significant radon anomalies. In total, 135 soil-gas and permeability measurements were collected and complemented with 180 indoor radon measurements for an identical 6 km^2 area. Both soil-gas radon and indoor radon concentrations ranged from very low (8.8 k Bq m^{-3}, 0.1 Bq m^{-3}) to extremely high (1433 k Bq m^{-3}, 65,000 Bq m^{-3}) values. Our method classifies almost 50% of the area as a high radon potential area, and allows assessment of geogenic controls on radon distribution by including other geological variables. Cumulatively, the percentage of indoor radon variance explained by soil-gas radon concentration, bedrock geology, deeper topsoil permeability and Quaternary geology is 34% (16%, 10%, 4% and 4% respectively). Soil-gas and indoor radon anomalies are associated with black shales, whereas the presence of karst and geological faults are other contributing factors. Sampling of radon soil-gas and soil permeability, used in conjunction with other geogenic data, can therefore facilitate rapid designation of radon priority areas. Such an approach demonstrates the usefulness of high-resolution geogenic maps in predicting indoor radon risk categories when compared to the application of indoor radon measurements alone. This method is particularly useful to assess radon potential in areas where indoor radon measurements are sparse or lacking, with particular application to rural areas, land rezoned for residential use, or for sites prior to building construction.

Keywords

Radon; Geogenic radon map; Indoor radon; Soil-gas concentrations; Geology

Abbreviations

GRP: Geogenic Radon Potential; IRC: Indoor Radon Concentration. SGRn; Soil-Gas Radon. RPA: Radon Priority Area.

4.1 Introduction:

The global population receives its most significant proportion of natural ionizing radiation from radon exposure (Monty, 2000). The World Health Organization classifies radon as a class I carcinogen, and reports that it is the second leading cause of lung cancer after tobacco smoking, and the most common cause of lung cancer in non-smokers (World Health Organization, 2009). A study of 66 countries reported 226,057 total radon-attributed lung cancer deaths in 2012 (Gaskin et al., 2018). Annually in Ireland, approximately 350 people are estimated to develop radon-induced lung cancer (Fuente et al., 2020; Murphy et al., 2021). Typical 5-year survival rates from the time of diagnosis for lung cancer are 20% (National Cancer Registry Ireland, 2020). When identified, radon priority area (RPA) can be the focus for radon testing and remediation (Bossew, 2018), or they may be used as a geospatial parameter in targeted lung cancer screening programmes (Elío et al., 2018; Petermann et al., 2022). Any efforts which identify radon priority areas will help to reduce the lung cancer mortality in the general population.

Radon is a naturally occurring radioactive noble gas that emanates from rock, soil, and water. It is a dense, odourless and colourless gas. Radon (^{222}Rn) is an intermediate decay product in the ^{238}U decay chain. As uranium emits alpha particles, it transforms into a series of different isotopes before decaying to lead (^{206}Pb). The isotopes of ^{219}Rn (actinon) and ^{220}Rn (thoron) are intermediate decay products of ^{235}U and ^{232}Th respectively. Radon concentrations in the atmosphere are generally low (typically 5 becquerels per cubic meter (Bqm^{-3})) (Barros et al., 2015; Gunning, 2016; Habib et al., 2018; Rafique et al., 2021). However, radon can occur at much higher concentrations in soil (typically 10's to 100's kBqm^{-3}) (Abdalla et al., 2021; Alonso et al., 2019), or enclosed spaces such as buildings and caves (typically 10's to 100's Bqm^{-3}) (Cucoş Dinu et al., 2017; Margineanu, 2019; Smith et al., 2019).

As radon decays over a short half-life (3.8 days), it emits alpha radiation (5.5909 MeV) as it transforms into polonium (^{218}Po and ^{214}Po). The short half-life of ^{218}Po and ^{214}Po (164.3µs and 3 min respectively) causes these isotopes to densely emit alpha radiation (energies of 6 MeV and 7.9 MeV respectively). The polonium isotopes, which are charged metal ions, can be inhaled either unattached or attached to airborne particulate matter. The polonium ions can become lodged in lung tissue and act as point sources of alpha radiation. For these reasons, there is a direct relationship between radon exposure and lung cancer (Marsh et al., 2021).

Globally, the detrimental health effects of radon exposure are recognized, and many countries have initiatives designed to mitigate these health issues (European Commission, 2013; Khan et al., 2019; United Nations Scientific Committee on the Effects of Atomic Radiation, 2015). In Ireland, the national radon action plan is supported by the 'National Radon Control Strategy', 'Radon in workplaces', 'Gamma radiation from building materials', and 'Indoor exposure to radon in domestic dwellings' (Radiological Protection Act, 1991; Ionising Radiation Regulations, 2019). Of particular importance is the original radon risk map, which outlines areas of radon priority, with high radon areas defined as "any area where it is predicted that 10 percent or more of homes will exceed the reference level of 200 Becquerel per cubic metre (Bqm^{-3})" (Fennell et al., 2002). In high radon areas, new buildings are obliged to have preventative measures in place to reduce excessive radon accumulation. Furthermore, in areas deemed high radon risk, employers are obliged to measure for radon and if necessary, ensure that radon is below the reference level (Radiological Protection Act, 1991 (Ionizing Radiation)

Regulations, 2019). Therefore, finding an effective method for defining high radon areas is crucial for radon mitigation (Bossew et al., 2020).

The original radon risk map of Ireland published by the Environmental Protection Agency (Fennell et al., 2002) has a 10 × 10 km^2 spatial resolution and is based exclusively on indoor radon concentration (IRC) (i.e. it does not contain any geological information). The Environmental Protection Agency in Ireland published an updated radon risk map in May 2022, which incorporates geogenic properties following the methodologies of Elío et al. (2017), (Environmental Protection Agency, 2022). Importantly, the literature on radon and geology indicates a high spatial variability of soil-gas radon (SGRn), over areas far smaller than 10 × 10 km^2 (Duggal et al., 2014, Idriss et al., 2014; Ravikumar et al., 2015).

It is noteworthy that the greatest contributor to IRC is SGRn (Chen and Ford, 2017; World Health Organization, 2007). Porosity, soil permeability, structural geology and the pressure difference between the ground below the building and the indoor ground level, influences SGRn concentrations (Sun et al., 2004; Jelle 2012; Kulali et al., 2017; Laiolo et al., 2016). Both occupancy style, ventilation and building characteristics affect the radon concentrations within dwellings (Liping et al., 2016; Schubert et al., 2018). Additionally, the climatic and seasonal conditions affect the atmospheric pressure, wind speed, temperature, humidity and precipitation, which influence soil-gas radon accumulating indoors (Sundal et al., 2008; Xie et al., 2015).

Ireland's National Radon Control Strategy targets geographical regions deemed to be radon prone, i.e. High Radon Areas (HRA) or Radon Priority Areas (RPA). The National Radon Control Strategy second phase knowledge gaps report states that the national radon risk map may be improved by researching areas with anomalously high radon levels associated with karstified limestones particularly around Castleisland and Tralee in North Co. Kerry (National

Radon Control Strategy, 2019). A specific area in Ireland was chosen as the focus of this study due to anomalous radon reported in the region, and the fact that it is underlain by karstified limestones. The study area is approximately 6 km^2 containing multiple geological units at a 1:100 K scale.

In this paper, the method of geogenic radon potential (GRP); a two-parameter method using SGRn and soil permeability measurements (Neznal et al., 2004), is assessed for suitability to identify radon-prone areas. Results are compared with the original radon map for Ireland (Fennell et al., 2002) and the updated EPA radon map of Ireland (Environmental Protection Agency, 2022). The approach for radon priority area assessment investigated in this study was tested for the townland of Castleisland, Co. Kerry, South-West Ireland (Fig. 4.1). This area was chosen considering one of Europe's highest, and Ireland's highest IRC measurement of 65,000 Bqm^{-3} was recorded here (seasonally adjusted average of multiple measurements of 49,000 Bqm^{-3}; Organo et al., 2004). Furthermore, the highest underground radon concentrations in Ireland were recorded in Crag Cave, Castleisland (11,285 Bqm^{-3}), during a reconnaissance survey of radon in three show caves in Ireland (Duffy et al., 1996).

Approximately half of the study site is classified as a high indoor radon area (Fig. 4.1) (Environmental Protection Agency, 2022; Fennell et al., 2002).

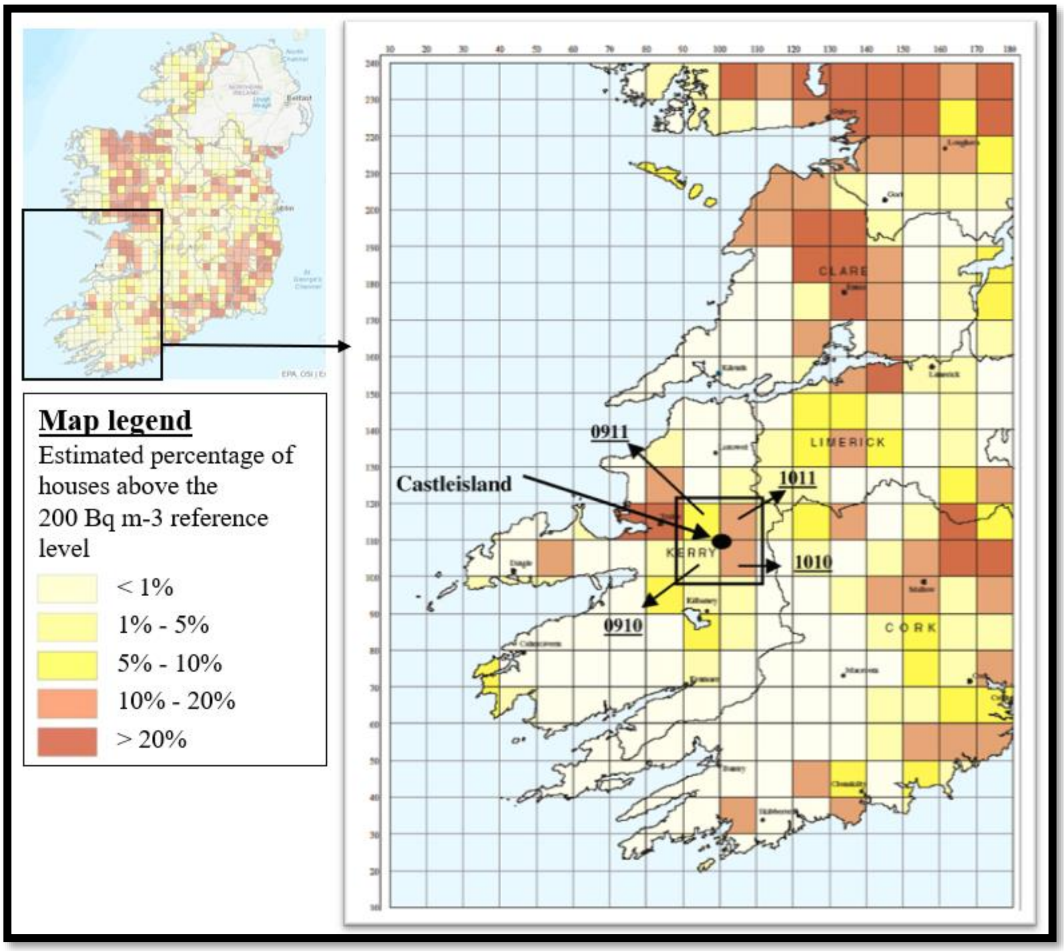

Figure 4.1 Top left shows the Indoor radon map for Ireland (Fennell et al., 2002). The right map is adapted from (Organo and Murphy, 2007) which pinpoints the location of the Castleisland study area with consideration to Ireland's radon map. The grids are 10 x 10 km^2. The map legend shows the estimated percentage of homes likely to exceed the 200 Bq m^{-3} reference level.

The main aims of this study are to investigate the use of GRP as a means to assess radon risk and to compare the resultant risk maps with the original map which relies solely on IRC data (Fig. 4.1) and with the new EPA indoor radon map, which incorporates geological parameters (Environmental Protection Agency, 2022). The data analysis presented here illustrates strong evidence for the GRP method being a suitable process for estimating radon risk in this area. We present results that demonstrate a high spatial variability of radon and that a locally occurring lithology is a major contributor to the high IRC measurements in the Castleisland area. We suggest that radon gas utilizes faults and karst, and is transported from source to areas underlain by limestones. The scientific approach described in this study validates the feasibility for using geogenic data when assessing and defining radon priority areas, especially at local scales and in rural regions with a low population density and limited availability of indoor radon data.

4.2 Materials and methods:

4.2.1 Study area

Upper Palaeozoic rocks form the bedrock geology of the Castleisland area (www.gsi.ie; Pracht, 1997). The primary bedrock type comprises various Dinantian (359 Ma – 326 Ma) limestones (un-bedded, bedded, bioclastic, argillaceous). The limestones formed in an open water sub-tidal zone on the continental shelf (Sleeman et al., 2004). The north of the study area is dominated by carboniferous siltstones (Cloone Flagstones) and Namurian (326 Ma – 313 Ma) Clare Shales (Pracht, 1997).

The shales accumulated in deep basins which formed after faulting caused by the Variscan orogeny (Sleeman et al., 2004). The Clare Shales are black shales, formed in a deep water euxinic paleoenvironment 326 Ma to 313 Ma overlying Viséan (346.7 Ma to 330.9 Ma) limestones (Hodson, 1954; Rider, 1974; Wignall and Best, 2000). Substantial concentrations (mean 10's to 100's mg/kg) of uranium are frequently reported to be contained within black shales (Lecomte et al., 2017; Soesoo et al., 2020). Elevated levels of uranium in organic rich black shales can be attributed to abiotic sequestering or symbiotic remediation processes, i.e. bacteria utilizing uranium for their growth while converting the mobile U(VI) to the immobile U(IV) (Anderson et al., 2003; Gadd, 2010; Koribanics et al., 2015; Min et al., 2005). In abiotic terms, uranium occurs in elevated concentrations in uranyl tricarbonate form, while anoxic conditions cause the uranium to present in higher concentrations as uranyl carbonate species, which allows for dissolved U(VI) to precipitate as U(IV) (Nagarajan et al., 2007; Hyun et al., 2014).

Geologically, Castleisland is located at, what is conventionally considered, the northern edge of the Variscan orogeny in Ireland, which caused large-amplitude folds during the late Carboniferous and early Permian periods (Sleeman et al., 2004). Primary structural features of the study area resulted from the Variscan orogeny (Pracht, 1997; Thornton, 1966), including an east-west anticlinal axial plane approximately 1 km to the south. The main faults are directed NS and NW-SE (Fig. 4.2). The limestone is extensively karstified, exhibiting sinkholes, springs and dolines (www.gsi.ie) and resulting in caves spanning 100's m^2 (Gunn, 1982). Streams in Crag cave (200 m east of the study area) have a north to south flow direction (Tooth and Fairchild, 2003).

Quaternary glaciations affected the area resulting in predominantly locally derived glacial till (Sleeman et al., 2004). Quaternary sediments consist of till derived from Namurian sandstones, siltstones, and shales in the north of the area and till derived from limestones in the south, with alluvium also present in the south.

The exact location of the study area was decided utilizing available information on regional geology (www.gsi.ie). Fig. 4.2 depicts the study area sampling grid superimposed on geological maps for the area. The grid acted as an aid to collect samples in an equal spatial pattern as much as possible (Fig. 4.2). In some scenarios it was not possible to collect data at certain locations due to a variety of reasons including the depth to bedrock being too shallow, or where the deeper topsoil was too impermeable to obtain a measurement for GRP calculation i.e. in some peaty areas. Furthermore, samples were not collected on artificial land (e.g. landscaped gardens). For these reasons, there are a lack of samples on the south-east of the map (Fig. 4.2) which correlates with the townland of Castleisland Co. Kerry.

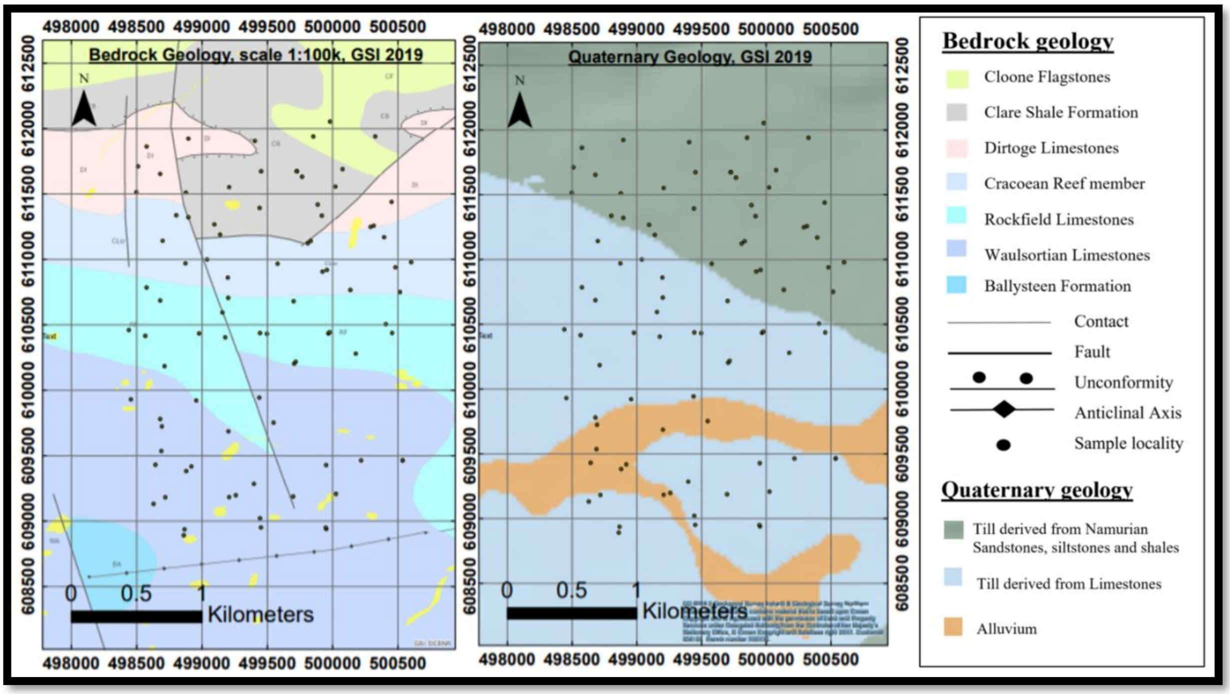

Figure 4.2 Illustration of how the sample area was chosen to include a range of geogenic features. The coordinate system used is the Irish Time Mercator (ITM). (a) Bedrock geology 1:100 k scale G.S.I. 2019, (b) Quaternary geology map 1:50 k G.S.I. The points on each map represent the data sample collection locations. The small text at the bottom right side of the Quaternary map reads "CC-BY 4.0 Geological Survey Ireland & Geological Survey Northern Ireland. This publication contains material that is based upon Crown Copyright and is reproduced with the permission of Land and Property Servies under Delegated Authority from the Controller of Her Majesty's Stationary Office, © Crown Copyright and database right. CustomerID4104. Permit number 100132."

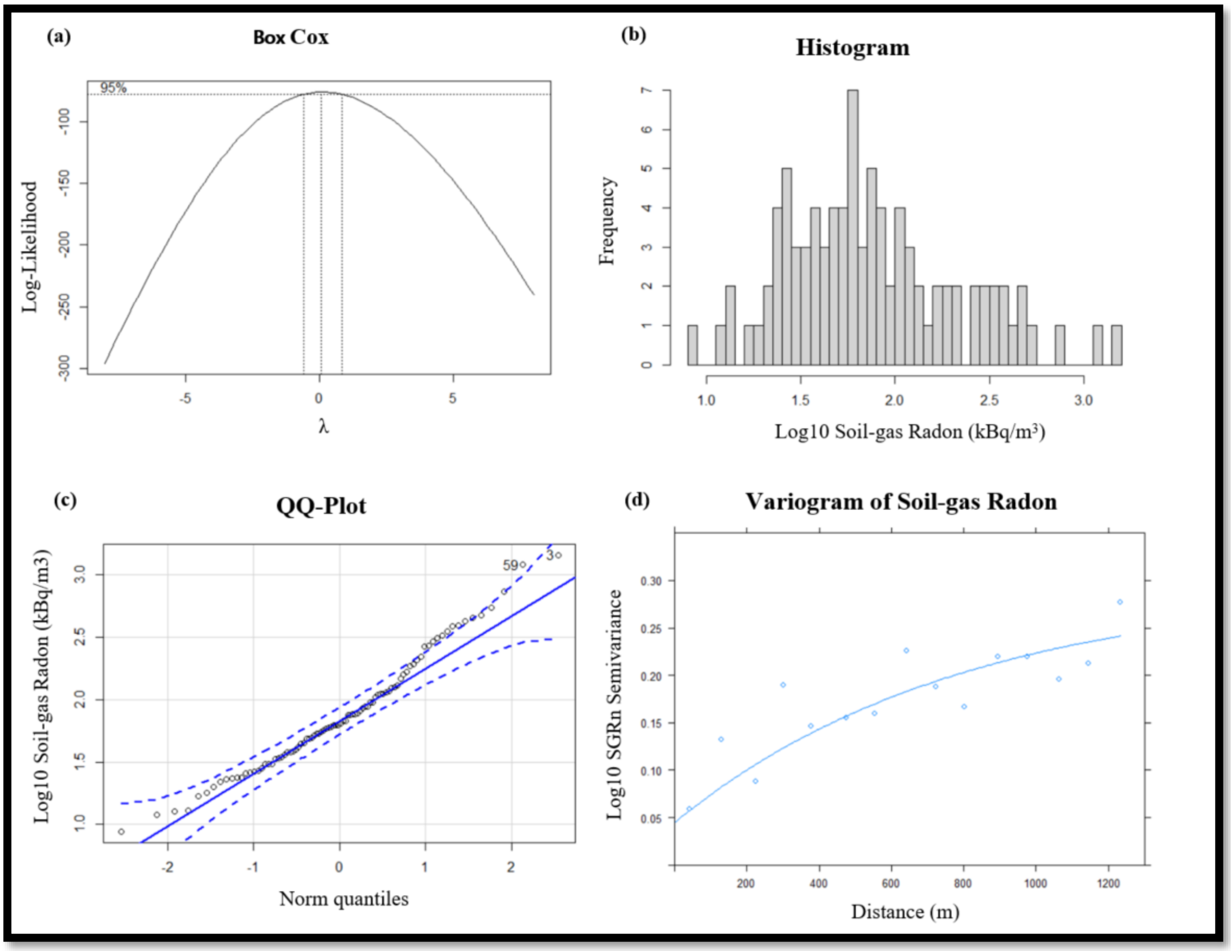

Figure 4.3. (a) BoxCox (b) Histogram (c) QQ-Plot and (d) Variogram. The variogram (d) uses the "Exp" model with a nugget of 0.045, range of 800 m and psill of 0.25. of Log10 transformed soil-gas radon.

4.2.2 Deeper topsoil permeability measurements

Deeper topsoil permeability measurements were collected using a Radon-Jok device which forms part of the well-established, standardized method (Neznal et al., 2004). A 1-m hollow tube, with a 'lost tip' attached to the bottom, was hammered vertically into the soil, and the tip was ejected at 80 cm to permit the extraction of a soil-gas sample. The hollow tube was connected to the Radon-Jok device using a rubber tube. The Radon-Jok device was activated, and the time to extract 2-L of air from the deeper topsoil was recorded. In cases of lower permeability, one or two weights were attached to the Radon-Jok device in order to reduce the amount of time taken to extract an air sample from the subsurface. The theory of calculating permeability using the Radon-Jok instrument is derived from Darcy's equation:

$Q = F. (k\mu). \Delta p$, rearranged as $k = (Q. \mu)/(F. \Delta p)$ (1)

Where: k is the permeability (in m^2), F is the shape factor (0.159 m for Radon-Jok), Q is the flow rate (m^3/s Δp is the pressure difference (Pa), and μ is the dynamic viscosity of air (1.75 × 10-5 Pa s @ 10C). Q is calculated from the time taken to fill the 2-L volume of the diaphragm. The pressure is provided by none, one or two weights, applying a pressure of 0, 2160 or 3750 Pa, respectively (Neznal et al., 2004).

4.2.3 Soil-gas measurements

In total, 135 SGRn samples were collected, including duplicate samples. Ninety-five of these were collected between the July 14, – July 22, 2018. The remaining 40 samples were collected between July 30, – August 2, 2019. In 2019, four samples were collected from control points over the collection period. In 2018, a total of 12 samples were collected from control points over the collection period. These duplicate samples were taken to assess any change in measurement due to atmospheric variability or daily weather fluctuations. In the 2018 field survey, 23 extra samples were collected in the north of the field study, due to a significant radon anomaly. Eight samples were incomplete due to either failure in obtaining permeability readings or soil-gas to sample. These additional, failed and control samples were removed from the dataset for geostatistical analysis to avoid biasing of results. The data analysis included 88 samples in total.

Soil gas was extracted and soil radon concentrations were measured following the procedure of (Neznal et al., 2004). The same hollow tube set-up was used for the deeper topsoil permeability samples to measure the SGRn. A 150 ml syringe was attached to the hollow tube to extract the soil-gas sample. The first two 150 ml samples were discarded to purge the pipe of any atmospheric air. The third sample was transferred into a 250 ml pre-vacuumed ionization chamber. The chamber pressure was equalised to the atmospheric pressure by introducing

100 ml of atmospheric air (atmospheric air contains negligible radon concentrations, typically less than 10 Bqm^{-3}) (Gunning, 2016). Variables of moisture content and particulate matter were mitigated by attaching an interface with a desiccant compartment (containing anhydrous calcium sulphate) and a 0.45 µm filter between the hollow tube and syringe. An RM-2 device was used to measure radon concentration within the soil-gas, 15 min after the sample was introduced into the chamber.

The lower and upper detection limit of the RM-2 device is 3 $kBqm^{-3}$ and 1400 $kBqm^{-3}$, respectively. The radon concentration uncertainty is represented by sigma(σ), where sigma (σ) is 0.33 x(concentration of radon ($kBqm^{-3}$))$^{0.5}$, which results in the radon concentration being reported as concentration of radon±sigma. Therefore, the RM-2 device has a radon concentration measurement uncertainty of less than 20%. Elío et al. (2019) reported an average relative standard deviation of 15% for replicate samples and an average 5.75% uncertainty for the same RM-2 device.

4.2.4 Geogenic Radon Potential calculation

We used the geogenic radon potential G(RP) index as defined by (Neznal et al., 2004). The equation for which is:

$$GRP = CRn / (-\log 10\ (k) - 10) \quad (2)$$

Where k (m^2) is the soil permeability and CRn is the concentration of radon (k Bqm^{-3}) in the soil-gas. This method uses both SGRn concentrations (k Bqm^{-3}) and deeper topsoil permeability measurements (m^2) and outputs a value representing GRP. The calculated GRP is conventionally reported without a unit because it is a categorical and relative value which represents the potential of radon gas entering a building. In order to facilitate comparison with other countries, GRP categories were chosen to reflect those most commonly used, which are 0–10, 10–35 and 35+, corresponding to low, medium and high values respectively. The GRP method as originally defined (Neznal et al., 2004) utilizes at least 15 samples of soil-gas radon and soil-permeability for a site less or equal to 800 m^2, otherwise individual SGRn and *k* samples are collected in a 10 × 10 m grid for a specific location (e.g. the area corresponding to a new building). The general GRP method of Neznal et al. (2004) has been adapted for different applications, for instance some studies in Germany use two measurements within a given sample site (Kemski et al., 1996), in other studies there is one sample per location (Singh et al., 2010). Additional differences in methodologies include some studies which use the maximum GRP and others use the median value (Günay et al., 2018; Kemski et al., 2001). In this study CRn and k measurements were taken at an approximate distribution every 250 m over a grid spacing, depending on deeper topsoil depth and anthropogenic factors such as modification of soil profiles, or building developments. The GRP values derived from the in-situ measurements were interpolated using an inverse distance weighted kriging method with a resolution of 9 m in ArcGIS (Fig. 4.5b).

4.3 Results

4.3.1 SGRn measurements

SGRn measurements from the study site range from 8.8 $kBqm^{-3}$ (s1031) to >1433 $kBqm^{-3}$ (s109). The highest measured value of >1433 $kBqm^{-3}$ is higher than the certified detection limit of the RM-2 device, so represents a minimum value. One percent of values are very low (<10 $kBqm^{-3}$), 17% of values are low (10–30 $kBqm^{-3}$), 18% of values are moderate (30–50 $kBqm^{-3}$), 15% of values are high (50–70 $kBqm^{-3}$), 13% of values are very high (70–100 $kBqm^{-3}$), and 36% of values are extremely high (+100 $kBqm^{-3}$) (Supplementary materials). The dataset used for analysis was log10 transformed (Fig. 4.3). The variogram (Fig. 4.3d) shows that the spatial variation at a local scale is very high, with the variation levelling at 700 m. The variogram model has a nugget effect of 0.001. The sill is 0.175, model “Sph” and range 800 m.

The daily repeats give an estimate of the cumulative measurement uncertainties plus the natural variability in soil-gas radon over relatively short time scales (i.e. days). The instrument is estimated to have a ± 20% uncertainty range, as previously determined by the manufacturer and by Elío et al. (2019). We measured between 2% and 6.8% variation from each of our four daily repeat sites, which is accounted for by the instrument measurement uncertainty (Table 4.1).

Table 4.1 Daily repeats of SGRn measurements in two localities in 2018 and 2019.

Locality ID	**Date**	**Replica**	**Rn(kBqm^{-3})**	**Mean (kBqm^{-3})**	**RSD (%)**	**RM-2 (%)**	**uncertainty**
60	July 14, 2018	A	408	438.4	9.6	6.8	
	July 15, 2018	B	462				
	July 19, 2018	C	460				
	July 20, 2018	D	488				
	July 21, 2018	E	374				
23	July 16, 2018	A	59.8	33.7	37.2	2.0	
	July 17, 2018	B	22.2				
	July 18, 2018	C	27.6				
	July 19, 2018	D	27.4				
	July 20, 2018	E	37.6				

Locality ID	Date	Replica	Rn(kBqm^{-3})	Mean (kBqm^{-3})	RSD (%)	RM-2 (%)	uncertainty
	July 21, 2018	F	27.7				
67a	July 30, 2019	A	50.6	55.6	12.7	2.5	
67b				112	1.3	3.5	
	July 31, 2019	B	60.6				
	August 01, 2019	A	111				
	August 02, 2019	B	113				

From 88 SGRn samples, 28 were collected above Waulsortian limestones, 2 above Cloone Flagstones, 19 above the Rockfield limestones, 16 above Cracoean Reef member, 8 above Dirtoge limestones, and 15 above Clare Shales. The box plot (Fig. 4.4) illustrates that samples collected above the Clare Shales contain a higher range of SGRn values. The lowest values are included within the Cloone Flagstones, followed by the Waulsortian limestones, Rockfield limestones, Dirtoge limestones, and Cracoean Reef member. The majority (87%) of samples collected above the Clare Shales are exceptionally high (>100 k Bqm^{-3}), whereas 86% of SGRn samples collected above the Waulsortian limestones measured below 100 k Bqm^{-3} (Supplementary data file).

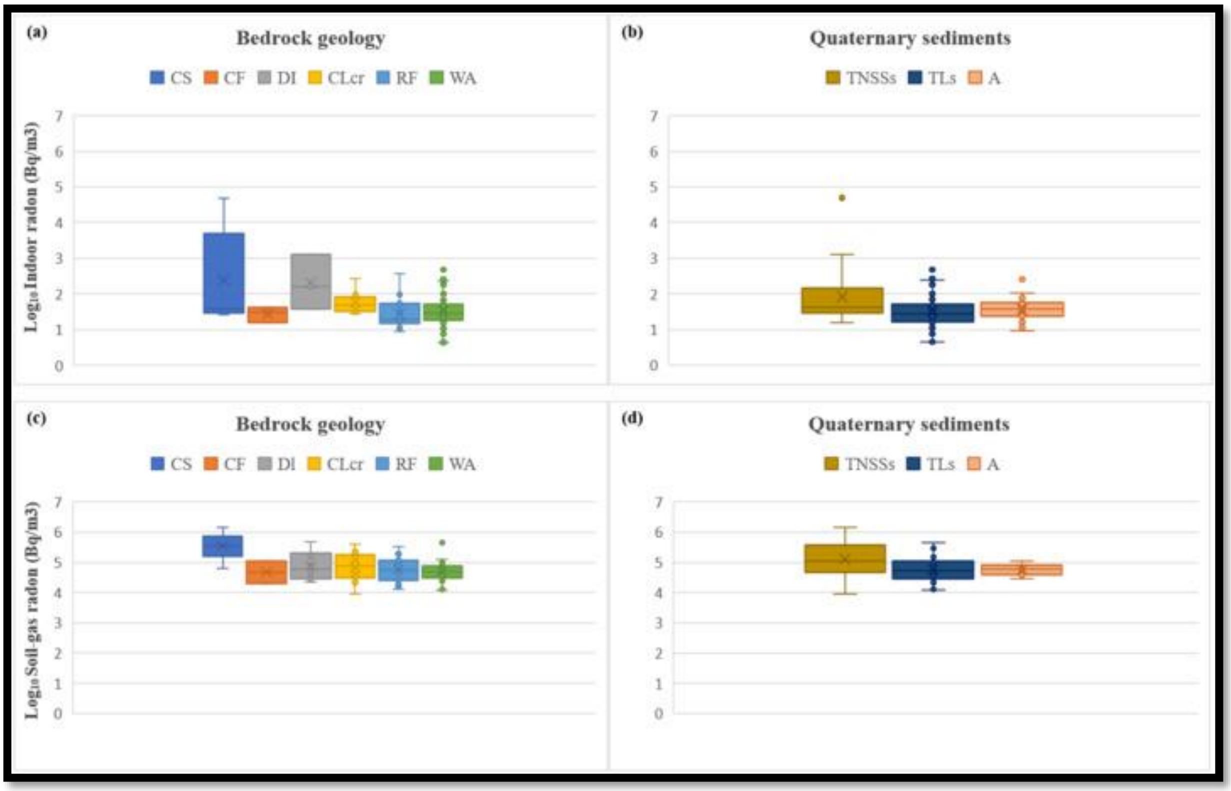

Figure 4.4. Soil-gas radon results grouped to (a) bedrock geology unit. The Stratigraphic codes' full names on the plot are CS – Clare Shales, CF, Cloone Flagstones, Dl – Dirtoge limestones, CLcr – Cracoean reef member, RF – Rockfield limestone Formation, WA – Waulsortian limestones. And (b) Quaternary Sediments. The full names of the stratigraphic codes are TNSSs – Till derived from Namurian sandstones, siltstones, and shales, TLs – Till derived from limestones, A – Alluvium. Figures (c) and (d) Boxplot of Log_{10} normal Indoor radon data grouped to (c) Bedrock geology and (d) Quaternary Sediments.

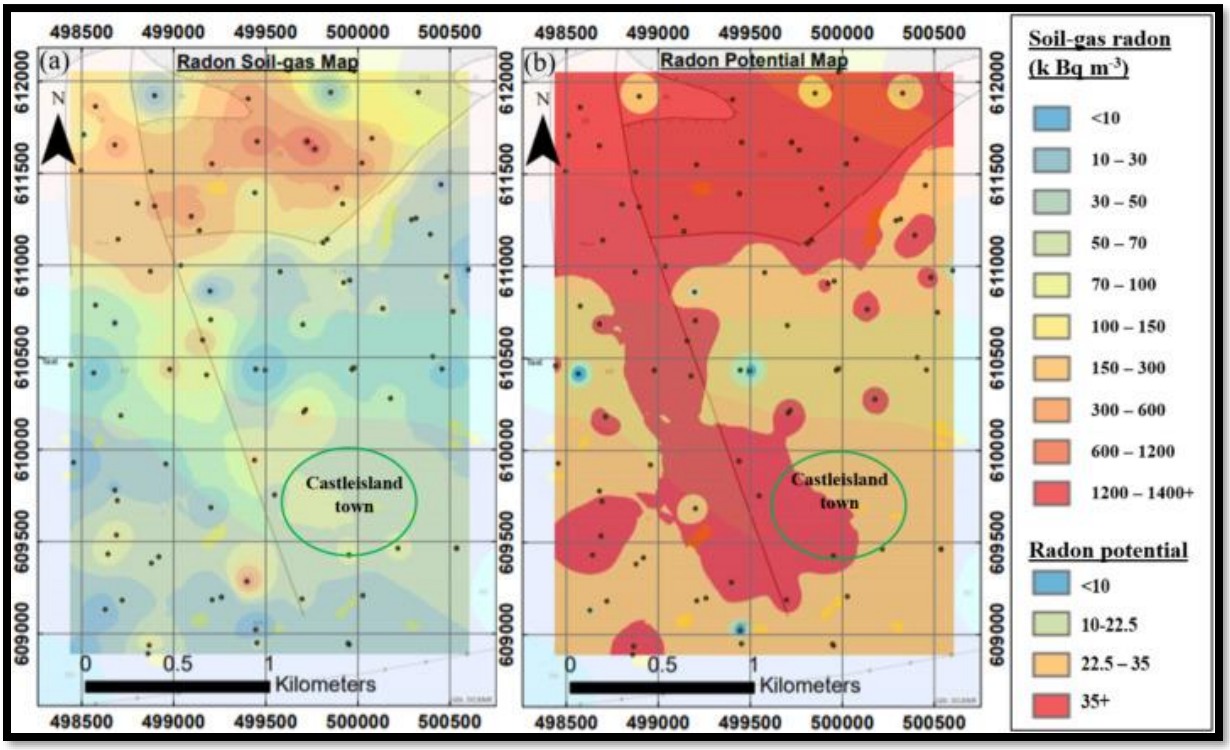

Figure 4.5 (a) Soil-gas radon map and (b) radon potential map produced using Inverse distance weighted function in ArcGIS. The resulting maps have been superimposed on top of the bedrock geology 1:100 k G.S.I. map for the area. Points on the map signify where samples were collected.

Analysis of variance (ANOVA) is a method used to statistically analyse the similarity of data groups based on the variance between their means (Larson, 2008). The application of ANOVA in geogenic studies is commonly used (Domingos et al., 2020; Drolet et al., 2014; Tositti et al., 2017). For the present study, one-way ANOVA is used to determine the general variance that geological factors cause in relation to SGRn. The ANOVA is repeated in a similar manner to determine the degree of IRC variation caused by geological factors, which is reported further in the results section below. The results of an ANOVA analysis statistically demonstrate a significant effect size variance of SGRn due to Quaternary geology and bedrock geology (Table 4.2).

*Table 4.2 ANOVA table of soil-gas radon effect size due to deeper topsoil permeability, Bedrock geology, and Quaternary geology. The Asterix symbols refer to the level of significance of the results. * equivalent to a p-value of 0.01, ** equivalent to a p- value of <0.001.*

Factor	Df	Sum Sq.	Mean Sq.	F value	Pr (>F)
Deeper topsoil permeability: variance explained 21%	4	4.327	1.082	5.578	0.000501***
Residuals	83	16.096	0.194		
Bedrock geology: variance explained 39%	5	7.728	1.546	9.983	1.74e-07 ***
Residuals	82	12.695	0.155		
Quaternary Sediments: Variance explained 13%	2	2.642	1.321	6.315	0.00726 **
Residuals	85	17.780	0.209		

Considering the Quaternary geology, 42 of the samples were collected above till derived from limestone, 37 above till derived from Namurian sandstones, siltstones, and shales, and nine were collected above alluvium (supplementary materials). The samples collected above till derived from Namurian sandstones, siltstones, and shales have mostly (59%) extremely high values of SGRn. In contrast, 38% of samples collected above the till derived from limestones are greater than 100 $kBqm^{-3}$. All of the extremely high (>100 $kBqm^{-3}$) SGRn values result in a high GRP (35+), although not all of the high GRP values are linked to extremely high SGRn concentrations.

Examining SGRn measurements in relation to bedrock geology (Fig. 4.5a) indicates higher concentrations above the Clare Shales in the north of the study area, with lower values generally above the limestones in the south of the study area. The map (Fig. 4.5a) reveals that higher

SGRn concentrations occur above the limestones along a local NW-SE fault. Overall, 74% of the study area SGRn ranges from 8.8 k Bq m^{-3} to 100 $kBqm^{-3}$, with the most significant area (57%) equating to a moderate to high SGRn range (30 $kBqm^{-3}$ – 70 $kBqm^{-3}$). Approximately 36% of the study area contains extremely high (100+ $kBqm^{-3}$) SGRn values.

4.3.2 Geogenic radon potential mapping

The GRP for the study area ranges from 5 to greater than 1200. radon potential values greater than 35 are considered exceptionally high (Neznal et al., 2004). The resulting map (figure 4.5b) shows 49% of the area has an GRP greater than 35, 50% is medium-high, with 1% of the site being less than 10. The north of the study area featuring Clare Shales has a GRP ranging from 200 to a maximum value of 1778, while the lowest radon potential values occur over the Rockfield limestones formation with a minimum value of 5.

4.3.3 Indoor radon

IRC values within the study area range from 4.4 Bqm^{-3} to 49,000 Bqm^{-3}. Table 4.3 shows that the amount of variance explained by geogenic factors using one-way ANOVA tests are 34% (16% by SGRn, 10% by bedrock geology, 4% by deeper topsoil permeability, and 4% by Quaternary geology).

*Table 4.3 . ANOVA table showing the variance of Indoor Radon measurements due to Bedrock geology, Quaternary geology, soil-gas radon, and deeper topsoil permeability. The Asterix symbols refer to the level of significance of the results. * equivalent to a p-value of <0.001.*

Factor	**Df**	**Sum Sq.**	**Mean Sq.**	**F value**	**Pr (>F)**
Bedrock geology: variance explained 10%	**7**	3.202	0.457	2.779	0.00921**
Residuals	**172**	28.315	0.165		

Factor	Df	Sum Sq.	Mean Sq.	F value	Pr (>F)
Quaternary geology: variance explained 4%	**2**	1.222	0.611	3.571	0.0302*
Residuals	**177**	30.295	0.171		
Soil-gas radon: variance explained 16%	**5**	5.009	1.002	6.576	1.25e-05 ***
Residuals	**174**	26.508	0.152		
Deeper topsoil permeability: Variance explained 4%	**4**	1.361	0.340	1.974	0.1
Residuals	**175**	30.157	0.172		

The IRC variogram (Fig. 4.6d) shows that the IRC measurements exhibit a relatively small degree of variation within a small spatial range (from approximately 100 m–700 m). The IRC values exhibit an increase in variation when the distance between the measurements is increased; this is reflected by the steep incline seen at approximately 800 m on the variogram.

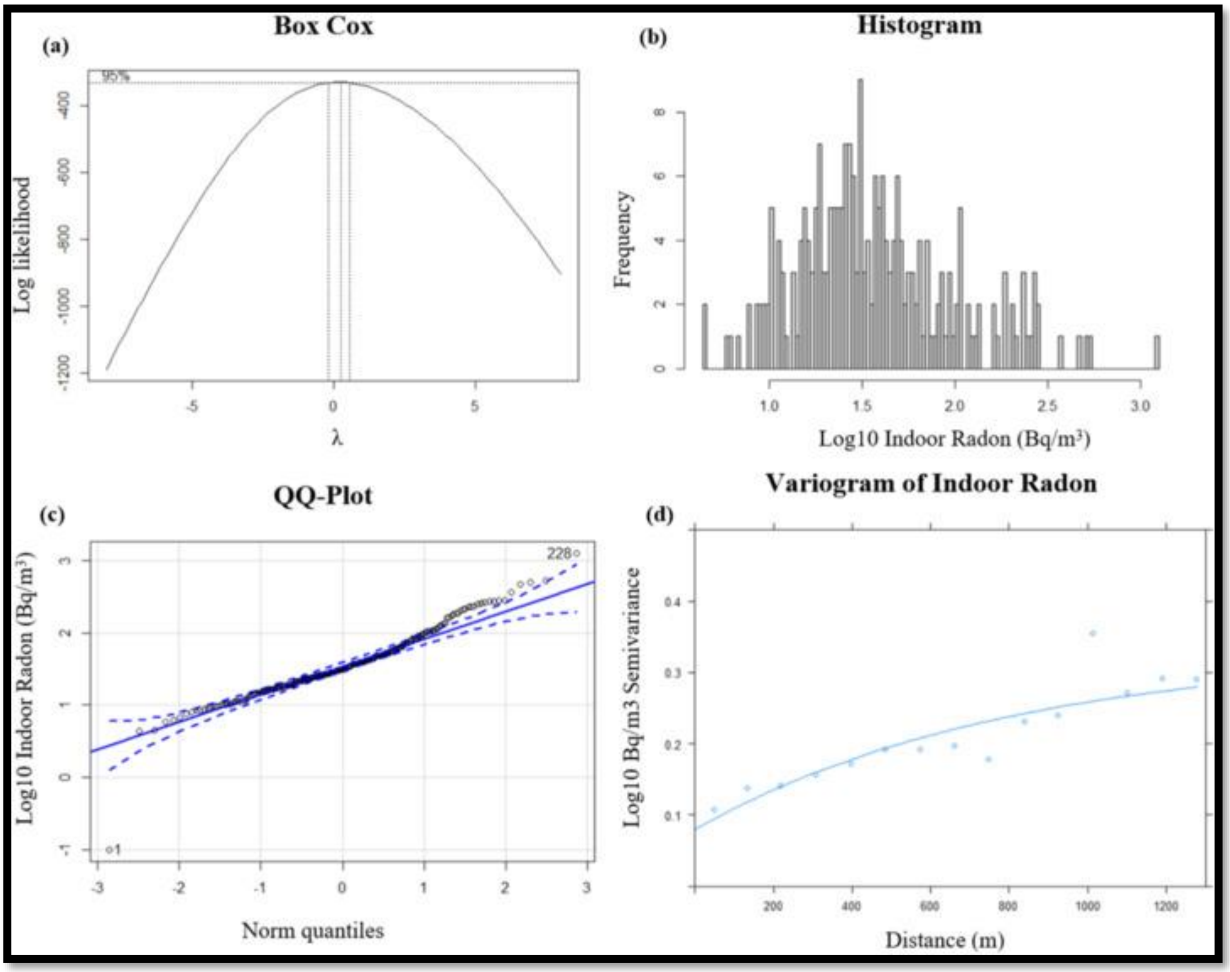

Figure 4.6. Indoor radon log10 transformed data distribution. (a) BoxCox (b) Histogram (c) QQ-Plot and (d) Variogram. The variogram (d) uses the "Exp" model with a nugget of 0.08, range of 800 m and psill of 0.25.

Geogenic context of indoor radon results

A total of 180 houses were sampled in the area. Specifically, 144, 18, 8, 3, 4, and 3 indoor radon measurements were collected above several different bedrock lithologies (Waulsortian limestones, Rockfield limestones, Cracoean Reef member, Dirtoge limestones, Clare Shales, Cloone Flagstones, respectively) (table 7.1.6 supplementary materials). Fifteen houses (8%) have radon levels above the reference level. The probability of exceeding the reference level (table 7.1.6 supplementary material) is 8% (11 of 144 houses) for the Waulsortian limestones, 6% (1 of 18 houses) for Rockfield limestones, 12% (1 of 8 houses) for the Cracoean Reef member, 33% (1 of 3 houses) for the Dirtoge limestones, 25% (1 of 4 houses) for the Clare Shales and 0% (0 of 3 houses) for the Cloone Flagstones.

4.4 Discussion

Indoor radon concentrations from the study area in Castleisland, SW Ireland are amongst the highest recorded within Europe (Organo and Murphy, 2007), and are in the upper range of those recorded globally (World Health Organization, 2007). The SGRn, as might be expected from this context, are also high compared to the published literature. The median SGRn in Castleisland is ca. 66 $kBqm^{-3}$ compared to ranges typically between ca. 10–40 $kBqm^{-3}$ from other countries (Giustini et al., 2019; Kikaj et al., 2016; Mitra et al., 2021; Nuhu et al., 2021). In more detail, Table 4.4 summarizes SGRn concentrations which are typically associated with a range of different lithologies. Analysis of SGRn from Castleisland indicates that 36% of the measured samples are greater than 100 $kBqm^{-3}$, compared to ca. 10% of samples from other representative studies (Elío et al., 2019; Haruna et al., 2020; O'Brien et al., 2011). Globally, and in general terms, very low to moderate (<10 to 70 $kBqm^{-3}$) SGRn values are associated with sedimentary lithologies (Fu et al., 2017; Khan et al., 2021; Kumar et al., 2014; Szabó et al., 2014). In comparison, the sedimentary lithologies in Castleisland are associated with extremely high SGRn values (with >46.7% of samples measuring >70 $kBqm^{-3}$). Although radon anomalies are sometimes associated with sedimentary rocks (not including placer deposits), most occurrences of SGRn anomalies (>70 to 4000 $kBqm^{-3}$) are associated with granites, gneiss, or uranium-bearing deposits (Esan et al., 2020; Kemski et al., 2001; Mitra et al., 2021; Pereira et al., 2010), which contrasts with the present study area.

Table 4.4 Summary of SGRn ranges associated with lithologies in selected regions globally.

Region	Main lithologies in region	Range ($kBqm^{-3}$)	Reference
Perak state, Malaysia	Clays, granites	0.11 to 434.5	Nuhu et al. (2021)
Celleno municipality, Italy	Potassic lavas, travertine, clay-sandy clay, tuff-tuffite	6.4 to 253	Giustini et al. (2019)
Osun state, Nigeria	Gneisses and schists	0.04 to 190	Esan et al. (2020)
West Bengal, India	Granites and Gneisses	2.13 to 786	Mitra et al. (2021)
Iberian uranium province, Portugal	Granites, metasedimentary schists and greywackes	5 to 12,850	Pereira et al. (2010)
Northern Taiwan	Sandstones with silt alterations, sandstones with shales alteration	6.6 to 32.2	Fu et al. (2017)
Nova Scotia, Canada	Metasandstone, slate, granite	0.8 to 154.6	O'Brien et al. (2011)
Lesser Himalayas, Pakistan	Slate, quartzite, granite, gneiss, limestone, shale	2.3–20.1	Khan et al. (2021)

Region	Main lithologies in region	Range ($kBqm^{-3}$)	Reference
Cooley Peninsula Ireland	Sandstones, shales, granites, marine shelf facies	3.5 to 112	Elío et al. (2019)
Estonia	Sand, silt, gravel of Baltic sea deposits Glaciolacustrine clay	1 to 184 24 to 1801.6	Petersell et al. (2015)
Dharamshala, India	Sandstones	13 2 to 66.2	Kumar et al. (2014)
Central Hungary	Fluvial sand Loess (silt cemented by carbonate)	1.2 to 24.9 4.9 to 44.1	Szabó et al. (2014)

In relation to the GRP, several studies categorize 41% or less of an area/dataset as being in a high class (Elío et al., 2019; Giustini et al., 2019; Nuhu et al., 2021) which is lower than the 49% area (64% of samples) classified as high in this present study. The GRP in Castleisland reaches a maximum value of 1778, which is considerably higher than the limit of 35 which is conventionally considered to be high (Neznal et al., 2004). For comparison with other countries, "extreme" GRP values of ca. 40–280 have been reported elsewhere (Ciotoli et al., 2017; Pásztor et al., 2016; Szabó et al., 2014).

The original radon map of Ireland (Fig. 4.1) (Fennell et al., 2002) classifies the east, and south-east, of the study region as having high radon priority (with between 10% and 20% of houses above the reference level); this is in agreement with the GRP mapping carried out in this study. The NW and SW of the survey site are deemed as a high radon priority on the EPA map. The GRP (Fig. 4.5b) for the same sites is moderate to high with certain zones having a very high

GRP. Although the EPA radon map of Ireland and the geogenic GRP map presented here are found to be in general agreement, the GRP map has higher spatial resolution and allows for more accurate representation of areas with lower population density where IRC measurements may be lacking.

The new EPA indoor radon (Environmental Protection Agency, 2022), has higher resolution and shows greater spatial variation of radon compared to the original radon map of Ireland (Fig. 4.1). The higher resolution in the new radon map arises from the inclusion of four geogenic parameters (bedrock geology, Quaternary geology, aquifer type and deeper topsoil permeability) (Elío et al., 2017; Environmental Protection Agency, 2022). The new EPA map indicates houses above the Clare Shales north of Castleisland have a low probability of exceeding the 200 Bqm^{-3} IRC reference level in Ireland (https://www.epa.ie/environment-and-you/radon/). In contrast, the SGRn and GRP maps developed in this study (Fig. 4.5), depict the highly anomalous SGRn (greater than 1400 $kBqm^{-3}$) and GRP (up to 1778) occurring above the Clare Shales and in the vicinity of the demolished house which measured an average IRC of 49,000 Bqm^{-3}.

The difference in designation of radon risk between the new EPA radon map and the maps created in this study, likely signifies the anomalous nature of the Clare Shales in Castleisland. Carboniferous shales from other parts of Ireland are not necessarily associated with such elevated SGRn and IRC values. In this respect, our study demonstrates that small-scale studies are useful to examine local exceptions to national-scale models.

ANOVA tests illustrate that bedrock geology explains the highest portion of the SGRn variance (39%), followed by deeper topsoil permeability (21%) and Quaternary geology (13%) (Table 4.2). It is possible to estimate the variance and concentration of SGRn with reference to bedrock geology and deeper topsoil permeability. In particular, the Clare Shales have significantly high

SGRn values compared to other bedrock geology types within the study area. SGRn values from samples collected over the Carboniferous limestones display higher than generally expected from such lithologies (range 9–472 $kBqm^{-3}$, median 57 $kBqm^{-3}$) with the highest values near local faults. More elevated SGRn and deeper topsoil permeability measurements along fault zones are commonly reported elsewhere (Miklyaev et al., 2021; Xuan et al., 2020).

The IRC results (Fig. 4.4a and 4.4b) and SGRn results share a similar trend (Fig. 4.4c and 4.4d). Noticeably, IRC data for the study area are mostly (91%) less than 200 Bqm^{-3}, aside from a few anomalous results, whereas, the SGRn results are typically (90%) between 10,000 and 350,000 Bqm^{-3}. A similar relationship between SGRn and IRC is noted by Yalım et al. (2018).

Additionally, the variogram 'range' for log_{10}soil-gas radon (Fig 4.3d) and log_{10}indoor radon (Fig 4.6d) displays the covariance of SGRn samples and IRC samples decreasing after 800 m, indicating spatial continuity between the IRC and SGRn measurements. As such, future work could incorporate a sample collection method that results in one sample per 800 meters. However, more research studies above different geology types that follows the approach set out in this paper would be needed to clarify if the 800 m variogram range obtained in this study is representative of soil-gas radon and indoor radon variations above different bedrock geology types in different areas. 4.4.1 Geogenic influence on indoor radon

The influence of geogenic factors on IRC concentrations is depicted in the ANOVA table (Table 4.3), which shows that bedrock geology (10%) explains over twice the variance of Quaternary geology (4%), both of which are significant ($p < 0.01$); this could reflect the higher resolution/greater range of bedrock types (6) compared to Quaternary types (3).

SGRn has the most significant influence (16%) on IRC measurements. This result signifies that the greatest contributor to IRC is the radon coming from the soil-gas, which is an established concept within the literature (Åkerblom et al., 1984; Chen and Ford, 2017; World Health

Organization, 2007). Since the SGRn ANOVA results (Table 4.2) show that bedrock geology has the most considerable influence (39%) on the SGRn concentrations, it can be argued that the bedrock geology impacts the IRC measurements indirectly by affecting the SGRn concentrations.

The combined effect of bedrock geology, Quaternary geology, SGRn and deeper topsoil permeability for influencing indoor radon is 34% (Table 4.3) which compares to 30% reported for Cooley Peninsula in NE Ireland (Elío et al., 2019). Variance of indoor radon explained by bedrock geology is 10% which is in line with studies from Northern Ireland (12.1%) and SW England (10%) (Appleton et al., 2015; Ferreira et al., 2018). However, greater variance of up to 20% has been attributed to bedrock geology units in Norway, England and Wales (Appleton and Miles, 2010; Watson et al., 2017).

Considering houses with IRC above the reference level for Ireland, there is a clear difference between those located over different bedrock geology types (table 6 supplementary materials). Assigning each bedrock type an “EPA-type category” results in three units (Dirtoge limestones, Cracoean Reef member, Clare Shales) classified as high radon areas (i.e. greater than 10% of homes surpassing the reference level). The Waulsortian limestones and the Rockfield limestones would be classified as a medium radon area (between 5% and 10%). Lastly, the Cloone Flagstones would be in the lowest radon category (less than 1% of homes exceeding the reference level). Dwellings built above the Dirtoge limestones and the Clare Shales have significantly higher probability of exceeding the IRC reference level compared to other bedrock types. IRC samples which exceeded the reference level from houses built over the Dirtoge limestones were located along a fault and at the Clare Shales boundary, likely explained by their proximity to the Clare Shales and coupled with the fact that the houses are located in an area with higher radon exhalation rates due to their proximity to a fault.

Analysing the variation of IRC with reference to the Quaternary geology indicates that the till derived from Namurian siltstones, sandstones and shales contain a higher percentage of IRC exceeding the reference level (table supplementary materials). Precisely, 16% of houses located above the till derived from Namurian siltstones, sandstones and shales surpassed the reference level, compared to 9% and 3% for till derived from limestones and Alluvium, respectively. This result reinforces that geogenic information influences IRC concentrations. In particular, houses above till derived from Namurian siltstones, sandstones and shales have higher probability of exceeding the reference level.

4.4.2 The use of geogenic data for mapping indoor radon.

Geogenic data (i.e. SGRn, bedrock and deeper topsoil permeability) sufficiently predict the IRC categories (i.e. low, moderate, high). Bedrock geology is the main contributor to SGRn (Table 2), whereas SGRn is most strongly associated with IRC (Table 4.3). As such, investigating geogenic maps of higher resolution (1:100 k) can quickly distinguish potential areas of elevated IRC. Precisely, pinpointing locations with radon source rocks and specific subsurface structures that enhance radon transportation to homes can be accomplished for regions with higher resolution geological maps which are generally publicly available. Utilizing geogenic maps for radon mapping can be extended to other bedrock units and validated by completing SGRn and deeper topsoil permeability (i.e. GRP) surveys for representative geology types.

GRP surveys provide a substantially quicker alternative at approximately six to ten samples per day, compared to IRC surveys which requires a three-month measurement period (Elío et al., 2019; Environmental Protection Agency, 2019). GRP surveys can be especially beneficial in areas rezoned for residential use where no previous IRC measurements exist. Another benefit to using this approach is that it assesses the amount of radon available to a building regardless of the building purpose or design (workplace or home), allowing the method to be applied to mapping both the radon risk of homes as well as workplaces.

Considering that geological information is freely available online for many countries, there are several potential benefits for integrating information from existing geological maps into radon surveys. Whereas SGRn surveys are weather-dependent, there are no such constraints on utilizing existing geological map data. Indoor radon measurements are useful for constructing radon hazard maps, however the measurements themselves are prone to human error (e.g., radon detectors must be installed in specific areas of a house with limited airflow), must take place over several months, are very costly and time-consuming, or simply may not be available. Using IRC data for mapping RPAs is increasingly complex and inefficient due to tighter regulations on General Data Protection Regulations (GDPR). Field surveys which utilize existing geological maps can specifically focus on areas where an elevated radon risk is suspected, based on the geological attributes. IRC measurements could then be collected to confirm the level of IRC in each workplace or home. Furthermore, for areas where there is a lack of IRC data, it is practical to utilize the available geological data and radon-potential surveys for IRC risk mapping.

4.4.3 Limitations:

Geogenic radon potential mapping is weather-dependent. Several days after rainfall should elapse before sampling to ensure that the soil is not water-saturated (Neznal et al., 2004). Due to weather conditions, atmospheric pressure, wind speed and temperature, SGRn varies on a daily basis (Arora et al., 2017; Kulali et al., 2017). Furthermore, SGRn varies on a seasonal basis; due to the overall mean differences in temperature and rainfall (Szabó et al., 2013). Considering these factors, it is important to ensure that soil gas samples are taken from a sufficient depth in the soil profile (usually 80–100 cm (Neznal et al., 2004)). Due to the high degree of spatial variation in SGRn concentrations, it is also important to collect several samples to obtain representative values for a given geology type, or region. Given that the original methodology of Neznal et al. (2004) has been adapted and used slightly differently in several studies, it is important to ensure different methodologies are taken into account when comparing GRP or RP from different study areas.

4.5 Conclusion

An approach to mapping radon-prone areas was investigated by collecting 135 soil-gas radon (SGRn) and deeper topsoil permeability measurements across approximately 50 locations in a 6 km^2 region around Castleisland in Co. Kerry, SW Ireland. The area was chosen due to the extremely high indoor radon concentrations (average reading of 49,000 Bqm^{-3} from several measurements) previously reported from the region (Organo et al., 2004), and due to the fact that there was not a clear understanding of the source of such high values. The indoor radon concentration (IRC) variance explained by geogenic factors (bedrock geology, Quaternary geology, deeper topsoil permeability, and SGRn) is 34%; with SGRn as the main contributor (16%). ANOVA tests illustrate that bedrock geology has the most substantial influence on SGRn concentrations (39%), although deeper topsoil permeability (21%) and Quaternary geology (13%) also have significant effects. Results demonstrate that spatially restricted black shales, locally known as the Clare Shales, are spatially associated with both SGRn and IRC anomalies, and likely act as a radon source which may also be transported via enhanced permeability in non-mineralised fault zones and extensive subterranean karst systems which are prevalent in the region.

Geological factors (especially SGRn, bedrock geology, and deeper topsoil permeability) sufficiently predict the IRC categories (i.e. low, moderate, high). Therefore, investigating the spatial variation and distribution of geological units in a given region can help to identify radon priority areas, particularly if reliable high-resolution maps are available, relevant radon-related data (e.g. soil properties) exist and lithologies are assigned with accuracy regarding their potential for being a point source of radon. Such an approach could pinpoint high radon areas in a very cost-efficient and time-efficient manner. The radon priority area category assigned using geological attributes can be confirmed by carrying out a geogenic radon potential survey for smaller representative areas, such as that presented in this study. Geogenic radon potential mapping can verify if an area is susceptible to high IRC. Such an approach is especially useful for areas where population density is low, and where few IRC measurements already exist. The methodology presented in this study highlights the use of combined experimental and theoretical approaches in the study of radon as a natural hazard. The approach used in this study integrates both relevant field data and geostatistical modelling, and is demonstrated to be beneficial in efforts to predict radon anomalies. Such an approach ultimately leads to a better understanding of radon in both the natural and built environments. Radon potential or hazard maps constructed using this methodology add considerable value to existing legacy geological datasets. This research also highlights the importance of reliable digital geoscience data applied to environmental exposure, and when utilized to protect the general public from the harmful effects of ionizing radiation.

4.6 Role of the funding source

The partial funding source (SUSI) for Méabh Banríon's Ph.D. had no involvement or role in the study design, the collection, analysis and interpretation of data; in writing of the report; and in the decision to submit the article for publication.

4.7 Declaration of competing interest

The authors declare that they have no known competing financial interests or personal relationships that could have appeared to influence the work reported in this paper.

4.8 Acknowledgements

We would like to thank the EPA for providing the InRn dataset, Ryan O'Toole, Patricia McGuire, and Winifred Duncan for part-taking in the soil-gas radon and soil permeability measurement surveys. Méabh H. Banríon would like to thank Student Universal Support Ireland (SUSI) for helping to fund their Ph.D.

4.9 References

Abdalla, A.M., Ismail, A.M., Al Madiy, A.A., 2021. Soil radon detection using active scintillation cell. J. Radiat. Res. Appl. Sci. 14, 16–22. https://doi.org/10.1080/16878507.2020.1783631

Åkerblom, G., Andersson, P., Clevensjö, B., 1984. Soil Gas Radon - A Source for Indoor Radon Daughters. Radiation Protection Dosimetry 7, 49–54. https://doi.org/10.1093/oxfordjournals.rpd.a082961

Alonso, H., Rubiano, J.G., Guerra, J.G., Arnedo, M.A., Tejera, A., Martel, P., 2019. Assessment of radon risk areas in the Eastern Canary Islands using soil radon gas concentration and gas permeability of soils. Science of The Total Environment 664, 449–460. https://doi.org/10.1016/j.scitotenv.2019.01.411

Anderson, R.T., Vrionis, H.A., Ortiz-Bernad, I., Resch, C.T., Long, P.E., Dayvault, R., Karp, K., Marutzky, S., Metzler, D.R., Peacock, A., White, D.C., Lowe, M., Lovley, D.R., 2003. Stimulating the In Situ Activity of Geobacter Species To Remove Uranium from the Groundwater of a Uranium-Contaminated Aquifer. Applied and Environmental Microbiology 69, 5884–5891. https://doi.org/10.1128/AEM.69.10.5884-5891.2003

Appleton, J.D., Daraktchieva, Z., Young, M.E., 2015. Geological controls on radon potential in Northern Ireland. Proceedings of the Geologists' Association 126, 328–345. https://doi.org/10.1016/j.pgeola.2014.07.001

Appleton, J.D., Miles, J.C.H., 2010. A statistical evaluation of the geogenic controls on indoor radon concentrations and radon risk. Journal of Environmental Radioactivity 101, 799–803. https://doi.org/10.1016/j.jenvrad.2009.06.002

Arceo, C., 2019. Indoor Radon Exposure and Thyroid Cancer Incidence: An Evaluation of the Existing Data for Guam, Mariana Islands. https://doi.org/10.13140/RG.2.2.23643.72487

Arora, B.R., Kumar, A., Walia, V., Yang, T.F., Fu, C.-C., Liu, T.-K., Wen, K.-L., Chen, C.-H., 2017. Assesment of the response of the meteorological/hydrological parameters on the soil gas radon emission at Hsinchu, northern Taiwan: A prerequisite to identify earthquake precursors. Journal of Asian Earth Sciences 149, 49–63. https://doi.org/10.1016/j.jseaes.2017.06.033

Ashok, G., Nagaiah, N., Prasad, N.S., Ambika, M., 2011. Study of radon exhalation rate from soil, Bangalore, South India. Radiation Protection and Environment 34, 235.

Barros, N., Field, D.W., Steck, D.J., Field, R.W., 2015. Comparative survey of outdoor, residential and workplace radon concentrations. Radiation Protection Dosimetry 163, 325–332. https://doi.org/10.1093/rpd/ncu185

Bossew, P., 2018. Radon Priority Areas - Definition, estimation and uncertainty. Nuclear Technology and Radiation Protection 33, 11–11. https://doi.org/10.2298/NTRP180515011B

Bossew, P., Cinelli, G., Ciotoli, G., Crowley, Q., Cort, M., Elío, J., Gruber, V., Petermann, E., Tollefsen, T., 2020. Development of a Geogenic Radon Hazard Index—Concept, History, Experiences. International Journal of Environmental Research and Public Health 17, 4134. https://doi.org/10.3390/ijerph17114134

Chen, J., Ford, K.L., 2017. A study on the correlation between soil radon potential and average indoor radon potential in Canadian cities. Journal of Environmental Radioactivity 166, 152–156. https://doi.org/10.1016/j.jenvrad.2016.01.018

Ciotoli, G., Voltaggio, M., Tuccimei, P., Soligo, M., Pasculli, A., Beaubien, S.E., Bigi, S., 2017. Geographically weighted regression and geostatistical techniques to construct the geogenic radon potential map of the Lazio region: A methodological proposal for the European Atlas of Natural Radiation. Journal of Environmental Radioactivity 166, 355–375. https://doi.org/10.1016/j.jenvrad.2016.05.010

Cucoş Dinu, A., Călugăr, M.I., Burghele, B.D., Dumitru, O.A., Cosma, C., Onac, B.P., 2017. Radon levels in Romanian caves: an occupational exposure survey. Environmental Geochemistry and Health 39, 1085–1099. https://doi.org/10.1007/s10653-016-9878-1

Dardac, M., 2022. Determining the geogenic influence for high indoor radon areas in Ireland. Submitted

Domingos, F., Cinelli, G., Neves, L., Pereira, A., Braga, R., Bossew, P., Tollefsen, T., 2020. Validation of a database of mean uranium, thorium and potassium concentrations in rock samples of Portuguese geological units, generated of literature data. Journal of Environmental Radioactivity 222, 106338. https://doi.org/10.1016/j.jenvrad.2020.106338

Drolet, J.-P., Martel, R., Poulin, P., Dessau, J.-C., 2014. Methodology developed to make the Quebec indoor radon potential map. Science of The Total Environment 473–474, 372–380. https://doi.org/10.1016/j.scitotenv.2013.12.039

Duffy, J.T., Madden, J.S., Mackin, G.M., McGarry, A.T., Colgan, P.A., 1996. A reconnaissance survey of radon in show caves in Ireland.Environment International 22, 415–423. https://doi.org/10.1016/S0160-4120(96)00140-7

Duggal, V., Rani, A., Mehra, R., 2014. Measurement of soil-gas radon in some areas of northern Rajasthan, India. Journal of Earth System Science 123, 1241–1247.

Elío, J., Crowley, Q., Scanlon, R., Hodgson, J., Long, S., 2019. Rapid radon potential classification using SGRn measurements in the Cooley Peninsula, County Louth, Ireland. Environmental Earth Sciences 78, 359. https://doi.org/10.1007/s12665-019-8339-4

Elío, J., Crowley, Q., Scanlon, R., Hodgson, J., Zgaga, L., 2018. Estimation of residential radon exposure and definition of Radon Priority Areas based on expected lung cancer incidence. Environment International 114, 69–76. https://doi.org/10.1016/j.envint.2018.02.025

Elío, Javier, Crowley, Q., Scanlon, R., Hodgson, J., Long, S., 2017. Logistic regression model for detecting radon prone areas in Ireland. Science of The Total Environment 599–600. https://doi.org/10.1016/j.scitotenv.2017.05.071

Environmental Protection Agency, 2019. EPA protocol for the measurement of radon in homes and workplaces.

Esan, D.T., Sridhar, M.K.C., Obed, R., Ajiboye, Y., Afolabi, O., Olubodun, B., Oni, O.M., 2020. Determination of Residential Soil Gas Radon Risk Indices Over the Lithological Units of a Southwestern Nigeria University. Scientific reports 10, 1–10.

European Commission, 2013. Council directive 2013/59/Euratom. Official Journal of the European Union 2013/59/EURATOM.

Fennell, S.G., Mackin, G.M., McGarry, A.T. and Pollard, D., 2002, February. Radon exposure in Ireland. In International Congress Series (Vol. 1225, pp. 71-77).

Ferreira, A., Daraktchieva, Z., Beamish, D., Kirkwood, C., Lister, T.R., Cave, M., Wragg, J., Lee, K., 2018. Indoor radon measurements in south west England explained by topsoil and stream sediment geochemistry, airborne gamma-ray spectroscopy and geology. Journal

of Environmental Radioactivity 181, 152–171. https://doi.org/10.1016/j.jenvrad.2016.05.007

Fu, C.-C., Yang, T.F., Chen, C.-H., Lee, L.-C., Wu, Y.-M., Liu, T.-K., Walia, V., Kumar, A., Lai, T.-H., 2017. Spatial and temporal anomalies of soil gas in northern Taiwan and its tectonic and seismic implications. Journal of Asian Earth Sciences 149, 64–77. https://doi.org/10.1016/j.jseaes.2017.02.032

Fuente, M., Long, S., Fenton, D., Hung, L.C., Goggins, J., Foley, M., 2020. Review of recent radon research in Ireland, OPTI-SDS project and its impact on the National Radon Control

Strategy. Applied Radiation and Isotopes 163, 109210. https://doi.org/10.1016/j.apradiso.2020.109210

Gadd, G.M., 2010. Metals, minerals and microbes: geomicrobiology and bioremediation. Microbiology 156, 609–643.

Gaskin, J., Coyle, D., Whyte, J., Krewksi, D., 2018. Global Estimate of Lung Cancer Mortality Attributable to Residential Radon. Environmental Health Perspectives 126, 057009. https://doi.org/10.1289/EHP2503

Giustini, F., Ciotoli, G., Rinaldini, A., Ruggiero, L., Voltaggio, M., 2019. Mapping the geogenic radon potential and radon risk by using Empirical Bayesian Kriging regression: A case study from a volcanic area of central Italy. Science of the Total Environment 661, 449–464.

Günay, O., Saç, M.M., İçhedef, M., Taşköprü, C., 2018. Soil gas radon concentrations along the Ganos Fault (GF). Arabian Journal of Geosciences 11, 213. https://doi.org/10.1007/s12517-018-3542-2

Gunn, J., 1982. Crag Cave, County Kerry. Irish Naturalists Journal Ltd. 20, 445–449.

Gunning, G.A., 2016. Studies of radon in Ireland: Outdoor levels, detector intercomparison and school remediation methods. Trinity College (Dublin, Ireland). School of Physics.

Guo, Q., Cheng, J.G., 2012. The Effect of Some Soil Characteristics on Soil Radon Concentration and Radon Exhalation from Soil Surface. Journal of Nuclear Science and Technology. https://doi.org/10.1080/18811248.2004.9726337

Habib, R.R., Nuwayhid, R.Y., Hamdan, Z., Alameddine, I., Katul, G., 2018. Indoor and Outdoor Radon Concentration Levels in Lebanon. Health Physics 115.

Haruna, R., Saleh, M.A., Hashim, S., Hamzah, K., Zainal, J., Sanusi, M.S.M., 2020. Assessment of geogenic radon potential in Johor Malaysia. Journal of Radioanalytical and Nuclear Chemistry 326, 1065–1074. https://doi.org/10.1007/s10967-020-07396-y

Hodson, F., 1954. The Carboniferous rocks of Foynes island, county Limerick. Geological Magazine 91, 153–160.

Idriss, H., Salih, I., Alaamer, A.S., Abdelgalil, M., Salih, S.A., Hasan, A.M., ELtahir, M.A., Ahamed, M.M., 2014. Study of radon in soil gas, trace elements and climatic parameters around South Kordofan state, Sudan. Environmental earth sciences 72, 335–339.

Jelle, B.P., 2012. Development of a model for radon concentration in indoor air. Science of The Total Environment 416, 343–350. https://doi.org/10.1016/j.scitotenv.2011.11.052

Kemski, J., Siehl, A., Stegemann, R., Valdivia-Manchego, M., 2001. Mapping the geogenic radon potential in Germany. Science of The Total Environment 272, 217–230. https://doi.org/10.1016/S0048-9697(01)00696-9

Kemski, J., Klingel, R., Siehl, A., 1996. Classification and mapping of radon-affected areas in Germany. Environment International 22, 789–798.

Khan, S.M., Gomes, J., Krewski, D.R., 2019. Radon interventions around the globe: A systematic review. Heliyon 5, e01737. https://doi.org/10.1016/j.heliyon.2019.e0173

Khan, F., Khattak, S.A., Wazir, Z., Waqas, M., 2021. Spatial distribution of radon concentrations in Balakot-Bagh (B–B) Fault Line and adjoining areas, Lesser Himalayas, North Pakistan. Environmental Earth Sciences 80, 291. https://doi.org/10.1007/s12665-021-09569-8

Kikaj, D., Jeran, Z., Bahtijari, M., Stegnar, P., 2016. Radon in soil gas in Kosovo. Journal of Environmental Radioactivity 164, 245–252. https://doi.org/10.1016/j.jenvrad.2016.07.037

Koribanics, N.M., Tuorto, S.J., Lopez-Chiaffarelli, N., McGuinness, L.R., Häggblom, M.M., Williams, K.H., Long, P.E., Kerkhof, L.J., 2015. Spatial Distribution of an Uranium-Respiring Betaproteobacterium at the Rifle, CO Field Research Site. PLOS ONE 10, e0123378. https://doi.org/10.1371/journal.pone.0123378

Kulali, F., Akkurt, I., Özgür, N., 2017. The effect of meteorological parameters on radon concentration in soil gas. Acta Physica Polonica A 132, 999–1001.

Kumar, A., Arora, V., Walia, V., Bajwa, B.S., Singh, S., Yang, T.F., 2014. Study of soil gas radon variations in the tectonically active Dharamshala and Chamba regions, Himachal Pradesh, India. Environmental Earth Sciences 72, 2837–2847.

Laiolo, M., Ranaldi, M., Tarchini, L., Carapezza, M.L., Coppola, D., Ricci, T., Cigolini, C., 2016. The effects of environmental parameters on diffuse degassing at Stromboli volcano: Insights from joint monitoring of soil CO2 flux and radon activity. Journal of Volcanology and Geothermal Research. http://dx.doi.org/10.1016/j.jvolgeores.2016.02.004 0377-0273

Larson, M.G., 2008. Analysis of variance. Circulation 117, 115–121. https://doi.org/10.1161/CIRCULATIONAHA.107.654335

Laurier, D., Valenty, M., Tirmarche, M., 2001. Radon exposure and the risk of leukemia: a review of epidemiological studies. Health Physics. https://doi.org/10.1097/00004032-200109000-00009

Lecomte, A., Cathelineau, M., Michels, R., Peiffert, C., Brouand, M., 2017. Uranium mineralization in the Alum Shale Formation (Sweden): Evolution of a U-rich marine black shale from sedimentation to metamorphism. Ore Geology Reviews 88, 71–98. https://doi.org/10.1016/j.oregeorev.2017.04.021

Liping, H.E., Chen, B., Zhao, C., Zhuo, W., 2016. The study on effects of indoor air filtration on radon exposure to residents. Chinese Journal of Radiological Medicine and Protection 36, 688–693.

Margineanu, R.M., 2019. Radon measurements in underground mines and caves from several European countries, in: AIP Conference Proceedings. AIP Publishing LLC, p. 050004.

Marsh, J.W., Tomášek, L., Laurier, D., Harrison, J.D., 2021. Effective dose coefficients for radon and progeny: A review of ICRP and UNSCEAR values. Radiation Protection Dosimetry 195, 1–20. https://doi.org/10.1093/rpd/ncab106

Miklyaev, P.S., Petrova, T.B., Shchitov, D.V., Sidyakin, P.A., Murzabekov, M.A., Marennyy, A.M., Nefedov, N.A., Sapozhnikov, Y.A., 2021. The results of long-term simultaneous measurements of radon exhalation rate, radon concentrations in soil gas and groundwater in the fault zone. Applied Radiation and Isotopes 167, 109460. https://doi.org/10.1016/j.apradiso.2020.109460

Min, M., Xu, H., Mostafa Fayek, Chen, J., 2005. Evidence of uranium biomineralization in sandstone-hosted roll-front uranium deposits, northwestern China. Ore Geology Reviews 26. https://doi.org/10.1016/j.oregeorev.2004.10.003

Mitra, S., Chowdhury, S., Mukherjee, J., Sutradhar, S., Mondal, S., Barman, C., Deb, A., 2021. Assessment of radon (222Rn) activity in groundwater and soil-gas in Purulia district, West Bengal, India. Journal of Radioanalytical and Nuclear Chemistry 330, 1331–1338.

Monty, C., 2000. UNSCEAR Report 2000: Sources and Effects of Ionizing Radiation. Journal of Radiological Protection 21. https://doi.org/10.1088/0952-4746/21/1/609

Mudelsee, M., Albert, J., Sirocko, F., 2020. Weather control in radon flux time series from Schleswig-Holstein, Germany. GEM International Journal on Geomathematics 11, 23. https://doi.org/10.1007/s13137-020-00156-w

Muntean, L.E., Cosma, C., Cucos, A., Dicu, T., Moldovan, D.V., 2014. Assessment of annual and seasonal variation of indoor radon levels in dwelling houses from Alba County, Romania. Rom Journ Phys 59, 163–71.

National Cancer Registry Ireland, 2020. Cancer in Ireland 1994-2018 with estimates for 2018-2020: Annual report of the National Cancer Registry.

National Radon Control Strategy, 2019. NRCS Knowledge Gaps Phase 2.

Neznal, Matěj, Neznal, Martin, Matolin, M., Barnet, I., Miksova, J., 2004. The new method for assessing the radon risk of building sites. Czech Geological Survey Prague.

Nuhu, H., Hashim, S., Aziz Saleh, M., Syazwan Mohd Sanusi, M., Hussein Alomari, A., Jamal, M.H., Abdullah, R.A., Hassan, S.A., 2021. Soil gas radon and soil permeability assessment: Mapping radon risk areas in Perak State, Malaysia. PloS one 16, e0254099.

O'Brien, K., Goodwin, T., Risk, D., 2011. Radon soil gas in the Halifax Regional Municipality, Nova Scotia, Canada. atlantic GeoloGy 47, 112–124.

Organo, C., Ellard, A., Fenton, D., Synnott, H., O'Colmáin, M., Prenter, S., O'Reilly, S., Colgan, P., 2004. High radon concentrations in a house near Castleisland, County Kerry (Ireland)—identification, remediation and post-remediation. Journal of Radiological Protection 24, 107. https://doi.org/10.1088/0952-4746/24/2/001

Organo, C., Murphy, P., 2007. The Castleisland Radon Survey—follow-up to the discovery of a house with extremely high radon concentrations in County Kerry (SW Ireland). Journal of Radiological Protection 27. https://doi.org/10.1088/0952-4746/27/3/002

Pásztor, L., Szabó, K.Z., Szatmári, G., Laborczi, A., Horváth, Á., 2016. Mapping geogenic radon potential by regression kriging. Science of The Total Environment 544, 883–891. https://doi.org/10.1016/j.scitotenv.2015.11.175

Petermann, E., Bossew, P., Hoffmann, B., 2022. Radon hazard vs. radon risk - On the effectiveness of radon priority areas. Journal of Environmental Radioactivity 244–245, 106833. https://doi.org/10.1016/j.jenvrad.2022.106833

Petersell, V., Jüriado, K., Raukas, A., Shtokalenko, M., Täht-Kok, K., 2015. Quaternary deposits and weathered bedrock material as a source of dangerous radon emissions in Estonia. Geologos 21.

Pereira, A., Godinho, M., Neves, L., 2010. On the influence of faulting on small-scale soil-gas radon variability: a case study in the Iberian Uranium Province. Journal of environmental radioactivity 101, 875–882.

Pracht, M., 1997. Geology of Kerry - Cork: A geological description to accompany the bedrock geology 1:100,000 scale map series, sheet 21, Kerry-Cork.

Radiological Protection Act 1991 (Ionising Radiation) Regulations, 2019. Statutory Instruments Ireland, S.I. No. 30 of 2019.

Rafique, M., Abbasi, S., Shahzadi, C., Basharat, M., Jabbar, A., Ur Rahman, S., 2021. Excessive Lifetime Cancer Risk Assessment due to Short-Term Indoor/Outdoor Ambient Radon and Gamma Dose Rate Exposures. Iranian Journal of Science and Technology, Transactions A: Science 45, 2181–2190. https://doi.org/10.1007/s40995-021-01192-3

Ravikumar, P., Davis, D., Somashekar, R., Prakash, K., 2015. Measurement of radon activity in soil gas using RAD7 in the Environs of Chitradurga District, Karnataka, India. Elixir Earth Sci 80, 31078–31082.

Rider, M., 1974. The Namurian of West County Clare. Presented at the Proceedings of the Royal Irish Academy. Section B: Biological, Geological, and Chemical Science, JSTOR, pp. 125–142.

Schubert, M., Musolff, A., Weiss, H., 2018. Influences of meteorological parameters on indoor radon concentrations (222Rn) excluding the effects of forced ventilation and radon exhalation from soil and building materials. Journal of environmental radioactivity 192, 81–85. https://doi.org/10.1016/j.jenvrad.2018.06.011

Singh, J., Singh, H., Singh, S., Bajwa, B., 2010. Measurement of soil gas radon and its correlation with indoor radon around some areas of Upper Siwaliks, India. Journal of Radiological Protection 30, 63.

Sleeman, A., MacConnell, B., Gatley, S., 2004. Understanding Earth Processes, Rocks and the Geological History of Ireland: A Companion to the 1: 1.000. 000 Scale Bedrock Geological Map of Ireland. Geological Survey of Ireland.

Smith, M.E., Dumitru, O.A., Burghele, B.D., Cucoș, A., Onac, B.P., 2019. Radon concentration in three Florida caves: Florida, Jennings, and Ocala. Carbonates and Evaporites 34, 433–439. https://doi.org/10.1007/s13146-018-0473-7

Soesoo, A., Vind, J., Hade, S., 2020. Uranium and Thorium Resources of Estonia. Minerals 10. https://doi.org/10.3390/min10090798

Sundal, A.V., Valen, V., Soldal, O., Strand, T., 2008. The influence of meteorological parameters on soil radon levels in permeable glacial sediments. Science of The Total Environment 389, 418–428. https://doi.org/10.1016/j.scitotenv.2007.09.001

Szabó, K.Z., Jordan, G., Horváth, Á., Szabó, C., 2014. Mapping the geogenic radon potential: methodology and spatial analysis for central Hungary. Journal of environmental radioactivity 129, 107–120.

Szabó, K.Z., Jordan, G., Horváth, Á., Szabó, C., 2013. Dynamics of soil gas radon concentration in a highly permeable soil based on a long-term high temporal resolution observation series. Journal of environmental radioactivity 124, 74–83. https://doi.org/10.1016/j.jenvrad.2013.04.004

Thornton, M.S., 1966. The Lower Carboniferous limestones of the Tralee Bay area, Co. Kerry, Ireland. Unpublished PhD thesis, University of Cambridge.

Tooth, A., Fairchild, I., 2003. Soil and karst aquifer hydrological controls on the geochemical evolution of speleothem-forming drip waters, Crag Cave, Southwest Ireland. Journal of Hydrology 273, 51–68. https://doi.org/10.1016/S0022-1694(02)00349-9

Tositti, L., Cinelli, G., Brattich, E., Galgaro, A., Mostacci, D., Mazzoli, C., Massironi, M., Sassi, R., 2017. Assessment of lithogenic radioactivity in the Euganean Hills magmatic district (NE Italy). Journal of Environmental Radioactivity 166, 259–269. https://doi.org/10.1016/j.jenvrad.2016.07.011

United Nations Scientific Committee on the Effects of Atomic Radiation, 2015. Report of the United Nations Scientific Committee on the effects of atomic radiation to the general assembly.

Victor, N.J., Siingh, D., Singh, RP, Singh, Rejesh, Kamra, A., 2019. Diurnal and seasonal variations of radon (222Rn) and their dependence on soil moisture and vertical stability of the lower atmosphere at Pune, India. Journal of Atmospheric and Solar-Terrestrial Physics 195, 105118.

Watson, R.J., Smethurst, M.A., Ganerød, G.V., Finne, I., Rudjord, A.L., 2017. The use of mapped geology as a predictor of radon potential in Norway. Journal of Environmental Radioactivity 166, 341–354. https://doi.org/10.1016/j.jenvrad.2016.05.031

Wignall, P., Best, J., 2000. The western Irish Namurian basin reassessed. Basin Research 12, 59–78. https://doi.org/10.1046/j.1365-2117.2000.00113.x

World Health Organization (Ed.), 2009. WHO handbook on indoor radon: a public health perspective. World Health Organization.

World Health Organization, 2007. International radon project: survey on radon guidelines, programmes and activities (No. WHO/HSE/RAD/07.01). World Health Organization.

Xuan, P., Duong, N., Chinh, V., Dang, P., Qua, N., Pho, N., 2020. Soil Gas Radon Measurement for Identifying Active Faults in Thua Thien Hue (Vietnam). Journal of Geoscience and Environment Protection 8. https://doi.org/10.4236/gep.2020.87003

Xie, D., Liao, M., Kearfott, K.J., 2015. Influence of environmental factors on indoor radon concentration levels in the basement and ground floor of a building–A case study. Radiation Measurements 82, 52–58.

Yalım, H.A., Gümüş, A., Başaran, C., Bağcı, M., Yıldız, A., Açil, D., Özçelik, M., İlhan, M.Z., Ünal, R., 2018. Comparison of radon concentrations in soil gas and indoor environment of Afyonkarahisar Province. Arabian Journal of Geosciences 11, 246. https://doi.org/10.1007/s12517-018-3546-y

Investigating topsoil geochemistry in relation to geogenic radon using multivariate geo-statistics, examples from local and regional scale data in Ireland.

Submitted to the Journal of Applied Geochemistry

Banríon M.H. (1)*, Elío J. (2), Crowley Q.G. (1)

Abstract

Radon is classified as a Class 1 carcinogen, being the leading cause of lung cancer in non-smokers. Understanding the prominent sources of radon helps to mitigate against the adverse effects of radon exposure, and contributes to sustainable development goal three - good health and well-being. Considering soil-gas radon is the main contributor to indoor radon, it is possible that soil geochemistry can be used as a proxy for the soil radon emanation potential or geogenic radon classes for a particular location. This paper investigates the relationship between soil geochemistry and geogenic radon at a range of spatial scales. A rigorous assessment is presented to investigate the relationship of geogenic radon and topsoil geochemistry; using univariate processes (i.e. r^2, ANOVA, Pearson r) and multivariate techniques (i.e. PCA, cluster analysis and machine learning algorithms including Gaussian process regression, logistic regression and random forest). A small area of 6 km^2 in SW Ireland was selected due to the presence of anomalously high indoor radon. A larger area of 17,983 km^2 from the Midlands of Ireland was selected to represent a range of geology and radon categories. Here, PCA, cluster analysis, and machine learning techniques were used to test the ability of soil geochemistry to predict geogenic radon classes. Data analysis reveals that certain elements correlating with geogenic radon also covary together within soil, here these are termed "radon-prone elements".

From the local scale data, La, V, Ba, Sr, U and Cr correlate with soil-gas radon and exhibit covariance. Analysis of regional data shows Y, Tl, Be, La, V and Cr associated with geogenic radon and share strong covariance from the PCA and cluster results. Gaussian process regression classifies samples with the highest precision of 73.9%. The feature importance (i.e. highest ranking elements for predicting geogenic radon class) from the models emphasises the association of certain elements with geogenic radon, such as Y, Tl, Be, Ba, La, V and U. Spatial covariance of radon-prone elements permits soil geochemistry to be used as a tool for understanding the distribution of geogenic radon. The methodology presented in this paper provides a comprehensive geo-statistical approach to investigate the relation between topsoil geochemistry and geogenic radon. This approach could be applied as a diagnostic tool to assist radon mitigation measures, hence adding value to legacy soil geochemistry datasets.

Keywords:

Geogenic Radon Potential, Radon, Topsoil Geochemistry, Machine learning algorithms, Principal Component Analysis.

Abbreviations:

IRC: Indoor radon concentration; PCA: Principal component analysis; ML: Machine learning; SGRn: Soil-gas radon; GPR: Gaussian process regression; RF: Random forest; LR: Logistic regression; GRP: Geogenic radon potential.

5.1 Introduction

The majority (80%) of radiation exposure received by the general public is from natural sources (United Nations Scientific Committee on the Effects of Atomic Radiation, 2011). Approximately 53% of natural radiation is caused by the inhalation of decay products from the uranium and thorium series, of which the isotope ^{222}Rn accounts for over 90% of these decay products (United Nations Scientific Committee on the Effects of Atomic Radiation, 2011; Zohuri, 2020). Radon (Rn) exposure is the leading cause of lung-cancer cases in non-smokers, with 3-15% of global lung-cancer cases attributed to radon (World Health Organization, 2009). It is estimated that up to 350 people are affected by Rn induced lung-cancer in Ireland (Elío et al., 2018; Environmental Protection Agency, 2022). The survival rate after 5 years since lung cancer diagnosis is between 12% and 25% (Lin et al., 2019; Schabath and Cote, 2019).

Prevention of radon exposure is paramount to reducing radon related lung-cancer cases. Internationally, several countries have implemented initiatives to reduce the harmful effects of radon exposure. Some initiatives include setting reference limits for acceptable levels of indoor radon concentration (IRC), and having prevention measures (i.e. radon barrier, sump, ventilation) in place for new buildings (Radiological Protection Act 1991 (Ionising Radiation) Regulations, 2019). It is important to note that there is no safe limit of radon exposure (World Health Organization, 2009). However, countries often decide the 'safe' IRC level based on average background levels and the realistic ability to lower IRCs to a 'safe' level (Degu Belete and Alemu Anteneh, 2021). In Ireland, 200 Becquerels per meter cubed (Bq m^{-3}) is the reference level for IRC in houses (Environmental Protection Agency, 2019; Fennell et al., 2002).

Radon is a radioactive noble gas that occurs naturally and is released from soil, water and rocks. There are three main radon isotopes, ^{222}Rn (radon), ^{220}Rn (thoron) and ^{219}Rn (actinon) which have half-lives of 3.8 days, 55.6 seconds and 3.96 seconds, respectively. Uranium (^{238}U) decays to radon (^{222}Rn) as an intermediate daughter product before completely decaying to the stable lead isotope (^{206}Pb). ^{220}Rn and ^{219}Rn are products of the ^{232}Th and ^{235}U decay chains, respectively. Importantly, if radon gas is inhaled while it changes into its daughter radioisotopes polonium (^{214}Po and ^{218}Po), the charged metal polonium ions can cause significant damage by emitting alpha radiation directly into lung cells; linking radon exposure to lung-cancer (Rodríguez-Martínez et al., 2021; Zagà et al., 2021)

Considering soil-gas radon (SGRn) is the prime contributor to IRC (World Health Organization, 2007), understanding the association of soil geochemistry with the natural distribution of Rn precursor elements (^{226}Ra, ^{238}U, ^{232}Th) could contribute to determining a soils potential for being a source of radon. By knowing the spatial variation of Rn precursor elements, one could gain insights to the geogenic radon available at a given area. Furthermore, it may be possible to indicate the presence of Rn precursor elements by distinguishing radon-prone elements (i.e. elements significantly correlated with ^{226}Ra, ^{238}U, ^{232}Th); allowing radon-prone elements to aid in determining radon-prone areas. As such, it may be possible to determine the radon risk of a region using reliable soil geochemical data.

In this study, topsoil geochemistry is used to understand the link between soil geochemical data and radon. The variation of natural terrestrial radiation is largely dependent on geology (Hamideen et al., 2020; Tzortzis et al., 2003). For example, granite and black shales contain radon precursor elements (Pereira et al., 2010; Petersell et al., 2015), whereas lithologies such as limestone generally lack radon predecessor elements being incorporated into the bedrock (Fu et al., 2017; Khan et al., 2021). As such, the spatial variation of radon coincides with lateral differences in bedrock geology (Giustini et al., 2019; Petersell et al., 2015). The spatial correlation of bedrock geology and radionuclides (i.e. ^{226}Ra, ^{232}Th, ^{40}K) in topsoils is reported in the literature (Faanu et al., 2011; Ribeiro et al., 2018). However, few studies investigate the association of a wider range of topsoil elements with geogenic radon.

Mapping geogenic radon variation using soil geochemistry is a viable application of soil geochemical data; since the geochemical composition of soils should range in concentration of radon-prone elements. It is possible radon-prone elements covary spatially for several reasons including association with different lithologies, weathering and mobility of elements.

The main purpose of this study is to test multivariate statistical methods (including PCA, cluster analysis, and Gaussian process classification) for analysing the relation between topsoil geochemistry and geogenic radon. The method is tested using high-resolution (1 sample per approximately 250 meters) in a 6 km^2 study area surrounding Castleisland, Co. Kerry, SW Ireland. The method is repeated using a larger topsoil dataset obtained from TELLUS Geological Survey Ireland (GSI) and compared with corresponding radon categories derived from Elío et al., (2020). The results demonstrate a correlation between topsoil elements and geogenic radon. Essentially confirming that topsoil geochemistry provides insight to geogenic radon risk. The geostatistical approach used in this research confirms the feasibility of using topsoil geochemistry for assessing geogenic radon risk at a local scale (< 10 km^2) and validated at larger scales (>10 km^2).

5.2 Methodology

5.2.1 Collection locations

A 6 km^2 area around Castleisland, Co. Kerry is utilized as case study for comparing to GSI TELLUS results for the Irish midlands (including data from counties Galway, Mayo, Offaly, Roscommon, Longford, Westmeath, Wicklow, Meath, Kildare and Dublin). The Castleisland area is located above of two main Quaternary geology types; glacial till derived from Limestones and glacial till derived from Namurian sandstones, siltstones and shales. The bedrock geology features a range of Dinantian (359 Ma – 326 Ma) limestones, Namurian (326Ma – 313Ma) shales and Carboniferous (359 Ma – 299 Ma) siltstones.

The TELLUS data used covers a wider range of Quaternary sediments including till derived from limestones, cherts, alluvium, Namurian sandstones and shales, blanket peat, Lower Palaeozoic and Devonian sandstones, Devonian and Carboniferous sandstones, gravels derived from limestones. The bedrock geology contains various types of limestones, shales, sandstones, metamorphic and some igneous rocks (detailed description of these geologies can be viewed on the Geological Survey of Ireland (GSI) online map viewer www.gsi.ie).

5.2.2 Collection method

The soil samples from the Castleisland area were collected based on the TELLUS soil-sampling method. Each sample is composed of five sub-samples from a 20 m^2 area; with one sample taken from each corner and the fifth sample taken from the centre of the 20 m^2 area. The soil was taken from the topsoil (0 – 20cm) and placed into a geochemical breathable bag labelled with the location and the symbol ‘A’ to indicate that the shallow topsoil was sampled. The same process is repeated except the soil is taken from the deeper topsoil at 35cm 50cm and placed in a bag labelled ‘S’. Soil-gas radon was collected in the same localities as the physical topsoil samples for the Castleisland dataset (Banríon et al., 2022). Whereas, the geogenic radon data for the TELLUS midlands area were derived from TELLUS airborne radiometric surveys (Elío et al., 2020).

Furthermore, notes were taken on soil characteristics for each sample site. Characteristics included moisture, texture (particle size and sorting), colour, contamination, clast content and composition, any change in these characteristics with depth were also noted. Information about the sample site location was noted including proximity of urban structures (powerlines, roads, tracks, hedges, ditches) and any streams within 100 meters of the sample site, these structures and streams were avoided where possible.

5.2.3 Analysis preparation method

The GSI TELLUS protocol for preparing samples prior to analysis was followed (Young et al., 2016). Each sample weight was measured before and after drying. The samples were placed in a foil tray to prevent sample loss and dried in a fan oven at 30 degrees Celsius for two weeks. Clumps of soil in each sample were broken with a mortar and pestle while avoiding breaking any clasts/small stones. Then each sample underwent dry-sieve shaking to obtain the <2mm fraction. A representative soil subsample of the <2mm soil fraction was obtained through the coning and quartering technique. The representative subsamples were pulverised to the 63um fraction using an agate ball mill.

Sample data processing

Soil samples collected from Castleisland Co. Kerry were analysed at Bureau Veritas Commodities Canada using an aqua regia-ICPMS method on 92 (48 topsoil, 33 deeper topsoil and 11 duplicate) samples for 37 elements (Mo, Cu, Pb, Zn, Ag, Ni, Co, Mn, Fe, As, U, Au, Th, Sr, Cd, Sb, Bi, V, Ca, P, La, Cr, Mg, Ba, Ti, B, Al, Na, K, W, Hg, Sc, Tl, S, Ga, Se, Te). A two-acid digest process was used, which doesn't digest silicate minerals; as such consideration must be given to mineral representativeness in each sample. The following reference materials were used during analysis STD DS11, STD OREAS262 and BVGE001.

TELLUS topsoil geochemistry was analysed using ICPMS for multiple elements (Al, Ba, Ca, Cr, Cu, Fe, K, Li, Mg, Mn, Na, Ni, P, S, Sr, Ti, V, Zn, Zr, Ag, As, Be, Bi, Cd, Ce, Co, Cs, Ga, Ge, Hf, Hg, In, La, Mo, Nb, Pb, Rb, Sb, Sc, Se, Sn, Te, Th, Tl, U, W, Ta, Au, Pd, Pt, Re and Y). Of the TELLUS top-soil midlands data, 4130 of 4279 samples were used for analysis. The 149 samples not used were not within the boundaries of a radon potential class reported by Elío et al. (2020), as such they could not be used for investigating the link with geogenic radon potential. The specific GSI TELLUS dataset investigated is ‘6117xxS-6174xxA_Shallow_Topsoil_Download’.

Data censoring in geochemistry occurs when the concentration of an element is more or less than the upper or lower detection limits (dl). There are several ways to treat censored data (i.e. replacing data with either half the value or third the value of the lower detection limit (Grunsky, 2010). The elements with more than 5% of values under the lower dl were omitted from the dataset for further analysis. In the Castleisland, Co. Kerry dataset, a total of 11 elements (Ag, Au, Cd, Bi, B, Ti, W, Tl, S, Se, Te) were removed from the dataset for further analysis due to 5% – 100% of measurements being below the dl. In the Tellus Midlands dataset, the elements (Ta, Au, Pd Pt and Re) were omitted due to more than 5% of values being below the dl. Values occurring below the detection limit were assigned ½ the lower detection limit value.

Data closure

Geochemical data is a subset of compositional data in which the concentrations of elements represent a proportion of the entire composition, leading to the constant sum (or data closure) issue (Aitchison, 1982). The isometric log ratio (ilr) transformation is used on data prior to univariate compositional data analysis i.e. correlation tests including coefficient of determination, correlation coefficient, and one-way ANOVA tests. The isometric log ratio transforms a composition from an Aitchison-simplex to D-1 (dimension minus 1) Euclidian vector space, retaining isometry (Egozcue et al., 2003). The ilr transformed dataset was back-transformed to obtain the original dimensionality of the starting dataset; this was done using ‘R’ software version 4.0.2 and the *‘compositions’* package.

The centred log ratio transformation is used on data to accommodate the data closure restraint, specifically prior to multivariate compositional data analysis.

equation Clr(x) = [log(x/(geomean(x)) … logxn/geomean(x)]

Clr-transformation projects the dataset onto Euclidean space, allowing for the interpretation of geochemical results without the issues of spurious correlation of dependent variables (Aitchison, 1982; Grunsky and Caritat, 2019; Wang et al., 2021).

Univariate analysis

The coefficient of determination (R^2) is a common statistical method used to measure the strength of the correlation between two variables. The correlation coefficient Pearson (r) is used to identify patterns between soil elements and SGRn or geogenic radon class. The SGRn and element compositions for samples collected in Castleisland, Co. Kerry are numerical input data, which is suitable for the R^2 and Pearson r calculation. The TELLUS midlands topsoil geochemistry data are numerical but the geogenic radon potential classes are categorical. As such, analysis of variance (ANOVA) is used to measure the relative variance of elements with regards to geogenic radon class.

Cluster analysis

There are many modifications of cluster analysis, in this study an unsupervised hierarchical learning algorithm is used; which results in variables being partitioned to groups based on the sum of the squared distances between a centroid and the data points. The resulting cluster groups of topsoil geochemistry can be applied to testing if elements correlated to radon variation are associated with one another. The ‘R’ software is used for PCA, cluster analysis and ANOVA analysis. The ‘cluster’ package and ‘prcomp’ function is used for cluster analysis and PCA respectively. For ANOVA analysis packages, ‘lsr’, ‘nlme’ and ‘pwr’ are utilized (‘R’ version 4.0.2).

Principal component analysis

Principal Component Analysis (PCA) is an affine geometric transformation technique, which allows for increased interpretability of a multivariate dataset (Tolosana-Delgado and McKinley, 2016). PCA is a linear dimensionality reduction technique based on Euclidian methods, that transforms multiple variables into a smaller number of principal components (PC's), where principal component 1 (PC1) represents the direction of maximal variance of the dataset (Mueller et al., 2020). After PC1 the second principal component (PC2) represents the second largest variance of the data, and is orthogonal to PC1 (Vermeesch, 2013).

The first several (n) PCs approximate the composition of elements which cause the highest degree of variation in the dataset. The last PCs explain the least variance, which may correspond to quasi-constant elements that could be utilized for studying immobile and mobile element migration if a geospatial/geochemical dataset is used (Tolosana-Delgado and McKinley, 2016). PCA aids in interpretation of elemental variance within a compositional dataset and can be used in the process discovery phase of research (Grunsky, 2010; McKinley et al., 2018).

Each principal component contains scores/eigenvalues and loadings/eigenvectors, the scores representing the samples in Euclidian space, and the loadings representing the size and direction of each variable (i.e. element) (Abdi and Williams, 2010). The positioning and size of each vector is significant; eigenvectors with small degrees of angels, and similar directions, depict variables with a higher degree of correlation/covariance. In comparison, eigenvectors with large differences between them have lower correlation (Demšar et al., 2013).

Machine learning

Many geological and environmental studies have utilised machine learning (ML) for classification processes, including random forest (RF) for determining mineral prospecting, determining aggregate provenance and radon mapping (Daviran et al., 2021; Dornan et al., 2020; Petermann et al., 2021). Gaussian process regression (GPR) has been used for its powerful interpolation techniques for natural hazard mapping, soil science and investigating heavy mineral pollution (Colkesen et al., 2016; Pham et al., 2021; Wang et al., 2022). Logistic regression (LR) has been applied to environmental pollution studies, mapping geogenic radon, and geochemical exploration (Aditya et al., 2018; Elío et al., 2017; Nathwani et al., 2022).

For the purposes of this study, four ML models are compared to investigate the suitability of using topsoil geochemistry for predicting geogenic radon potential categories. Results from RF, GPR and LR are compared with a control model which acts as a baseline. The ML algorithms (RF, LR, GPR) have been chosen in this study due to their robustness and ability to analysis large (>1000 samples) multivariate datasets.

In simple terms, Random Forest (RF) can be used as a supervised classification algorithm that aims to predict which group an observation belongs to. RF consists of an ensemble of dissimilar decision trees, which assigns features at each node that reflect the greatest separation between observations. As an ensemble ML algorithm, RF uses results from numerous individual decision trees ('weak learners') to form a 'strong learner' with the most frequently occurring features assigned as important for classifying observations (Farhadi et al., 2022; Shang et al., 2019). A more elaborate explanation of the mathematical theory underpinning RF can be found in the literature (Biau and Scornet, 2016; Breiman, 2001; Schonlau and Zou, 2020). The 'RandomForestClassifier' function in the sklearn library (python version 3.6) was used to implement the random forest model.

Gaussian Process Regression (GPR), is a nonparametric classification ML algorithm based on the theory of Bayesian probability. GPR operates by calculating the probability distribution of all functions fitted to the data. The GPR model initially forms a prior distribution, then uses the training dataset to reallocate probabilities and form a posterior probability distribution. The test dataset is used to calculate probabilities with unseen samples. Thorough explanations of the theory underlying GPR can be found in the literature (Bernardo et al., 1998; Bousquet et al., 2011; Kanagawa et al., 2018). The 'GaussianProcessClassifier' function in the sklearn library (python version 3.6) was used to train and test the GRP model.

Logistic Regression (LR) is utilized for binary classification problems which fits independent variables and log odds to a generalized linear equation (equation1);

$\log(p/1\text{-}p) = \beta_0 + \beta_1 x_1 + \ldots + \beta_i x_i$ equation 1

where p is the predicted probability, β is the regression coefficient and x represents independent variables. The logistic function (equation 2) builds on the linear equation;

$P(Y=1|x) = 1/1 + e^{-(\beta_0 + \beta_1 x_1 + \ldots + \beta_i x_i)}$ equation 2:

where Y is the binary variable, *e* is the Euler's number. The logistic equation is used to predict the probability of independent variables occurring in a binary class. More details regarding the LR mathematical model are published in the literature (Hastie et al., 2009; Kirasich et al., 2018; Sperandei, 2014). Specifically, the sklearn library is used in python (version 3.6), utilizing the 'LogisticRegression' function.

The airborne geogenic radon potential (GRP) categories (High, Medium-High, Medium-Low and Low) published by Elio et al. (2020) are used as response variables in the machine learning models. The four groups are assigned to two classes to help balance the spatial data. The Low category is assigned to class 1 and the Medium-Low, Medium-High and High groups are assigned to class 2. The Low GRP category has significantly less probability (6.93%) of having indoor radon concentration above the 200 Bq m^{-3} reference level compared to the remaining GRP classes (average 16.98%) (Elío et al., 2020).

Cross-validating data is important for determining the stability of model parameters. Spatial cross-validating aims to eliminate overfitting in the model due to spatial autocorrelation (Pohjankukka et al., 2017; Talebi et al., 2022). The TELLUS Midlands dataset was spatially cross-validated using 5-fold spatial blocking. This was achieved by splitting the dataset into 5 separate spatial blocks, 4 blocks were used for training the model and the remaining block was used to test the model, and iterated 10 times. To aid in balancing the model, equal amounts of samples from classes 1 and 2 were extracted during the training and testing process. The 5-fold cross-validation was repeated 10 times for RF, GPR, LR and a control model.

5.3 Results and Discussion

Two case studies at local and regional scales are utilized to investigate using topsoil geochemistry for understanding geogenic radon distribution and variation in topsoil. Summary statistics (i.e. mean, min, max, quartiles 1-3, standard deviation, skewness and Kurtosis) for the Castleisland, Co. Kerry dataset TELLUS Midlands dataset are included in the supplementary materials (*supp.matt*) 7.2.1 and 7.2.2, respectively

5.3.1 Castleisland, Co. Kerry – local scale case study.

The r^2 and Pearson r are calculated for each element versus every other variable including soil-gas radon (SGRn) concentration for both ilr-transformed deeper topsoil and topsoil samples from Castleisland Co. Kerry (*supp.matt 7.2.3-7.2.6*). There is a relative correlation between log_{10}SGRn and soil geochemistry in Castleisland. Specifically, , U, Sr, Cu, V, P, Ba, Sb, Mo, La and Cr have the relatively strongest Pearson correlation coefficients (0.62 – 0.46) and r^2 values (0.5 – 0.21) associated with log_{10}SGRn (*supp.matt 7.2.3*). The r^2 and Pearson r results from the deeper topsoil geochemistry report the same top ten elements correlated to log_{10}SGRn (*supp.matt 7.2.5-7.2.6*). Additionally, heatmaps can aid visualisation of canonical pathways between variables; heatmaps produced for soil geochemical parameters relating to the Castleisland case study area are shown in figure 5.1 and figure 5.2.

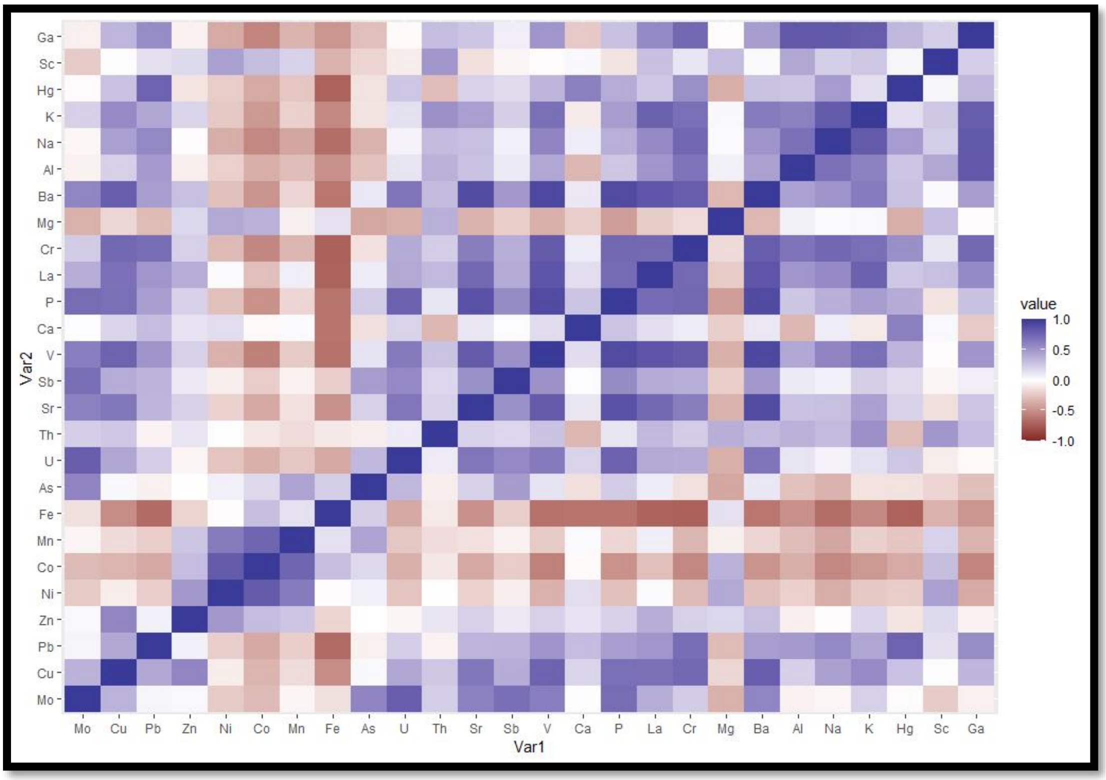

Figure 5.1 Canonical heatmap ilr transformed Castleisland shallow topsoil.

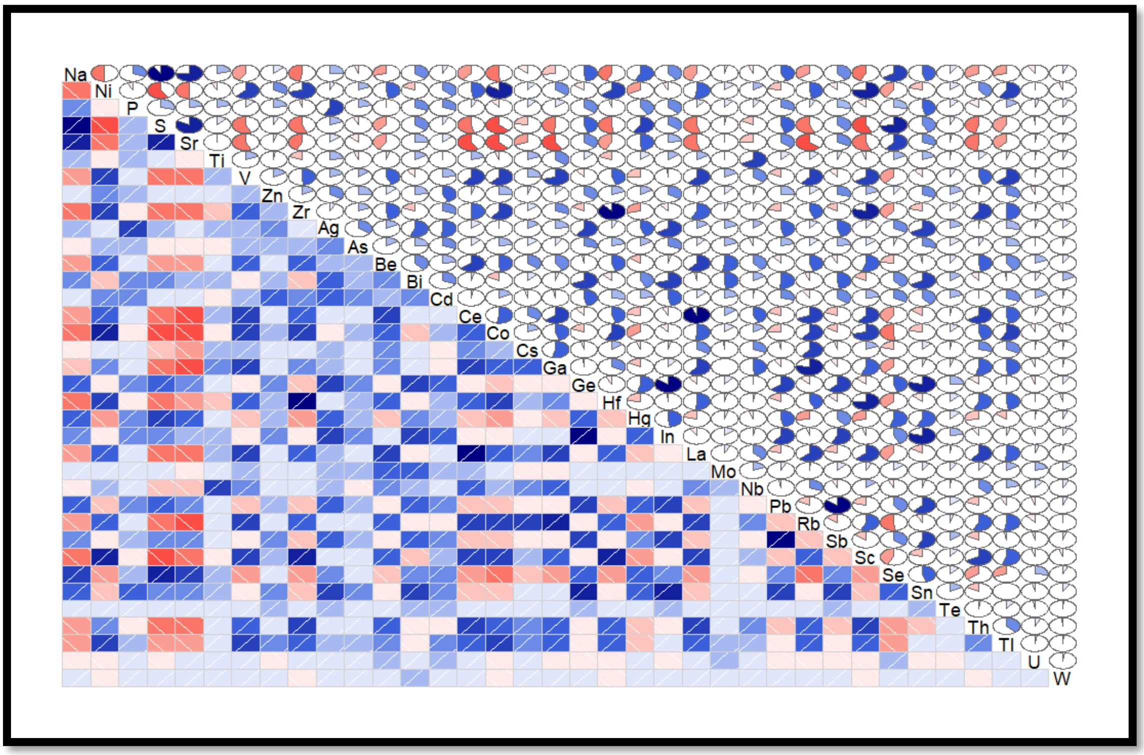

Figure 5.2 Canonical heatmap ilr transformed Castleisland shallow topsoil.

With regard to PCA, there are (n-1) PCs in an analysis. The PCs of interest are the ones that explain more variance than an individual variable would explain if the variables explained equal variance; i.e. if the 26 variables contributed equally to the variance, they would each explain 3.8% (100/26) of the variance. PC5 is the cut off for analysis as it is the last component that explains more than 3.8% of the variance. Table 5.1 summarises the loadings for PC1-5, as well as the standard deviation, proportion of variance and cumulative variance. The first 5 PCs explain 84% of the dataset variance, with the first two PCs accounting for 63% of the variance. The most influential loadings are highlighted in **bold** for positive correlation and underlined to indicate a negative correlation.

Table 5.1 Loadings values for PC1 to PC5 of Clr-transformed shallow topsoil geochemistry Castleisland, Co. Kerry.

Loading	**PC1**	**PC2**	**PC3**	**PC4**	**PC5**
Hg	**0.083**	-0.121	*-0.369*	**0.458**	0.106
Sr	**0.078**	*-0.344*	0.082	-0.098	-0.116
U	**0.05**	*-0.308*	-0.09	0.092	**0.191**
Ca	**0.043**	-0.098	-0.428	0.076	*-0.405*
V	**0.035**	*-0.357*	**0.149**	0.047	0.026
Sb	**0.021**	*-0.283*	-0.03	*-0.299*	**0.213**
P	**0.008**	*-0.353*	-0.034	0.059	-0.008
Cu	**0.006**	*-0.312*	-0.018	-0.01	*-0.249*
Pb	-0.015	-0.117	*-0.272*	**0.379**	**0.213**
Mo	-0.068	*-0.288*	0.057	*-0.253*	**0.356**
La	-0.114	*-0.26*	0.097	-0.081	*-0.385*
Ba	-0.121	*-0.312*	**0.141**	0.184	-0.104

Na	-0.211	**0.044**	**0.193**	**0.374**	-0.031
Mn	-0.218	-0.004	*-0.243*	*-0.262*	-0.087
Ga	-0.225	**0.066**	**0.296**	**0.252**	0.093
K	-0.231	-0.046	**0.342**	-0.035	-0.174
As	-0.233	-0.129	-0.143	*-0.167*	**0.358**
Cr	-0.254	-0.148	0.06	**0.205**	0.067
Co	-0.27	**0.063**	*-0.272*	-0.102	0.015
Ni	-0.271	**0.034**	*-0.257*	-0.104	-0.135
Zn	-0.273	-0.072	-0.153	-0.037	-0.204
Th	-0.278	0.005	**0.144**	-0.093	-0.062
Fe	-0.284	**0.046**	-0.078	-0.073	**0.289**
Mg	-0.285	**0.102**	-0.065	-0.032	-0.027
Al	-0.292	0.004	0.087	**0.201**	0.067
Sc	-0.296	**0.041**	-0.087	0.04	-0.066
Standard deviation	3.118	2.583	1.61	1.283	1.093
Proportion of Variance	0.374	0.257	0.1	0.063	0.046
Cumulative Proportion	0.374	0.631	0.73	0.794	0.84

PC1 accounts for 37% of the total variance. The highest loadings (>0.005) relate to the elements Hg, Sr, U, Ca, V, Sb, P and Cu (table 5.1). The PC1 score map shows the lowest scorings occurring above the Rockfield limestones and the eastern boundary of the Clare shales and Dirtoge limestones (fig.5.3). The lowest scores are located above the Waulsortian limestones and the western boundary of the Dirtoge limestones and Cracoean reef member (fig.5.3). The lowest loadings (<-0.25) are associated with the elements Sc, Al, Mg, Fe, Th, Zn, Ni, Co and

Cr. The deeper topsoil PCA results display a similar trend of the same elements associated with high and low PC1 loadings (*supp.matt 7.2.7*).

PC2 accounts for 27% of the total variance. The highest loadings (>0.005) relate to the elements Mg, Ga, Co, Fe, Na, Sc, Ni, Th and Al. The highest scores are associated with samples collected from the west of the study area as well as above the Waulsortian limestones. The lowest loadings (<-0.25) are associated with the elements V, P, Sr, Ba, Cu, U, Mo, Sb and La. The PC2 score map shows the lowest scorings occurring above the Clare Shales. There is spatial correlation between high PC1 scores and low PC2 scores with the high geogenic radon potential in the same area reported by Banríon et al. (2022).

The score maps (*supp.matt 7.2.8*) for PC3, PC4 and PC5 don't appear to strongly correspond with any variation in geology or geogenic radon potential as reported by Banríon et al., (2022). Nonetheless, PC3 accounts for 10% of the total variance. The highest loadings (>0.08) relate to the elements K, Ga, Na, V, Th, Ba, La, Al and Sr. The elevated PC3 scores mostly occur in the north and east of the study area. The lowest loadings (<-0.14) are associated with the elements Ca, Hg, Co, Ni, Mn, Pb, Zn and As. Some of the lowest PC3 scores are observed above the till derived from limestones, especially in close proximity to a local NW-SE fault (Banríon et al., 2022).

PC4 accounts for 6.3% of the total variance. The highest loadings (>0.18) relate to the elements Hg, Pb, Na Ga, Cr, Al and Ba. The majority of high PC4 scores occur above the limestones east to the NW-SE fault with lower scores located to the west to the NW-SE fault. The lowest loadings (<-0.08) are associated with the elements Sb, Mn, Mo, As, Ni, Co, Sr, Th and La. The PC4 score map shows lowest scorings occurring mostly in the west of the study area.

PC5 account for 4.6% dataset variance. The high scores of PC5 occur in the centre and in the NW and NE of the study area, with lower scores occurring in the rest of the area. High PC5 loadings (>0.19) are associated with As, Mo, Fe, Sb, Pb and U. Negative PC5 loadings (<-0.1) are linked to Ca, La, Cu, Zn, K, Ni, Sr and Ba.

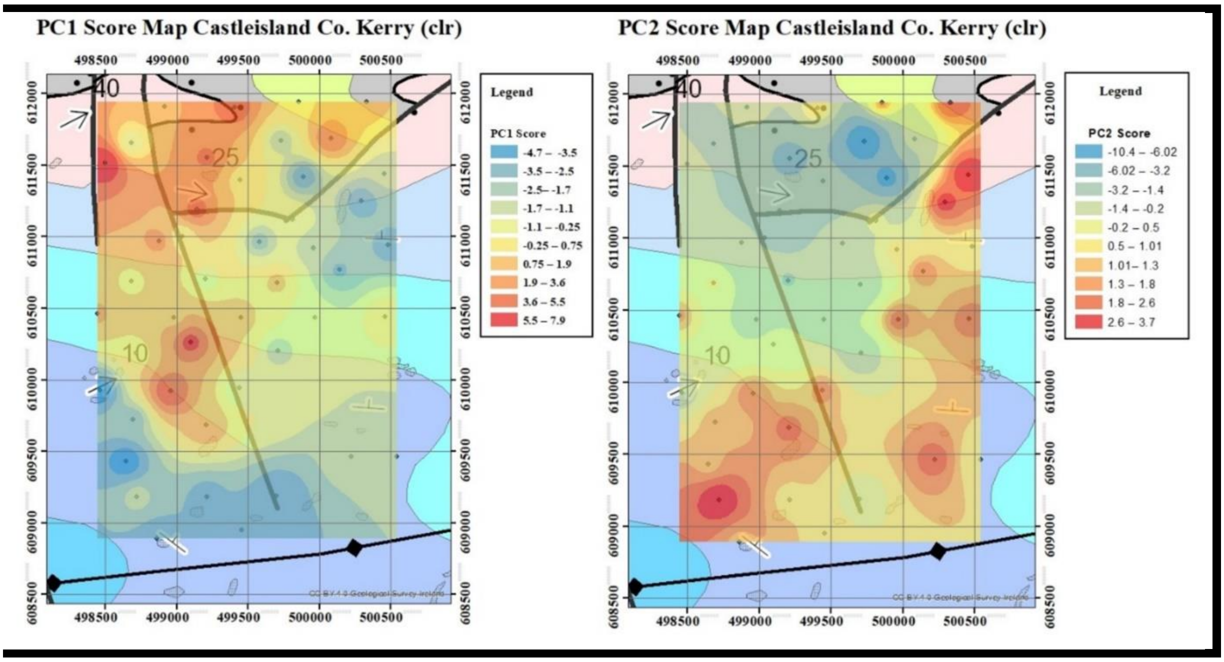

Figure 5.3 Principal component score maps for PC1 (left) and PC2 (right) shallow topsoil Castleisland, Co. Kerry dataset.

The cluster analysis groupings are almost identical to the PCA variable clusters. Specifically, the elements clustered to the left (*low PC1 and high PC2*) of the PCA graph (Mg, Na, Co, Sc, Th, Al, Ni, Mn, K, Zn, Ga, Fe, As and Cr) are all grouped together on the right of the cluster analysis graph (fig.5.4). Similarly, the elements clustered with low PC2 scores (La, Ba, Mo, Cu, P, Sb, U, V and Sr) are all grouped together to the left of the cluster analysis graph. The exceptions are Pb and Hg which are clustered together on the PCA graph but are end members on cluster analysis graph. The deeper topsoil analysis depicts a similar pattern of elements correlated with radon covarying together with the PCA and cluster analysis results (*supp.matt 7.2.9*).

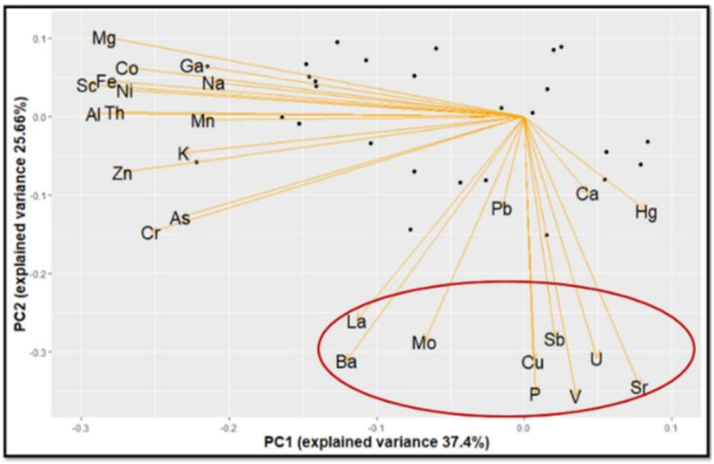

Figure 5.4 PC1 vs PC2 plot for shallow topsoil Castleisland Co. Kerry data.

The Pearson r correlation and r^2 results show that shallow topsoil elements (including P, Sr, Ba, V, Mo, U and Cu) have a correlation with SGRn in Castleisland, Co. Kerry (*supp.matt 7.2.3*). Elements correlated with SGRn (including La, Ba, Mo, P, Cu V and U) group together on the PC1 vs PC2 biplot (fig.5.4). The concept of elements associated with high SGRn covarying with one another is reinforced by the PCA results; the biplot depicts elements related to higher SGRn covarying together, with low PC2 scores and moderate-high PC1 scores (fig.5.4a). The aforementioned results support the hypothesis that elements associated with geogenic radon exhibit covariance within the earth surface.

The PC2 score map (fig.5.3) is superimposed on the bedrock geology map for the Castleisland area, which visually depicts low PC2 scores occurring above the spatial boundaries of the Clare shales. The low PC2 associated elements (P, Sr, Ba, V, Mo, U and Cu) underpins elevated SGRn considering low PC2 scores are spatially restricted to the anomalously high SGRn reported above the Clare shales (fig.5.4) (Banríon et al., 2022). These elements may be a geochemical signature of high SGRn in Castleisland. The occurrence of low PC2 scores above the Clare shales, as well as the presence of radon's parent isotope, uranium, reinforces that the Clare shales may be acting as a source of radon in the Castleisland area.

Furthermore, high PC2 scores (fig.5.4) coincide with lower SGRn reported in the Castleisland area (Banríon et al., 2022). The elements associated with high PC2 loadings (including Fe, Mg, Co, Ni, Sc and Mn) depict a negative correlation with SGRn (*supp.matt 7.2.3*). Overall, the local scale case study in Castleisland, Co. Kerry shows topsoil elements sharing geospatial covariance, as well as correlation to SGRn in the earth surface. The results presented here validate that earth surface geochemistry can give insight into geogenic radon potential.

Adapting local scale data to investigate geogenic phenomena comes with the risk of not being able to extrapolate results to other geological areas. In order to validate the multivariate analytical approach of investing geogenic radon presented in this study, we tested the methods on regional data from the Irish midlands.

5.3.2 Ireland midlands (TELLUS, GSI) – regional case study.

The ANOVA method was used to investigate the relative correlation/covariance of geogenic radon class with topsoil geochemistry in the TELLUS Midlands Clr-transformed dataset (*supp.matt 7.2.10*). A relative covariance can be observed between geogenic radon categories and the topsoil elements. One-way ANOVA results demonstrate elements including S, Na, Sr, Cr, Ni, Co, Al, V, Sc, Zr, Se, Y, Fe, La, Hf, Rb, Li, Ce, and Tl (Be, Hg, Th, Ga, Ta, Mn) significantly (*equivalent p value <0.*005) explain relatively more variance in RP class (11-29%) opposed to other elements analysed (supp.matt 7.2.10). Canonical heatmaps are shown below for the soil geochemical parameters measured in the TELLUS Midlands study area, using ilr-transformed data (fig.5.5 and fig.5.6).

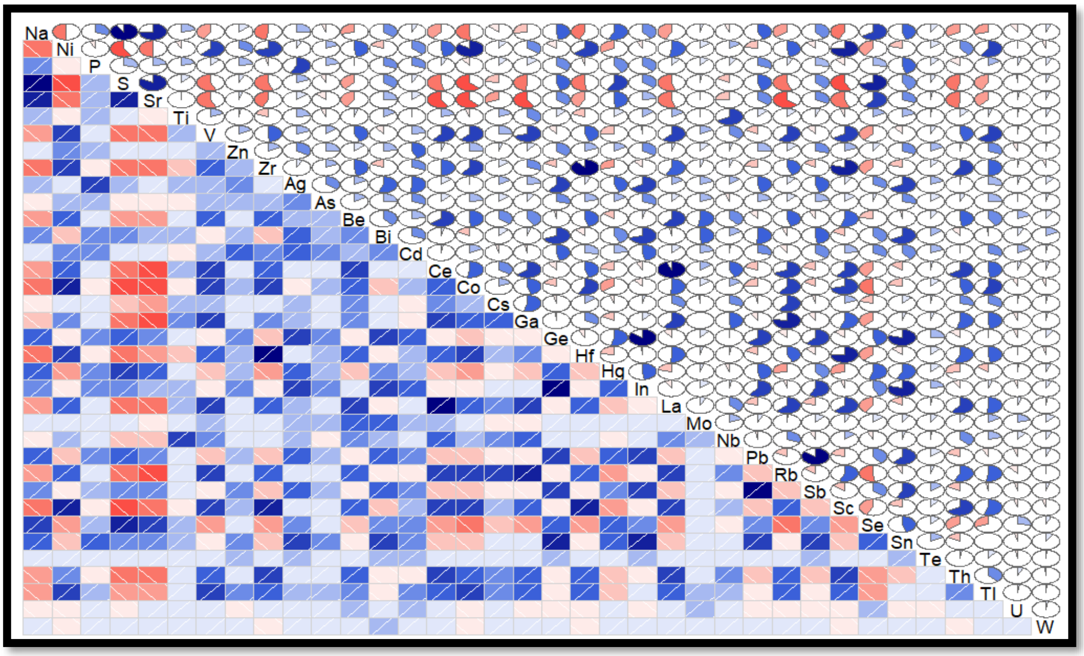

Figure 5.5 TELLUS Midlands shallow topsoil geochemistry ilr-transformed canonical heatmap. Dark blue is strong positive correlation, dark red is strong negative correlation.

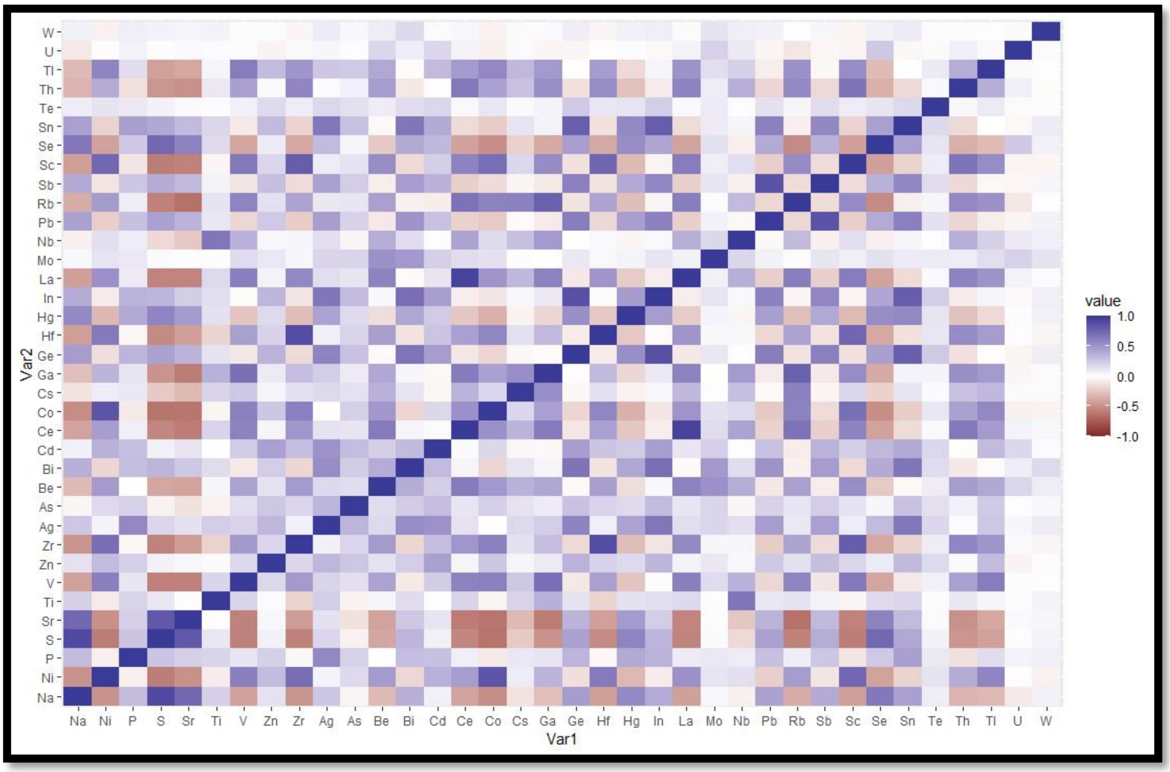

Figure 5.6 TELLUS Midlands shallow topsoil geochemistry ilr-transformed canonical heatmap

Principal component analysis results

Considering PCA, each of the 47 variables would explain 3.1% (100/47) of the variance if they contributed equally. The top 4 PCs each explain more than 3.1% of the variance (table 5.2), as such PC4 will be the cut-off threshold for further analysis. The initial 4 PCs explain 80% of the dataset variance.

PC1 accounts for ca. 60% of the total variance. The highest loadings (> -0.025) relate to the elements S, Na, Se, Sr, Ca and Hg (table 5.2). The PC1 score map shows the highest scorings occurring above granitic bedrocks in the west and east of the Irish Midlands (fig.5.7). High PC1 scores are also observed above undifferentiated Visean limestones, dark limestones and shales, as well as oolitic and packstone limestones (fig.5.7). The lowest scores in the west are observed above dolomitic and peloidal limestones and calcareous shales. Low PC1 scores are also seen above some Waulsortian limestones as well as dark limestone and shales in the east of the Midlands (fig.5.7). The lowest loadings (< -0.17) are associated with the elements Be, V, Cr, Al, Sc, Co, La, Ce, Ga, Li, Tl, Ni, Rb, Y, Fe and Th (table 5.2).

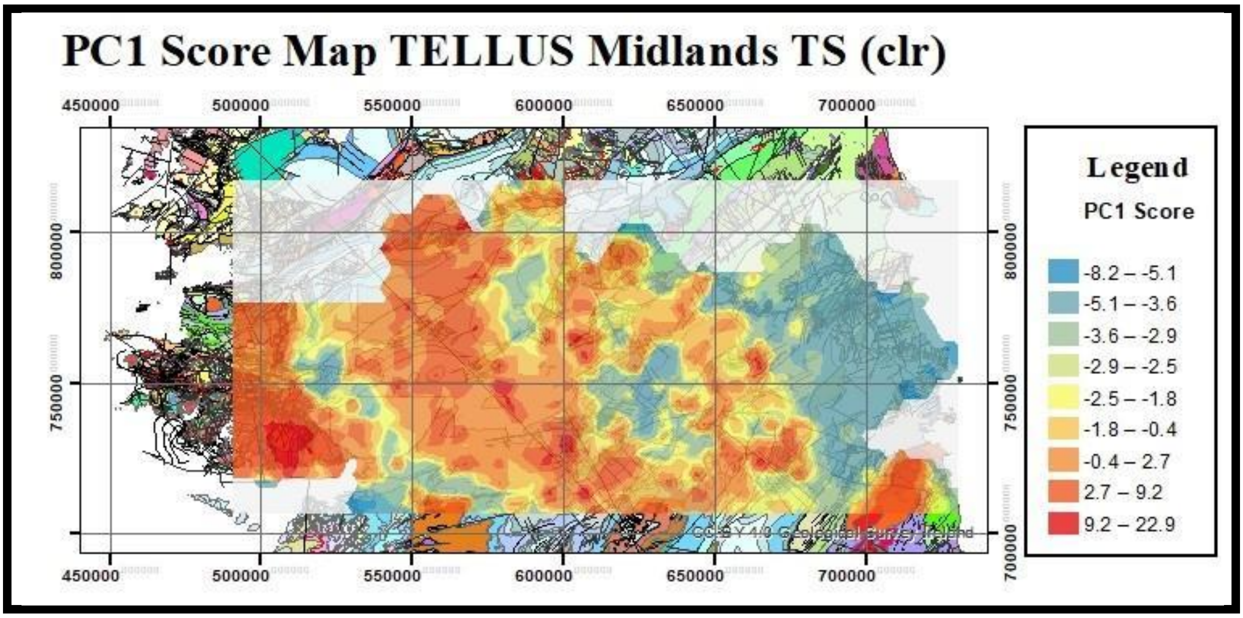

Figure 5.7 PC1 score map of TELLUS Midlands topsoil data, superimposed onto the bedrock geology (1:100k) GSI map. The PC score map was made in ARCGIS using the Inverse-distance weighted geostatistical function (grid output size = 50 m, major and minor semiaxis = 50000, smoothing factor = 0.2).

PC2 accounts for 9.5% of topsoil geochemistry variance. The highest positive loadings (> 0.18) are associated with Se, Hg, Sb, Sr, S, Pb, Ca, Cd, Sn, Bi and Ge (table 5.2). Positive PC2 loadings occur above the Shannapheasteen and Galway Granite and Wicklow Granite (*supp.matt 7.2.12*). Higher PC2 loadings also occur scattered in the middle and east of the study area with no apparent constraint to geological parameters. The most negative PC2 loadings (< -0.06) are linked to Rb, Li, Cs, Th, Th, Ce, Al, K, Ga, La and Cr (table 5.2). Low scores are found above the undifferentiated Visean limestones, dark fine-grained limestone and shale, as well as in proximity to black mudstone, siltstone and greywacke (*supp.matt 7.2.12*).

PC3 accounts for 7.5% of the topsoil variance. The highest PC3 loadings (> 0.8) are associated with Ca, Sr, U, Zr, Cd, Y, Hf, Se, Ni, Mn, S and Mo (table 5.2). High PC3 scores generally occur in dark limestones, fossiliferous limestones and shales between the Galway and Wicklow granites (*supp.matt 7.2.12*). The most negative loadings (< -0.11) are linked to Bi, Pb, Na, Sn, In, W, Ge, Ti and K (table 5.2). Low PC3 scores distinctly occur above the Galway and Wicklow granites as well as in the mudstone, siltstone conglomerate and sandstone in the south of the study area (*supp.matt 7.2.12*).

Highly positive PC4 loadings (> 0.08) are linked with Mg, Na, Ca, Sr, Ba, K, Zn, In and Ge (table 5.2). High PC4 scores are concentrated in the northeast of the study area, especially in the proximity of calcareous red-mica greywacke, and black mudstone and greywacke (*supp.matt 7.2.12*). Low PC4 loadings are associated with Ag, Hg, U, Sn, Pb, Bi and Cd (table 5.2). Low scores are found above dark limestones and shales, Visean limestones and pale skeletal limestones (*supp.matt 7.2.12*).

Table 5.2 Principal component analysis eigenvector (loading) results for PC1-PC4 of Clr-transformed shallow topsoil TELLUS GSI Midlands, Ireland.

Eigenvectors	**PC1**	**PC2**	**PC3**	**PC4**
S	0.123	0.275	0.096	0.025

Na	0.054	0.132	-0.27	0.466
Se	0.023	0.365	0.134	-0.018
Sr	0.011	0.277	0.323	0.193
Ca	-0.016	0.211	0.383	0.194
Hg	-0.025	0.363	-0.052	-0.196
Pb	-0.082	0.256	-0.284	-0.121
Mg	-0.087	0.057	-0.088	0.63
Sb	-0.096	0.28	-0.104	-0.01
W	-0.102	0.105	-0.164	-0.089
Sn	-0.106	0.19	-0.259	-0.13
Bi	-0.108	0.188	-0.312	-0.102
Ti	-0.117	-0.053	-0.125	0.077
U	-0.123	0.075	0.229	-0.147
Mo	-0.123	0.119	0.094	-0.026
Cd	-0.131	0.2	0.156	-0.099
Ge	-0.132	0.18	-0.131	0.09
In	-0.14	0.094	-0.19	0.093
Ba	-0.141	0.052	0.043	0.191
P	-0.148	0.092	0.054	-0.082
Te	-0.151	0.146	-0.023	0.046
As	-0.152	0.112	0.058	-0.067
Zn	-0.154	0.087	-0.002	0.111
Cu	-0.157	0.067	0.075	-0.059
Ag	-0.157	0.089	-0.1	-0.209

Mn	-0.162	-0.041	0.101	0.042
Nb	-0.164	-0.047	-0.073	0.033
Hf	-0.165	-0.032	0.153	0.006
K	-0.165	-0.096	-0.124	0.124
Zr	-0.169	-0.017	0.174	-0.002
Cs	-0.169	-0.116	-0.084	-0.08
Th	-0.171	-0.114	0.071	-0.032
Fe	-0.171	-0.025	0.063	0.029
Y	-0.172	-0.022	0.155	-0.064
Rb	-0.174	-0.141	-0.076	0.022
Ni	-0.175	-0.003	0.134	0.071
Tl	-0.175	-0.045	0.015	-0.088
Li	-0.175	-0.123	0.023	0.034
Ga	-0.177	-0.082	-0.11	0.029
Ce	-0.178	-0.099	-0.003	-0.033
La	-0.178	-0.082	0.026	-0.044
Co	-0.179	-0.045	0.079	0.057
Sc	-0.179	-0.043	0.053	0.057
Al	-0.18	-0.099	-0.053	0.021
Cr	-0.181	-0.067	0.034	0.041
V	-0.182	-0.041	-0.003	-0.01
Be	-0.182	-0.015	0.034	0
Standard deviation	5.296628	2.106877	1.876334	1.237675
Proportion of Variance	0.5969	0.09445	0.07491	0.03259

Cumulative Proportion	0.5969	0.69134	0.76625	0.79884

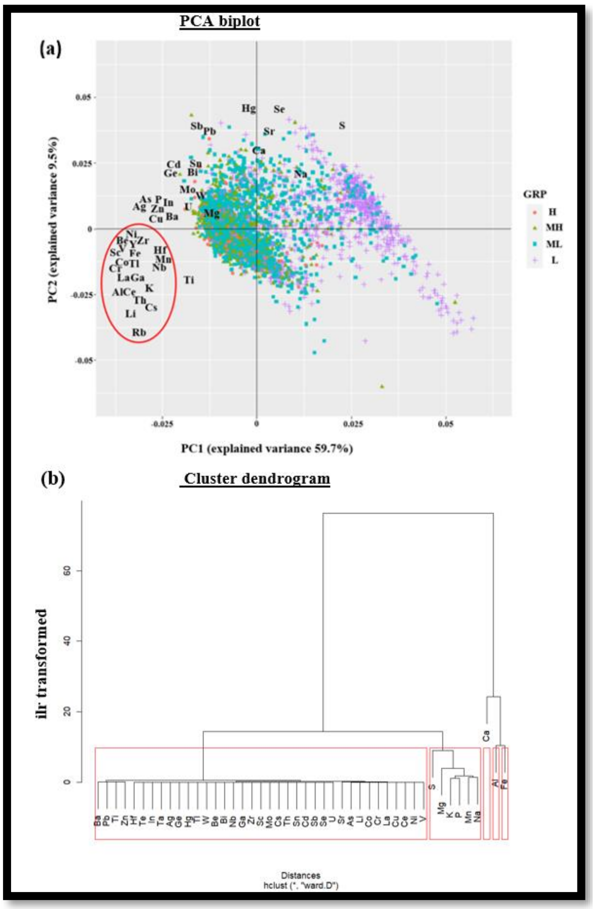

Figure 5.8 (a) PC1 vs PC2 biplot and (b) hierarchical dendrogram for TELLUS Midlands topsoil data. PC score results are grouped to geogenic radon potential reported by Elío et al. (2020). The 'R' software was used, specifically the prcomp library with the centre and scale argument set to true.

Elements with stronger ANOVA effect size related to geogenic radon (i.e. Cr, Ni, Co, Al, V, Sc, Y, Tl) consistently group together on both PCA and cluster analysis, reinforcing the covariance and correlation of grouped elements (fig.5.8). Additionally, elements including Sr, S and Na explain relatively strong variance in RP class and group together in the top-right of the PCA (fig. 5.8). Specifically, elements corresponding to low PC1 and low PC2 values on the biplot are also grouped together on the cluster analysis (*supp.matt 13*). The PCA and cluster analysis results indicate that radon-prone elements have geospatial restraint, suggesting topsoil geochemistry can be used as a tool to understand the geogenic radon potential in an area.

Explicitly, if a topsoil sample contains elevated concentrations of radon-prone elements (Cr, Ni, Co, Al, V, Sc, Y, Tl)), then it may correlate with higher geogenic radon potential.

Furthermore, areas with high PC1 scores compare with low GRP areas reported by Elío et al. (2020). In detail, positive scores are observed above the Galway granite in the west and above the Wicklow granite in the east of Ireland, which also corresponds to low GRP values in the same area reported by Elío et al. (2020). The lowest PC1 scores (fig.5.7) generally correspond with high to medium GRP values reported by Elío et al. (2020). Significant (<0.05) ANOVA results show 33% of GRP variance is explained by PC1 score distribution, which is greater than the 0.5% - 1.1% variance explained by PC2 – PC4 (*supp.matt 7.2.14*). Additional ANOVA results show that bedrock lithology explains PC1 variance by 14% (*supp.matt 7.2.14*), highlighting that the variation within PC1 is related to GRP distribution more than bedrock lithology spatial distributions.

High PCA loadings (S, Na, Se, Sr, Ca and Hg) occur above various limestones including the Waulsortian limestones, Croghan limestone Formation, Ballymore limestone Formation, Cong canal Formation and the majority of the Burren Formation. The association of high PCA loadings and limestones with low geogenic radon is reasonably understood by the naturally low uranium content in limestone lithologies. However, some of the highest PCA loadings (S, Na, Se, Sr, Ca and Hg) also occur above the Devonian granites in Co. Galway and Co. Wicklow, where a higher concentration of uranium and radon prone elements would be expected (i.e if soil formed from the underlying bedrock and little chemical and physical weathering occurred). The lack of radon prone elements in soils above the Devonian granites indicates that (a) the soil did not form from the underlying bedrock or (b) weathering has occurred that has mobilised radon prone elements to be deposited above different bedrock geologies.

The positive correlation between low PCA loadings (i.e. Be, V, Cr, Al, Co, Ni, La, Li, Tl, Rb, Y) and geogenic radon potential is depicted in Tukey boxplots (section 7.2.11). The lowest PCA loadings share a similar geospatial trend, with the relative concentrations of these elements being consistently lower in soils above some bedrock lithologies (i.e. 1. Argyll Group; Psammitic and pelitic schist and 3. Granite and granodiorite) while higher relative concentrations are present in soils above bedrock lithologies including 2. Marine shelf facies (limestones and calcareous shale) and 4. Marine basinal facies (Lucan and Tobercolleen Formations) (section 7.2.11).

The negative correlation between high ranking PCA elements (i.e. S, Na, Se, Hg) and geogenic radon potential can be observed on the Tukey box-plots (section 7.2.11). The high ranking PCA elements share a similar geospatial trend, with their concentrations relatively higher in soils above certain bedrock groups (i.e. 1. Argyll Group; Psammitic and pelitic schist and 3. Granite and granodiorite) and relatively lower concentrations in bedrock groups including 2. marine shelf facies (limestone and calcareous shale), 4. marine basinal facies (Lucan Formation and Tobercolleen Formation – dark-grey argillaceous and cherty limestone and shale), and 11. Deep marine turbidite sequence (mudstone, greywacke and conglomerate).

Low PCA loadings (including Be, V, Cr, Co, La, Y, Tl, Ni, Li and Rb) are observed above Namurian (undifferentiated) sandstones, siltstones and shales, as well as in soils above siltstones and sandstones in the east of the study area including the Balrickard Formation (Namurian sandstone and shale), Walshestown Formation (Namurian shale, sandstone limestone), Denhamstown Formation (Silurian greywacke sandstone and siltstone) and Clatterstown Formation (Silurian siltstone and sandstone). Low PCA loadings also occur in soils above the limestones and shales located in the north east of the study area (i.e. Mornington Formation, Crufty Formation, the Lucan Formation, the Loughshinny Formation (dark micrite and calcarenite and shale), Clontail Formation (calcareous red-mica greywacke).

There is a more subtle geospatial trend observable for the high ranking PCA elements; specifically, highly ranked PCA elements have relatively low concentrations in soils above bedrock groups 11 to 13 (11. Deep marine turbiditic sequence (mudstone, greywacke and conglomerate), 12. marine greywacke and shale, Ordovician – Silurian) Moffat shale facies and 13. Navan group (dark-grey limestone, mudstone, sandstone and minor evaporite). To add, the concentrations of these elements gradually increase in soils above bedrock units 6 to 8 (i.e. 6. Marine, shelf and ramp facies (argillaceous dark-grey bioclastic limestone), 7. Waulsortian pale grey massive limestone, 8. Basalt, trachyte, syenite, tuff and gabbro, dolerite and diorite, and 9. continental redbed facies).

In contrast, the lowest ranking loadings decrease in relative concentration above bedrock groups 6 to 8 (i.e. 6. Marine, shelf and ramp facies (argillaceous dark-grey bioclastic limestone), 7. Waulsortian pale grey massive limestone, 8. Basalt, trachyte, syenite, tuff and gabbro, dolerite and diorite), and decrease in concentration above bedrock groups 10 to 12 (i.e. 10. Fluvio-deltaic and basinal marine (turbiditic) shale, sandstone, siltstone and coal), 11. Deep marine turbiditic sequence (mudstone, greywacke and conglomerate) and 12. marine greywacke and shale, (Ordovician – Silurian) Moffat shale facies. The trends described above indicate the presence of an inverse trend for elements grouped as high or low ranking in the PCA results. There is clear preliminary evidence for elements within the soil having an affinity and covarying above the various bedrock geology groups across the midlands study area which will be elaborated at the end of the discussion section. Machine Learning

The TELLUS midlands dataset is large enough to justify using machine learning (ML) techniques to test if geogenic radon class can be predicted using topsoil geochemistry. Four ML algorithms are tested, for Random Forest (RF), Logistic Regression (LR), Gaussian Process Regression (GPR) and a control model.

Model performance

The accuracy, precision, recall, f1-score and ROC-AUC results for RF, LR, GPR and the control machine learning model are reported in table 5.3. The GPR model is the most accurate (74.1%), followed by LR (73.9%) and RF (73.3%), although the accuracies of these models are within uncertainty of one another (table 5.3). The GPR, LR and RF models are significantly more accurate compared to the control model accuracy (50.2%).

Table 5.3 Accuracy, Precision, Recall, f1-score and ROC-AUC results for Random Forest, Logistic Regression, Gaussian Process Regression and the control machine learning model. Values reported in parentheses '( )' refer to the standard deviation.

Model type	Accuracy (Stdev) %	Precision	Recall	F1 - score	ROC-AUC
Random Forest	73.3 (4.3)	74.8 (4.4)	73.3 (4.3)	72.9 (4.5)	0.81 (0.05)
Logistic Regression	73.9 (3.6)	76.4 (3.8)	73.9 (3.6)	73.3 (3.6)	0.8 (0.04)
Gaussian Process Regression	74.1 (3.6)	75.5 (3.9)	74.1 (3.7)	73.8 (3.7)	0.81 (0.04)
Control	50.2 (2.8)	50.2 (2.8)	50.2 (2.8)	50.2 (2.8)	0.5 (0.0)

The average true positive, true negative, false positive and false negative results from each model were used to compute a simplified confusion matrix (table 5.4). The type I and type II error percentages are reported in the parentheses in table 5.4. Type I errors (false positives) represent samples that were mistakenly classified in a high GRP class. Type II errors (false negatives) occur when a model misclassifies a high-risk GRP sample as being in the low-risk GRP class.

The type I error is lowest in the LR model (22%), followed by GPR (23%) and RF (32%). The control model has the highest rate of type I and type II errors (49.9%). The RF model has the lowest rate (23%) of type II errors followed by GPR (29%) and LR (29.4%). Overall, the percentage of correctly classified samples is consistently higher in the GPR model (73.9%), LR (73.7%) and RF (72.8%) algorithms compared to the control model (50.1%) (table 5.4). Models chosen for low type I errors would minimize the amount of resources spent on targeting low geogenic radon areas which are mistakenly classified as high. Whereas a model with the lowest type II error, would be the most effective for targeting areas associated with a higher geogenic radon potential probability. There are pros and cons to using each model. However, the GPR model overall has a stronger classification performance.

*Table 5.4 Confusion matrix results for Random Forest, Gaussian Process Regression, Logistic Regression and a Control model applied to classifying topsoil samples into Geogenic Radon Potential class 1 (representing an average 6.1% probability of indoor radon concentration being above the 200 Bq m^{-3} reference level) and class 2 (representing an average 16.9% probability of indoor radon concentration being above the reference level). The asterix '*Type I' refers to the percentage rate of false positives, while '**Type II' refers to the percentage rate of false negatives.*

Model	Confusion matrix	Predicted GRP class 1	Predicted GRP class 2
Random Forest	GRP class 1	13330 (68%)	6170 (32%) *Type I
	GRP class 2	4424 (23%) **Type II	15076 (77%)
	Percentage of samples correctly classified: 72.8%		
Gaussian Process Regression	GRP class 1	13198 (77%)	3886 (23%)
	GRP class 2	6302 (29%)	15614 (71%)
	Percentage of samples correctly classified: 73.9%		
Logistic Regression	GRP class 1	12930 (77.8%)	3682 (22.2%)
	GRP class 2	6570 (29.4%)	15818 (70.6%)

	Percentage of samples correctly classified: 73.7%		
Control model	GRP class 1	13742 (50.1%)	13670 (49.9%)
	GRP class 2	13498 (49.9%)	13570 (50.1%)
	Percentage of samples correctly classified: 50.1%		

Feature importance

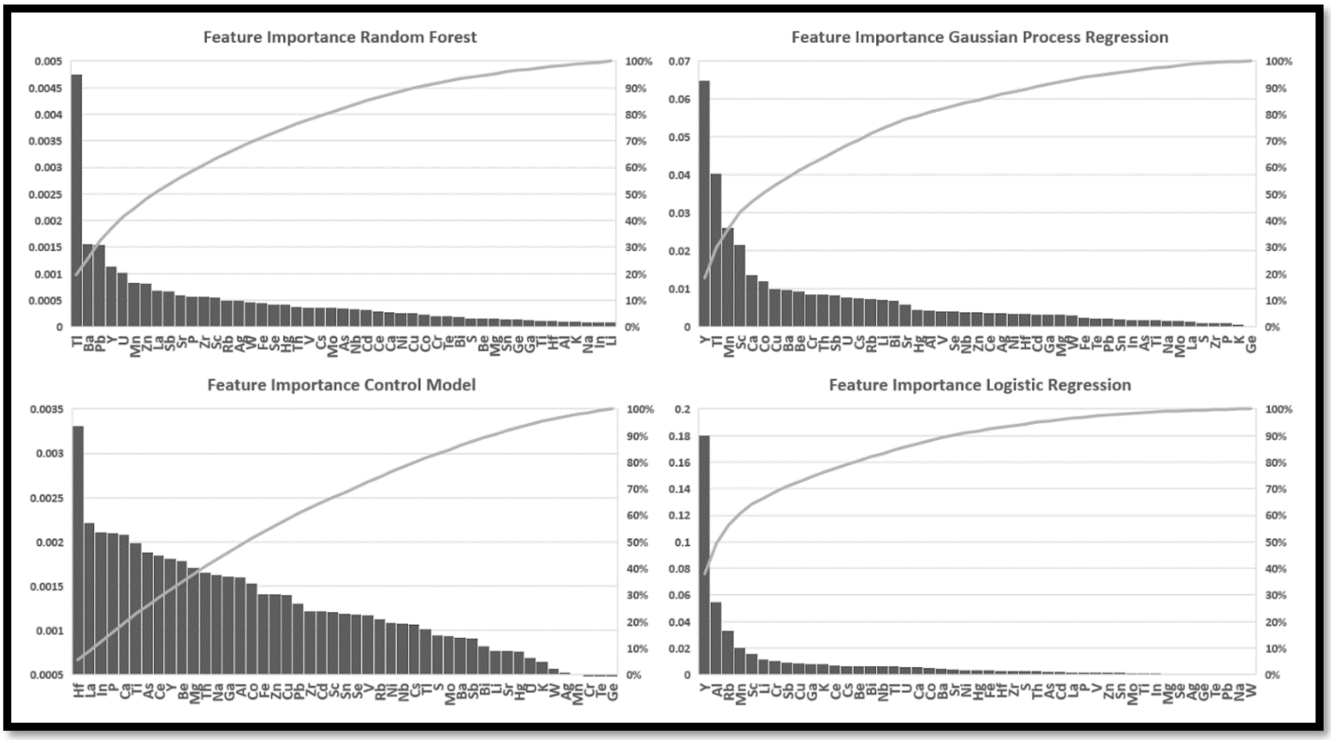

Figure 5.9 Feature importance for each of the four machine learning models, random forest, gaussian process regression, the control model and logistic regression.

The feature importance is calculated for each of the four models using sklearn libraries in python (fig.5.9). The LR, RF and GPR models show a pattern of elements that rank among the most important features in at least two models (fig.5.9); these elements include Y, Tl, Mn, Sc, Ba, Sb, Th, Cr and Ca. Some elements are ranked as important features in individual models. For instance, random forest also ranks Pb, U, Zn, Sr, P and Zr among the important features, gaussian process regression additionally ranks Co, Cu, Be highly, whereas logistic regression includes Al, Rb, Li among its most important features (fig.5.9). There are several elements which are consistent with ANOVA results showing positive correlation to geogenic radon class such as Cr, Co, Y, Tl, Al, Rb, Sr, Se. Furthermore, the feature importance results output elements that consistently covary and correlate together on univariate and multivariate analysis; reinforcing that the topsoil geochemistry is intrinsically linked to geogenic radon variation.

5.3.3 Irish midlands (TELLUS) – regional data used to test local scale data from Castleisland Co. Kerry.

The Irish midlands topsoil dataset was adjusted to contain only the elements present in the Castleisland, Co. Kerry dataset; in order to test the viability of using a model trained on regional scale data from the Irish midlands, to test topsoil data from a different geological region in Castleisland, Co. Kerry. Two of the highest accuracy machine learning models, logistic regression and Gaussian process regression are chosen for this purpose (table 5.5). The same ML process is followed using 5-fold spatial cross-validation repeated 10 times.

Model performance

The average model performance of logistic regression and Gaussian process regression is marginally less accurate when omitting elements that are not present in the Castleisland dataset (table 5.5). However, the average model performance is still within standard deviation of the models trained using the complete TELLUS dataset. The ROC-AUC is greater than 0.8 for both logistic regression and Gaussian process regression (*supp.matt 7.2.15*). To add, the rate of type I and type II errors and percentage of correctly classified samples are within margin of the models trained using the complete TELLUS topsoil geochemistry dataset (table 5.6).

Table 5.5 Accuracy, Precision, Recall, f1-score and ROC-AUC results for Random Forest, Logistic Regression, Gaussian Process Regression and the control machine learning model. Values reported in parentheses '( )' refer to the standard deviation.

Model type	Accuracy (Stdev) %	Precision	Recall	F1 - score	ROC-AUC

Logistic Regression	72.3 (5.3)	75.2 (8.1)	72.3 (5.3)	71 (7.5)	0.8 (0.06)
Gaussian Process Regression	73.1 (4.9)	74.9 (4.3)	73.1 (4.9)	72.5 (5.5)	0.81 (0.05)

*Table 5.6 Confusion matrix results for Random Forest, Gaussian Process Regression, Logistic Regression and a Control model applied to classifying topsoil samples into Geogenic Radon Potential class 1 (representing an average 6.1% probability of indoor radon concentration being above the 200 Bq m^{-3} reference level) and class 2 (representing an average 16.9% probability of indoor radon concentration being above the reference level). The asterix '*Type I' refers to the percentage rate of false positives, while '**Type II' refers to the percentage rate of false negatives.*

Model	Confusion matrix	Predicted GRP class 1	Predicted GRP class 2
Gaussian Process Regression	GRP class 1	13170 (75.4%)	4298 (24.6%)
	GRP class 2	6330 (29.4%)	15202 (70.6%)
	Percentage of samples correctly classified: 72.7%		
Logistic Regression	GRP class 1	12208 (78.7%)	3308 (21.3%)
	GRP class 2	7246 (31%)	16146 (69%)
	Percentage of samples correctly classified: 72.9%		

Feature importance

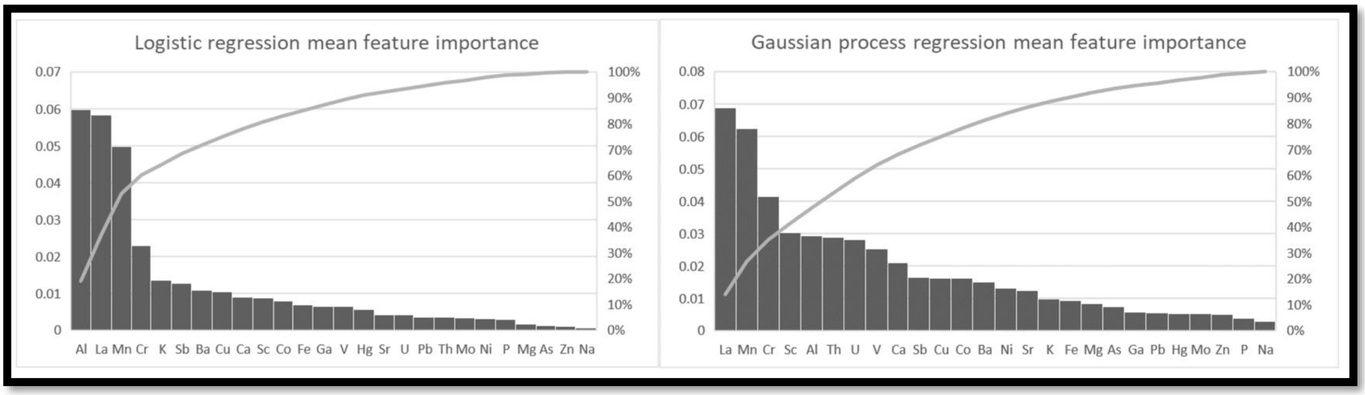

Figure 5.10 Mean feature importance from models trained on TELLUS Midlands shallow topsoil geochemistry limited to elements measured in Castleisland Co. Kerry. (a) Logistic regression (LR) and Gaussian process regression (GPR).

Both logistic regression and Gaussian process regression models include elements Al, La, Cr and Mn among the most important features (fig.5.10). Logistic regression also ranks K, Sb, Ba and Cu highly; whereas Gaussian process regression also includes Sc, Th, U, V and Ca as important features (fig.5.10).

Comparing the TELLUS ANOVA results (*supp.matt. 7.2.10*) with the importance features above demonstrates that the commonly ranked elements (Cr, Al, La and V) are relatively highly correlated to geogenic radon. GPR includes more elements correlated to geogenic radon (Th, Sc and V)) than the LR model , when only considering the elements ranking in either LR or GPR. Several elements such as La, Ba, V, U, Cu, Sb are consistent with elements highly correlated with soil-gas radon in Castleisland, Co. Kerry. To add, the important features Ca, K, Th and Cr are negatively correlated with soil-gas radon measured from Castleisland, Co Kerry. The result of certain elements consistently reoccurring when testing for geochemical link to geogenic radon demonstrates that the geochemical composition of soil may be indicative of geogenic radon class. Specifically, if there is a relatively higher concentration of radon-prone elements (i.e. La, Ba, U, V, Cu, Sb) in a soil sample then the soil may be acting as a source of radon. Conversely, if elements negatively correlated to geogenic radon (i.e. Ca, K, Th, Cr) are present in higher concentrations in the soil then it would be expected that the soil geochemistry is not acting as a source of radon.

Model verification

The Castleisland topsoil dataset was tested on the highest accuracy model which is the Gaussian process regression model (73.1%). To elaborate, topsoil samples from Castleisland were input to the model where each sample was assigned to class 1 or class 2 according to the Gaussian process regression model trained using the TELLUS midlands topsoil geochemistry. The average soil-gas radon for the Castleisland topsoil samples predicted to be in class 1 or class 2 are significantly different, 74.8 k Bqm^{-3} and 174.4 k Bqm^{-3} respectively (*supp.matt 7.2.16*). The aforementioned result indicates that a model trained using data from a certain geological region, (i.e. Irish Midlands), can be extrapolated and used to classify soil samples collected from a different geological region, (i.e. SW Ireland). However, the model could be improved since it only obtains 73.1% accuracy and misclassification occurs as reported in the confusion matrix (table 5.6).

Geochemical soil samples indicate if the soil is prone to being a source of radon. Local and regional scale topsoil geochemistry is investigated for its viability as a geogenic radon mapping technique. The soil geochemistry is analysed for indications of radon-prone elements being statistically and spatially associated using PCA, cluster analysis and machine learning algorithms including random forest, logistic regression and Gaussian process regression.

Geological meaning of affinities

The affinities between shallow topsoil geochemistry and geogenic radon potential across the Irish Midlands is influenced by different geological processes. At any given location, the geochemistry of each topsoil sample is an integration of previous processes involved in rock formation, weathering processes, glacial processes and soil formation processes, and possibly anthropogenic processes. It is important to highlight that affinities between elements can change if chemical and physical parameters change. Starting from formation of bedrock geology areas underlain by the Leinster Granite are geochemically influenced by magmatic differentiation and crystal fractionation processes. For example, minerals formed in the Leinster Granites (Co. Wicklow SE Ireland) include muscovite ($(KAl_2(AlSi_3O_{10)}(OH)_2)$), microcline ($KAlSi_3O^8$), plagioclase feldspar ($(Ca, Na)(AlSi_3O_8)$), pyroxenes ($(Mg, Fe, Li, Ca, Na,)(Al, Fe, Cr, Ti, Mg, Fe, Mn)(Si, Al, Fe)_2O_6$) and accessary minerals tourmaline ($(Ca,K,Na)(Al,Fe,Li,Mg,Mn)_3 (Al,Cr,Fe,V)_6(BO_3)_3(Si,Al,B)_6O_{18}(OH,F)$), apatite ($Ca_5(PO_4)$), zircon (ZrSiO4), titanite ($CaTiSiO_5$), cassiterite (SnO_2), beryl ($Be_3Al_2Si_6O_{18}$) and rutile (TiO_2)

(Bruck, 1968; O'Connor and Brück, 1978; Roycroft, 1989). Sunsequent residual magmas of the Wicklow granites (SE Ireland), with possible addition of water, produced the Leinster pegmatites with lithium rich minerals that have distinct geochemical signatures compared to the granitoids; including spodumene ($LiAl(SiO_3)_2$), muscovite, alkali feldspar ($(K,Na)AlSi_3O_8$), microcline and high concentrations of Li, Rb and Cs (Barros and Menuge, 2016; Luecke, 1981). The above minerals formed during development of the Leinster Granite highlighting that certain elements covary together (i.e. Li and Rb in spodumene, Li, Al, V, Na, Cr, in tourmaline, Ca and P in apatite, Be and Al in beryl), in magmatic environments. Subsequent chemical weathering, glacial processes, and soil formation processes may modify geochemical signatures in soil minerals which contain components of Leinster Granite lithologies. For instance, TELLUS Midlands topsoils include areas underlain by the Leinster Granite and associated pegmatites, however the covariation between alkali metals Li and Rb (Pearson r value 0.73) or transition elements Cr and V (Pearson r value 0.85) found in the topsoils is not diagnostic of the Leinster Granite.

To elaborate, lithium and rubidium can be adsorbed to clay surfaces in shales or incorporated by isomorphous substitution of magnesium or iron; and is retained during diagenetic process changing kaolinite ($Al_2Si_2O_5(OH)_4$) to illite ($(K,H_3O)(Al,Mg,Fe)_2(Si,Al)_4O_{10}[(OH)_2(H_2O)]$) or chlorite ($(Mg,Fe)_3(Si,Al)_4O_{10}(OH)_2 \cdot (Mg,Fe)_3(OH)_6$) in marine environments (Horstman, 1957; Reynolds Jr, 1963; Starkey, 1982). Whereas, in granitoids, Li and Rb relate to the fractional crystallisation of residual magmas creating Li, Rb enriched spodumene and lepidolite minerals (Barros and Menuge, 2016; Horstman, 1957; Liu et al., 2022). Considering the Li and Rb correlation with high geogenic radon in the Midlands study area is located above limestone and shale Formations, it's reasonable that the covariance of Li and Rb is related to clay minerals within shales or impure limestones. However, an investigation of the mineralogy present in the topsoils would be necessary to confirm this hypothesis.

It is possible that physical weathering and leaching of the granites could be the potential source of Li, Cs and Rb covariation observed in the high geogenic radon regions (i.e. above the bedrock Formations in the east of the study area and in tills derived from limestones and tills derived from Silurian and Namurian sandstones and shales). It's possible these [Li, Rb, Cs] element affinities within soils correlating to higher geogenic radon potential areas are due to clay minerals illite and chlorite, which are reported to incorporate traces of radon precursor elements uranium and radium by adsorption in phosphorous-rich environments (Benedicto et al., 2014; Kim et al., 2017; Liao et al., 2020; Mei et al., 2022; Ticknor, 1998).

Confirming the geological meaning of element affinities within the topsoil would require knowing the minerals present, along with petrographic microscopy to identify textures and characteristics of minerals, to gain insight to the geological processes and controls responsible for the geochemical affinities. Elements can covary together within minerals that form in different lithological settings. For example, chlorite can be found in relation to sedimentary (e.g. adsorption with sandstone and clay deposits), igneous (e.g. hydrothermal chlorite alteration of phyllosilicates including biotite) and metamorphic processes (e.g. greenschist formation) (Liao et al., 2020; Murakami et al., 1996; Worden et al., 2020; Zane et al., 1998). Future research using XRD to determine mineralogy content would be necessary to progress understanding of the geological processes influencing covariations between topsoil elements, and their relation to the geogenic radon.

The affinity between Co with Ni (0.85), Cr (0.68) and V (0.62) in high geogenic regions could be related to sulphide, ferromagnesian and oxide minerals. For example, Ni and Co can covary together in Siegenite ($(Ni,Co)_3S_4$), pyrrhotite ($Fe_{(1-x)}S$) or pentilandite ($(Fe,Ni)_9S_8$) as stoichiometric lattice substitutions in hydrothermal sulphide deposits or Ni, Co, along with Cr and V can be adsorbed onto fine-grained inorganic particles (Jansson and Liu, 2020; Kovalev et al., 2014; Loring, 1976). As such, it is possible for covariances between Ni, Co, V, Cr and V to form as a result of different geological processes. However, considering the geology underlying Co, Ni, V and Cr covariances is dominated by sedimentary lithologies, it is likely the [Co, Ni, V, Cr] affinity relates to sedimentary processes, namely adsorption onto clay Formations or shale layers within limestones. However, the Navan Zn-Pb deposit in Co. Meath, that formed as a result of hydrothermal sulphides interacting with carbonate host lithologies, could contribute to the Co, Ni and Fe affinity (Ashton et al., 1980; Johnston et al., 2013; Marks et al., 2017; Yesares et al., 2019). The latter highlights that heterogenous geological processes across the Midlands study area could be contributing to the affinity between elements. Considering the primary lithologies that underly high geogenic radon areas are sedimentary, the covariance between Cr, V, Co and Ni are more likely explained by sedimentary processes, such as adsorption onto fine grained detrital particles. As such, it is important to consider that covariance of element pairs are influence by a range of different geological processes, and that it is not always possible to link covariance of elements in soil with that of the underlying bedrock geology (especially without mineralogical and petrographic data).

The PC1 Score map superimposed in the 1:100k bedrock map (figure 5.7) displays an affinity between high loadings (red on figure 5.7) in soils located above various limestone lithologies in the west of the Midlands study area including the Ballymore limestone Formation (Dark fine-grained limestone and shale), Undifferentiated Visean limestones and the Boyle Sandstone Formation (Sandstones and red-green conglomerates), and the highest PC1 loadings above the Galway granites, the Wicklow granites (figure 5.3). The affinity between low geogenic radon potential and high PC1 loading elements, including Se, S and Hg may be caused by heterogeneous mineralization processes linked to underlying bedrock geology.

For instance, Se, S and Hg can mineralise as HgS (metacinnabar) – HgSe (tiemannite) series in volcanogenic/seafloor massive sulphide environments (Belogub et al., 2020; Fallon et al., 2019; Liu et al., 2017; Vasil'ev, 2011). To add, selenium can occur in significant quantities in pyrite (FeS_2), ferroselite ($FeSe_2$) marcasite (FeS_2), and clausthalite (PbSe) related to shale or sandstone deposits with sulphide mineralisation, where Se commonly substitutes for S (Coleman and Delevaux, 1957; Long et al., 2016; Ryser et al., 2005). However, the affinity [of Se, Hg, S] in soils above the Galway and Wicklow granites is likely related to weathering of iron-rich or selenide minerals (i.e. biotite ($K(Mg,Fe)_3AlSi_3O_{10}(F,OH)_2$), ferroselite ($FeSe_2$), tiemannite (HgSe)) (Howard III, 1977; Iida et al., 2011; Koljonen, 1976; Malisa, 2001; Wells, 1967). The Se, S and Hg affinity in soils above the Ballymore Limestone Formation or Boyle Sandstone Formation, in the west of the TELLUS Midlands, is likely related to sedimentary processes of adsorption onto fine-grained particles or sorption onto certain minerals during diagenesis, within shale, sandstone or limestone Formations (Iida et al., 2011; Long et al., 2016; McGrath et al., 2008; Naftz and Barclay, 1991; Ochoa-González et al., 2013; Wells, 1967). Selenium enrichment is reported for the Namurian shales in Ireland, along with covariation of selenium with radon precursor uranium and trace elements Cu, Cd, Ni, Co, Mo and Te (Armstrong et al., 2019; Gallagher et al., 2022; Parnell et al., 2016). Black shales from other Formations report enrichment in Se, Hg, Mo and U (Jiang et al., 2006).

The anomalously high soil-gas radon in the Castleisland study area occurs in soils above the Clare shales and in the proximity of till derived from Namurian Sandstones, Siltstones and Shales (Banríon et al., 2022). The affinity between Mo, Ba, V, Cu, U, Sb, P and La in soils from the high soil-gas radon area in Castleisland, is reasonably related to the underlying Clare Shale bedrock lithology. Phosphate deposits containing collophane ($Ca_5(PO_4)_3 . (OH,F,Cl)$) and fluorapatite ($Ca_5(PO_4)_3F$) minerals within the Clare Shales may explain the covariation of phosphate with the area of extremely elevate soil-gas radon (MacDermot et al., 2003). The

Namurian shales are reported to contain enrichments of redox-sensitive elements including V, U, Cu, Ba and Mo (Armstrong et al., 2019; Jones and Plant, 1989; Park et al., 2010; Thomson, 1971). Black shales from other Formations contain enrichments of Mo, Cr, U, V, Sb, Cu, Ba, Y, Sr and La (Armstrong et al., 2023; Fan et al., 2004; Fyffe and Pickerill, 1993; Jiang et al., 2006; Yu et al., 2003). The anomalously high soil-gas radon in Castleisland correlates with elevated U concentrations up to 37.2 mg kg^{-1}, which is considerably higher than the 2 mg kg^{-1} median value for the Castleisland study area (table 7.2.1). The occurrence of uranium in black shales can be simplified to two process (a) the deposition of uranium in the ocean and (b) the redox-conditions of the ocean influencing U sorption (Partin et al., 2010). The affinity for U with Mo, V, Sb, Ba, P, Cu, Sr, and La likely relates to their tendency to accumulate under anoxic conditions in Black Shale Formations (Algeo and Maynard, 2004; Elbaz-Poulicheet et al., 1997; Jiang et al., 2007; Mehta and Kocar, 2019; Wang et al., 2023; Zhongcheng and Guizhi, 1991).

Soil-gas radon samples with the lowest concentrations were collected from till derived from limestones and above various limestone lithologies, including the Rockfield limestones and Waulsortian limestones (Banríon et al., 2022). The covariance of Mg, Al, Fe and Na in the low soil-gas radon areas is likely related to clay or silicate minerals resulting from carbonate weathering including smectite ($(Ca,Mg)_{0.33}$ + Al_2 $Si_{3.67}$ $Al_{0.33}$ O_{10} OH_2), kaolinite (Al4Si4O10(OH)8), goethite (FeO(OH)) or glauconite ($(K,Na)(Fe,Al,Mg)_2(Si,Al)_4O_{10}(OH)_2$) (Massoud et al., 2023; Robinson, 1980; Ross and Hendricks, 1945). Trace minerals including chlorite ($(Mg,Fe)_3(Si,Al)_4O_{10}(OH)_2 \cdot (Mg,Fe)_3(OH)_6$), albite ($NaAlSi_3O_8$) and halite (NaCl) have been reported for Limestone Formations which could further explain the affinity of these [Mg, Al, Fe, Na] elements in areas underlain by Carboniferous limestones in the low soil-gas radon area of Castleisland (Carroll and Hathaway, 1953; Decima et al., 1988; MOLENAAR and de JONG, 1987; Wunsch et al., 2014).

To conclude, heterogenous geological controls exists across the two perspective study areas (TELLUS Midlands and Castleisland, Co. Kerry), which contribute to geochemical affinities within the topsoil samples and their link to geogenic radon variation. In the Midlands study area, certain lithologies are more dominant, i.e. Devonian (Galway and Wicklow) granites, Variscan limestones/Lucan Formation/Waulsortian limestones/Namurian and Silurian sandstones and shales, However, there are distinct differences in geological processes involved in the formation of these different rock types, and there are potentially different controls on processes influencing topsoil geochemistry occurring at local scales within the study area i.e. spatially restricted enrichment in Pb-Zn. Due to the fact that areas of high geogenic radon in the TELLUS Midlands are not spatially associated with the Leinster and Galway granites, it can be deduced that geological controls on topsoil element covariances to geogenic radon risk are most likely dominated by sedimentary processes. Specific mineralogical analysis, i.e. petrography and provenance studies, on bedrock and soil samples from the two perspective study areas is necessary to verify the geological processes influencing topsoil geochemical affinities and their link to geogenic radon flux.

Limitations

There are some discrepancies between the feature importance from various models, highlighting that the feature importance may be calculated slightly differently depending on the model type. For example, random forest calculates important features using information from the mean decrease gini/impurity decrease of each feature; whereas, linear models utilize coefficients from each input variable. Although the machine learning algorithms explored in this study show promising results for future model development, the model results are based on the average results of multiple iterations of spatially cross-validated data. Ideally, only one model should be used for identifying radon-prone soil samples. However, the results presented in this study show that machine learning techniques applied to soil geochemistry provide a viable alternative for understanding radon risk.

5.4 Conclusion

Exposure to indoor radon gas is a major contributor to lung cancer globally (Gaskin et al., 2018; World Health Organization, 2009), and it is in interest of human wellbeing to provide rigorous research aimed at understanding natural radon distribution. Considering soil-gas is the main contributor to indoor radon, our study sets out to investigate if topsoil geochemistry (a) share a correlation with geogenic radon, and (b) if radon-prone elements covary together geospatially at local and regional scales. Multiple methods of analysing data are used to investigate the extent topsoil geochemistry can be used to understand geogenic radon distribution. Elements that are relatively more correlated with geogenic radon consistently group together when comparing PCA and cluster analysis results for both local scale (Castleisland, Co. Kerry) and regional scale data (TELLUS Midlands). The feature importance from several machine learning algorithms designed to test the relation of topsoil geochemistry to geogenic radon, reinforce the hypotheses that topsoil geochemistry can be indicative of geogenic radon. In particular, Y, U, Ba, V, La, Sb, Mo, Cu are elements commonly associated with elevated geogenic radon at local and/or regional scales. Additionally, Ca, Na, K, S are among elements frequently negatively correlated with geogenic radon. The results demonstrate the value that local and regional topsoil geochemical surveys can have in determining radon prone areas. The analytical approach used in this paper contributes a robust and novel method for extracting useful information from topsoil geochemical data. Machine learning results demonstrate a rigorous method for testing and interpreting large datasets (> 1000 samples) applied to geogenic radon studies, although the methodologies are also applicable to other areas of research such as resource exploration (i.e. topsoil geochemistry applied to predicting underlying bedrock opposed to geogenic radon).

Overall, this study contributes to the understanding of geogenic radon distribution in that topsoil geochemistry varies geospatially in relation to geogenic radon. As such the methods presented here can be used to map and investigate if an area is prone to geogenic radon.

5.5 Role of Funding source

The partial SUSI grant provided to for Méabh Banríon's Ph.D. had no involvement or role in the study design, the collection, analysis and interpretation of data; in writing of the report; and in the decision to submit the article for publication.

The ICPMS analysis of the Castleisland Co. Kerry soil samples was carried out by BV laboratory in Vancouver Canada, sponsored by Association of Applied Geochemists. The in-kind analytical support did not play a role in the study design, collection, sample preparation, processing of results, interpretation or writing of the report.

5.6 Declaration of competing interests

The authors declare that they have no known competing financial interests or personal relationships that could have appeared to influence the work reported in this paper.

5.7 Acknowledgements

We are thankful for the in-kind analytical support provided for the Castleisland soil sample ICPMS analysis by the Association of Applied Geochemists in collaboration with Bureau Veritas Commodities Canada (BVCC) laboratory in Vancouver, Canada.

This research contains Irish Public Sector Data (Geological Survey Ireland) licensed under a Creative Commons Attribution 4.0 International (CC BY 4.0) licence. Specially, the TELLUS midlands topsoil geochemistry dataset was used (file name: 58xxxxA-65xxxxA_Shallow_Topsoil_Download_v1.1, https://www.gsi.ie/en-ie/data-and-maps/Pages/Geochemistry.aspx)

We would like to thank Winifred Duncan for her assistance in preparing the Castleisland soil samples for analysis. Méabh H. Banríon would like to thank Student Universal Support Ireland (SUSI) for partially funding their Ph.D.

5.8 References

Abdi, H., Williams, L.J., 2010. Principal component analysis. Wiley interdisciplinary reviews: computational statistics 2, 433–459.

Aditya, C.R., Deshmukh, C.R., Nayana, D.K., Vidyavastu, P.G., 2018. Detection and prediction of air pollution using machine learning models. International Journal of Engineering Trends and Technology (IJETT) 59, 204–207.

Aitchison, J., 1982. The statistical analysis of compositional data. Journal of the Royal Statistical Society: Series B (Methodological) 44, 139–160.

Algeo, T.J., Maynard, J.B., 2004. Trace-element behavior and redox facies in core shales of Upper Pennsylvanian Kansas-type cyclothems. Chemical geology 206, 289–318.

Armstrong, J., Parnell, J., Boyce, A., Perez, M., 2023. Trace element release from Bowland Shale into spring water, Lancashire. Geological Society, London, Special Publications 534, SP534-2022.

Armstrong, J.G.T., Parnell, J., Bullock, L.A., Boyce, A.J., Perez, M., Feldmann, J., 2019. Mobilisation of arsenic, selenium and uranium from Carboniferous black shales in west Ireland. Applied Geochemistry 109, 104401. https://doi.org/10.1016/j.apgeochem.2019.104401

Ashton, J., Black, A., Geraghty, J., Holdstock, M., Hyland, E., Bowden, A., Earls, G., O'Connor, P., Pyne, J., 1980. The geological setting and metal distribution patterns of Zn-Pb-Fe mineralization in the Navan Boulder Conglomerate. The Irish minerals industry 1990, 171–210.

Banríon, M., Elío, J., Crowley, Q., 2022. Using geogenic radon potential to assess radon priority area designation, a case study around Castleisland, Co. Kerry, Ireland. Journal of Environmental Radioactivity 251, 106956.

Barros, R., Menuge, J.F., 2016. The origin of spodumene pegmatites associated with the Leinster Granite in southeast Ireland. The Canadian Mineralogist 54, 847–862.

Belogub, E., Ayupova, N., Krivovichev, V., Novoselov, K., Blinov, I., Charykova, M., 2020. Se minerals in the continental and submarine oxidation zones of the South Urals volcanogenic-hosted massive sulfide deposits: A review. Ore Geology Reviews 122, 103500.

Benedicto, A., Missana, T., Fernández, A.M., 2014. Interlayer Collapse Affects on Cesium Adsorption Onto Illite. Environ. Sci. Technol. 48, 4909–4915. https://doi.org/10.1021/es5003346

Bernardo, J., Berger, J., Dawid, A., Smith, A., 1998. Regression and classification using Gaussian process priors. Bayesian statistics 6, 475.

Biau, G., Scornet, E., 2016. A random forest guided tour. Test 25, 197–227.

Bousquet, O., von Luxburg, U., Rätsch, G., 2011. Advanced Lectures on Machine Learning: ML Summer Schools 2003, Canberra, Australia, February 2-14, 2003, Tübingen, Germany, August 4-16, 2003, Revised Lectures. Springer.

Breiman, L., 2001. Random forests. Machine learning 45, 5–32.

Bruck, P., 1968. The geology of the Leinster granite in the Enniskerry-Lough Dan area, Co. Wicklow. Presented at the Proceedings of the Royal Irish Academy. Section B: Biological, Geological, and Chemical Science, JSTOR, pp. 53–70.

Carroll, D., Hathaway, J.C., 1953. Clay minerals in a limestone soil profile. Clays and clay minerals 2, 171–182.

Coleman, R.G., Delevaux, M.H., 1957. Occurrence of selenium in sulfides from some sedimentary rocks of the western United States. Economic geology 52, 499–527.

Colkesen, I., Sahin, E.K., Kavzoglu, T., 2016. Susceptibility mapping of shallow landslides using kernel-based Gaussian process, support vector machines and logistic regression. Journal of African Earth Sciences 118, 53–64.

Daviran, M., Maghsoudi, A., Ghezelbash, R., Pradhan, B., 2021. A new strategy for spatial predictive mapping of mineral prospectivity: Automated hyperparameter tuning of random forest approach. Computers & Geosciences 148, 104688. https://doi.org/10.1016/j.cageo.2021.104688

Decima, A., McKenzie, J., Schreiber, B., 1988. The origin of" evaporitive" limestones; an example from the Messinian of Sicily (Italy). Journal of Sedimentary Research 58, 256–272.

Degu Belete, G., Alemu Anteneh, Y., 2021. General Overview of Radon Studies in Health Hazard Perspectives. Journal of Oncology 2021.

Demšar, U., Harris, P., Brunsdon, C., Fotheringham, A.S., McLoone, S., 2013. Principal component analysis on spatial data: an overview. Annals of the Association of American Geographers 103, 106–128.

Dornan, T., O'Sullivan, G., O'Riain, N., Stueeken, E., Goodhue, R., 2020. The application of machine learning methods to aggregate geochemistry predicts quarry source location: An example from Ireland. Computers & Geosciences 140, 104495. https://doi.org/10.1016/j.cageo.2020.104495

Egozcue, J.J., Pawlowsky-Glahn, V., Mateu-Figueras, G., Barcelo-Vidal, C., 2003. Isometric logratio transformations for compositional data analysis. Mathematical geology 35, 279–300.

Elbaz-Poulicheet, F., Nagy, A., Cserny, T., 1997. The Distribution of Redox Sensitive Elements (U, As, Sb, V and Mo) along a River-Wetland-Lake System (Balaton Region, Hungary). Aquatic Geochemistry 3, 267–282. https://doi.org/10.1023/A:1009616214030

Elío, J., Crowley, Q., Scanlon, R., Hodgson, J., Long, S., 2017. Logistic regression model for detecting radon prone areas in Ireland. Science of The Total Environment 599–600. https://doi.org/10.1016/j.scitotenv.2017.05.071

Elío, J., Crowley, Q., Scanlon, R., Hodgson, J., Long, S., Cooper, M., Gallagher, V., 2020. Application of airborne radiometric surveys for large-scale geogenic radon potential classification. Journal of the European Radon Association.

Elío, J., Crowley, Q., Scanlon, R., Hodgson, J., Zgaga, L., 2018. Estimation of residential radon exposure and definition of Radon Priority Areas based on expected lung cancer incidence. Environment International 114, 69–76. https://doi.org/10.1016/j.envint.2018.02.025

Environmental Protection Agency, 2022. New EPA Radon maps show more homes and workplaces at risk from cancer-causing gas. https://www.epa.ie/news-releases.

Environmental Protection Agency, 2019. National Radon Control Strategy. Straiteis Naisiunta um Rialu Radoin. Phase 1 2014-2018.

Faanu, A., Darko, E., Ephraim, J., 2011. Determination of natural radioactivity and hazard in soil and rock samples in a mining area in Ghana. West African Journal of Applied Ecology 19.

Fallon, E.K., Frische, M., Petersen, S., Brooker, R.A., Scott, T.B., 2019. Geological, mineralogical and textural impacts on the distribution of environmentally toxic trace elements in seafloor massive sulfide occurrences. Minerals 9, 162.

Fan, D., Zhang, T., Ye, J., 2004. The Xikuangshan Sb deposit hosted by the Upper Devonian black shale series, Hunan, China. Ore Geology Reviews 24, 121–133.

Farhadi, S., Afzal, P., Boveiri Konari, M., Daneshvar Saein, L., Sadeghi, B., 2022. Combination of Machine Learning Algorithms with Concentration-Area Fractal Method for Soil

Geochemical Anomaly Detection in Sediment-Hosted Irankuh Pb-Zn Deposit, Central Iran. Minerals 12. https://doi.org/10.3390/min12060689

Fennell, S.G., Mackin, G.M., Madden, J.S., McGarry, A.T., Duffy, J.T., O'colmain, M., Colgan, P.A., Pollard, D., 2002. Radon in dwellings: the Irish National Radon survey. Radiological Protection Institute of Ireland Dublin.

Fu, C.-C., Yang, T.F., Chen, C.-H., Lee, L.-C., Wu, Y.-M., Liu, T.-K., Walia, V., Kumar, A., Lai, T.-H., 2017. Spatial and temporal anomalies of soil gas in northern Taiwan and its tectonic and seismic implications. Journal of Asian Earth Sciences 149, 64–77. https://doi.org/10.1016/j.jseaes.2017.02.032

Fyffe, L.R., Pickerill, R.K., 1993. Geochemistry of Upper Cambrian-Lower Ordovician black shale along a northeastern Appalachian transect. Geological Society of America Bulletin 105, 897–910.

Gallagher, V., Grunsky, E.C., Fitzsimons, M.M., Browne, M.A., Lilburn, S., Symons, J., 2022. Tellus regional stream water geochemistry: environmental and mineral exploration applications. Geochemistry: Exploration, Environment, Analysis 22, geochem2021-050.

Gaskin, J., Coyle, D., Whyte, J., Krewksi, D., 2018. Global Estimate of Lung Cancer Mortality Attributable to Residential Radon. Environmental Health Perspectives 126, 057009. https://doi.org/10.1289/EHP2503

Grunsky, E.C., 2010. The interpretation of geochemical survey data. Geochemistry: Exploration, Environment, Analysis 10, 27–74.

Grunsky, E.C., Caritat, P. de, 2019. State-of-the-art analysis of geochemical data for mineral exploration. Geochemistry: Exploration, Environment, Analysis 20, 217–232. https://doi.org/10.1144/geochem2019-031

Hastie, T., Tibshirani, R., Friedman, J.H., Friedman, J.H., 2009. The elements of statistical learning: data mining, inference, and prediction. Springer.

Hellmann, R., Wirth, R., Daval, D., Barnes, J.-P., Penisson, J.-M., Tisserand, D., Epicier, T., Florin, B., Hervig, R.L., 2012. Unifying natural and laboratory chemical weathering with interfacial dissolution–reprecipitation: A study based on the nanometer-scale chemistry of fluid–silicate interfaces. Chemical Geology 294–295, 203–216. https://doi.org/10.1016/j.chemgeo.2011.12.002

Horstman, E.L., 1957. The distribution of lithium, rubidium and caesium in igneous and sedimentary rocks. Geochimica et Cosmochimica Acta 12, 1–28.

Howard III, J.H., 1977. Geochemistry of selenium: formation of ferroselite and selenium behavior in the vicinity of oxidizing sulfide and uranium deposits. Geochimica et Cosmochimica Acta 41, 1665–1678.

Iida, Y., Tanaka, T., Yamaguchi, T., Nakayama, S., 2011. Sorption Behavior of Selenium (—II) on Rocks under Reducing Conditions. Journal of nuclear science and technology 48, 279–291.

Jansson, N.F., Liu, W., 2020. Controls on cobalt and nickel distribution in hydrothermal sulphide deposits in Bergslagen, Sweden - constraints from solubility modelling. GFF 142, 87–95. https://doi.org/10.1080/11035897.2020.1751270

Jiang, S.-Y., Chen, Y.-Q., Ling, H.-F., Yang, J.-H., Feng, H.-Z., Ni, P., 2006. Trace- and rare-earth element geochemistry and Pb–Pb dating of black shales and intercalated Ni–Mo–PGE–Au sulfide ores in Lower Cambrian strata, Yangtze Platform, South China. Mineralium Deposita 41, 453–467. https://doi.org/10.1007/s00126-006-0066-6

Jiang, S.-Y., Zhao, H.-X., Chen, Y.-Q., Yang, T., Yang, J.-H., Ling, H.-F., 2007. Trace and rare earth element geochemistry of phosphate nodules from the lower Cambrian black shale sequence in the Mufu Mountain of Nanjing, Jiangsu province, China. Chemical Geology 244, 584–604.

Johnston, J., Raub, T., Ashton, J., 2013. Mineral magnetism identifies the presence of pyrrhotite in the Navan Zn-Pb deposit, Ireland: implications for low temperature pyrite to pyrrhotite reduction, timing of mineralization and future exploration strategies. Mineral deposit research for a hi-tech world, Uppsala 323–325.

Jones, D., Plant, J., 1989. Geochemistry of shales. Springer.

Kanagawa, M., Hennig, P., Sejdinovic, D., Sriperumbudur, B.K., 2018. Gaussian processes and kernel methods: A review on connections and equivalences. arXiv preprint arXiv:1807.02582.

Khan, F., Khattak, S.A., Wazir, Z., Waqas, M., 2021. Spatial distribution of radon concentrations in Balakot-Bagh (B–B) Fault Line and adjoining areas, Lesser Himalayas, North Pakistan. Environmental Earth Sciences 80, 291. https://doi.org/10.1007/s12665-021-09569-8

Kim, E., Ahn, H., Jo, H.Y., Ryu, J.-H., Koh, Y.-K., 2017. Chlorite alteration in aqueous solutions and uranium removal by altered chlorite. Journal of hazardous materials 327, 161–170.

Kirasich, K., Smith, T., Sadler, B., 2018. Random forest vs logistic regression: binary classification for heterogeneous datasets. SMU Data Science Review 1, 9.

Koljonen, T., 1976. Luikolahti: Selenium in the vicinity of copper ore. Journal of Geochemocal Exploration 5, 263–265.

Kovalev, SG, Puchkov, V., Kovalev, SS, 2014. First findings of siegenite (CoNi 2 S 4) in picritic and picrodoleritic complexes of the Southern Urals. Presented at the Doklady Earth Sciences, Springer, pp. 796–802.

Lewin, J., Gibbard, P.L., 2010. Quaternary river terraces in England: Forms, sediments and processes. Geomorphology 120, 293–311. https://doi.org/10.1016/j.geomorph.2010.04.002

Liao, R., Shi, Z., Chen, Y., Zhang, J., Wang, X., Hou, Y., Zhang, K., 2020. Characteristics of uranium sorption on illite in a ternary system: effect of phosphate on adsorption. Journal of Radioanalytical and Nuclear Chemistry 323, 159–168.

Lin, H.-T., Liu, F.-C., Wu, C.-Y., Kuo, C.-F., Lan, W.-C., Yu, H.-P., 2019. Epidemiology and Survival Outcomes of Lung Cancer: A Population-Based Study. BioMed Research International 2019, 8148156. https://doi.org/10.1155/2019/8148156

Liu, J., Rong, Y., Zhang, S., 2017. Mineralogy of Zn–Hg–S and Hg–Se–S Series Minerals in Carbonate-Hosted Mercury Deposits in Western Hunan, South China. Minerals 7, 101.

Liu, Y., Ma, B., Lv, Y., Wang, C., Chen, Y., 2022. Thorough extraction of lithium and rubidium from lepidolite via thermal activation and acid leaching. Minerals Engineering 178, 107407.

Long, J.A., Large, R.R., Lee, M.S., Benton, M.J., Danyushevsky, L.V., Chiappe, L.M., Halpin, J.A., Cantrill, D., Lottermoser, B., 2016. Severe selenium depletion in the Phanerozoic oceans as a factor in three global mass extinction events. Gondwana Research 36, 209–218.

Loring, D.H., 1976. Distribution and partition of cobalt, nickel, chromium, and vanadium in the sediments of the Saguenay fjord. Can. J. Earth Sci. 13, 1706–1718. https://doi.org/10.1139/e76-180

Lowe, J.J., Walker, M., 2014. Reconstructing quaternary environments. Routledge.

Luecke, W., 1981. Lithium pegmatites in the Leinster Granite (southeast Ireland). Chemical Geology 34, 195–233. https://doi.org/10.1016/0009-2541(81)90113-3

MacDermot, C., McConnell, B., Pracht, M., 2003. Bedrock geology 1: 100, 000 Sacle map series, sheet 14, Galway Bay. Geological Survey of Ireland, Dublin.

Malisa, E.P., 2001. The Behaviour of Selenium in Geological Processes. Environmental Geochemistry and Health 23, 137–158. https://doi.org/10.1023/A:1010908615486

Marks, F.R., Menuge, J.F., Boyce, A.J., Blakeman, R.J., 2017. Controls on the formation of a large Zn-Pb Irish-type deposit: evidence from the Navan halo. Programme and 61.

Massoud, A., Abdou, F.S., Yousif, M., 2023. Evaluation of mineral compositions of surface and subsurface rock samples by neutron activation analysis. International Journal of Environmental Analytical Chemistry 103, 528–545. https://doi.org/10.1080/03067319.2020.1862095

McGrath, D., Fleming, G.A., Culleton, N., 2008. Trace elements and heavy metals in Irish soils. Teagasc, Wexford, Ireland 210.

McKinley, J.M., Grunsky, E., Mueller, U., 2018. Environmental monitoring and peat assessment using multivariate analysis of regional-scale geochemical data. Mathematical Geosciences 50, 235–246.

Mehta, N., Kocar, B.D., 2019. Geochemical conditions conducive for retention of trace elements and radionuclides during shale–fluid interactions. Environmental Science: Processes & Impacts 21, 1764–1776.

Mei, H., Aoyagi, N., Saito, T., Kozai, N., Sugiura, Y., Tachi, Y., 2022. Uranium (VI) sorption on illite under varying carbonate concentrations: Batch experiments, modeling, and cryogenic time-resolved laser fluorescence spectroscopy study. Applied Geochemistry 136, 105178. https://doi.org/10.1016/j.apgeochem.2021.105178

Molenaar, N., de Jong, A.F.M., 1987. Authigenic quartz and albite in Devonian limestones: origin and significance. Sedimentology 34, 623–640. https://doi.org/10.1111/j.1365-3091.1987.tb00791.x

Mueller, U., Delgado, R.T., Grunsky, E.C., McKinley, J.M., 2020. Biplots for compositional data derived from generalized joint diagonalization methods. Applied Computing and Geosciences 8, 100044.

Murakami, T., Isobe, H., Sato, T., Ohnuki, T., 1996. Weathering of chlorite in a quartz-chlorite schist: I. Mineralogical and chemical changes. Clays and Clay Minerals 44, 244–256.

Naftz, D.L., Barclay, C.V., 1991. Selenium and associated trace elements in soil, rock, water and streambed sediment of the proposed Sandstone Reservoir, south-central Wyoming. US Department of the Interior, US Geological Survey.

Nathwani, C.L., Wilkinson, J.J., Fry, G., Armstrong, R.N., Smith, D.J., Ihlenfeld, C., 2022. Machine learning for geochemical exploration: classifying metallogenic fertility in arc magmas and insights into porphyry copper deposit formation. Mineralium Deposita. https://doi.org/10.1007/s00126-021-01086-9

Ochoa-González, R., Díaz-Somoano, M., Martínez-Tarazona, M.R., 2013. Influence of Limestone Characteristics on Mercury Re-emission in WFGD Systems. Environ. Sci. Technol. 47, 2974–2981. https://doi.org/10.1021/es304090e

O'connor, P., Brück, P., 1978. Age and origin of the Leinster Granite. Journal of Earth Sciences 105–113.

Park, M., Chon, H.-T., Marton, L., 2010. Mobility and accumulation of selenium and its relationship with other heavy metals in the system rocks/soils–crops in areas covered by black shale in Korea. Journal of Geochemical Exploration 107, 161–168.

Parnell, J., Brolly, C., Spinks, S., Bowden, S., 2016. Selenium enrichment in Carboniferous Shales, Britain and Ireland: Problem or opportunity for shale gas extraction? Applied Geochemistry 66, 82–87.

Partin, C., Bekker, A., Scott, C., Gill, B., Lyons, T., 2010. Uranium in shales as a proxy for the evolution of surficial redox conditions. GeoCanada 2010: Abstract.

Pereira, A., Godinho, M., Neves, L., 2010. On the influence of faulting on small-scale soil-gas radon variability: a case study in the Iberian Uranium Province. Journal of environmental radioactivity 101, 875–882.

Petermann, E., Meyer, H., Nussbaum, M., Bossew, P., 2021. Mapping the geogenic radon potential for Germany by machine learning. Science of The Total Environment 754, 142291. https://doi.org/10.1016/j.scitotenv.2020.142291

Petersell, V., Jüriado, K., Raukas, A., Shtokalenko, M., Täht-Kok, K., 2015. Quaternary deposits and weathered bedrock material as a source of dangerous radon emissions in Estonia. Geologos 21.

Pham, B.T., Ly, H.-B., Al-Ansari, N., Ho, L.S., 2021. A Comparison of Gaussian Process and M5P for Prediction of Soil Permeability Coefficient. Scientific Programming 2021, 3625289. https://doi.org/10.1155/2021/3625289

Pohjankukka, J., Pahikkala, T., Nevalainen, P., Heikkonen, J., 2017. Estimating the prediction performance of spatial models via spatial k-fold cross validation. International Journal of Geographical Information Science 31, 2001–2019.

Radiological Protection Act 1991 (Ionising Radiation) Regulations, 2019. Statutory Instruments Ireland, S.I. No. 30 of 2019.

Reynolds Jr, R., 1963. Potassium-rubidium ratios aud polymorphism in illites and microclines from the clay size fractions of proterozoic carbonate rocks. Geochimica et Cosmochimica Acta 27, 1097–1112.

Ribeiro, F.C.A., Silva, J.I.R., Lima, E.S.A., do Amaral Sobrinho, N.M.B., Perez, D.V., Lauria, D.C., 2018. Natural radioactivity in soils of the state of Rio de Janeiro (Brazil): Radiological characterization and relationships to geological formation, soil types and soil properties. Journal of Environmental Radioactivity 182, 34–43. https://doi.org/10.1016/j.jenvrad.2017.11.017

Robinson, P., 1980. Determination of calcium, magnesium, manganese, strontium, sodium and iron in the carbonate fraction of limestones and dolomites. Chemical Geology 28, 135–146. https://doi.org/10.1016/0009-2541(80)90041-8

Rodríguez-Martínez, Á., Ruano-Ravina, A., Torres-Durán, M., Provencio, M., Parente-Lamelas, I., Vidal-García, I., Martínez, C., Hernández-Hernández, J., Abdulkader-Nallib, I., Castro-Añón, O., Varela-Lema, L., Piñeiro-Lamas, M., Fidalgo, P.S., Fernández-Villar, A., Barros-Dios, J., Pérez-Ríos, M., 2021. Residential Radon and Small Cell Lung Cancer. Final Results of the Small Cell Study. Archivos de Bronconeumología. https://doi.org/10.1016/j.arbres.2021.01.027

Ross, C.S., Hendricks, S.B., 1945. Minerals of the montmorillonite group: Their origin and relation to soils and clays. US Government Printing Office.

Roycroft, P.D., 1989. Zoned muscovite from the Leinster Granite, SE Ireland. Mineralogical Magazine 53, 633–635.

Ruiz-Agudo, E., Putnis, C.V., Rodriguez-Navarro, C., Putnis, A., 2012. Mechanism of leached layer formation during chemical weathering of silicate minerals. Geology 40, 947–950. https://doi.org/10.1130/G33339.1

Ryser, A.L., Strawn, D.G., Marcus, M.A., Johnson-Maynard, J.L., Gunter, M.E., Möller, G., 2005. Micro-spectroscopic investigation of selenium-bearing minerals from the Western US Phosphate Resource Area. Geochemical Transactions 6, 1. https://doi.org/10.1186/1467-4866-6-1

Schabath, M.B., Cote, M.L., 2019. Cancer Progress and Priorities: Lung Cancer. Cancer Epidemiology, Biomarkers & Prevention 28, 1563–1579. https://doi.org/10.1158/1055-9965.EPI-19-0221

Schonlau, M., Zou, R.Y., 2020. The random forest algorithm for statistical learning. The Stata Journal 20, 3–29.

Shang, Q., Tan, D., Gao, S., Feng, L., 2019. A Hybrid Method for Traffic Incident Duration Prediction Using BOA-Optimized Random Forest Combined with Neighborhood Components Analysis. Journal of Advanced Transportation 2019, 4202735. https://doi.org/10.1155/2019/4202735

Sperandei, S., 2014. Understanding logistic regression analysis. Biochemia medica 24, 12–18.

Starkey, H.C., 1982. The role of clays in fixing lithium. US Government Printing Office.

Starr, M., Lindroos, A.-J., Ukonmaanaho, L., 2014. Weathering release rates of base cations from soils within a boreal forested catchment: variation and comparison to deposition, litterfall and leaching fluxes. Environmental Earth Sciences 72, 5101–5111. https://doi.org/10.1007/s12665-014-3381-8

Talebi, H., Peeters, L.J.M., Otto, A., Tolosana-Delgado, R., 2022. A Truly Spatial Random Forests Algorithm for Geoscience Data Analysis and Modelling. Mathematical Geosciences 54, 1–22. https://doi.org/10.1007/s11004-021-09946-w

Thomson, I., 1971. Regional geochemical studies of black shale facies with particular reference to trace element disorders in animals.

Ticknor, K., 1998. The sorption of strontium, barium and radium by chlorite and kaolinite: effects of sorbent concentration and competition from group IIA elements.

Tolosana-Delgado, R., McKinley, J., 2016. Exploring the joint compositional variability of major components and trace elements in the Tellus soil geochemistry survey (Northern Ireland). Applied Geochemistry 75, 263–276.

United Nations Scientific Committee on the Effects of Atomic Radiation, 2011. Report of the United Nations Scientific Committee on the Effects of Atomic Radiation (UNSCEAR) 2011.

Vasil'ev, V., 2011. New data on the composition of metacinnabar and Hg-sphalerite with an isomorphous Cd admixture. Russian Geology and Geophysics 52, 701–708.

Vermeesch, P., 2013. Multi-sample comparison of detrital age distributions. Chemical Geology 341, 140–146. https://doi.org/10.1016/j.chemgeo.2013.01.010

Wang, L., Liu, B., McKinley, J.M., Cooper, M.R., Li, C., Kong, Y., Shan, M., 2021. Compositional data analysis of regional geochemical data in the Lhasa area of Tibet, China. Applied Geochemistry 135, 105108. https://doi.org/10.1016/j.apgeochem.2021.105108

Wang, Y., Zhao, Y., Xu, S., 2022. Application of VNIR and machine learning technologies to predict heavy metals in soil and pollution indices in mining areas. Journal of Soils and Sediments. https://doi.org/10.1007/s11368-022-03263-3

Wang, Z., Tan, J., Hilton, J., Dick, J., Wen, Z., 2023. Trace element enrichment mechanisms in black shales during the early cambrian (ca. 521–514 Ma), South China. Marine and Petroleum Geology 149, 106083.

Wells, N., 1967. Selenium content of soil-forming rocks. New Zealand journal of geology and geophysics 10, 198–208.

Worden, R., Griffiths, J., Wooldridge, L., Utley, J., Lawan, A.Y., Muhammed, D., Simon, N., Armitage, P., 2020. Chlorite in sandstones. Earth-Science Reviews 204, 103105.

World Health Organization (Ed.), 2009. WHO handbook on indoor radon: a public health perspective. World Health Organization.

World Health Organization, 2007. International radon project: survey on radon guidelines, programmes and activities (No. WHO/HSE/RAD/07.01). World Health Organization.

Wunsch, A., Navarre-Sitchler, A.K., Moore, J., McCray, J.E., 2014. Metal release from limestones at high partial-pressures of CO2. Chemical Geology 363, 40–55. https://doi.org/10.1016/j.chemgeo.2013.10.036

Yesares, L., Drummond, D.A., Hollis, S.P., Doran, A.L., Menuge, J.F., Boyce, A.J., Blakeman, R.J., Ashton, J.H., 2019. Coupling Mineralogy, Textures, Stable and Radiogenic Isotopes in Identifying Ore-Forming Processes in Irish-Type Carbonate-Hosted Zn–Pb Deposits. Minerals 9. https://doi.org/10.3390/min9060335

Young, M., Knights, K., Smyth, D., Glennon, M., Scanlon, R., Gallagher, V., 2016. The Tellus geochemical surveys, results and applications. Unearthed: Impacts of the Tellus Surveys of the North of Ireland. Royal Irish Academy 33–52.

Yu, B., Chen, J., Li, X., Lin, C., 2003. Geochemistry of black shale at the bottom of the Lower Cambrian in Tarim Basin and its significance for lithosphere evolution. Science in China Series D: Earth Sciences 46, 498–507.

Zagà, V., Cattaruzza, M.S., Martucci, P., Pacifici, R., Trisolini, R., Bartolomei, P., Giacobbe, R., Patelli, M., Paioli, D., Esposito, M., 2021. The “polonium in vivo” study: polonium-210 in bronchial lavages of patients with suspected lung cancer. Biomedicines 9, 4.

Zane, A., Sassi, R., Guidotti, C.V., 1998. New data on metamorphic chlorite as a petrogenetic indicator mineral, with special regard to greenschist-facies rocks. The Canadian Mineralogist 36, 713–726.

Zhongcheng, W., Guizhi, L., 1991. Barite and witherite deposits in Lower Cambrian shales of South China; stratigraphic distribution and geochemical characterization. Economic Geology 86, 354–363.

Zohuri, B., 2020. 2 - Nuclear fuel cycle and decommissioning, in: Khan, S.U.-D., Nakhabov, A. (Eds.), Nuclear Reactor Technology Development and Utilization. Woodhead Publishing, pp. 61–120. https://doi.org/10.1016/B978-0-12-818483-7.00002-0

Chapter 6

Synthesis

6.1 Summary

The primary research objectives of this thesis are to

(d) Develop a decision matrix for radon mapping and modelling for the non-specialist, which takes into account different possible available datasets, and the possible intended purposes of mitigation measures.

(e) Investigate the use of radon potential and soil geochemistry in determining the radon risk of a small area (Castleisland, Co. Kerry). Secondary objectives are to assess the assigned legislative radon risk designation, and investigate the source of radon anomalies in the area.

(f) Develop novel statistical and modelling methodologies to utilise legacy soil geochemistry and geological map datasets for regional or national scale radon mapping or modelling.

The main contribution of this thesis can be compartmentalised to six findings:

Finding 1: Decision making tools: there are various reasons and methods for mapping radon prone areas. With regard to radon, the primary aims of EU legislation and Irelands Building Regulations are to mitigate the harmful effects (i.e. lung cancer) caused by long term radon exposure. As such, strategies for attenuating radon exposure are designed to reduce the amount of natural radiation received by (a) individuals and (b) the collective. Distinct radon maps are appropriate depending on the specific scenario for producing the map. The third chapter demonstrates the various common radon mapping techniques (probability, average, collective dose) and contributes decision-making tools to efficiently determine which map is most appropriate depending on the purpose as well as the data available. To add, it is beneficial to map radon using geological methods considering geogenic radon quantifies the amount of radon available to become indoor radon regardless of building type (i.e. house, workplaces); which is significant when planning actions to reduce radon depending on building type.

Finding 2: The spatial resolution adopted for radon mapping can have a significant impact on the areas estimated to be radon prone. For example, fig.3.2a in chapter 3 demonstrates that the smallest spatial resolution (1 x 1 km grids) allows for the highest precision and detailed spatial variation, when determining radon prone areas. Whereas the larger areas (i.e. county administrative units (fig.3.2f)) results in the least precise representation of radon in the area. In contrast, a map with geological data integrated allows for the spatial variation of radon to be represented more accurately; especially considering the spatial information provided by geological databases allows radon risk to be determined in areas that lack indoor radon data. The spatial resolution used for radon mapping should be carefully considered since the resolution can result in discrepancies in assigned radon priority areas even if the exact same dataset is used.

Finding 3: Geological processes underpin the radon distribution in Irelands highest known indoor radon region around Castleisland Co. Kerry. The geogenic method used in chapter four follows a series of analysis integrating soil-gas radon, soil-permeability and indoor radon compared with maps of bedrock geology and Quaternary geology. The indoor radon concentration variation attributed to geogenic factors is 34% with soil-gas radon as the main contributor (16%). Whereas bedrock geology accounts for 39% of soil-gas radon variance. Spatial association of black shales (the Clare Shales) with extremely high indoor radon and soil-gas radon values indicate that these black shales may be providing the geochemical composition for the overlain soils to act as source of radon. Furthermore, the soil depth is very shallow (<30 cm) above the Clare shales in the location of the highest soil-gas radon measurement; reinforcing that the bedrock in this specific area may have a greater influence on the soil geochemical composition.

Specifically, samples collected above the Clare shales contain the highest geogenic radon potential (1778) and soil-gas radon (>1443 k Bq m^{-3}) measured in the study area which corresponds with Irelands highest indoor radon measurement (65,000 Bq m^{-3}). There is a clear spatial correlation of extremely high soil-gas radon and the underlying Clare shales bedrock. Despite the latter, the new EPA radon map delineates the area above the Clare shales as having the lowest probability of houses containing indoor radon levels over the reference level (200 Bq m^{-3}). The inconsistency between the maps produced in this thesis and the new EPA map highlight the importance of examining the designated radon potential of geological parameters when producing a radon map; for example, correctly assigning the radon potential of a bedrock lithology. To elaborate, when using any geological map to model radon, it is paramount all parameters are assigned a value/category that reflects their ability to either be a source of radon or provide a transport mechanism for gas to reach the Earth's surface.

Examining the variation of soil-gas radon above structural geology features, like faults and karstic bedrock, signifies subsurface deformities may be exploited by radon gas to move within the local area. The latter is a significant sub-finding as it underscores that an area underlain with soils that don't act as a source of radon can still be prone to higher radon levels depending if there is a source within reasonable distance and a pathway for the radon to reach the receptive area. The natural transportation of radon gas through subsurface structures is the likely cause of soil-gas samples collected above limestone lithologies having a mean of 57 k Bq m^{-3}, with values elevated near karstic springs (>100 k Bq m^{-3}) and reaching up to 472 k Bq m^{-3} in the proximity of faults. In comparison, soil-gas radon above limestone lithologies reported in the peer-reviewed literature is typically less than 40 k (Kikaj et al., 2016; Swakoń et al., 2005).

Furthermore, the results in this thesis underline the importance of local scale studies to verify and improve regional scale models. Local scale studies are important to verify regional scale models because although we can reasonably, with expert advice, use regional geological data to model radon, it is best to use primary data that directly measures radon. Understandably, it is more time and cost efficient to adopt proxy datasets that are already available at national scales to model radon prone areas. However, it would be best practice to verify a large-scale model with strategic and localised research; as there may be exceptions to the model as there is in the case of the Castleisland area.

Finding 4: The mapping approach outlined in chapter 4 is efficient and tactical at investigating the radon potential at local scales. Measuring the geogenic radon potential (i.e. soil-gas radon and soil permeability) is a rapid method to determine the availability of radon to the earth surface. The approach of strategically designing a survey area to include samples collected above various geological features is proven to be effective at determining the geological impact on radon variations as well as the distribution of radon in an area. Explicitly, the method of sampling over several geology classes as outlined from the available geological maps for the area (fig 4.2), and measuring in a systematic manner (i.e. target sample from each corner and the centre of 500 m^2 grid cells) allows for a spatially distributed and representative dataset to be obtained.

The mapping procedure adopted in chapter 4 goes further than monitoring the radon concentration in the subsoil gas and aims to investigate if the spatial distribution of soil-gas radon is statistically associated with geological boundaries. Such a method could be adopted to investigate radon variation in other areas; and if research is conducted over representative bedrock/quaternary geology types, then results could be extrapolated to other areas with similar geology in order to direct resources/research towards areas that may be at risk to higher radon levels. From the results of this thesis, it is a reasonable interpretation that other areas in the proximity of black phosphatic shales are prone to radon; especially if there are structural transport mechanisms for radon in the subsurface or if the depth to bedrock is relatively shallow.

Finding 5: The soil geochemistry is statistically linked to radon variation. Chapter 5 examines the covariance and correlation of topsoil geochemistry in relation to radon. Specifically, r^2, Pearson r and ANOVA results indicate the relative correlation of up to 47 elements with geogenic radon. Elements including La, V, Ba, Sr, U, P, Cu, Mo and Cr are deemed radon prone from the Castleisland dataset (i.e. r^2 values range from 0.21 – 0.5 and Pearson r values between 0.46 – 0.62). Whereas, elements including S, Cr, Ni, Co, V and Zr explain the geogenic radon variance in the region by ca. 15-30% when investigating the TELLUS midlands dataset.

In addition, the covariance tests demonstrate how the radon-prone elements covary together while non radon-prone elements also share a distinct covariance. Explicitly, Principal Component Analysis (PCA) and cluster analysis of the Castleisland dataset depict elements La, V, Ba, Sr, P, Cu, U, Mo and Sb covarying together (figure 5.2). To add, the elements that least correlate (Mg, Ga, Fe, Na, Sc, Ni and Al) to soil-gas radon also covary together. A similar pattern of radon-prone elements covarying together is also found when using the regional TELLUS midlands dataset. Distinctively, some of the radon-prone elements (i.e. Y, La, V, Cr, Ce and Co) group together on both the cluster analysis and PC1 vs PC2 biplot (figure 5.7). Whereas, non radon-prone elements (i.e. Na, Se, Ca, Hg, Pb, Sb, Sn and Bi) also distinctly group together on the cluster analysis and PCA biplots. The aforementioned results reinforce the hypothesis that elements correlated with geogenic radon are also associated with each other. Consequently, understanding the spatial variance of radon-prone elements in the earth surface can advance our understanding where radon prone areas may be located. Indirectly, the research elaborated in chapter 5 adds to the value of national soil geochemical surveys which can also be utilised for environmental strategies to mitigate radon.

Subsequently, the TELLUS midlands topsoil geochemistry dataset is trained and tested on several machine learning (ML) models to investigate the relation of topsoil geochemistry and geogenic radon. Explicitly, four algorithms (Gaussian process regression, logistic regression, random forest and a control model) are adopted to examine the feasibility of using a machine learning approach to model radon. Aside from the control model, the ML models resulted in ca. 74% accuracy and ca. 76% precision with ROC-AUC values above 0.8. The feature importance results from the ML models depict a range of elements (i.e. Y, Tl, Be, Ba, La, V and U) that are positively correlated with geogenic radon. Furthermore, the ML models also identify several elements (Sb, K, Ca and Pb) that least explain the variance of geogenic radon.The preceding results further underpin the hypothesis that it is feasible to use soil geochemistry to understand the spatial variance of geogenic radon. To elaborate, the pattern of radon prone elements consistently grouping together in various types of analysis (correlation, covariance, classification/regression) augments the theorem that these elements are indicative of higher geogenic radon.

Finding 6: The modelling approach used in chapter 5 demonstrates a robust method for investigating topsoil geochemical link to geogenic radon at local and regional scales. Conducting a range of correlation and covariance tests (i.e. Pearson r, r^2, ANOVA, cluster analysis and principal component analysis) allows for (a) elements correlated to geogenic radon to be identified and (b) the relationship between elements correlated to geogenic radon to be distinguished. Comparing the multivariate analysis results (i.e. PCA and cluster analysis) with univariate modes of analysis (i.e. Tukey plots, r^2) gives insight and allows verification of trends between elements correlated with geogenic radon.

Furthermore, the machine learning (ML) algorithms explored in chapter 5 of this thesis demonstrate the potential ML can have for modelling radon. Specifically, the highest accuracy ML models, logistic regression (73.9%) and Gaussian process regression (74.1%) correctly rank elements (Tl, Y, U, Ba, V, La, Sb, Mo, Cu) correlated to geogenic radon (from r^2 and ANOVA results). Model verification was investigated by testing the Castleisland topsoil dataset on the Gaussian process regression model trained using the TELLUS midlands data. In consequence, the average soil-gas radon was calculated for the samples predicted to be in a (a) high GRP class and (b) low GRP class. On average, the samples predicted to be in the low GRP class were substantially lower (74.8 k Bqm^{-3}) when compared to samples predicted to be in a higher GRP class (174.4 k Bqm^{-3}). Overall, results from both local and regional scales demonstrate that there is a statistical association of elements within the topsoil samples and geogenic radon.

Furthermore, machine learning techniques are particularly promising for processing substantially large (>4000 samples) soil geochemical datasets. Machine learning techniques like gaussian process regression and logistic regression are powerful algorithms that can aid in determining the elements that influence geogenic radon. The range of univariate, multivariate and machine learning techniques utilized in chapter 5 is effective at distinguishing radon prone elements within the topsoil. Multivariate analysis is undoubtedly effective in aiding interpretation of intrinsic processes for relatively large datasets. However, univariate analysis is still a rudimentary and a useful tool for validating results from multivariate analysis. The aforementioned results reiterate the robustness of the overall methodological process followed in chapter 5.

6.2 Suggested further work

6.2.0 Geogenic radon surveys over other areas in Ireland with black shales.

Considering the anomalously high geogenic radon occurring over the parameters of the black shales in Castleisland, the foremost suggested further work would be to conduct in situ research in other areas underlain by black shales in Ireland. The presence of black shales are reported in Co. Cork, Co. Kerry, Co. Clare and Co. Leitrim in the west and north-west (Armstrong et al., 2019; Brandon, 1972; Wignall et al., 2016).

6.2.1 Airborne radiometric survey

The concept originally behind chapter 5 was to test and compare the feasibility of using different geogenic datasets (topsoil geochemistry and aerial radiation monitoring (ARM)) for mapping radon risk at a local scale. A data collection survey was planned involving an unmanned aerial vehicle (UAV) (aka drone) with an attached $CeBr_3$ scintillation radiation detector and a NaI detector. To elaborate, the feasibility of applying airborne radiometric data (equivalent ^{214}Bi, ^{232}Th and ^{238}U) for mapping geogenic radon was going to be tested. The method would serve as a comparison to the topsoil geochemical results for accuracy, efficiency and precision.

The main aim of the UAV investigative approach was to validate the practicality and efficiency of aerial radiation monitoring applied to local areas with suspected high radon anomalies. Sub-aims include assessing ARM survey data for statistical and spatial correlation with geological parameters (i.e. TELLUS airborne radiometric surveys (^{214}Bi, ^{232}Th and ^{238}U) bedrock geology and Quaternary geology). The possible discrepancies between the TELLUS airborne radiometric data (collected in 200m lines) and the UAV survey (aimed to be collected in 50m lines) would be investigated for the Castleisland area. Any statistical correlation of UAV data and major and trace elemental data would be verified.

However, the Covid-19 pandemic lockdowns resulted in major delays securing the drone equipment. Instead, a handheld gamma ray detector (GT-40) was obtained and the field survey was completed in June 2021. The GT-40 survey resulted in a low resolution geogenic radon map (Appendix B: 8.1). There are correlations with soil-gas radon and bedrock geology as seen from the tables and figures included in appendix B. Despite the aforementioned results, we thought the research could bring more value by aiming to scientifically extrapolate a geogenic radon modelling method to other geological regions as opposed to validating a radon mapping technique applied to the same 6 km^2 local area around Castleisland. As such, it was decided to reiterate the modelling method using topsoil geochemistry on regional scale data obtained from the GSI TELLUS midlands survey as elaborated in chapter 5.

6.2.2 Radon transport in water.

Understanding the structural groundwater characteristics are relevant to understanding radon distribution and transport mechanisms in the subsurface. Radon is slightly soluble in water and can be transported dozens of kilometres in groundwater (Crandall et al., 1999). Research conducted by (Elio et al., 2017) reported that the probability of indoor radon is partially dependent on the type of aquifer system. For example, regionally important karst aquifers contributed the highest probability of a house having elevated indoor radon compared to the other aquifer types; whereas regionally important sand/gravel aquifers contributed the lowest probability of a house having elevated indoor radon (Elio et al., 2017).

Further research could involve measuring the ratio of radon and thoron concentrations within the ground water to determine if the aquifer system is contributing to the transportation of radon in the Castleisland study area. Knowing the radon and thoron ratio in the groundwater will determine if radon (if any) in the groundwater is sourced from more than 55.6 seconds (thoron half-life) away. There will be uncertainty to the distance which the water has travelled in 56.6 seconds and as such, this experiment will only be able to conclude with certainty the presence of radon in the ground water. Further extrapolations would carry little certainty unless thoroughly investigated.

In theory, the role of karst limestone could be investigated by calculating the Reynolds number, the hydraulic head, and velocity of water flow (using Darcy's law), as well by measuring the drawdown of a pumping well. However, the equations associated with these calculations carry important assumptions. For example, Darcy's law assumes that the flow is laminar opposed to turbulent, that the flow is steady and that the testing temperature is 27 degrees Celsius among additional assumptions. These make calculating the accurate groundwater flow velocity more intricate especially if the aquifer is not homogeneous, as is true for karst aquifers.

Hypothetically, further research could include a more in-depth study of the groundwater behaviour. A tensiometer would be used to measure the soil moisture content to better understand the relative drainage capabilities of the soil cover in the study area. A better understanding of the drainage in the study area could be obtained by measuring the spontaneous potential of the earth surface (Artugyan and Urdea, 2015). The spontaneous potential would be measured using a voltmeter, this technique typically involves placing one of two electrode probes into the soil and the other down a borehole or in a sinkhole. The spontaneous potential can give insight to many parameters including bed thickness, resistivity of a permeable bed and resistivity of mud.

There is one well-known cave in the study area called Crag cave. Crag cave could be visited and data on the water level, water temperature and flow direction could be collected. Groundwater flow rate is commonly measured using Darcy's law which requires information on conduit length, height, flow direction and cross-sectional area perpendicular to flow. However, since karst aquifers are not homogeneous and the karst conduits usually change in dimension, the use of Darcy's law to determine ground water flow rate in Crag cave would be inapplicable.

Moreover, the topography of the study area would be analysed in order to assist in determining the hydraulic pressure and gradient. Geomorphology would be studied in order to identify any potential open or closed sinkholes, springs and minor faults which could all contribute to groundwater recharge/discharge. Ideally, with sufficient equipment and time, geophysics could be implemented with the use of ground radar penetration in order to image and confirm the structure beneath the earth surface.

6.2.3. Spectroscopy for identifying mineral types:

X-ray diffraction is a common non-destructive technique used to investigate the structure of inorganic crystalline materials, especially for rock samples. However, the XRD technique used on soil samples results in more intricate patterns considering soil samples are less crystalline compared to rock samples (Fang et al., 2017; Hong et al., 2014; Yin et al., 2018). Alternatively, visible and near-infrared reflectance spectroscopy (VNIR, 350-2500nm) can be used to measure the visible and near infrared light reflected from material surfaces within the soil sample. Furthermore, VNIR can also be used to investigate multiple mineralogic soil properties including clay content/composition, mineral alteration/weathering degree (except for quartz and feldspar due to weak absorption) (Gomez et al., 2008; Zhao et al., 2018).

In order to test the mineralogy type in the soil samples, a methodology as follows may be used to prepare samples for analysis: Dry-sieve shake to obtain 2mm fraction. Remove organic matter using 30% H_2O_2 and heating on a hot plate (Nelson and Sommers, 1983). Remove sesquioxides by heating in a water bath at 70 degrees C. Mount representative samples in petri dishes and minimise the influence of material roughness by levelling the surface (Coblinski et al., 2021).

The data interpretation can be an intricate process requiring continuum removal approaches i.e. isolate absorption features for identification and remove background noise (Clark and Roush, 1984). Smoothing techniques i.e. averaging spectra, Savitzky-Golay to remove baseline float and enhance signal to noise ratio, Norris transform to remove effects caused by variance in particle-size (Norris and Williams, 1984; Savitzky and Golay, 1964; Stenberg et al., 2010). Derivative algorithms could be used to highlight positions that characterise the spectral maximum, minimum, and inflection points.

The overall aim of implementing the VNIR or XRD analysis would be to (a) determine the presence and frequency of mineralogy types and (b) compare the minerology results with the soil geochemistry and statistically analyse the influence of minerology on element concentration in the soil samples. For example, based on the covariance of radon prone elements (such as Y, La, V, Ce, Al, Ni, Co, U, Sb and Mo) as determined in chapter 5, these elements could be sourced from uranium accessory minerals such as allanite ($Ca(Ce,La,Y,Ca)Al_2(Fe_{2+},Fe_{3+})(SiO_4)(Si_2O_7)O(OH)$) or carnotite ($K_2(UO_2)_2(VO_4)_2 \cdot 3H_2O$). Alternatively, pyrite minerals can contain a range of trace elements including Ni, Co, Mo and Sb. (Gregory et al., 2015; Koglin et al., 2010). In contrast, non radon-prone elements such as Ca, Na and Mg could be sourced from minerals including calcite ($CaCO_3$), dolomite ($CaMg(CO_3)_2$) or feldspar ($NaAlSi_3O_8$). However, explicit analysis would need to be conducted to determine such a hypothesis.

References

Abbady, A.G.E., Uosif, M.A.M., El-Taher, A., 2005. Natural radioactivity and dose assessment for phosphate rocks from Wadi El-Mashash and El-Mahamid Mines, Egypt. Journal of Environmental Radioactivity 84, 65–78. https://doi.org/10.1016/j.jenvrad.2005.04.003

Abdalla, A.M., Ismail, A.M., Al Madiy, A.A., 2021. Soil radon detection using active scintillation cell. J. Radiat. Res. Appl. Sci. 14, 16–22. https://doi.org/10.1080/16878507.2020.1783631

Abdi, H., Williams, L.J., 2010. Principal component analysis. Wiley interdisciplinary reviews: computational statistics 2, 433–459.

Abed, A.M., Jaber, O., Alkuisi, M., Sadaqah, R., 2016. Rare earth elements and uranium geochemistry in the Al-Kora phosphorite province, Late Cretaceous, northwestern Jordan. Arabian Journal of Geosciences 9, 1–19.

Abed, N.S., Monsif, M.A., Zakaly, H.M., Awad, H.A., Hessien, M.M., Yap, C.K., 2022. Assessing the radiological risks associated with high natural radioactivity of microgranitic rocks: A case study in a northeastern desert of Egypt. International Journal of Environmental Research and Public Health 19, 473.

Aditya, C.R., Deshmukh, C.R., Nayana, D.K., Vidyavastu, P.G., 2018. Detection and prediction of air pollution using machine learning models. International Journal of Engineering Trends and Technology (IJETT) 59, 204–207.

Aitchison, J., 1982. The statistical analysis of compositional data. Journal of the Royal Statistical Society: Series B (Methodological) 44, 139–160.

Akbari, K., Mahmoudi, J., Ghanbari, M., 2013. Influence of indoor air conditions on radon concentration in a detached house. 116. https://doi.org/10.1016/j.jenvrad.2012.08.013

References

Åkerblom, G., Andersson, P., Clevensjö, B., 1984. Soil Gas Radon - A Source for Indoor Radon Daughters. Radiation Protection Dosimetry 7, 49–54. https://doi.org/10.1093/oxfordjournals.rpd.a082961

Al-Bassam, K.S., 2007. Uranium in the Iraqi phosphorites. Iraqi Bulletin of Geology and Mining 3, 13–31.

Algeo, T.J., Maynard, J.B., 2004. Trace-element behavior and redox facies in core shales of Upper Pennsylvanian Kansas-type cyclothems. Chemical geology 206, 289–318.

Al-Khawlany, A., Khan, A., Pathan, J., 2018. Review on studies in natural background radiation. Radiation Protection and Environment.

Alonso, H., Rubiano, J.G., Guerra, J.G., Arnedo, M.A., Tejera, A., Martel, P., 2019. Assessment of radon risk areas in the Eastern Canary Islands using soil radon gas concentration and gas permeability of soils. Science of The Total Environment 664, 449–460. https://doi.org/10.1016/j.scitotenv.2019.01.411

Alshahrani, B.E., 2021. Natural radioactivity level in pumice rock, in Saudi Arabia and effect on human health. null 1–12. https://doi.org/10.1080/03067319.2021.1907363

Andersen, C.E., Ulbak, K., Damkjær, A., Gravesen, P., 2001. Radon i danske boliger. Kortlægning af lands-, amts-og kommuneværdier.

Anderson, R.T., Vrionis, H.A., Ortiz-Bernad, I., Resch, C.T., Long, P.E., Dayvault, R., Karp, K., Marutzky, S., Metzler, D.R., Peacock, A., White, D.C., Lowe, M., Lovley, D.R., 2003. Stimulating the In Situ Activity of *Geobacter* Species To Remove Uranium from the Groundwater of a Uranium-Contaminated Aquifer. Applied and Environmental Microbiology 69, 5884–5891. https://doi.org/10.1128/AEM.69.10.5884-5891.2003

Antovic, N., Vukotic, P., Zekic, R., Svrkota, R., Ilic, R., 2007. Indoor radon concentrations in urban settlements on the Montenegrin Coast. Radiation Measurements 42, 1573–1579. https://doi.org/10.1016/j.radmeas.2007.06.003

Appleton, J.D., Daraktchieva, Z., Young, M.E., 2015. Geological controls on radon potential in Northern Ireland. Proceedings of the Geologists' Association 126, 328–345. https://doi.org/10.1016/j.pgeola.2014.07.001

Appleton, J.D., Miles, J.C.H., 2010. A statistical evaluation of the geogenic controls on indoor radon concentrations and radon risk. Journal of Environmental Radioactivity 101, 799–803. https://doi.org/10.1016/j.jenvrad.2009.06.002

Armstrong, J., Parnell, J., Boyce, A., Perez, M., 2023. Trace element release from Bowland Shale into spring water, Lancashire. Geological Society, London, Special Publications 534, SP534-2022.

Armstrong, J.G.T., Parnell, J., Bullock, L.A., Boyce, A.J., Perez, M., Feldmann, J., 2019. Mobilisation of arsenic, selenium and uranium from Carboniferous black shales in west Ireland. Applied Geochemistry 109, 104401. https://doi.org/10.1016/j.apgeochem.2019.104401

Arora, B.R., Kumar, A., Walia, V., Yang, T.F., Fu, C.-C., Liu, T.-K., Wen, K.-L., Chen, C.-H., 2017. Assesment of the response of the meteorological/hydrological parameters on the soil gas radon emission at Hsinchu, northern Taiwan: A prerequisite to identify earthquake precursors. Journal of Asian Earth Sciences 149, 49–63. https://doi.org/10.1016/j.jseaes.2017.06.033

Artugyan, L., Urdea, P., 2015. A complex approach in the interdisciplinary field of karst geomorphology. The case study of Anina karst area (Banat Mountains, Romania). Forum geografic XV.

Ashton, J., Black, A., Geraghty, J., Holdstock, M., Hyland, E., Bowden, A., Earls, G., O'Connor, P., Pyne, J., 1980. The geological setting and metal distribution patterns of Zn-Pb-Fe mineralization in the Navan Boulder Conglomerate. The Irish minerals industry 1990, 171–210.

Baluci, C., Vincenti, K., Tilluck, B., Conchin, S., Formosa, S., Grech, D., 2013. National mapping survey of indoor radon levels in the Maltese Islands (2010-2011).

Banríon, M., Elío, J., Crowley, Q., 2022. Using geogenic radon potential to assess radon priority area designation, a case study around Castleisland, Co. Kerry, Ireland. Journal of Environmental Radioactivity 251, 106956.

Baptista, E., Pereira, A.J.S.C., Domingos, F.P., Sêco, S.L.R., 2022. Radon and thoron concentrations in the southwest region of Angola: dose assessment and implications for risk mapping. Environmental Geochemistry and Health. https://doi.org/10.1007/s10653-022-01226-8

Barros, N., Field, D.W., Steck, D.J., Field, R.W., 2015. Comparative survey of outdoor, residential and workplace radon concentrations. Radiation Protection Dosimetry 163, 325–332. https://doi.org/10.1093/rpd/ncu185

Barros, R., Menuge, J.F., 2016. The origin of spodumene pegmatites associated with the Leinster Granite in southeast Ireland. The Canadian Mineralogist 54, 847–862.

Baxter, S., Graham, N.T., Feely, M., Reavy, R.J., Dewey, J.F., 2005. A microstructural and fabric study of the Galway Granite, Connemara, western Ireland. Geological Magazine 142, 81–95. https://doi.org/10.1017/S0016756804000378

Beck, B.F., 2010. CH Holland, IS Sanders (eds): The Geology of Ireland, 2nd edn.

Belogub, E., Ayupova, N., Krivovichev, V., Novoselov, K., Blinov, I., Charykova, M., 2020. Se minerals in the continental and submarine oxidation zones of the South Urals volcanogenic-hosted massive sulfide deposits: A review. Ore Geology Reviews 122, 103500.

Benedicto, A., Missana, T., Fernández, A.M., 2014. Interlayer Collapse Affects on Cesium Adsorption Onto Illite. Environ. Sci. Technol. 48, 4909–4915. https://doi.org/10.1021/es5003346

Bernardo, J., Berger, J., Dawid, A., Smith, A., 1998. Regression and classification using Gaussian process priors. Bayesian statistics 6, 475.

Biau, G., Scornet, E., 2016. A random forest guided tour. Test 25, 197–227.

Bineng, G.S., Tokonami, S., Hosoda, M., Tchuente Siaka, Y.F., Issa, H., Suzuki, T., Kudo, H., Bouba, O., 2020. The importance of direct progeny measurements for correct estimation of effective dose due to radon and thoron. Frontiers in Public Health 8, 17.

Bochicchio, F., Campos-Venuti, G., Piermattei, S., Nuccetelli, C., Risica, S., Tommasino, L., Torri, G., Magnoni, M., Agnesod, G., Sgorbati, G., Bonomi, M., Minach, L., Trotti, F., Malisan, M.R., Maggiolo, S., Gaidolfi, L., Giannardi, C., Rongoni, A., Lombardi, M., Cherubini, G., D'Ostilio, S., Cristofaro, C., Pugliese, M., Martucci, V., Crispino, A., Cuzzocrea, P., Santamaria, A.S., Cappai, M., 2005. Annual average and seasonal variations of residential radon concentration for all the Italian Regions. Radiation Measurements 686–694. https://doi.org/10.1016/j.radmeas.2004.12.023

Bossew, P., 2018. Radon Priority Areas - Definition, estimation and uncertainty. Nuclear Technology and Radiation Protection 33, 11–11. https://doi.org/10.2298/NTRP180515011B

Bossew, P., 2014. Determination of radon prone areas by optimized binary classification. Journal of Environmental Radioactivity 129, 121–132. https://doi.org/10.1016/j.jenvrad.2013.12.015

Bossew, P., Cinelli, G., Ciotoli, G., Crowley, Q., Cort, M., Elío, J., Gruber, V., Petermann, E., Tollefsen, T., 2020. Development of a Geogenic Radon Hazard Index—Concept, History, Experiences. International Journal of Environmental Research and Public Health 17, 4134. https://doi.org/10.3390/ijerph17114134

Bousquet, O., von Luxburg, U., Rätsch, G., 2011. Advanced Lectures on Machine Learning: ML Summer Schools 2003, Canberra, Australia, February 2-14, 2003, Tübingen, Germany, August 4-16, 2003, Revised Lectures. Springer.

Bowie, C., Bowie, S.H.U., 1991. Radon and health. The Lancet 337, 409–413.

Brandon, A., 1972. Clastic dykes in the Namurian shales of Co. Leitrim, Republic of Ireland. Geological Magazine 109, 361–367.

Braun, J., Riotte, J., Battacharya, S., Violette, A., Prunier, J., Bouvier, V., Candaudap, F., Maréchal, J., Ruiz, L., Panda, S.R., 2017. REY-Th-U solute dynamics in the critical zone: Combined influence of chemical weathering, atmospheric deposit leaching, and vegetation cycling (Mule Hole Watershed, South India). Geochemistry, Geophysics, Geosystems 18, 4409–4425.

Breiman, L., 2001. Random forests. Machine learning 45, 5–32.

Brennand, T.P., 1962. The Carboniferous geology of the Castleisland area. Unpublished PhD thesis, University of Dublin.

Bruck, P., 1968. The geology of the Leinster granite in the Enniskerry-Lough Dan area, Co. Wicklow. Presented at the Proceedings of the Royal Irish Academy. Section B: Biological, Geological, and Chemical Science, JSTOR, pp. 53–70.

Building Regulations, 1997. Building Regulations. Statutory Instruments No. 497 of 1997.

Bute, S.I., Yang, X., Suh, C.E., Girei, M.B., Usman, M.B., 2020. Mineralogy, geochemistry and ore genesis of Kanawa uranium mineralization, Hawal Massif, eastern Nigeria terrane: Implications for uranium prospecting in Nigeria and Cameroon. Ore Geology Reviews 120, 103381. https://doi.org/10.1016/j.oregeorev.2020.103381

Butler, K.M., Huntington-Moskos, L., Rayens, M.K., Wiggins, A.T., Hahn, E.J., 2018. Perceived Synergistic Risk for Lung Cancer After Environmental Report-Back Study on Home Exposure to Tobacco Smoke and Radon. Am J Health Promot 33, 597–600. https://doi.org/10.1177/0890117118793886

Carroll, D., Hathaway, J.C., 1953. Clay minerals in a limestone soil profile. Clays and clay minerals 2, 171–182.

Casal-Mouriño, A., Ruano-Ravina, A., Torres-Durán, M., Parente-Lamelas, I., Provencio-Pulla, M., Castro-Añón, O., Vidal-García, I., Pena-Álvarez, C., Abal-Arca, J., Piñeiro-Lamas, M., Fuente-Merino, I., Fernández-Villar, A., Abdulkader, I., Valdés-Cuadrado, L., Barros-Dios, J.M., Pérez-Ríos, M., 2020. Lung cancer survival in never-smokers and exposure to residential radon: Results of the LCRINS study. Cancer Letters 487, 21–26. https://doi.org/10.1016/j.canlet.2020.05.022

Castillo, P.I., Townley, B.K., Emery, X., Puig, Á.F., Deckart, K., 2015. Soil gas geochemical exploration in covered terrains of northern Chile: data processing techniques and interpretation of contrast anomalies. Geochemistry: Exploration, Environment, Analysis 15, 222–233.

Chen, J., 2022. Assessment of thoron contribution to indoor radon exposure in Canada. Radiation and Environmental Biophysics 61, 161–167. https://doi.org/10.1007/s00411-021-00956-0

Chen, J., Bergman, L., Falcomer, R., Whyte, J., 2015. Results of simultaneous radon and thoron measurements in 33 metropolitan areas of Canada. Radiation Protection Dosimetry 163, 210–216. https://doi.org/10.1093/rpd/ncu141

Chen, J., Dessau, J.C., Frenette, E., Moir, D., Cornett, R.J., 2010. Preliminary assessment of thoron exposure in Canada. Radiation Protection Dosimetry 141, 322–327. https://doi.org/10.1093/rpd/ncq226

Chen, J., Ford, K.L., 2017. A study on the correlation between soil radon potential and average indoor radon potential in Canadian cities. Journal of Environmental Radioactivity 166, 152–156. https://doi.org/10.1016/j.jenvrad.2016.01.018

Chen, X., Wen, C., Meng, D., Li, B., Jiang, B., Qin, J., 2022. Implications of Major and Trace Element Migration in Altered Granites for Hydrothermal Alteration and Granite-Related Uranium Mineralization in the Sanjiu Ore Field, South China. Minerals 12. https://doi.org/10.3390/min12020144

Cinelli, G., de, C., Tollefsen, T., Achatz, M., Ajtic, J., Ballabio, C., Barnet, I., Bochicchio, F., Borrelli, P., Bossew, P., Braga, R., Brattich, E., Briganti, A., Carpentieri, C., Castellani, C.-M., Castelluccio, M., Chiaberto, E., Ciotoli, G., Coletti, C., Cucchi, A., Daraktchieva, Z., Di Carlo, C., De France, J., Dehandschutter, B., Domingos, F., Dudar, T., Elio, J., Falletti, P., Ferreira, A., Finne, I.E., 2020. European atlas of natural radiation. https://doi.org/10.2760/46388

Cinelli, G., Tollefsen, T., Bossew, P., Gruber, V., Bogucarskis, K., De Felice, L., De Cort, M., 2019. Digital version of the European Atlas of natural radiation. Journal of Environmental Radioactivity 196, 240–252. https://doi.org/10.1016/j.jenvrad.2018.02.008

Cinelli, G., Tondeur, F., Dehandschutter, B., 2011. Development of an indoor radon risk map of the Walloon region of Belgium, integrating geological information. Environmental Earth Sciences 62, 809–819. https://doi.org/10.1007/s12665-010-0568-5

Ciotoli, G., Voltaggio, M., Tuccimei, P., Soligo, M., Pasculli, A., Beaubien, S.E., Bigi, S., 2017. Geographically weighted regression and geostatistical techniques to construct the geogenic radon potential map of the Lazio region: A methodological proposal for the European Atlas of Natural Radiation. Journal of Environmental Radioactivity 166, 355–375. https://doi.org/10.1016/j.jenvrad.2016.05.010

Clark, R.N., Roush, T.L., 1984. Reflectance spectroscopy: Quantitative analysis techniques for remote sensing applications. Journal of Geophysical Research: Solid Earth 89, 6329–6340.

Coblinski, J.A., Inda, A.V., Demattê, J.A.M., Dotto, A.C., Gholizadeh, A., Giasson, É., 2021. Identification of minerals in subtropical soils with different textural classes by VIS–NIR–SWIR reflectance spectroscopy. CATENA 203, 105334. https://doi.org/10.1016/j.catena.2021.105334

Coleman, R.G., Delevaux, M.H., 1957. Occurrence of selenium in sulfides from some sedimentary rocks of the western United States. Economic geology 52, 499–527.

Colkesen, I., Sahin, E.K., Kavzoglu, T., 2016. Susceptibility mapping of shallow landslides using kernel-based Gaussian process, support vector machines and logistic regression. Journal of African Earth Sciences 118, 53–64.

Crandall, C.A., Katz, B.G., Hirten, J.J., 1999. Hydrochemical evidence for mixing of river water and groundwater during high-flow conditions, lower Suwannee River basin, Florida, USA. Hydrogeology Journal.

References

Cucoş Dinu, A., Călugăr, M.I., Burghele, B.D., Dumitru, O.A., Cosma, C., Onac, B.P., 2017. Radon levels in Romanian caves: an occupational exposure survey. Environmental Geochemistry and Health 39, 1085–1099. https://doi.org/10.1007/s10653-016-9878-1

Cumberland, S., Grice, K., Douglas, G., Moreau, J.W., 2016. Uranium mobility in organic matter-rich sediments: A review of geological and geochemical processes. Earth-Science Reviews Volume 159, pp. 160-185. https://doi.org/10.1016/j.earscirev.2016.05.010}

Cuney, M., 2008. The extreme diversity of uranium deposits. Mineralium Deposita 44, 3. https://doi.org/10.1007/s00126-008-0223-1

Cvetković, M., Kapuralić, J., Pejić, M., Kolenković Močilac, I., Rukavina, D., Smirčić, D., Kamenski, A., Matoš, B., Špelić, M., 2021. Soil gas measurements of radon, CO2 and hydrocarbon concentrations as indicators of subsurface hydrocarbon accumulation and hydrocarbon seepage. Sustainability 13, 3840.

Daraktchieva, Z., Appleton, J., Reese, D., 2015. Radon in Northern Ireland: Indicative Atlas. Centre for Radiation, Chemical and Environmental Hazards, Public Health England.

Darby, S., Hill, D., Auvinen, A., Barros-Dios, J.M., Baysson, H., Bochicchio, F., Deo, H., Falk, R., Forastiere, F., Hakama, M., Heid, I., Kreienbrock, L., Kreuzer, M., Lagarde, F., Mäkeläinen, I., Muirhead, C., Oberaigner, W., Pershagen, G., Ruano-Ravina, A., Ruosteenoja, E., Schaffrath Rosario, v, Tirmarche, M., Tomáscaron;ek, L., Whitley, E., Wichmann, H.-E., Doll, R., 2005. Radon in homes and risk of lung cancer: collaborative analysis of individual data from 13 European case-control studies. BMJ 2005;330:223. https://doi.org/10.1136/bmj.38308.477650.63

Dardac, M., 2018. Determining the geogenic influence for high indoor radon areas in ireland. Trinity College Dublin.

Daviran, M., Maghsoudi, A., Ghezelbash, R., Pradhan, B., 2021. A new strategy for spatial predictive mapping of mineral prospectivity: Automated hyperparameter tuning of random forest approach. Computers & Geosciences 148, 104688. https://doi.org/10.1016/j.cageo.2021.104688

Decima, A., McKenzie, J., Schreiber, B., 1988. The origin of" evaporitive" limestones; an example from the Messinian of Sicily (Italy). Journal of Sedimentary Research 58, 256–272.

Degu Belete, G., Alemu Anteneh, Y., 2021. General Overview of Radon Studies in Health Hazard Perspectives. Journal of Oncology 2021.

Demšar, U., Harris, P., Brunsdon, C., Fotheringham, A.S., McLoone, S., 2013. Principal component analysis on spatial data: an overview. Annals of the Association of American Geographers 103, 106–128.

Domingos, F., Cinelli, G., Neves, L., Pereira, A., Braga, R., Bossew, P., Tollefsen, T., 2020. Validation of a database of mean uranium, thorium and potassium concentrations in rock samples of Portuguese geological units, generated of literature data. Journal of Environmental Radioactivity 222, 106338. https://doi.org/10.1016/j.jenvrad.2020.106338

Dorn, F.E., 1901. "Ueber die von radioaktiven Substanzen ausgesandte Emanation.

Dornan, T., O’Sullivan, G., O’Riain, N., Stueeken, E., Goodhue, R., 2020. The application of machine learning methods to aggregate geochemistry predicts quarry source location: An example from Ireland. Computers & Geosciences 140, 104495. https://doi.org/10.1016/j.cageo.2020.104495

Dosseto, A., Buss, H., Suresh, P.O., 2011. The delicate balance between soil production and erosion, and its role on landscape evolution. Applied Geochemistry 26, S24–S27. https://doi.org/10.1016/j.apgeochem.2011.03.020

Drolet, J.-P., Martel, R., Poulin, P., Dessau, J.-C., 2014. Methodology developed to make the Quebec indoor radon potential map. Science of The Total Environment 473–474, 372–380. https://doi.org/10.1016/j.scitotenv.2013.12.039

Duffy, J.T., Madden, J.S., Mackin, G.M., McGarry, A.T., Colgan, P.A., 1996. A reconnaissance survey of radon in show caves in Ireland. Environment International 22, 415–423. https://doi.org/10.1016/S0160-4120(96)00140-7

Duggal, V., Rani, A., Mehra, R., 2014. Measurement of soil-gas radon in some areas of northern Rajasthan, India. Journal of Earth System Science 123, 1241–1247.

Dungca, J., Galupino, J., 2017. Artificial neural network permeability modeling of soil blended with fly ash. GEOMATE 12, 77–82. https://doi.org/10.21660/2017.31.6549

Egli, M., Mirabella, A., Fitze, P., 2001. Clay mineral formation in soils of two different chronosequences in the Swiss Alps. Geoderma 104, 145–175. https://doi.org/10.1016/S0016-7061(01)00079-9

Egozcue, J.J., Pawlowsky-Glahn, V., Mateu-Figueras, G., Barcelo-Vidal, C., 2003. Isometric logratio transformations for compositional data analysis. Mathematical geology 35, 279–300.

Elbaz-Poulicheet, F., Nagy, A., Cserny, T., 1997. The Distribution of Redox Sensitive Elements (U, As, Sb, V and Mo) along a River-Wetland-Lake System (Balaton Region, Hungary). Aquatic Geochemistry 3, 267–282. https://doi.org/10.1023/A:1009616214030

Elders, W., Moore, J., 2016. Geology of geothermal resources. Geothermal Power Generation 7–32.

Elío, J., Crowley, Q., Scanlon, R., Hodgson, J., Long, S., 2019. Rapid radon potential classification using soil-gas radon measurements in the Cooley Peninsula, County Louth, Ireland. Environmental Earth Sciences 78, 359. https://doi.org/10.1007/s12665-019-8339-4

Elío, J., Crowley, Q., Scanlon, R., Hodgson, J., Long, S., 2017. Logistic regression model for detecting radon prone areas in Ireland. Science of The Total Environment 599–600. https://doi.org/10.1016/j.scitotenv.2017.05.071

Elío, J., Crowley, Q., Scanlon, R., Hodgson, J., Long, S., Cooper, M., Gallagher, V., 2020. Application of airborne radiometric surveys for large-scale geogenic radon potential classification. Journal of the European Radon Association.

Elío, J., Crowley, Q., Scanlon, R., Hodgson, J., Zgaga, L., 2018. Estimation of residential radon exposure and definition of Radon Priority Areas based on expected lung cancer incidence. Environment International 114, 69–76. https://doi.org/10.1016/j.envint.2018.02.025

Environmental Protection Agency, 2022. New EPA Radon maps show more homes and workplaces at risk from cancer-causing gas. https://www.epa.ie/news-releases.

Environmental Protection Agency, 2019a. EPA protocol for the measurement of radon in homes and workplaces.

Environmental Protection Agency, 2019b. National Radon Control Strategy. Straiteis Naisiunta um Rialu Radoin. Phase 1 2014-2018.

Environmental Protection Agency Ireland, 2020. Radon Map :: Environmental Protection Agency, Ireland [WWW Document]. URL https://www.epa.ie/radiation/radonmap/

EPA, 2019. EPA Protocol for the measurement of radon in homes and workplaces.

Esan, D.T., Sridhar, M.K.C., Obed, R., Ajiboye, Y., Afolabi, O., Olubodun, B., Oni, O.M., 2020. Determination of Residential Soil Gas Radon Risk Indices Over the Lithological Units of a Southwestern Nigeria University. Scientific reports 10, 1–10.

European Commission, 2013. Council directive 2013/59/Euratom. Official Journal of the European Union 2013/59/EURATOM.

Faanu, A., Darko, E., Ephraim, J., 2011. Determination of natural radioactivity and hazard in soil and rock samples in a mining area in Ghana. West African Journal of Applied Ecology 19.

Fabritius, O., Puhakka, E., Li, X., Nurminen, A., Siitari-Kauppi, M., 2022. Radium sorption on biotite; surface complexation modeling study. Applied Geochemistry 140, 105289.

Fallon, E.K., Frische, M., Petersen, S., Brooker, R.A., Scott, T.B., 2019. Geological, mineralogical and textural impacts on the distribution of environmentally toxic trace elements in seafloor massive sulfide occurrences. Minerals 9, 162.

Fan, D., Zhang, T., Ye, J., 2004. The Xikuangshan Sb deposit hosted by the Upper Devonian black shale series, Hunan, China. Ore Geology Reviews 24, 121–133.

Fang, Q., Hong, H., Zhao, L., Furnes, H., Lu, H., Han, W., Liu, Y., Jia, Z., Wang, C., Yin, K., 2017. Tectonic uplift-influenced monsoonal changes promoted hominin occupation of the Luonan Basin: insights from a loess-paleosol sequence, eastern Qinling Mountains, central China. Quaternary Science Reviews 169, 312–329.

Farhadi, S., Afzal, P., Boveiri Konari, M., Daneshvar Saein, L., Sadeghi, B., 2022. Combination of Machine Learning Algorithms with Concentration-Area Fractal Method for Soil Geochemical Anomaly Detection in Sediment-Hosted Irankuh Pb-Zn Deposit, Central Iran. Minerals 12. https://doi.org/10.3390/min12060689

Fennell, Stephen G., Mackin, G.M., Madden, J.S., McGarry, A.T., Duffy, J.T., O’colmain, M., Colgan, P.A., Pollard, D., 2002. Radon in dwellings: the Irish National Radon survey. Radiological Protection Institute of Ireland Dublin.

Fennell, S.G, Mackin, G.M., McGarry, A.T., Pollard, D., 2002. Radon exposure in Ireland. International Congress Series 1225, 71–77. https://doi.org/10.1016/S0531-5131(01)00549-0

Ferreira, A., Daraktchieva, Z., Beamish, D., Kirkwood, C., Lister, T.R., Cave, M., Wragg, J., Lee, K., 2018. Indoor radon measurements in south west England explained by topsoil and stream sediment geochemistry, airborne gamma-ray spectroscopy and geology. Journal of Environmental Radioactivity 181, 152–171. https://doi.org/10.1016/j.jenvrad.2016.05.007

Friedmann, H., 2005. Final results of the Austrian radon project. Health Physics 89, 339–348. https://doi.org/10.1097/01. HP.0000167228.18113.27

Friedmann, H., Baumgartner, A., Bernreiter, M., Gräser, J., Gruber, V., Kabrt, F., Kaineder, H., Maringer, F.J., Ringer, W., Seidel, C., Wurm, G., 2017. Indoor radon, geogenic radon surrogates and geology – Investigations on their correlation. Journal of Environmental Radioactivity 166, 382–389. https://doi.org/10.1016/j.jenvrad.2016.04.028

Friedmann, H., Gröller, J., 2010. An approach to improve the Austrian Radon Potential Map by Bayesian statistics. Journal of Environmental Radioactivity 101, 804–808. https://doi.org/10.1016/j. jenvrad.2009.11.008

Fu, C.-C., Yang, T.F., Chen, C.-H., Lee, L.-C., Wu, Y.-M., Liu, T.-K., Walia, V., Kumar, A., Lai, T.-H., 2017. Spatial and temporal anomalies of soil gas in northern Taiwan and its tectonic and seismic implications. Journal of Asian Earth Sciences 149, 64–77. https://doi.org/10.1016/j.jseaes.2017.02.032

Fuente, M., Long, S., Fenton, D., Hung, L.C., Goggins, J., Foley, M., 2020. Review of recent radon research in Ireland, OPTI-SDS project and its impact on the National Radon Control Strategy. Applied Radiation and Isotopes 163, 109210. https://doi.org/10.1016/j.apradiso.2020.109210

Fyffe, L.R., Pickerill, R.K., 1993. Geochemistry of Upper Cambrian-Lower Ordovician black shale along a northeastern Appalachian transect. Geological Society of America Bulletin 105, 897–910.

Gaafar, I., Hanfi, M., El-Ahll, L.S., Zeidan, I., 2021. Assessment of radiation hazards from phosphate rocks, Sibaiya area, central eastern desert, Egypt. Applied Radiation and Isotopes 173, 109734. https://doi.org/10.1016/j.apradiso.2021.109734

Gadd, G.M., 2010. Metals, minerals and microbes: geomicrobiology and bioremediation. Microbiology 156, 609–643.

Gallagher, V., Grunsky, E.C., Fitzsimons, M.M., Browne, M.A., Lilburn, S., Symons, J., 2022. Tellus regional stream water geochemistry: environmental and mineral exploration applications. Geochemistry: Exploration, Environment, Analysis 22, geochem2021-050.

Gallagher, V., Knights, K.V., Carey, S., Glennon, M., Scanlon, R., 2016. Atlas of topsoil geochemistry of the Northern Counties of Ireland: Data from the Tellus and Tellus border projects. Geological Survey of Ireland.

Gaskin, J., Coyle, D., Whyte, J., Krewksi, D., 2018. Global Estimate of Lung Cancer Mortality Attributable to Residential Radon. Environmental Health Perspectives 126, 057009. https://doi.org/10.1289/EHP2503

Giustini, F., Ciotoli, G., Rinaldini, A., Ruggiero, L., Voltaggio, M., 2019. Mapping the geogenic radon potential and radon risk by using Empirical Bayesian Kriging regression: A case study from a volcanic area of central Italy. Science of the Total Environment 661, 449–464.

Gomez, C., Lagacherie, P., Coulouma, G., 2008. Continuum removal versus PLSR method for clay and calcium carbonate content estimation from laboratory and airborne hyperspectral measurements. Geoderma 148, 141–148.

Goodfellow, B.W., Fredin, O., Derron, M.-H., Stroeven, A.P., 2009. Weathering processes and Quaternary origin of an alpine blockfield in Arctic Sweden. Boreas 38, 379–398. https://doi.org/10.1111/j.1502-3885.2008.00061.x

Gregory, D.D., Large, R.R., Halpin, J.A., Baturina, E.L., Lyons, T.W., Wu, S., Danyushevsky, L., Sack, P.J., Chappaz, A., Maslennikov, V.V., 2015. Trace element content of sedimentary pyrite in black shales. Economic Geology 110, 1389–1410.

Grunsky, E.C., 2010. The interpretation of geochemical survey data. Geochemistry: Exploration, Environment, Analysis 10, 27–74.

Grunsky, E.C., Caritat, P. de, 2019. State-of-the-art analysis of geochemical data for mineral exploration. Geochemistry: Exploration, Environment, Analysis 20, 217–232. https://doi.org/10.1144/geochem2019-031

Günay, O., Saç, M.M., İçhedef, M., Taşköprü, C., 2018. Soil gas radon concentrations along the Ganos Fault (GF). Arabian Journal of Geosciences 11, 213. https://doi.org/10.1007/s12517-018-3542-2

Gunn, J., 1982. Crag Cave, County Kerry. Irish Naturalists Journal Ltd. 20, 445–449.

Gunning, G.A., 2016. Studies of radon in Ireland: Outdoor levels, detector intercomparison and school remediation methods. Trinity College (Dublin, Ireland). School of Physics.

Ha, M., Hwang, S., Kang, S., Park, N.-W., Chang, B.-U., Kim, Y., 2017. Geographical Correlations between Indoor Radon Concentration and Risks of Lung Cancer, Non-Hodgkin's Lymphoma, and Leukemia during 1999–2008 in Korea. International Journal of Environmental Research and Public Health 14, 344. https://doi.org/10.3390/ijerph14040344

Habib, R.R., Nuwayhid, R.Y., Hamdan, Z., Alameddine, I., Katul, G., 2018. Indoor and Outdoor Radon Concentration Levels in Lebanon. Health Physics 115.

Hamideen, M.S., Bdair, O.M., Chandrasekaran, A., Saleh, H., Elimat, Z., 2020. Multivariate statistical investigations of natural radioactivity and radiological hazards in building materials mainly used in Amman Province, Jordan. International Journal of Environmental Analytical Chemistry 100, 189–203.

Hampson, S.E., Andrews, J.A., Lee, M.E., Foster, L.S., Glasgow, R.E., Liechtenstein, E., 1998. Lay Understanding of Synergistic Risk: The Case of Radon and Cigarette Smoking. Risk Analysis 18, 343–350. https://doi.org/10.1111/j.1539-6924.1998.tb01300.x

Harb, S., Abbady, A.E.-B., El-Kamel, A.E.-H., Saleh, I.I., Abd El-Mageed, A.I., 2012. Natural radioactivity and their radiological effects for different types of rocks from Egypt. Radiation Physics and Chemistry 81, 221–225. https://doi.org/10.1016/j.radphyschem.2011.11.005

Haruna, R., Saleh, M.A., Hashim, S., Hamzah, K., Zainal, J., Sanusi, M.S.M., 2020. Assessment of geogenic radon potential in Johor Malaysia. Journal of Radioanalytical and Nuclear Chemistry 326, 1065–1074. https://doi.org/10.1007/s10967-020-07396-y

Hastie, T., Tibshirani, R., Friedman, J.H., Friedman, J.H., 2009. The elements of statistical learning: data mining, inference, and prediction. Springer.

Heimsath, A.M., Dietrich, W.E., Nishiizumi, K., Finkel, R.C., 1997. The soil production function and landscape equilibrium. Nature 388, 358–361. https://doi.org/10.1038/41056

Hellmann, R., Wirth, R., Daval, D., Barnes, J.-P., Penisson, J.-M., Tisserand, D., Epicier, T., Florin, B., Hervig, R.L., 2012. Unifying natural and laboratory chemical weathering with interfacial dissolution–reprecipitation: A study based on the nanometer-scale chemistry of fluid–silicate interfaces. Chemical Geology 294–295, 203–216. https://doi.org/10.1016/j.chemgeo.2011.12.002

Hickey, C., 2019. Setting the Scene.

Highland, L.M., 2018. Landslide hazard and risk: Current and future directions for the United States Geological Survey's Landslide Program, in: Landslide Risk Assessment. Routledge, pp. 207–213.

Hitzman, M., 1995. Geological setting of the Irish Zn-Pb-(Ba-Ag) orefield.

Hodson, F., 1954. The Carboniferous Rocks of Foynes Island, County Limerick.

Holliday, K., Hartmann, T., Poineau, F., Rory Kennedy, J., Czerwinski, K., 2009. Synthesis and characterization of zirconia–magnesia inert matrix fuel: Uranium homolog studies. Journal of Nuclear Materials 393, 224–229. https://doi.org/10.1016/j.jnucmat.2009.06.007

Hong, H., Churchman, G.J., Yin, K., Li, R., Li, Z., 2014. Randomly interstratified illite–vermiculite from weathering of illite in red earth sediments in Xuancheng, southeastern China. Geoderma 214, 42–49.

Horstman, E.L., 1957. The distribution of lithium, rubidium and caesium in igneous and sedimentary rocks. Geochimica et Cosmochimica Acta 12, 1–28.

House, P.K., 2005. Using geology to improve flood hazard management on alluvial fans-an example from laughlin, Nevada. JAWRA Journal of the American Water Resources Association 41, 1431–1447.

Howard III, J.H., 1977. Geochemistry of selenium: formation of ferroselite and selenium behavior in the vicinity of oxidizing sulfide and uranium deposits. Geochimica et Cosmochimica Acta 41, 1665–1678.

Hyun, S.P., Davis, J.A., Hayes, K.F., 2014. Abiotic U (VI) reduction by aqueous sulfide. Applied geochemistry 50, 7–15.

Ibrahim, M.E., Saleh, G.M., Abd El-Naby, H.H., 2001. Uranium mineralization in the two mica granite of Gabal Ribdab area, South Eastern Desert, Egypt. Applied Radiation and Isotopes 55, 861–872. https://doi.org/10.1016/S0969-8043(01)00122-1

ICRP, 2019. Radiological protection from naturally occuring radioactive material (NORM) in industrial processes. 142.

Idriss, H., Salih, I., Alaamer, A.S., Abdelgalil, M., Salih, S.A., Hasan, A.M., ELtahir, M.A., Ahamed, M.M., 2014. Study of radon in soil gas, trace elements and climatic parameters around South Kordofan state, Sudan. Environmental earth sciences 72, 335–339.

Iida, Y., Tanaka, T., Yamaguchi, T., Nakayama, S., 2011. Sorption Behavior of Selenium (—II) on Rocks under Reducing Conditions. Journal of nuclear science and technology 48, 279–291.

Ioannides, K., Papachristodoulou, C., Stamoulis, K., Karamanis, D., Pavlides, S., Chatzipetros, A., Karakala, E., 2003. Soil gas radon: a tool for exploring active fault zones. Applied Radiation and Isotopes 59, 205–213.

Irish Cancer Society, 2016. 12 ways to reduce your risk of getting cancer.

Jansson, N.F., Liu, W., 2020. Controls on cobalt and nickel distribution in hydrothermal sulphide deposits in Bergslagen, Sweden - constraints from solubility modelling. GFF 142, 87–95. https://doi.org/10.1080/11035897.2020.1751270

Je, H., Kang, C., Chon, H., 1999. A Preliminary Study on Soil–Gas Radon Geochemistry According to Different Bedrock Geology in Korea. Environmental Geochemistry and Health 21, 117–131. https://doi.org/10.1023/A:1006613016217

Jelle, B.P., 2012. Development of a model for radon concentration in indoor air. Science of The Total Environment 416, 343–350. https://doi.org/10.1016/j.scitotenv.2011.11.052

Jiang, S.-Y., Chen, Y.-Q., Ling, H.-F., Yang, J.-H., Feng, H.-Z., Ni, P., 2006. Trace- and rare-earth element geochemistry and Pb–Pb dating of black shales and intercalated Ni–Mo–PGE–Au sulfide ores in Lower Cambrian strata, Yangtze Platform, South China. Mineralium Deposita 41, 453–467. https://doi.org/10.1007/s00126-006-0066-6

Jiang, S.-Y., Zhao, H.-X., Chen, Y.-Q., Yang, T., Yang, J.-H., Ling, H.-F., 2007. Trace and rare earth element geochemistry of phosphate nodules from the lower Cambrian black shale sequence in the Mufu Mountain of Nanjing, Jiangsu province, China. Chemical Geology 244, 584–604.

Johnson, D.L., Watson-Stegner, D., 1987. Evolution model of pedogenesis. Soil Science 143, 349–366.

Johnston, J., Raub, T., Ashton, J., 2013. Mineral magnetism identifies the presence of pyrrhotite in the Navan Zn-Pb deposit, Ireland: implications for low temperature pyrite to pyrrhotite reduction, timing of mineralization and future exploration strategies. Mineral deposit research for a hi-tech world, Uppsala 323–325.

Jones, D., Plant, J., 1989. Geochemistry of shales. Springer.

Kanagawa, M., Hennig, P., Sejdinovic, D., Sriperumbudur, B.K., 2018. Gaussian processes and kernel methods: A review on connections and equivalences. arXiv preprint arXiv:1807.02582.

Kemski, J., Klingel, R., Siehl, A., 1996. Classification and mapping of radon-affected areas in Germany. Environment International 22, 789–798.

Kemski, J., Siehl, A., Stegemann, R., Valdivia-Manchego, M., 2001. Mapping the geogenic radon potential in Germany. Science of The Total Environment 272, 217–230. https://doi.org/10.1016/S0048-9697(01)00696-9

Khan, F., Khattak, S.A., Wazir, Z., Waqas, M., 2021. Spatial distribution of radon concentrations in Balakot-Bagh (B–B) Fault Line and adjoining areas, Lesser Himalayas, North Pakistan. Environmental Earth Sciences 80, 291. https://doi.org/10.1007/s12665-021-09569-8

Khan, S.M., Gomes, J., Krewski, D.R., 2019. Radon interventions around the globe: A systematic review. Heliyon 5, e01737. https://doi.org/10.1016/j.heliyon.2019.e01737

Kiczka, M., Wiederhold, J.G., Frommer, J., Voegelin, A., Kraemer, S.M., Bourdon, B., Kretzschmar, R., 2011. Iron speciation and isotope fractionation during silicate weathering and soil formation in an alpine glacier forefield chronosequence. Geochimica et Cosmochimica Acta 75, 5559–5573. https://doi.org/10.1016/j.gca.2011.07.008

Kikaj, D., Jeran, Z., Bahtijari, M., Stegnar, P., 2016. Radon in soil gas in Kosovo. Journal of Environmental Radioactivity 164, 245–252. https://doi.org/10.1016/j.jenvrad.2016.07.037

Kim, E., Ahn, H., Jo, H.Y., Ryu, J.-H., Koh, Y.-K., 2017. Chlorite alteration in aqueous solutions and uranium removal by altered chlorite. Journal of hazardous materials 327, 161–170.

Kim, S.W., Kee, W.-S., Lee, S., Lee, B.C., Byun, U.H., 2021. Tracking and Evaluating the Concentrations of Natural Radioactivity According to Chemical Composition in the Precambrian and Mesozoic Granitic Rocks in the Jangsu-gun Area, Central Southwestern South Korea. Minerals 11. https://doi.org/10.3390/min11070684

Kirasich, K., Smith, T., Sadler, B., 2018. Random forest vs logistic regression: binary classification for heterogeneous datasets. SMU Data Science Review 1, 9.

Koglin, N., Frimmel, H.E., Lawrie Minter, W.E., Brätz, H., 2010. Trace-element characteristics of different pyrite types in Mesoarchaean to Palaeoproterozoic placer deposits. Mineralium Deposita 45, 259–280. https://doi.org/10.1007/s00126-009-0272-0

Koljonen, T., 1976. Luikolahti: Selenium in the vicinity of copper ore. Journal of Geochemocal Exploration 5, 263–265.

Koribanics, N.M., Tuorto, S.J., Lopez-Chiaffarelli, N., McGuinness, L.R., Häggblom, M.M., Williams, K.H., Long, P.E., Kerkhof, L.J., 2015. Spatial Distribution of an Uranium-Respiring Betaproteobacterium at the Rifle, CO Field Research Site. PLOS ONE 10, e0123378. https://doi.org/10.1371/journal.pone.0123378

Kovalev, SG, Puchkov, V., Kovalev, SS, 2014. First findings of siegenite (CoNi 2 S 4) in picritic and picrodoleritic complexes of the Southern Urals. Presented at the Doklady Earth Sciences, Springer, pp. 796–802.

Kreuzer, M., Fenske, N., Schnelzer, M., Walsh, L., 2015. Lung cancer risk at low radon exposure rates in German uranium miners. British journal of cancer 113, 1367–1369.

Krewski, D., Lubin, J.H., Zielinsk, J.M., Alavanja, M., Catalan, V.S., Field, R.W., Klot, J.B., Letournea, E.G., Lynch, C.F., Lyon, J.I., Sandler, D.P., Schoenberg, J.B., Steck, D.J., Stolwijk, J.A., Weinberg, C., Wilcox, H.B., 2019. Residential Radon and Risk of Lung Cancer A Combined Analysis of 7 North American Case-Control Studies. Epidemiology 16. https://doi.org/0.1097/01.ede.0000152522.80261.e3

Kropat, G., Bochud, F., Jaboyedoff, M., Laedermann, J.-P., Murith, C., Palacios, M., Baechler, S., 2014. Major influencing factors of indoor radon concentrations in Switzerland. Journal of environmental radioactivity 129, 7–22.

Kulali, F., Akkurt, I., Özgür, N., 2017. The effect of meteorological parameters on radon concentration in soil gas. Acta Physica Polonica A 132, 999–1001.

Kumar, A., Arora, V., Walia, V., Bajwa, B.S., Singh, S., Yang, T.F., 2014. Study of soil gas radon variations in the tectonically active Dharamshala and Chamba regions, Himachal Pradesh, India. Environmental Earth Sciences 72, 2837–2847.

Laiolo, M., Ranaldi, M., Tarchini, L., Carapezza, M.L., Coppola, D., Ricci, T., Cigolini, C., 2016. The effects of environmental parameters on diffuse degassing at Stromboli volcano: Insights from joint monitoring of soil CO2 flux and radon activity. Journal of Volcanology and Geothermal Research. http://dx.doi.org/10.1016/j.jvolgeores.2016.02.004 0377-0273

Lantz, P.M., Mendez, D., Philbert, M.A., 2013. Radon, smoking, and lung cancer: the need to refocus radon control policy. American journal of public health 103, 443–447.

Larson, M.G., 2008. Analysis of variance. Circulation 117, 115–121. https://doi.org/10.1161/CIRCULATIONAHA.107.654335

Lecomte, A., Cathelineau, M., Michels, R., Peiffert, C., Brouand, M., 2017. Uranium mineralization in the Alum Shale Formation (Sweden): Evolution of a U-rich marine black shale from sedimentation to metamorphism. Ore Geology Reviews 88, 71–98. https://doi.org/10.1016/j.oregeorev.2017.04.021

Leuraud, K., Schnelzer, M., Tomasek, L., Hunter, N., Timarche, M., Grosche, B., Kreuzer, M., Laurier, D., 2011. Radon, Smoking and Lung Cancer Risk: Results of a Joint Analysis of Three European Case-Control Studies Among Uranium Miners. Radiation research 176, 375–87. https://doi.org/10.2307/41318201

Lewin, J., Gibbard, P.L., 2010. Quaternary river terraces in England: Forms, sediments and processes. Geomorphology 120, 293–311. https://doi.org/10.1016/j.geomorph.2010.04.002

Li, C., Wang, C., Yu, J., Fan, Y., Liu, D., Zhou, W., Shi, 2020. Residential Radon and Histological Types of Lung Cancer: A Meta-Analysis of Case–Control Studies. Int. J. Environ. Res. Public Health 17. https://doi.org/10.3390/ijerph17041457

Liao, R., Shi, Z., Chen, Y., Zhang, J., Wang, X., Hou, Y., Zhang, K., 2020. Characteristics of uranium sorption on illite in a ternary system: effect of phosphate on adsorption. Journal of Radioanalytical and Nuclear Chemistry 323, 159–168.

Lin, H.-T., Liu, F.-C., Wu, C.-Y., Kuo, C.-F., Lan, W.-C., Yu, H.-P., 2019. Epidemiology and Survival Outcomes of Lung Cancer: A Population-Based Study. BioMed Research International 2019, 8148156. https://doi.org/10.1155/2019/8148156

Liping, H.E., Chen, B., Zhao, C., Zhuo, W., 2016. The study on effects of indoor air filtration on radon exposure to residents. Chinese Journal of Radiological Medicine and Protection 36, 688–693.

Liu, B., Mastalerz, M., Schieber, J., Teng, J., 2020. Association of uranium with macerals in marine black shales: Insights from the Upper Devonian New Albany Shale, Illinois Basin. International Journal of Coal Geology 217, 103351. https://doi.org/10.1016/j.coal.2019.103351

Liu, J., Rong, Y., Zhang, S., 2017. Mineralogy of Zn–Hg–S and Hg–Se–S Series Minerals in Carbonate-Hosted Mercury Deposits in Western Hunan, South China. Minerals 7, 101.

Liu, Y., Ma, B., Lv, Y., Wang, C., Chen, Y., 2022. Thorough extraction of lithium and rubidium from lepidolite via thermal activation and acid leaching. Minerals Engineering 178, 107407.

Long, J.A., Large, R.R., Lee, M.S., Benton, M.J., Danyushevsky, L.V., Chiappe, L.M., Halpin, J.A., Cantrill, D., Lottermoser, B., 2016. Severe selenium depletion in the Phanerozoic oceans as a factor in three global mass extinction events. Gondwana Research 36, 209–218.

Long, S.C., Fenton, D., Scivyer, C., Monahan, E., 2016. Factors underlying persistently high radon levels in a house located in a karst limestone region of Ireland – lessons learned about remediation. Nukleonika 61, 327–332. https://doi.org/10.1515/nuka-2016-0054

López, P.O., Dauer, L.T., Loose, R., Martin, C.J., Miller, D.L., Vañó, E., Doruff, M., Padovani, R., Massera, G., Yoder, C., 2018. ICRP Publication 139: Occupational Radiological Protection in Interventional Procedures. Ann ICRP 47, 1–118. https://doi.org/10.1177/0146645317750356

Lorenzo-González, M., Torres-Durán, M., Barbosa-Lorenzo, R., Provencio-Pulla, M., Barros-Dios, J.M., Ruano-Ravina, A., 2019. Radon exposure: a major cause of lung cancer. Expert Rev. Respir. Med 13, 839–850. https://doi.org/10.1080/17476348.2019.1645599

Loring, D.H., 1976. Distribution and partition of cobalt, nickel, chromium, and vanadium in the sediments of the Saguenay fjord. Can. J. Earth Sci. 13, 1706–1718. https://doi.org/10.1139/e76-180

Lowe, J.J., Walker, M., 2014. Reconstructing quaternary environments. Routledge.

Lucchetti, C., Briganti, A., Castelluccio, M., Galli, G., Santilli, S., Soligo, M., Tuccimei, P., 2019. Integrating radon and thoron flux data with gamma radiation mapping in radon-prone areas. The case of volcanic outcrops in a highly-urbanized city (Roma, Italy). Journal of Environmental Radioactivity 202, 41–50. https://doi.org/10.1016/j.jenvrad.2019.02.004

Ludewig, P., Lorenser, E., 1924. Untersuchung der Grubenluft in den Schneeberger Gruben auf den Gehalt an Radiumemanation. Zeitschrift für Physik 22, 178–185.

Luecke, W., 1981. Lithium pegmatites in the Leinster Granite (southeast Ireland). Chemical Geology 34, 195–233. https://doi.org/10.1016/0009-2541(81)90113-3

MacDermot, C., McConnell, B., Pracht, M., 2003. Bedrock geology 1: 100, 000 Sacle map series, sheet 14, Galway Bay. Geological Survey of Ireland, Dublin.

Mahajan, S., Walia, V., Bajwa, B., Kumar, A., Singh, S., Seth, N., Dhar, S., Gill, G., Yang, T., 2010. Soil-gas radon/helium surveys in some neotectonic areas of NW Himalayan foothills, India. Natural Hazards and Earth System Sciences 10, 1221–1227.

Malczewski, D., Dziurowicz, M., Kalab, Z., Rösnerová, M., 2021. Natural radioactivity of rocks from the historic Jeroným Mine in the Czech Republic. Environmental Earth Sciences 80, 650. https://doi.org/10.1007/s12665-021-09944-5

Malczewski, D., Żaba, J., 2012. Natural radioactivity in rocks of the Modane–Aussois region (SE France). Journal of Radioanalytical and Nuclear Chemistry 292, 123–130. https://doi.org/10.1007/s10967-011-1428-9

Malisa, E.P., 2001. The Behaviour of Selenium in Geological Processes. Environmental Geochemistry and Health 23, 137–158. https://doi.org/10.1023/A:1010908615486

Margineanu, R.M., 2019. Radon measurements in underground mines and caves from several European countries, in: AIP Conference Proceedings. AIP Publishing LLC, p. 050004.

Marks, F.R., Menuge, J.F., Boyce, A.J., Blakeman, R.J., 2017. Controls on the formation of a large Zn-Pb Irish-type deposit: evidence from the Navan halo. Programme and 61.

Marsh, J.W., Tomášek, L., Laurier, D., Harrison, J.D., 2021. Effective dose coefficients for radon and progeny: A review of ICRP and UNSCEAR values. Radiation Protection Dosimetry 195, 1–20. https://doi.org/10.1093/rpd/ncab106

Massoud, A., Abdou, F.S., Yousif, M., 2023. Evaluation of mineral compositions of surface and subsurface rock samples by neutron activation analysis. International Journal of Environmental Analytical Chemistry 103, 528–545. https://doi.org/10.1080/03067319.2020.1862095

McArdle, P., Kennedy, M., 1986. The east Carlow deformation zone and its regional implications.

McCarthy Jr, J.H., Reimer, G.M., 1986. Advances in soil gas geochemical exploration for natural resources: Some current examples and practices. Journal of Geophysical Research: Solid Earth 91, 12327–12338.

McConnell, B., Philcox, M., 1994. Geology of Kildare-Wicklow: a geological description to accompany the bedrock geology 1: 100,000 Map Series, Sheet 16, Kildare-Wicklow. Published under the authority of the Director of the Geological Survey of ….

McGrath, D., Fleming, G.A., Culleton, N., 2008. Trace elements and heavy metals in Irish soils. Teagasc, Wexford, Ireland 210.

McIlwaine, R., Cox, S.F., Doherty, R., Palmer, S., Ofterdinger, U., McKinley, J.M., 2014. Comparison of methods used to calculate typical threshold values for potentially toxic elements in soil. Environmental Geochemistry and Health 36, 953–971. https://doi.org/10.1007/s10653-014-9611-x

McKelvey, V.E., Everhart, D.L., Garrels, R.M., 1955. Origin of uranium deposits.

McKinley, J.M., Grunsky, E., Mueller, U., 2018. Environmental monitoring and peat assessment using multivariate analysis of regional-scale geochemical data. Mathematical Geosciences 50, 235–246.

McKinley, J.M., Ofterdinger, U., Young, M., Barsby, A., Gavin, A., 2013. Investigating local relationships between trace elements in soils and cancer data. Spatial Statistics 5, 25–41. https://doi.org/10.1016/j.spasta.2013.05.001

Meenakshi, C., Mohankumar, M.N., 2013. Synergistic effect of radon in blood cells of smokers – An in vitro study. Mutation Research/Genetic Toxicology and Environmental Mutagenesis 757, 79–82. https://doi.org/10.1016/j.mrgentox.2013.06.018

Mehta, N., Kocar, B.D., 2019. Geochemical conditions conducive for retention of trace elements and radionuclides during shale–fluid interactions. Environmental Science: Processes & Impacts 21, 1764–1776.

Mei, H., Aoyagi, N., Saito, T., Kozai, N., Sugiura, Y., Tachi, Y., 2022. Uranium (VI) sorption on illite under varying carbonate concentrations: Batch experiments, modeling, and cryogenic time-resolved laser fluorescence spectroscopy study. Applied Geochemistry 136, 105178. https://doi.org/10.1016/j.apgeochem.2021.105178

Miklyaev, P.S., Petrova, T.B., Shchitov, D.V., Sidyakin, P.A., Murzabekov, M.A., Marennyy, A.M., Nefedov, N.A., Sapozhnikov, Y.A., 2021. The results of long-term simultaneous measurements of radon exhalation rate, radon concentrations in soil gas and groundwater in the fault zone. Applied Radiation and Isotopes 167, 109460. https://doi.org/10.1016/j.apradiso.2020.109460

Miles, J., 1997. Calibration and standardisation of etched track detectors, in: Radon Measurements By Etched Track Detectors: Applications in Radiation Protection, Earth Sciences and the Environment. World Scientific, pp. 143–154.

Miles, J., Appleton, J., Rees, D., Green, B., Adlam, K., Myers, A., 2007. Indicative Atlas of Radon in England and Wales (Chilton). Health Protection Agency.

Min, M., Xu, H., Mostafa Fayek, Chen, J., 2005. Evidence of uranium biomineralization in sandstone-hosted roll-front uranium deposits, northwestern China. Ore Geology Reviews 26. https://doi.org/10.1016/j.oregeorev.2004.10.003

Mingxing, L., Xiaoyong, Y., Wei, S., Jianyu, M., Chiyang, L., 2006. REE/trace element characteristics of sandstone-type uranium deposits in the Ordos basin.

Ministry of Environment of the Slovak Republic, 81102 Bratislava (Slovakia), 2003. Report on state of the environment of the Slovak Republic 2002. Ministry of Environment of the Slovak Republic, Slovakia.

Mitra, S., Chowdhury, S., Mukherjee, J., Sutradhar, S., Mondal, S., Barman, C., Deb, A., 2021. Assessment of radon (222Rn) activity in groundwater and soil-gas in Purulia district, West Bengal, India. Journal of Radioanalytical and Nuclear Chemistry 330, 1331–1338.

Moldrup, P., Olesen, T., Komatsu, T., Schjønning, P., Rolston, D., 2001. Tortuosity, diffusivity, and permeability in the soil liquid and gaseous phases. Soil Science Society of America Journal 65, 613–623.

Molenaar, N., de Jong, A.F.M., 1987. Authigenic quartz and albite in Devonian limestones: origin and significance. Sedimentology 34, 623–640. https://doi.org/10.1111/j.1365-3091.1987.tb00791.x

Monastero, R.N., Meliker, J.R., 2020. Incidence of brain and spinal cord cancer and county-level radon levels in New Jersey, Wisconsin, Minnesota, Pennsylvania, and Iowa, USA. Environmental Geochemistry and Health 42, 389–395. https://doi.org/10.1007/s10653-019-00368-6

Monty, C., 2000. UNSCEAR Report 2000: Sources and Effects of Ionizing Radiation. Journal of Radiological Protection 21. https://doi.org/10.1088/0952-4746/21/1/609

Moreno, V., Bach, J., Baixeras, C., Font, Ll., 2014. Radon levels in groundwaters and natural radioactivity in soils of the volcanic region of La Garrotxa, Spain. Journal of Environmental Radioactivity 128, 1–8. https://doi.org/10.1016/j.jenvrad.2013.10.021

Mueller, U., Delgado, R.T., Grunsky, E.C., McKinley, J.M., 2020. Biplots for compositional data derived from generalized joint diagonalization methods. Applied Computing and Geosciences 8, 100044.

Muntean, L., Cosma, C., Cucos, A., Dicu, T., Moldovan, D., 2014. Assessment of annual and seasonal variation of indoor radon levels in dwelling houses from Alba County, Romania. Rom Journ Phys 59, 163–71.

Murakami, T., Isobe, H., Sato, T., Ohnuki, T., 1996. Weathering of chlorite in a quartz-chlorite schist: I. Mineralogical and chemical changes. Clays and Clay Minerals 44, 244–256.

Murphy, P., Dowdall, A., Long, S., Curtin, B., Fenton, D., 2021. Estimating population lung cancer risk from radon using a resource efficient stratified population weighted sample survey protocol – Lessons and results from Ireland. Journal of Environmental Radioactivity 233, 106582. https://doi.org/10.1016/j.jenvrad.2021.106582

Murty, V.R.K., Karunakara, N., 2008. Natural radioactivity in the soil samples of Botswana. Radiation Measurements 43, 1541–1545. https://doi.org/10.1016/j.radmeas.2008.10.004

Musso, A., Tikhomirov, D., Plötze, M.L., Greinwald, K., Hartmann, A., Geitner, C., Maier, F., Petibon, F., Egli, M., 2022. Soil Formation and Mass Redistribution during the Holocene Using Meteoric 10Be, Soil Chemistry and Mineralogy. Geosciences 12. https://doi.org/10.3390/geosciences12020099

Naftz, D.L., Barclay, C.V., 1991. Selenium and associated trace elements in soil, rock, water and streambed sediment of the proposed Sandstone Reservoir, south-central Wyoming. US Department of the Interior, US Geological Survey.

Nagarajan, R., Madhavaraju, J., Nagendra, R., Armstrong-Altrin, J.S., Moutte, J., 2007. Geochemistry of Neoproterozoic shales of the Rabanpalli Formation, Bhima Basin, Northern

Karnataka, southern India: implications for provenance and paleoredox conditions. Revista mexicana de ciencias geológicas 24, 150–160.

Nathwani, C.L., Wilkinson, J.J., Fry, G., Armstrong, R.N., Smith, D.J., Ihlenfeld, C., 2022. Machine learning for geochemical exploration: classifying metallogenic fertility in arc magmas and insights into porphyry copper deposit formation. Mineralium Deposita. https://doi.org/10.1007/s00126-021-01086-9

National Cancer Registry Ireland, 2020. Cancer in Ireland 1994-2018 with estimates for 2018-2020: Annual report of the National Cancer Registry.

National Radon Control Strategy, 2019. NRCS Knowledge Gaps Phase 2.

Nelson, D. a, Sommers, L., 1983. Total carbon, organic carbon, and organic matter. Methods of soil analysis: Part 2 chemical and microbiological properties 9, 539–579.

Neri, M., Ferrera, E., Giammanco, S., Currenti, G., Cirrincione, R., Patanè, G., Zanon, V., 2016. Soil radon measurements as a potential tracer of tectonic and volcanic activity. Scientific Reports 6, 24581. https://doi.org/10.1038/srep24581

Neznal, Matěj, Neznal, Martin, Matolin, M., Barnet, I., Miksova, J., 2004. The new method for assessing the radon risk of building sites. Czech Geological Survey Prague.

Norris, K., Williams, P., 1984. Optimization of mathematical treatments of raw near-infrared signal in the. Cereal Chem 61, 158–165.

Nuhu, H., Hashim, S., Aziz Saleh, M., Syazwan Mohd Sanusi, M., Hussein Alomari, A., Jamal, M.H., Abdullah, R.A., Hassan, S.A., 2021. Soil gas radon and soil permeability assessment: Mapping radon risk areas in Perak State, Malaysia. PloS one 16, e0254099.

O’Brien, K., Goodwin, T., Risk, D., 2011. Radon soil gas in the Halifax Regional Municipality, Nova Scotia, Canada. atlantic GeoloGy 47, 112–124.

Ochoa-González, R., Díaz-Somoano, M., Martínez-Tarazona, M.R., 2013. Influence of Limestone Characteristics on Mercury Re-emission in WFGD Systems. Environ. Sci. Technol. 47, 2974–2981. https://doi.org/10.1021/es304090e

O'connor, P., Brück, P., 1978. Age and origin of the Leinster Granite. Journal of Earth Sciences 105–113.

Organo, C., Ellard, A., Fenton, D., Synnott, H., O'Colmáin, M., Prenter, S., O'Reilly, S., Colgan, P., 2004. High radon concentrations in a house near Castleisland, County Kerry (Ireland)—identification, remediation and post-remediation. Journal of Radiological Protection 24, 107. https://doi.org/10.1088/0952-4746/24/2/001

Organo, C., Murphy, P., 2007. The Castleisland Radon Survey—follow-up to the discovery of a house with extremely high radon concentrations in County Kerry (SW Ireland). Journal of Radiological Protection 27. https://doi.org/10.1088/0952-4746/27/3/002

Padilla, G.D., Hernández, P.A., Padrón, E., Barrancos, J., Pérez, N.M., Melián, G., Nolasco, D., Dionis, S., Rodríguez, F., Calvo, D., 2013. Soil gas radon emissions and volcanic activity at El Hierro (Canary Islands): The 2011-2012 submarine eruption. Geochemistry, Geophysics, Geosystems 14, 432–447.

Padrón, E., Padilla, G., Hernández, P.A., Pérez, N.M., Calvo, D., Nolasco, D., Barrancos, J., Melián, G.V., Dionis, S., Rodríguez, F., 2013. Soil gas geochemistry in relation to eruptive fissures on Timanfaya volcano, Lanzarote Island (Canary Islands, Spain). Journal of Volcanology and Geothermal Research 250, 91–99. https://doi.org/10.1016/j.jvolgeores.2012.10.013

Pal, R., Patra, A.C., Bakshi, A.K., Dhabekar, B., Reddy, P.J., Sengupta, P., Sapra, B.K., 2021. Investigations on baseline levels for natural radioactivity in soils, rocks, and lakes of Larsemann

Hills in East Antarctica. Environmental Monitoring and Assessment 193, 822. https://doi.org/10.1007/s10661-021-09446-8

Pandurang, A., Kerur, B., Siddanna, R., Mishra, R., 2014. Radon, thoron and their progeny concentration variations in dwellings of Gogi region, Yadgir district of Karnataka, India. Journal of Radioanalytical and Nuclear Chemistry 302, 1321–1326. https://doi.org/10.1007/s10967-014-3608-x

Park, E.J., Lee, H., Kim, H.C., Sheen, S.S., Koh, S.B., Park, K.S., Cho, N.H., Lee, C.-M., Kang, D.R., 2020. Residential Radon Exposure and Cigarette Smoking in Association with Lung Cancer: A Matched Case-Control Study in Korea. International journal of environmental research and public health 17, 2946.

Park, M., Chon, H.-T., Marton, L., 2010. Mobility and accumulation of selenium and its relationship with other heavy metals in the system rocks/soils–crops in areas covered by black shale in Korea. Journal of Geochemical Exploration 107, 161–168.

Parnell, J., Brolly, C., Spinks, S., Bowden, S., 2016. Selenium enrichment in Carboniferous Shales, Britain and Ireland: Problem or opportunity for shale gas extraction? Applied Geochemistry 66, 82–87.

Partin, C., Bekker, A., Scott, C., Gill, B., Lyons, T., 2010. Uranium in shales as a proxy for the evolution of surficial redox conditions. GeoCanada 2010: Abstract.

Pásztor, L., Szabó, K.Z., Szatmári, G., Laborczi, A., Horváth, Á., 2016. Mapping geogenic radon potential by regression kriging. Science of The Total Environment 544, 883–891. https://doi.org/10.1016/j.scitotenv.2015.11.175

Pereira, A., Godinho, M., Neves, L., 2010. On the influence of faulting on small-scale soil-gas radon variability: a case study in the Iberian Uranium Province. Journal of environmental radioactivity 101, 875–882.

Perri, F., Scarciglia, F., Apollaro, C., Marini, L., 2015. Characterization of granitoid profiles in the Sila Massif (Calabria, southern Italy) and reconstruction of weathering processes by mineralogy, chemistry, and reaction path modeling. Journal of Soils and Sediments 15, 1351–1372. https://doi.org/10.1007/s11368-014-0856-x

Petermann, E., Bossew, P., Hoffmann, B., 2022. Radon hazard vs. radon risk - On the effectiveness of radon priority areas. Journal of Environmental Radioactivity 244–245, 106833. https://doi.org/10.1016/j.jenvrad.2022.106833

Petermann, E., Meyer, H., Nussbaum, M., Bossew, P., 2021. Mapping the geogenic radon potential for Germany by machine learning. Science of The Total Environment 754, 142291. https://doi.org/10.1016/j.scitotenv.2020.142291

Petersell, V., Åkerblom, G., Ek, B.-M., Enel, M., Mõttus, V., Täht, K., 2004. The radon risk map of Estonia. Tallinn-Stockholm.

Petersell, V., Jüriado, K., Raukas, A., Shtokalenko, M., Täht-Kok, K., 2015. Quaternary deposits and weathered bedrock material as a source of dangerous radon emissions in Estonia. Geologos 21.

Pham, B.T., Ly, H.-B., Al-Ansari, N., Ho, L.S., 2021. A Comparison of Gaussian Process and M5P for Prediction of Soil Permeability Coefficient. Scientific Programming 2021, 3625289. https://doi.org/10.1155/2021/3625289

Phillips, W., Sevastopulo, G., 1986. The stratigraphic and structural setting of Irish mineral deposits. Presented at the Geology and genesis of mineral deposits in Ireland, pp. 1–30.

Pohjankukka, J., Pahikkala, T., Nevalainen, P., Heikkonen, J., 2017. Estimating the prediction performance of spatial models via spatial k-fold cross validation. International Journal of Geographical Information Science 31, 2001–2019.

Pracht, M., 1997. Geology of Kerry - Cork: A geological description to accompany the bedrock geology 1:100,000 scale map series, sheet 21, Kerry-Cork.

Pracht, M., Somerville, I.D., Wang, Y., 2015. A revised Mississippian lithostratigraphy of County Galway (western Ireland) with an analysis of carbonate lithofacies, biostratigraphy, depositional environments and palaeogeographic reconstructions utilising new borehole data. Journal of Palaeogeography 4, 1–26. https://doi.org/10.3724/SP.J.1261.2015.00065

Radiological Protection Act 1991 (Ionising Radiation) Regulations, 2019. Statutory Instruments Ireland, S.I. No. 30 of 2019.

Radvanyi, P., Villain, J., 2017. The discovery of radioactivity. Comptes Rendus Physique 18, 544–550. https://doi.org/10.1016/j.crhy.2017.10.008

Rafique, M., Abbasi, S., Shahzadi, C., Basharat, M., Jabbar, A., Ur Rahman, S., 2021. Excessive Lifetime Cancer Risk Assessment due to Short-Term Indoor/Outdoor Ambient Radon and Gamma Dose Rate Exposures. Iranian Journal of Science and Technology, Transactions A: Science 45, 2181–2190. https://doi.org/10.1007/s40995-021-01192-3

Ramola, R.C., Prasad, M., 2020. Significance of thoron measurements in indoor environment. Journal of Environmental Radioactivity 225, 106453. https://doi.org/10.1016/j.jenvrad.2020.106453

Ravikumar, P., Davis, D., Somashekar, R., Prakash, K., 2015. Measurement of radon activity in soil gas using RAD7 in the Environs of Chitradurga District, Karnataka, India. Elixir Earth Sci 80, 31078–31082.

Raza, A., Gholami, R., Rezaee, R., Rasouli, V., Rabiei, M., 2019. Significant aspects of carbon capture and storage–A review. Petroleum 5, 335–340.

Reavy, R.J., 2001. Caledonian granites–emplacement. Open University Geological Society Journal 22.

Reynolds Jr, R., 1963. Potassium-rubidium ratios aud polymorphism in illites and microclines from the clay size fractions of proterozoic carbonate rocks. Geochimica et Cosmochimica Acta 27, 1097–1112.

Ribeiro, F.C.A., Silva, J.I.R., Lima, E.S.A., do Amaral Sobrinho, N.M.B., Perez, D.V., Lauria, D.C., 2018. Natural radioactivity in soils of the state of Rio de Janeiro (Brazil): Radiological characterization and relationships to geological formation, soil types and soil properties. Journal of Environmental Radioactivity 182, 34–43. https://doi.org/10.1016/j.jenvrad.2017.11.017

Rider, M., 1974. The Namurian of West County Clare. Presented at the Proceedings of the Royal Irish Academy. Section B: Biological, Geological, and Chemical Science, JSTOR, pp. 125–142.

Riebe, C.S., Kirchner, J.W., Finkel, R.C., 2003. Long-term rates of chemical weathering and physical erosion from cosmogenic nuclides and geochemical mass balance. Geochimica et Cosmochimica Acta 67, 4411–4427. https://doi.org/10.1016/S0016-7037(03)00382-X

Rigby, J.G., La Pointe, D.D., 1993. Wind and barometric pressure effects on radon in two mitigated houses, in: The 1993 International Radon Conference. pp. 61–68.

Robinson, P., 1980. Determination of calcium, magnesium, manganese, strontium, sodium and iron in the carbonate fraction of limestones and dolomites. Chemical Geology 28, 135–146. https://doi.org/10.1016/0009-2541(80)90041-8

Rodríguez-Martínez, Á., Ruano-Ravina, A., Torres-Durán, M., Provencio, M., Parente-Lamelas, I., Vidal-García, I., Martínez, C., Hernández-Hernández, J., Abdulkader-Nallib, I., Castro-Añón, O., Varela-Lema, L., Piñeiro-Lamas, M., Fidalgo, P.S., Fernández-Villar, A., Barros-Dios, J., Pérez-Ríos, M., 2021. Residential Radon and Small Cell Lung Cancer. Final Results of the Small Cell Study. Archivos de Bronconeumología. https://doi.org/10.1016/j.arbres.2021.01.027

Romer, R.L., Cuney, M., 2018. Phanerozoic uranium mineralization in Variscan Europe – More than 400 Ma of tectonic, supergene, and climate-controlled uranium redistribution. Ore Geology Reviews 102, 474–504. https://doi.org/10.1016/j.oregeorev.2018.09.013

Rosario, A.S., Wichmann, H.-E., 2006. ENVIRONMENTAL POLLUTANTS | Radon, in: Laurent, G.J., Shapiro, S.D. (Eds.), Encyclopedia of Respiratory Medicine. Academic Press, Oxford, pp. 120–125. https://doi.org/10.1016/B0-12-370879-6/00135-6

Ross, C.S., Hendricks, S.B., 1945. Minerals of the montmorillonite group: Their origin and relation to soils and clays. US Government Printing Office.

Roycroft, P.D., 1989. Zoned muscovite from the Leinster Granite, SE Ireland. Mineralogical Magazine 53, 633–635.

Ruano-Ravina, A., Dacosta-Urbieta, A., Miguel Barros-Dios, J., T Kelsey, K., 2018. Radon exposure and tumors of the central nervous system. Gaceta Sanitaria 32. https://doi.org/10.1016/j.gaceta.2017.01.002

Ruiz-Agudo, E., Putnis, C.V., Rodriguez-Navarro, C., Putnis, A., 2012. Mechanism of leached layer formation during chemical weathering of silicate minerals. Geology 40, 947–950. https://doi.org/10.1130/G33339.1

Ryser, A.L., Strawn, D.G., Marcus, M.A., Johnson-Maynard, J.L., Gunter, M.E., Möller, G., 2005. Micro-spectroscopic investigation of selenium-bearing minerals from the Western US Phosphate Resource Area. Geochemical Transactions 6, 1. https://doi.org/10.1186/1467-4866-6-1

Safari, M., Gholami, R., Jami, M., Ananthan, M.A., Rahimi, A., Khur, W.S., 2021. Developing a porosity-permeability relationship for ellipsoidal grains: A correction shape factor for Kozeny-Carman’s equation. Journal of Petroleum Science and Engineering 205, 108896.

Samet, J.M., 1989. Radon and lung cancer. JNCI: Journal of the National Cancer Institute 81, 745–758.

Savitzky, A., Golay, M.J., 1964. Smoothing and differentiation of data by simplified least squares procedures. Analytical chemistry 36, 1627–1639.

Schabath, M.B., Cote, M.L., 2019. Cancer Progress and Priorities: Lung Cancer. Cancer Epidemiology, Biomarkers & Prevention 28, 1563–1579. https://doi.org/10.1158/1055-9965.EPI-19-0221

Schonlau, M., Zou, R.Y., 2020. The random forest algorithm for statistical learning. The Stata Journal 20, 3–29.

Schubert, M., Musolff, A., Weiss, H., 2018. Influences of meteorological parameters on indoor radon concentrations (222Rn) excluding the effects of forced ventilation and radon exhalation from soil and building materials. Journal of environmental radioactivity 192, 81–85. https://doi.org/10.1016/j.jenvrad.2018.06.011

Schwela, D., 2014. Pollution, Indoor Air, in: Wexler, P. (Ed.), Encyclopedia of Toxicology (Third Edition). Academic Press, Oxford, pp. 1003–1017. https://doi.org/10.1016/B978-0-12-386454-3.01028-9

Sevastopulo, G.D., Wyse Jackson, P., 2009. Carboniferous: Mississippian (Tournaisian and Viséan). The geology of Ireland 215–268.

Shang, Q., Tan, D., Gao, S., Feng, L., 2019. A Hybrid Method for Traffic Incident Duration Prediction Using BOA-Optimized Random Forest Combined with Neighborhood Components Analysis. Journal of Advanced Transportation 2019, 4202735. https://doi.org/10.1155/2019/4202735

Shepherd, R.G., 1989. Correlations of permeability and grain size. Groundwater 27, 633–638.

Shimoike, Y., Kazahaya, K., Shinohara, H., 2002. Soil gas emission of volcanic CO2 at Satsuma-Iwojima volcano, Japan. Earth, planets and space 54, 239–247.

Singh, J., Singh, H., Singh, S., Bajwa, B., 2010. Measurement of soil gas radon and its correlation with indoor radon around some areas of Upper Siwaliks, India. Journal of Radiological Protection 30, 63.

Sleeman, A., MacConnell, B., Gatley, S., 2004. Understanding Earth Processes, Rocks and the Geological History of Ireland: A Companion to the 1: 1.000. 000 Scale Bedrock Geological Map of Ireland. Geological Survey of Ireland.

Smith, M.E., Dumitru, O.A., Burghele, B.D., Cucoș, A., Onac, B.P., 2019. Radon concentration in three Florida caves: Florida, Jennings, and Ocala. Carbonates and Evaporites 34, 433–439. https://doi.org/10.1007/s13146-018-0473-7

Soesoo, A., Vind, J., Hade, S., 2020. Uranium and Thorium Resources of Estonia. Minerals 10. https://doi.org/10.3390/min10090798

Somerville, I.D., Strogen, P., Jones, G.Ll., 1992. Mid-Dinantian Waulsortian buildups in the Dublin Basin, Ireland. Sedimentary Geology 79, 91–116. https://doi.org/10.1016/0037-0738(92)90006-D

Sperandei, S., 2014. Understanding logistic regression analysis. Biochemia medica 24, 12–18.

Starkey, H.C., 1982. The role of clays in fixing lithium. US Government Printing Office.

Starr, M., Lindroos, A.-J., Ukonmaanaho, L., 2014. Weathering release rates of base cations from soils within a boreal forested catchment: variation and comparison to deposition, litterfall and leaching fluxes. Environmental Earth Sciences 72, 5101–5111. https://doi.org/10.1007/s12665-014-3381-8

Stenberg, B., Rossel, R.A.V., Mouazen, A.M., Wetterlind, J., 2010. Visible and near infrared spectroscopy in soil science. Advances in agronomy 107, 163–215.

Strogen, P., Somerville, I., Pickard, N., Jones, G.L., Fleming, M., 1996. Controls on ramp, platform and basinal sedimentation in the Dinantian of the Dublin Basin and Shannon Trough, Ireland. Geological Society, London, Special Publications 107, 263–279.

Sukanya, S., Noble, J., Joseph, S., 2022. Application of radon (222Rn) as an environmental tracer in hydrogeological and geological investigations: An overview. Chemosphere 303, 135141. https://doi.org/10.1016/j.chemosphere.2022.135141

Sun, K., Guo, Q., Cheng, J.G., 2004. The Effect of Some Soil Characteristics on Soil Radon Concentration and Radon Exhalation from Soil Surface. Journal of Nuclear Science and Technology 41, 1113–1117. https://doi.org/10.1080/18811248.2004.9726337

Sun, X., Yang, P., Xiang, Y., Si, X., Liu, D., 2018. Across-fault distributions of radon concentrations in soil gas for different tectonic environments. Geosciences Journal 22, 227–239.

Sundal, A.V., Valen, V., Soldal, O., Strand, T., 2008. The influence of meteorological parameters on soil radon levels in permeable glacial sediments. Science of The Total Environment 389, 418–428. https://doi.org/10.1016/j.scitotenv.2007.09.001

Sutton, G.A., Napier, S.T., John, M., Taylor, A., 1993. Uranium-238 decay chain data. Science of The Total Environment 130–131, 393–401. https://doi.org/10.1016/0048-9697(93)90094-M

Swakoń, J., Kozak, K., Paszkowski, M., Gradziński, R., Łoskiewicz, J., Mazur, J., Janik, M., Bogacz, J., Horwacik, T., Olko, P., 2005. Radon concentration in soil gas around local disjunctive tectonic zones in the Krakow area. Journal of Environmental Radioactivity 78, 137–149. https://doi.org/10.1016/j.jenvrad.2004.04.004

Swanson, Vernon E, Swanson, Vernon Emanuel, 1961. Geology and geochemistry of uranium in marine black shales: a review. US Government Printing Office Washington, DC.

Szabó, K.Z., Jordan, G., Horváth, Á., Szabó, C., 2014. Mapping the geogenic radon potential: methodology and spatial analysis for central Hungary. Journal of environmental radioactivity 129, 107–120.

Szabó, K.Z., Jordan, G., Horváth, Á., Szabó, C., 2013. Dynamics of soil gas radon concentration in a highly permeable soil based on a long-term high temporal resolution observation series. Journal of environmental radioactivity 124, 74–83. https://doi.org/10.1016/j.jenvrad.2013.04.004

Taboada, T., Cortizas, A.M., García, C., García-Rodeja, E., 2006. Uranium and thorium in weathering and pedogenetic profiles developed on granitic rocks from NW Spain. Science of the Total Environment 356, 192–206.

Talebi, H., Peeters, L.J.M., Otto, A., Tolosana-Delgado, R., 2022. A Truly Spatial Random Forests Algorithm for Geoscience Data Analysis and Modelling. Mathematical Geosciences 54, 1–22. https://doi.org/10.1007/s11004-021-09946-w

Taylor, J.A., Watson, M.A., Devereux, T.R., Michels, R.Y., Saccomanno, G., Anderson, M., Devereux, T.R., 1994. p53 mutation hotspot in radon-associated lung cancer. The Lancet 343, 86–87. https://doi.org/10.1016/S0140-6736(94)90818-4

Thomson, I., 1971. Regional geochemical studies of black shale facies with particular reference to trace element disorders in animals.

Thornton, M.S., 1966. The Lower Carboniferous limestones of the Tralee Bay area, Co. Kerry, Ireland. Unpublished PhD thesis, University of Cambridge.

Ticknor, K., 1998. The sorption of strontium, barium and radium by chlorite and kaolinite: effects of sorbent concentration and competition from group IIA elements.

Tollefsen, T., Cinelli, G., Bossew, P., Gruber, V., De Cort, M., 2014. From the European indoor radon map towards an atlas of natural radiation. Radiation Protection Dosimetry 162, 129–134. https://doi.org/10.1093/rpd/ncu244

Tolosana-Delgado, R., McKinley, J., 2016. Exploring the joint compositional variability of major components and trace elements in the Tellus soil geochemistry survey (Northern Ireland). Applied Geochemistry 75, 263–276.

Tommasino, L., 2005. Radiochemical Methods | Radon., in: Worsfold, P., Townshend, A., Poole, C. (Eds.), Encyclopedia of Analytical Science (Second Edition). Elsevier, Oxford, pp. 32–44. https://doi.org/10.1016/B0-12-369397-7/00520-3

Tooth, A., Fairchild, I., 2003. Soil and karst aquifer hydrological controls on the geochemical evolution of speleothem-forming drip waters, Crag Cave, Southwest Ireland. Journal of Hydrology 273, 51–68. https://doi.org/10.1016/S0022-1694(02)00349-9

Tositti, L., Cinelli, G., Brattich, E., Galgaro, A., Mostacci, D., Mazzoli, C., Massironi, M., Sassi, R., 2017. Assessment of lithogenic radioactivity in the Euganean Hills magmatic district

(NE Italy). Journal of Environmental Radioactivity 166, 259–269. https://doi.org/10.1016/j.jenvrad.2016.07.011

Tushe, K.B., Bylyku, E., Xhixha, G., Dhoqina, P., Daci, B., Cfarku, F., Xhixha, M.K., Strati, V., 2016. FIRST STEP TOWARDS THE GEOGRAPHICAL DISTRIBUTION OF INDOOR RADON IN DWELLINGS IN ALBANIA. Radiation Protection Dosimetry 172, 488–495. https://doi.org/10.1093/rpd/ncv494

Tzortzis, M., Tsertos, H., Christofides, S., Christodoulides, G., 2003. Gamma-ray measurements of naturally occurring radioactive samples from Cyprus characteristic geological rocks. Radiation Measurements 37, 221–229. https://doi.org/10.1016/S1350-4487(03)00028-3

United Nations Scientific Committee on the Effects of Atomic Radiation, 2015. Report of the United Nations Scientific Committee on the effects of atomic radiation to the general assembly.

United Nations Scientific Committee on the Effects of Atomic Radiation, 2011. Report of the United Nations Scientific Committee on the Effects of Atomic Radiation (UNSCEAR) 2011.

United Nations Scientific Committee on the Effects of Atomic Radiation, Annex, B., 2000. Exposures from natural radiation sources. New york, United Nation 9, 11.

United Nations, U.N.S.C. on the E. of A.Radiation., 1958. Report of the United Nations Scientific Committee on the Effects of Atomic Radiation (UNSCEAR) 1958: Report to the General Assembly, with Scientific Annexes. 229. https://doi.org/10.18356/0b0b1bc1-en

Vahakangas, K.H., Metcalf, R.A., Welsh, J.A., Bennett, W.P., Harris, C.C., Samet, J.M., Lane, D.P., 1992. Mutations of p53 and ras genes in radon-associated lung cancer from uranium miners. The Lancet 339, 576–580. https://doi.org/10.1016/0140-6736(92)90866-2

Vasil’ev, V., 2011. New data on the composition of metacinnabar and Hg-sphalerite with an isomorphous Cd admixture. Russian Geology and Geophysics 52, 701–708.

Vermeesch, P., 2013. Multi-sample comparison of detrital age distributions. Chemical Geology 341, 140–146. https://doi.org/10.1016/j.chemgeo.2013.01.010

Vuckovic, B., Gulan, L., Milenkovic, B., Stajic, J.M., Milic, G., 2016. Indoor radon and thoron concentrations in some towns of central and South Serbia. Journal of Environmental Management 183, 938–944. https://doi.org/10.1016/j.jenvman.2016.09.053

Walsh, P.M., National Cancer Registry, EPA, 2017. A revision of the number of radon-related lung cancers in Ireland: preliminary results.

Wang, L., Liu, B., McKinley, J.M., Cooper, M.R., Li, C., Kong, Y., Shan, M., 2021. Compositional data analysis of regional geochemical data in the Lhasa area of Tibet, China. Applied Geochemistry 135, 105108. https://doi.org/10.1016/j.apgeochem.2021.105108

Wang, Y., Zhao, Y., Xu, S., 2022. Application of VNIR and machine learning technologies to predict heavy metals in soil and pollution indices in mining areas. Journal of Soils and Sediments. https://doi.org/10.1007/s11368-022-03263-3

Wang, Z., Tan, J., Hilton, J., Dick, J., Wen, Z., 2023. Trace element enrichment mechanisms in black shales during the early cambrian (ca. 521–514 Ma), South China. Marine and Petroleum Geology 149, 106083.

Watson, R.J., Smethurst, M.A., Ganerød, G.V., Finne, I., Rudjord, A.L., 2017. The use of mapped geology as a predictor of radon potential in Norway. Journal of Environmental Radioactivity 166, 341–354. https://doi.org/10.1016/j.jenvrad.2016.05.031

Wells, N., 1967. Selenium content of soil-forming rocks. New Zealand journal of geology and geophysics 10, 198–208.

Wignall, P., Best, J., 2000. The western Irish Namurian basin reassessed. Basin Research 12, 59–78. https://doi.org/10.1046/j.1365-2117.2000.00113.x

Wignall, P.B., Somerville, I.D., Braithwaite, K., 2016. The Clare Shales. A Field Guide to the Carboniferous sediments of the Shannon Basin, western Ireland 97–111. https://doi.org/10.1002/9781119257141.ch6

Worden, R., Griffiths, J., Wooldridge, L., Utley, J., Lawan, A.Y., Muhammed, D., Simon, N., Armitage, P., 2020. Chlorite in sandstones. Earth-Science Reviews 204, 103105.

World Health Organisation, I.A. for R. on C., 2016. The European Code Against Cancer. URL https://www.europeancancerleagues.org/cancer-prevention-the-european-code-against-cancer/

World Health Organization (Ed.), 2009. WHO handbook on indoor radon: a public health perspective. World Health Organization.

World Health Organization, 2007. International radon project: survey on radon guidelines, programmes and activities (No. WHO/HSE/RAD/07.01). World Health Organization.

Wunsch, A., Navarre-Sitchler, A.K., Moore, J., McCray, J.E., 2014. Metal release from limestones at high partial-pressures of CO2. Chemical Geology 363, 40–55. https://doi.org/10.1016/j.chemgeo.2013.10.036

Xie, D., Liao, M., Kearfott, K.J., 2015. Influence of environmental factors on indoor radon concentration levels in the basement and ground floor of a building–A case study. Radiation Measurements 82, 52–58.

Xuan, P., Duong, N., Chinh, V., Dang, P., Qua, N., Pho, N., 2020. Soil Gas Radon Measurement for Identifying Active Faults in Thua Thien Hue (Vietnam). Journal of Geoscience and Environment Protection 8. https://doi.org/10.4236/gep.2020.87003

Yalım, H.A., Gümüş, A., Başaran, C., Bağcı, M., Yıldız, A., Açil, D., Özçelik, M., İlhan, M.Z., Ünal, R., 2018. Comparison of radon concentrations in soil gas and indoor environment of

Afyonkarahisar Province. Arabian Journal of Geosciences 11, 246. https://doi.org/10.1007/s12517-018-3546-y

Yarmoshenko, I.V., Malinovsky, G.P., 2016. Lung cancer mortality and radon exposure in Russia. Nukleonika 61, 263–268. https://doi.org/10.1515/nuka-2016-0044

Yesares, L., Drummond, D.A., Hollis, S.P., Doran, A.L., Menuge, J.F., Boyce, A.J., Blakeman, R.J., Ashton, J.H., 2019. Coupling Mineralogy, Textures, Stable and Radiogenic Isotopes in Identifying Ore-Forming Processes in Irish-Type Carbonate-Hosted Zn–Pb Deposits. Minerals 9. https://doi.org/10.3390/min9060335

Yin, K., Hong, H., Churchman, G.J., Li, Z., Fang, Q., 2018. Mixed-layer illite-vermiculite as a paleoclimatic indicator in the Pleistocene red soil sediments in Jiujiang, southern China. Palaeogeography, Palaeoclimatology, Palaeoecology 510, 140–151.

Young, M., Knights, K., Smyth, D., Glennon, M., Scanlon, R., Gallagher, V., 2016. The Tellus geochemical surveys, results and applications. Unearthed: Impacts of the Tellus Surveys of the North of Ireland. Royal Irish Academy 33–52.

Yu, B., Chen, J., Li, X., Lin, C., 2003. Geochemistry of black shale at the bottom of the Lower Cambrian in Tarim Basin and its significance for lithosphere evolution. Science in China Series D: Earth Sciences 46, 498–507.

Zagà, V., Cattaruzza, M.S., Martucci, P., Pacifici, R., Trisolini, R., Bartolomei, P., Giacobbe, R., Patelli, M., Paioli, D., Esposito, M., 2021. The “polonium in vivo” study: polonium-210 in bronchial lavages of patients with suspected lung cancer. Biomedicines 9, 4.

Zane, A., Sassi, R., Guidotti, C.V., 1998. New data on metamorphic chlorite as a petrogenetic indicator mineral, with special regard to greenschist-facies rocks. The Canadian Mineralogist 36, 713–726.

Zhao, L., Hong, H., Liu, J., Fang, Q., Yao, Y., Tan, W., Yin, K., Wang, C., Chen, M., Algeo, T.J., 2018. Assessing the utility of visible-to-shortwave infrared reflectance spectroscopy for analysis of soil weathering intensity and paleoclimate reconstruction. Palaeogeography, Palaeoclimatology, Palaeoecology 512, 80–94.

Zhongcheng, W., Guizhi, L., 1991. Barite and witherite deposits in Lower Cambrian shales of South China; stratigraphic distribution and geochemical characterization. Economic Geology 86, 354–363.

Zinn, Y.L., Faria, J.A. de, Araujo, M.A. de, Skorupa, A.L.A., 2020. Soil parent material is the main control on heavy metal concentrations in tropical highlands of Brazil. CATENA 185, 104319. https://doi.org/10.1016/j.catena.2019.104319

Zmazek, B., Živčić, M., Todorovski, L., Džeroski, S., Vaupotič, J., Kobal, I., 2005. Radon in soil gas: how to identify anomalies caused by earthquakes. Applied geochemistry 20, 1106–1119.

Zohuri, B., 2020. 2 - Nuclear fuel cycle and decommissioning, in: Khan, S.U.-D., Nakhabov, A. (Eds.), Nuclear Reactor Technology Development and Utilization. Woodhead Publishing, pp. 61–120. https://doi.org/10.1016/B978-0-12-818483-7.00002-0

Zupančič, N., Turniški, R., Miler, M., Grčman, H., 2018. Geochemical fingerprint of insoluble material in soil on different limestone formations. CATENA 170, 10–24. https://doi.org/10.1016/j.catena.2018.05.040

Appendix A supplementary materials in thesis chapters

7.1 Chapter 4 supplementary materials

Table 7.1.1 Classification of SGRn concentrations. Modified from Table 1 (Elío et al., 2019).

Classification	**Measure SGRn concentration [k Bq m^{-3}]**	**% of samples in each class**
Extremely High	>=100	36
Very High	70 <= Rn <100	13
High	50 <= Rn 70	15
Moderate	30 <= Rn 50	18
Low	10 <= Rn 30	17

Table 7.1.2 The number of radon soil-gas samples in each Quaternary geology type which are above/below the extreme radon category.

Soil-gas radon (SG Rn)	**kBqm^{-3}**	**Total**	**Bedrock**					
			Waulsortian Limestones	**Rockfield Limestones**	**Cracoean Reef member**	**Dirtoge Limestones**	**Clare Shales**	**Cloone Flagstones**
SG Rn	<100	56	24	13	11	5	2	1
	>100	32	4	6	5	3	13	1
	total	88	28	19	16	8	15	2
Percentage of samples in each bedrock unit below/above the 100kBqm^{-3} threshold								
SG Rn	<100	64%	86%	68%	69%	63%	13%	50%
	>100	36%	14%	32%	31%	37%	87%	50%
Percentage of samples below/above the 100kBqm^{-3} threshold across the various bedrock units								
SG Rn	<100	-	43%	23%	19.5%	9%	3.5%	2%
	>100	-	12.5%	18.5%	16%	9%	41%	3%
Log-normal distribution ($k = (\ln 100 - \ln GM)/\ln GSD$)								
	GM	79.8	50.32	58.48	71.11	76.45	347	47.33
	GSD	3.03	2.38	2.4	2.74	2.78	5.73	2.74

Table 7.1.3. The number of soil-gas samples in each Radon Potential category above/below 100kBq/m3.

Soil-gas Radon	$kBqm^{-3}$	Total	Radon potential category		
			V low (<10)	M-H (10-35)	H (35 +)
SG Rn	<100	56	3	35	18
	>100	32	0	0	32
	total	88	3	35	50
Percentage of samples in each radon risk classification below/above the 100kBqm^{-3} threshold					
SG Rn	<100	64%	100%	100%	36%
	>100	36%	0%	0%	64%
Percentage of samples below/above the 100kBqm^{-3} threshold in each radon risk classification					
SG Rn	<100	-	5.5%	62.5%	32%
	>100	-	0%	0%	100%
Log-normal distribution ($\hat{k} = (\ln 100 - \ln GM)/\ln GSD$)					
GM		79.8	13.8	34.2	160.3
GSD		3.05	1.2	1.7	2.5

Table 7.1.4 The percentage area of each radon potential category in the study area.

Radon potential	Percentage area (%)
<10	1
10-35	50
35+	49

Table 7.1.5. The number of Indoor Radon measurements above/below the reference level is grouped to the different Quaternary Geology types.

		Total	Formation		
Indoor radon (InRn)	**Bqm^{-3}**		**Till derived from Limestones**	**Till derived from Namurian siltstones, sandstones and shales**	**Alluvium**
InRn	**<200**	165	118	16	31
	>200	15	11	3	1
	total	180	129	19	32
Percentage in each Quaternary formation of houses below/above the reference level					
InRn	**<200**	92%	91%	84%	97%
	>200	8%	9%	16%	3%
Percentage of houses below/above the reference level in each Quaternary formation					
InRn	**<200**	-	72%	9%	19%
	>200	-	73%	20%	7%
Log-normal distribution ($k = (\ln 200 - \ln GM)/\ln GSD$)					
InRn	**GM**	34.5	31.5	58.5	36.4
	GSD	2.62	2.65	3.5	1.97

Table 7.1.6 The amount of Indoor Radon measurements which are above/below the reference level grouped to the different bedrock types.

Indoor radon (IRC)	**Bq m^{-3}**	**Total**	***Bedrock geology (1:100k) GSI 2019***					
			Waulsortian Limestone	**Rockfield Limestones**	**Cracoean Reef member**	**Dirtoge Limestones**	**Clare Shales**	**Cloone Flagstones**
IRC	**<200**	165	133	17	7	2	3	3
	>200	15	11	1	1	1	1	0
	Total	180	144	18	8	3	4	3

Percentage of houses in each radon risk classification below/above the reference level								
IRC	**<200**	92%	92%	94%	88%	67%	75%	100%
	>200	8%	8%	6%	12%	33%	25%	0%
Percentage of houses below/above the reference level in each radon risk classification								
IRC	**<200**	-	81%	10%	4%	1%	2%	2%
	>200	-	73%	6.75%	6.75%	6.75%	6.75%	0%
Log-normal distribution ($k = (\ln 200 - \ln GM)/\ln GSD$)								
IRC	**GM**	34.5	32.78	27.7	58.2	200	62.9	27.2
	GSD	2.62	2.5	2.62	2.37	9.63	3.85	1.59

Table 7.1.7 The number of Indoor Radon measurements above/below the reference level is grouped into different Quaternary geology types.

Indoor radon (IRC)	**Bq m^{-3}**	**Total**	***Quaternary Geology 1:500k GSI 2017***		
			Till derived from Limestones	**Till derived from Namurian siltstones, sandstones and shales**	**Alluvium**
IRC	**<200**	165	118	16	31
	>200	15	11	3	1

	Total	180	129	19	32
Percentage in each Quaternary formation of houses below/above the reference level					
IRC	**<200**	92%	91%	84%	97%
	>200	8%	9%	16%	3%
Percentage of houses below/above the reference level in each Quaternary formation					
IRC	**<200**	-	72%	9%	19%
	>200	-	73%	20%	7%
Log-normal distribution ($\hat{k} = (\ln 200 - \ln GM)/\ln GSD$)					
IRC	**GM**	34.5	31.5	58.5	36.4
	GSD	2.62	2.65	3.5	1.97

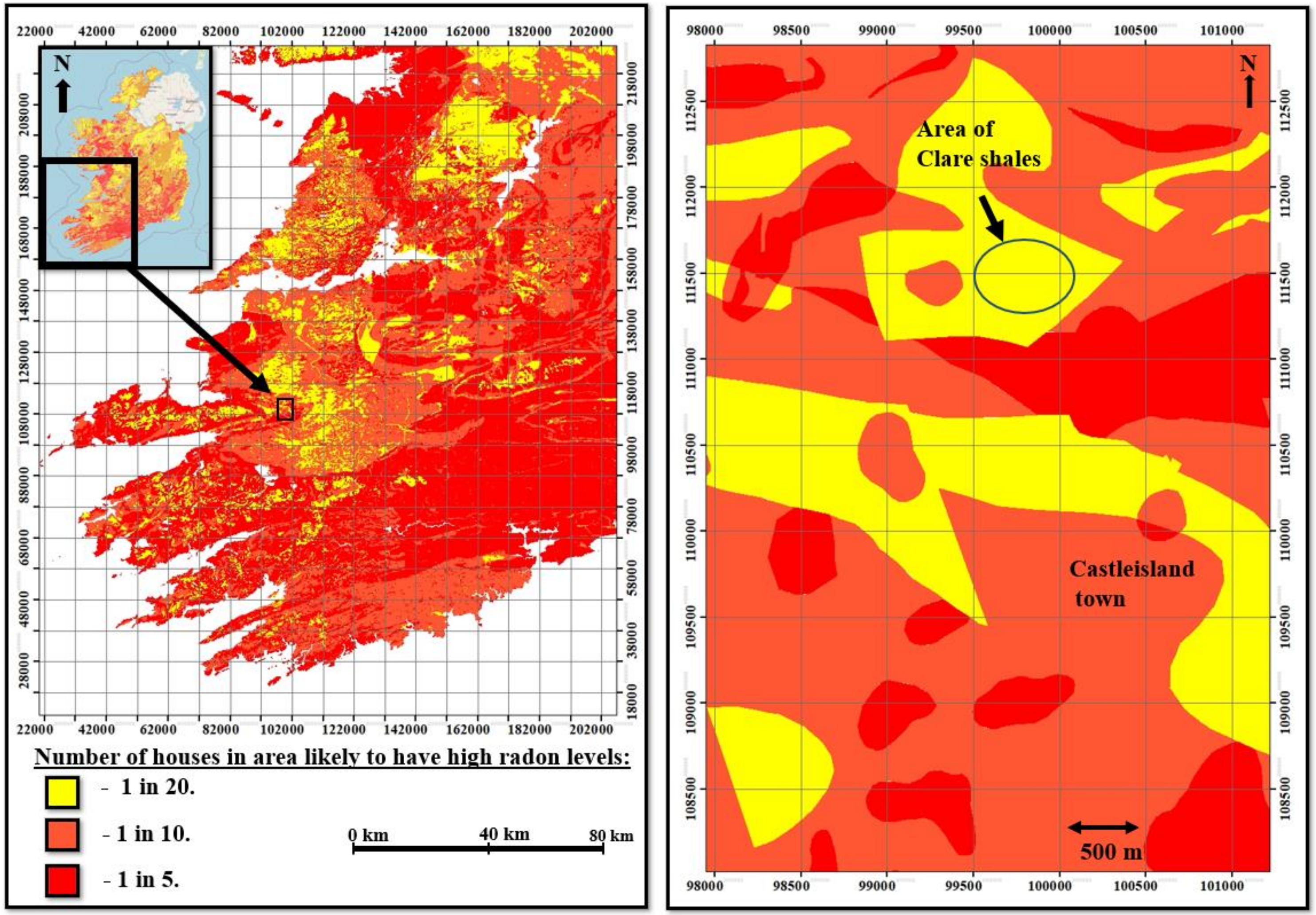

Figure 7.1.1 Supplementary materials Castleisland Co. Kerry study area in relation to the Irish EPA radon map published may 2022

Appendix A

Table 7.1.8: Raw data of soil-gas radon, and soil permeability measurements collected from Castleisland, Co. Kerry SW Ireland study area.

Locality	Sample Number	Date	X.ITM	Y.ITM	Weights	Seconds (RadonJok)	Radon Concentration (kBq/m3)	Soil Permeability (k)	*Soil Permeability Category	Radon Potential
-	2	14/07/2018	499863	611825	-	-	21.7			-
_	3	14/07/2018	499829	611755	-	_	_			-
~71	4	14/07/2018	499726	611673	2	8	732	7.83E-12	h	660.7972451
-	5	14/07/2018	488739	611534	2	28	>1433	2.24E-12	m	867.7170648
-	6	14/07/2018	499625	611437	2	13.95	149	4.49E-12	h	107.5888181
-	5	14/07/2018	488739	611534	2	175	1263	3.58E-13	m	515.9048434
-	7	14/07/2018	499886	611626	2	14.9	1433	4.47E-12	h	1061.308716
60	8	14/07/2018	499886	611419	2	1140	408	5.49E-14	l	124.8445446
71	9	14/07/2018	499766	611631	1	88	1433	1.24E-12	m	750.5026137

-	10	14/07/2018	499091	611167	1	24	159	4.53E-12	h	117.5784889
21	11	14/07/2018	499139	611189	2	165	268	3.80E-13	l	110.301707
58	12	14/07/2018	498897	611321	2	197	390	3.18E-13	l	155.7485394
20	13	14/07/2018	498874	610968	2	530	295	1.18E-13	l	100.429546
51	14	14/07/2018	499039	610999	2	92	148	6.81E-13	m	67.8376798
-	15	14/07/2018	499186	610899	2	499	188	1.26E-13	l	64.45497547
-	16	14/07/2018	499391	610942	1	13	148	8.37E-12	h	136.4249735
60 (daily repeat)	daily rep.60	14/07/2018	499886	611419	2	1140	462	5.49E-14	l	141.4086857
57	17	15/07/2018	498498	611514	2	169	209	3.71E-13	l	85.56022338
64	18	15/07/2018	498519	611879	2	16	-	3.91E-12	m	-
~69	19	15/07/2018	498569	611707	-	-	270	-	-	-

69	20	15/07/2018	498681	611653	2	6	472	1.04E-11	E	479.9751796
20	22	15/07/2018	498803	611336	2	198	222	3.16E-13	l	88.40655333
42	23	15/07/2018	499439	609942	1	12	111	9.06E-12	h	105.4899642
10	24	15/07/2018	499095	610262	-	-	_	-	-	-
~10	25	15/07/2018	499179	610404	2	147	131	4.26E-13	m	54.84151836
~53	26	15/07/2018	499949	610913	-	difficult to extract gas	Redo	2.40E-13	l	-
72	26	15/07/2018	500077	611689	-	easy to extract gas	160	6.16E-12	h	131.3446727
67	27	16/07/2018	499852	611939	-	easy to extract gas	20	6.16E-12	h	15.69527535
68	28	16/07/2018	500327	611939	-	difficult to extract gas	73.5	2.40E-13	l	27.68294616

23	29	16/07/2018	500291	611248	-	easy to extract gas	59.8	6.16E-12	h	48.57274689
61	30	16/07/2018	500452	611439	-	easy to extract gas	26.9	6.16E-12	h	21.39513851
54	31	16/07/2018	500601	610977	-	easy to extract gas	8.8	6.16E-12	h	6.443323566
~71	32	16/07/2018	499773	611637	-	easy to extract gas	754	6.16E-12	h	622.0285443
~71	33	17/07/2018	499766	611623	-	medium to extract	1433	1.48E-12	m	782.0565571
22	34	17/07/2018	499811	611122	-	easy to extract gas	88.5	6.16E-12	h	72.28087334
53	35	17/07/2018	499956	610918	-	easy to extract gas	26.5	6.16E-12	h	21.06471166
16	36	17/07/2018	500136	610766	-	easy to extract gas	51.4	6.16E-12	h	41.63378304

48	37	17/07/2018	499967	610434	-	difficult to extract gas	67.2	2.40E-13	l	25.2773936
49	38	17/07/2018	500457	610437	-	medium to extract	23.8	1.48E-12	m	12.45173848
34	39	17/07/2018	500537	609463	-	difficult to extract gas	36.1	2.40E-13	l	13.40236428
4	40	17/07/2018	500218	609463	-	difficult to extract gas	76.9	2.40E-13	l	28.98118087
39	41	17/07/2018	500537	609464	-	easy to extract gas	95.4	6.16E-12	h	77.9807365
12	42	17/07/2018	500177	610278	-	easy to extract gas	54.9	6.16E-12	h	44.52501798
23	43	17/07/2018	500291	611248	-	easy to extract gas	22.2	6.16E-12	e	17.51262303

60	44	17/07/2018	499886	611419	-	difficult to extract gas	166	5.49E-14	l	63.00256712
38	45	18/07/2018	499951	609427	-	easy to extract gas	77.8	6.16E-12	h	63.44195512
33	46	18/07/2018	499952	608939	-	easy to extract gas	34.7	6.16E-12	h	27.83846208
3	47	18/07/2018	499697	609188	-	easy to extract gas	53.4	6.16E-12	h	43.28591729
23	48	18/07/2018	500291	611248	-	easy to extract gas	27.6	6.16E-12	e	21.9733855
60	49	18/07/2018	499886	611419	-	difficult to extract gas	460	5.49E-14	l	175.2616867
31	50	19/07/2018	498861	608891	-	easy to extract gas	44.5	6.16E-12	h	35.93391989

30	51	19/07/ 2018	498 528	608 891	-	mediu m to extract	25.5	1.48E-12	m	13.380 15758
1	52	19/07/ 2018	498 720	609 181	-	difficu lt to extract gas	37.8	2.40E-13	l	14.051 48164
2	53	19/07/ 2018	499 209	609 183	-	easy to extract gas	38	6.16E-12	h	30.564 48358
36	54	19/07/ 2018	498 919	609 417	-	difficu lt to extract gas	60.1	2.40E-13	l	22.566 37404
35	55	19/07/ 2018	498 643	609 431	-	easy to extract gas	85.9	6.16E-12	h	70.133 09882
5	56	19/07/ 2018	498 694	609 723	-	easy to extract gas	75.1	6.16E-12	h	61.211 57388
40	57	19/07/ 2018	498 457	609 929	-	easy to extract gas	13	6.16E-12	h	9.9128 05487

9	58	19/07/2018	498714	610184	-	easy to extract gas	76.3	6.16E-12	h	62.20285443
45	59	19/07/2018	498441	610459	-	easy to extract gas	57.2	6.16E-12	h	46.42497236
13	60	19/07/2018	498681	610686	-	easy to extract gas	48.9	6.16E-12	h	39.56861523
65	61	19/07/2018	498915	611909	-	easy to extract gas	Redo	6.16E-12	h	-
66	62	19/07/2018	499405	611904	-	difficult to extract gas	351	2.40E-13	l	133.641809
70	63	19/07/2018	499305	611765	-	difficult to extract gas	too hard to extract	2.40E-13	l	-
59	64	19/07/2018	499441	611393	-	easy to extract gas	81	6.16E-12	h	66.08536991

23	65	19/07/2018	500291	611248	-	easy to extract gas	27.4	6.16E-12	e	21.80817207
60	66	19/07/2018	499886	611419	-	difficult to extract gas	488	5.49E-14	l	149.3840129
23	67	20/07/2018	500291	611248	-	easy to extract gas	37.6	6.16E-12	e	30.23405673
46	68	20/07/2018	498979	610434	-	difficult to extract gas	192	2.40E-13	l	72.93024436
14	69	20/07/2018	499201	610705	-	easy to extract gas	104	6.16E-12	h	85.08491376
43	70	20/07/2018	499939	609947	-	difficult to extract gas	62.7	2.40E-13	l	23.55914177
11	71	20/07/2018	499706	610203	-	difficult to extract gas	126	2.40E-13	l	47.72921751

15	72	20/07/2018	499702	610679	-	difficult to extract gas	59.5	2.40E-13	l	22.3372738
52	73	20/07/2018	499579	610965	-	medium to extract	34	1.48E-12	m	18.02225306
60	74	20/07/2018	499886	611419	-	difficult to extract gas	374	5.49E-14	l	308.1230372
A	75	21/07/2018	499878	611442	-	difficult to extract gas	Change batteries, redo.	2.40E-13	l	-
B	76	21/07/2018	499832	611485	-	easy to extract	325	6.16E-12	h	267.6457481
C	77	21/07/2018	499902	611486	-	medium to extract	391	1.48E-12	m	212.9902635
D	78	21/07/2018	499962	611502	-	difficult to extract gas	400	2.40E-13	l	152.3516623

E	79	21/07/2018	499861	611621	-	medium to extract	>1433	1.48E-12	m	782.0565571
F directly above demolished house	80	21/07/2018	499821	611622	-	difficult to extract gas	>1441	2.40E-13	l	549.8405858
32	81	21/07/2018	499452	608950	-	difficult to extract gas	62.3	2.40E-13	l	23.40640827
6	82	22/07/2018	499203	609685	-	easy to extract gas	40	6.16E-12	h	32.21661783
41	83	22/07/2018	498957	609921	-	easy to extract gas	41.5	6.16E-12	h	33.45571852

7	84	22/07/2018	499548	609753	-	easy to extract gas	67.2	6.16E-12	h	54.6856436
54	85	22/07/2018	500481	610939	-	easy to extract gas	64.4	6.16E-12	h	52.37265566
23	86	22/07/2018	499579	610965	-	easy to extract gas	27.7	6.16E-12	e	22.05599221
47	87	22/07/2018	499445	610436	-	difficult to extract gas	23.4	2.40E-13	l	8.553075779
70	88	22/07/2018	499208	611551	-	medium to extract	314	1.48E-12	m	170.9383396
65	89	22/07/2018	498896	611922	-	easy to extract gas	23.1	6.16E-12	h	18.25608344
G	90	22/07/2018	499837	611598	-	easy to extract gas	303	6.16E-12	h	249.4722714
H	91	23/07/2018	499842	611564	-	easy to extract gas	1414	6.16E-12	h	1167.232846

I	92	23/07/2018	499877	611568	-	medium to extract	210	1.48E-12	m	114.1409361
J	93	23/07/2018	499991	611620	-	difficult to extract gas	444	2.40E-13	l	169.1523469
68	1	30/07/2019	500327	611939	2	420	62.7	1.49E-13	l	21.82989902
67	2	30/07/2019	499852	611939	2	62	50.6	1.01E-12	m	24.85541289
71	3	30/07/2019	499726	611673	2	4	1433	1.57E-11	h	1778.419194
78	4	30/07/2019	499452.8195	611673	2	29	1205	2.16E-12	m	722.885422
77	5	30/07/2019	499766	611631	2	100	1433	6.26E-13	l	649.9785899
72	6	31/07/2019	500022	611555	2	38	550	1.65E-12	m	307.9195757
53	9	31/07/2019	499923	610905	2	96	95.3	6.52E-13	l	43.14958622
22	10	31/07/2019	499834	611140	2	142	88.4	4.41E-13	l	37.10562795

60	11	31/07/2019	499886	611419	2	3	389	2.09E-11	h	570.3611422
76	13	31/07/2019	500394	611168	2	3	48.5	2.09E-11	h	69.82513983
23	14	31/07/2019	500316	611256	1	28	44.8	3.88E-12	h	31.04775527
48	15	31/07/2019	499978	610442	1	34	26.1	3.20E-12	m	16.78872614
33	16	31/07/2019	499947	608948	2	14	30.5	4.47E-12	h	21.86355246
75	17	31/07/2019	500027	609207	2	145	30.3	4.32E-13	l	12.39153446
67	19	31/07/2019	499980	612053	2	62	60.6	1.01E-12	m	29.86658484
2	20	01/08/2019	499259	609198	2	73	28	8.58E-13	l	13.06574461
32	21	01/08/2019	499445	609021	2	111	12	5.64E-13	l	4.89221022
74	22	01/08/2019	499398	609284	2	4.3	452	1.46E-11	h	539.0752152
31	23	01/08/2019	498867	608936	2	7	124	8.95E-12	h	117.3386975
1	25	01/08/2019	498629	609131	1	65	17.8	1.67E-12	m	9.456875156

35	26	01/08/2019	498690	609535	1	4.5	109	2.42E-11	h	175.1016796
5	27	01/08/2019	498681	609779	1	27	23.8	4.03E-12	h	16.34483895
20	29	01/08/2019	498699	611141	2	1200	187	5.22E-14	l	56.66704999
45	30	01/08/2019	498566	610415	2	1200	16.7	5.22E-14	l	4.783186478
13	31	01/08/2019	498576	610784	2	1200	53.4	5.22E-14	l	15.9642657
12	32	01/08/2019	499095	611266	2	203	427	3.09E-13	l	169.6774773
59	35	01/08/2019	499917	611334	2	289	117	2.17E-13	l	43.54276987
67	36	01/08/2019	499980	612045	2	62	111	1.01E-12	m	55.12289149
14	37	02/08/2019	499157	610594	1	200	329	3.13E-13	l	130.9810266
11	38	02/08/2019	499718	610216	2	1075	115	5.83E-14	l	35.24438317
47	39	02/08/2019	499497	610431	2	97	12.7	6.46E-13	l	5.342657928
15	40	02/08/2019	500517	610750	2	38	30.5	1.65E-12	m	16.54576955

49	41	02/08/2019	500408	610504	2	132	38.2	4.75E-13	l	16.00878987
21	42	02/08/2019	499198	610859	2	270	21.8	2.32E-13	l	7.895196562
58	43	02/08/2019	498877	611509	2	4	270	1.57E-11	h	334.0745553
69	44	02/08/2019	498576	611862	2	93	166	6.74E-13	l	75.9797086
64	45	02/08/2019	498512	611710	2	75	75.2	8.35E-13	l	35.70378982
36	47	02/08/2019	498879	609382	2	210	58.7	2.98E-13	l	22.84814808
9	48	02/08/2019	498737	610214	1	60	49.1	1.04E-12	m	24.27698076
67	51	02/08/2019	499985	612046	2	62	113	1.01E-12	m	56.12512588
			*Due to technical difficulty with the instrument, 45 measurements were rated according to their relative ease in extracting air from the soil using the RadonJok set up; these samples were then assigned a permeability value equivalent to low (2.40E-13 m^2), medium (1.48E-12 m^2) and high (6.16E-12 m^2) in line with *(Neznal et al., 2004).							

7.2 Chapter 5 supplementary materials

Supplementary materials index

7.2.1 (Table) Statistical analysis of Castleisland, Co. Kerry topsoil geochemistry.
File name: 1. ICPMS_TopSoil_Castleisland_Summary_Stats

7.2.2 (Table) Statistical analysis of TELLUS GSI Midlands topsoil Geochemistry dataset.
File name: 2. TELLUSMidlandsRPprojectTS-Summarystats

7.2.3 (Table) Simplified R^2, Spearman r and Pearson r for ilr-transformed shallow topsoil geochemistry Castleisland, Co. Kerry
File name: Simplified_r2_spearmanr_andPearsonr_Log10SoilgasRadon_shallowtopsoil_Castleisland

7.2.4 (Table) R^2 of Castleisland, Co. Kerry shallow topsoil geochemistry ilr-transformed.
File name: ILR_ShallowTopsoil_r2Table_Castleisland_Co.Kerry

7.2.5 (Table) Coefficient of determination (R^2) of Castleisland, Co. Kerry deeper topsoil geochemistry ilr-transformed.
File name: 5. ILR_DeeperTopsoil_r2Table_CastleislandCoKerry

7.2.6 (Table) Correlation coefficient (Pearson r) of Castleisland, Co. Kerry shallow and deeper topsoil geochemistry ilr-transformed.
File name: ILR_ShallowandDeeper_Topsoil__PearsonsCorrplot_Castleisland_Co.Kerry

7.2.7 (Table) PCA Summary of Castleisland, Co. Kerry deeper topsoil geochemistry Clr-transformed.
File name: CLR_DeeperTopsoil_PCASummary_Castleisland_Co.Kerry

7.2.8 (Figures) PC3 to PC5 score maps of Castleisland, Co. Kerry topsoil geochemistry Clr-transformed.
File name: PC3 to PC5 Score maps of shallow topsoil Castleisland, Co, Kerry, Ireland

7.2.9 (Figure) (A) PC1 vs PC2 biplot and (B) Cluster analysis of deeper topsoil geochemistry Clr-transformed Castleisland, Co. Kerry.
File name: PCA biplot and cluster analysis of deeper topsoil geochemistry, Castleisland, Co. Kerry

7.2.10 (Table) ANOVA of shallow topsoil geochemistry from TELLUS Midlands ilr-transformed.
File name: Anova_TELLUS_Midlands_ShallowTopsoilElementsvsGeogenicRadonClass

7.2.11 (Figures) Tukey-boxplots comparing shallow topsoil geochemistry with (a) geogenic radon potential and (b) bedrock lithology.

File name: TukeyBoxplots_ShallowTopsoil_vs_(a)Bedrock_and_(b)GeogenicRadonClass_TELLUS Midlands

7.2.12 (Figures) PC2 to PC4 score maps of TELLUS Midlands Clr-transformed topsoil geochemistry.

File name: PC1_4_ScoreMaps_TELLUSMidlands

7.2.13 (Figure) Cluster analysis dendrogram TELLUS Midlands Clr-transformed shallow topsoil geochemistry.

File name: 13. Cluster analysis dendrogram TELLUS Midlands

7.2.14 (Table) ANOVA PC1-4 vs (a) geogenic radon class and (b) bedrock lithology of Clr-transformed shallow topsoil TELLUS Midlands.

File name: 14. ANOVA PCA_vs_(a)Geogenicradon_(b)Bedrocklithology

7.2.15 (Figures) Receiving Operator Characteristic and Area Under Curve graphs for (a) Random forest, (b) logistic regression, (c) Gaussian process regress and (d) control models using clr-transformed shallow topsoil TELLUS Midlands. As well as ROC-AUC graphs for (a) logistic regression and (b) Gaussian process regress using clr-transformed shallow topsoil geochemistry TELLUS Midlands limited to elements present in Castleisland.

File name: 15. Receiving Operator Characteristic (ROC_AUC) for machine learning models using Clr-transformed shallow topsoil geochemistry TELLUS Midlands

7.2.16 (Figure) Gaussian process regression model verification (model trained on TELLUS Midlands data and tested on Castleisland data). Boxplot average soil-gas radon of (a) predicted low geogenic radon and (b) predicted high geogenic radon class

File name: 16. Boxplot average soil-gas radon of (a) predicted low geogenic radon and (b) predicted high geogenic radon class

7.2.17 (Figure) Complete canonical heatmap(s) of isometric log ratio transformed TELLUS midlands data. Heatmap includes all topsoil elements analysed.

File name: TELLUS Midlands ilr canonical heatmap1

File name: TELLUS Midlands ilr canonical heatmap2

7.2.18 (Figures) Canonical heatmap(s) of isometric log ratio transformed shallow topsoil elements from Castleisland, Co. Kerry, SW Ireland.

File name: Castleisland Co. Kerry, ilr canonical heatmap1

File name: Castleisland Co. Kerry, ilr canonical heatmap2

7.2.19 Pearson correlation coefficient Tellus Midlands topsoil geochemistry

File name: TELLUS_Midlands_mgkg_RPproject_ilr_pearsoncorrcoefficient

7.2.20 (Figure) Cluster dendrogram of ilr transformed topsoil data from Castleisland, Co. Kerry study area

Shallow topsoil and deeper topsoil geochemistry Castleisland

Table 7.2.1 Summary statistics for shallow topsoil geochemistry Castleisland Co. Kerry dataset.

Element	N	NAs	Minimum	Maximum	First Quartile	Third Quartile	Mean	Median	Sum	Element	SE Mean	LCL Mean	UCL Mean	Variance	Stdev	Skewness	Kurtosis
Mo	47	0	0.6	30.8	1.6	3.2	3.3	2.2	154.9	Mo	0.66	1.98	4.62	20.22	4.5	4.93	26.91
Cu	47	0	18.7	346	32.05	53.25	53.66	38.5	2522.1	Cu	7.74	38.08	69.24	2816.35	53.07	3.89	17.44
Pb	47	0	14	69.7	21.2	32.15	27.98	25.6	1314.9	Pb	1.47	25.02	30.93	101.38	10.07	1.78	4.61
Zn	47	0	15	166	44	80	65.81	58	3093	Zn	4.73	56.29	75.32	1049.94	32.4	1.01	0.85
Ni	47	0	4.6	95.6	13.4	28.15	24.3	21.8	1142	Ni	2.17	19.93	28.66	221.12	14.87	2.33	8.85
Co	47	0	0.7	28.5	4.6	13	9.33	8.2	438.7	Co	0.87	7.57	11.09	35.94	6	0.98	1.01
Mn	47	0	16	3502	158	624.5	543.55	281	25547	Mn	105.91	330.37	756.74	527204.6	726.09	2.57	6.36

Fe	47	0	4100	47300	20900	35800	27504.26	28900	1292700	Fe	1567.33	24349.38	30659.13	1.15E+08	10745.09	-0.45	-0.63
As	47	0	3	33.5	8.1	13.55	11.29	10.4	530.5	As	0.87	9.55	13.03	35.21	5.93	1.43	3.07
U	47	0	0.8	37.2	1.3	2.9	3.45	2	162	U	0.81	1.81	5.08	31.1	5.58	4.83	25.74
Th	47	0	0.4	2.8	1.15	2	1.56	1.6	73.4	Th	0.09	1.39	1.74	0.36	0.6	0	-0.9
Sr	47	0	12	310	16	35.5	40.26	22	1892	Sr	8.48	23.19	57.32	3377.28	58.11	3.42	11.28
Sb	47	0	0.1	4.8	0.3	0.5	0.58	0.4	27.3	Sb	0.12	0.33	0.83	0.71	0.84	3.66	13.38
V	47	0	25	233	33.5	55	50	39	2350	V	5.11	39.71	60.29	1227.09	35.03	3.43	13.82
Ca	47	0	900	15300	1650	5000	4251.06	2900	199800	Ca	535.95	3172.25	5329.87	13500379	3674.29	1.57	1.67
P	47	0	580	7210	865	1565	1358.09	1110	63830	P	150.47	1055.2	1660.97	1064138	1031.57	4.07	19.57
La	47	0	4	31	7	12	10.51	9	494	La	0.81	8.89	12.14	30.65	5.54	1.96	3.81
Cr	47	0	15	43	23	30.5	26.83	26	1261	Cr	0.89	25.04	28.62	36.97	6.08	0.52	0.35
Mg	47	0	600	3900	1400	2650	2048.94	2200	96300	Mg	117.87	1811.68	2286.2	652988	808.08	-0.01	-0.96
Ba	47	0	37	281	52.5	79.5	72.57	65	3411	Ba	5.8	60.9	84.24	1579.64	39.74	3.43	14.23
Al	47	0	6400	27000	13400	20100	16314.89	15900	766800	Al	684.96	14936.13	17693.66	22051295	4695.88	-0.17	-0.64
Na	47	0	100	230	125	190	157.45	150	7400	Na	5.32	146.75	168.15	1328.12	36.44	0.06	-1.25
K	47	0	400	1800	1000	1500	1255.32	1300	59000	K	48.17	1158.36	1352.28	109047.2	330.22	-0.55	-0.27
Hg	47	0	0.04	0.28	0.08	0.13	0.12	0.1	5.45	Hg	0.01	0.1	0.13	0	0.05	1.14	0.72
Sc	47	0	1.1	5.8	2.1	3.4	2.79	2.7	131.1	Sc	0.15	2.49	3.09	1.04	1.02	0.53	0.1

Ga	4 7	0	2	8	4	6	5.23	5	246	Ga	0.1 9	4.85	5.62	1.75	1.32	-0.2	0.04

7.2.2 (Table) Statistical analysis of TELLUS GSI Midlands topsoil Geochemistry dataset.

File name: 2. TELLUSMidlandsRPprojectTS-Summarystats

Table 7.2.2 TELLUSMidlandsRPprojectTS-Summarystats

Element	N	NAs	Minimum	Maximum	1. Quartile	3. Quartile
Al_mgkg_ICPar	4130	0	100	92700	5300	14200
B_mgkg_ICPar	4130	0	5	20	5	10
Ba_mgkg_ICPar	4130	0	2	2120	30.6	93.3
Ca_mgkg_ICPar	4130	0	200	250000	2300	8000
Cr_mgkg_ICPar	4130	0	0.17	148.5	9.9325	25.3
Cu_mgkg_ICPar	4130	0	0.08	315	9.6525	23.6
Fe_mgkg_ICPar	4130	0	100	170500	8895	21400
K_mgkg_ICPar	4130	0	50	4300	600	1800
Li_mgkg_ICPar	4130	0	0.05	78.8	3.9	13.5
Mg_mgkg_ICPar	4130	0	200	33000	1000	2200
Mn_mgkg_ICPar	4130	0	0.05	15300	154.625	900.75
Na_mgkg_ICPar	4130	0	5	1360	160	270
Ni_mgkg_ICPar	4130	0	0.19	121	10.2	34.1
P_mgkg_ICPar	4130	0	60	3630	620	1030
S_mgkg_ICPar	4130	0	100	10900	500	1900
Sr_mgkg_ICPar	4130	0	0.66	578	15.1	31
Ti_mgkg_ICPar	4130	0	5	1310	30	60
V_mgkg_ICPar	4130	0	0.2	149.5	15.4	37.175
Zn_mgkg_ICPar	4130	0	1.2	9120	34.6	95.775
Zr_mgkg_ICPar	4130	0	0.03	9.07	0.7925	3
Ag_mgkg_ICPar	4130	0	5.00E-04	0.65	0.064	0.114
As_mgkg_ICPar	4130	0	0.07	146	4.7425	11.05
Be_mgkg_ICPar	4130	0	0.005	17.05	0.28	0.84
Bi_mgkg_ICPar	4130	0	0.00025	15.55	0.0786	0.136
Cd_mgkg_ICPar	4130	0	0.014	12.4	0.378	1.275
Ce_mgkg_ICPar	4130	0	0.128	282	14.55	35
Co_mgkg_ICPar	4130	0	0.041	40.2	2.7325	9.5
Cs_mgkg_ICPar	4130	0	0.0025	27.2	0.344	0.92
Ga_mgkg_ICPar	4130	0	0.024	17	1.56625	4.07
Ge_mgkg_ICPar	4130	0	0.0025	0.341	0.032	0.059
Hf_mgkg_ICPar	4130	0	0.001	0.324	0.022	0.09

Hg_mgkg_ICPar	4130	0	0.002	9.26	0.077	0.133
In_mgkg_ICPar	4130	0	0.0025	0.334	0.012	0.024
La_mgkg_ICPar	4130	0	0.07	114.5	7.46	17.65
Mo_mgkg_ICPar	4130	0	0.04	62.8	0.6	1.56
Nb_mgkg_ICPar	4130	0	0.004	5.82	0.171	0.38275
Pb_mgkg_ICPar	4130	0	0.068	649	16.55	29
Rb_mgkg_ICPar	4130	0	0.026	54.3	4.35	16.25
Sb_mgkg_ICPar	4130	0	0.005	11.55	0.267	0.595
Sc_mgkg_ICPar	4130	0	0.022	10.9	0.94525	3.15
Se_mgkg_ICPar	4130	0	0.013	39.6	0.561	1.38
Sn_mgkg_ICPar	4130	0	0.005	19	0.5225	0.87
Ta_mgkg_ICPar	4130	0	0.0025	0.1	0.0025	0.0025
Te_mgkg_ICPar	4130	0	0.0015	1.835	0.009	0.023
Th_mgkg_ICPar	4130	0	0.001	20.4	0.4005	1.41
Tl_mgkg_ICPar	4130	0	5.00E-04	2.6	0.097	0.252
U_mgkg_ICPar	4130	0	0.013	109	0.803	1.52375
W_mgkg_ICPar	4130	0	5.00E-04	16.35	0.039	0.083
Y_mgkg_ICPar	4130	0	0.061	132.5	4.95	18.85
Au_mgkg_ICPar	4130	0	1.00E-04	1.285	3.00E-04	9.00E-04
Pd_mgkg_ICPar	4130	0	5.00E-04	0.257	5.00E-04	0.001
Pt_mgkg_ICPar	4130	0	0.001	1.3	0.001	0.001
Re_mgkg_ICPar	4130	0	1.00E-04	0.1015	1.00E-04	8.00E-04

Continued table.. TELLUSMidlandsRPprojectTS-Summarystats

Element	Mean	Median	Sum	SE Mean	LCL Mean	
Al_mgkg_ICPar	10066.68	10300	41575400	98.99177	9872.606	
B_mgkg_ICPar	7.285714	5	30090	0.039326	7.208614	
Ba_mgkg_ICPar	77.0468	57.4	318203.3	1.442967	74.21781	
Ca_mgkg_ICPar	10083.22	3550	41643700	325.5335	9444.999	
Cr_mgkg_ICPar	18.38518	18.9	75930.81	0.186548	18.01945	
Cu_mgkg_ICPar	18.00198	16.475	74348.18	0.221302	17.56811	
Fe_mgkg_ICPar	15580.09	15600	64345770	163.472	15259.6	
K_mgkg_ICPar	1245.484	1200	5143850	11.5002	1222.938	
Li_mgkg_ICPar	9.493935	9	39209.95	0.117626	9.263325	
Mg_mgkg_ICPar	1852.76	1400	7651900	24.57529	1804.579	
Mn_mgkg_ICPar	624.7857	492	2580365	12.91567	599.4641	
Na_mgkg_ICPar	225.115	200	929725	1.574826	222.0275	

Ni_mgkg_ICPar	23.35036	23.7	96437	0.246314	22.86745	
P_mgkg_ICPar	834.954	820	3448360	5.684538	823.8092	
S_mgkg_ICPar	1367.458	700	5647600	20.6588	1326.955	
Sr_mgkg_ICPar	29.73692	20.6	122813.5	0.511735	28.73364	
Ti_mgkg_ICPar	52.80509	40	218085	0.849602	51.13941	
V_mgkg_ICPar	26.68419	26.95	110205.7	0.252448	26.18925	
Zn_mgkg_ICPar	70.6186	65.4	291654.8	2.298041	66.1132	
Zr_mgkg_ICPar	2.00191	1.98	8267.89	0.021621	1.959522	
Ag_mgkg_ICPar	0.091439	0.088	377.6415	0.000755	0.089959	
As_mgkg_ICPar	8.916056	7.89	36823.31	0.122629	8.675638	
Be_mgkg_ICPar	0.590884	0.61	2440.35	0.00722	0.576728	
Bi_mgkg_ICPar	0.120754	0.105	498.7152	0.003968	0.112975	
Cd_mgkg_ICPar	0.950541	0.771	3925.736	0.012886	0.925277	
Ce_mgkg_ICPar	25.36665	26.6	104764.2	0.249927	24.87665	
Co_mgkg_ICPar	6.450577	6.6	26640.88	0.06813	6.317005	
Cs_mgkg_ICPar	0.702913	0.643	2903.03	0.011899	0.679583	
Ga_mgkg_ICPar	2.969206	2.89	12262.82	0.030083	2.910228	
Ge_mgkg_ICPar	0.047705	0.046	197.0215	0.000386	0.046948	
Hf_mgkg_ICPar	0.05919	0.058	244.455	0.000666	0.057883	
Hg_mgkg_ICPar	0.117583	0.098	485.618	0.002442	0.112796	
In_mgkg_ICPar	0.018779	0.018	77.559	0.000188	0.01841	
La_mgkg_ICPar	12.94213	13.35	53451	0.127187	12.69278	
Mo_mgkg_ICPar	1.336167	1	5518.37	0.026871	1.283486	
Nb_mgkg_ICPar	0.31243	0.262	1290.336	0.004396	0.303812	
Pb_mgkg_ICPar	25.96872	22.3	107250.8	0.359379	25.26414	
Rb_mgkg_ICPar	10.90318	10.85	45030.14	0.119389	10.66912	
Sb_mgkg_ICPar	0.490515	0.395	2025.825	0.006923	0.476943	
Sc_mgkg_ICPar	2.164298	2.155	8938.55	0.022366	2.120448	
Se_mgkg_ICPar	1.368131	0.82	5650.381	0.029074	1.31113	
Sn_mgkg_ICPar	0.814304	0.68	3363.075	0.011624	0.791516	
Ta_mgkg_ICPar	0.002641	0.0025	10.9075	3.20E-05	0.002578	
Te_mgkg_ICPar	0.018434	0.016	76.1335	0.000551	0.017354	
Th_mgkg_ICPar	0.969363	0.9455	4003.468	0.011907	0.946019	
Tl_mgkg_ICPar	0.181705	0.183	750.442	0.001985	0.177814	
U_mgkg_ICPar	1.668174	1.09	6889.56	0.053657	1.562978	
W_mgkg_ICPar	0.104502	0.058	431.592	0.007656	0.089492	

Y_mgkg_ICPar	12.89603	11.675	53260.6	0.160919	12.58054	
Au_mgkg_ICPar	0.00139	6.00E-04	5.7388	0.000371	0.000661	
Pd_mgkg_ICPar	0.001489	5.00E-04	6.148	0.000121	0.001252	
Pt_mgkg_ICPar	0.006457	0.001	26.666	0.00059	0.0053	
Re_mgkg_ICPar	0.001251	4.00E-04	5.1668	5.80E-05	0.001137	
Element	**UCL Mean**	**Variance**	**Stdev**	**Skewness**	**Kurtosis**	
Al_mgkg_ICPar	10260.76	40471396	6361.713	0.728633	6.291087	
B_mgkg_ICPar	7.362815	6.387226	2.527296	0.312568	-1.25634	
Ba_mgkg_ICPar	79.8758	8599.294	92.73238	7.914529	116.1024	
Ca_mgkg_ICPar	10721.44	4.38E+08	20920.44	5.928422	46.63964	
Cr_mgkg_ICPar	18.75092	143.7245	11.98852	0.916933	5.037822	
Cu_mgkg_ICPar	18.43585	202.2645	14.22197	5.458165	76.23371	
Fe_mgkg_ICPar	15900.58	1.1E+08	10505.54	2.965189	32.41712	
K_mgkg_ICPar	1268.031	546211.7	739.0614	0.45895	-0.34584	
Li_mgkg_ICPar	9.724544	57.14185	7.559223	1.621868	8.179424	
Mg_mgkg_ICPar	1900.941	2494292	1579.333	5.338062	66.15439	
Mn_mgkg_ICPar	650.1074	688943.9	830.0265	8.587477	121.8167	
Na_mgkg_ICPar	228.2025	10242.72	101.2063	1.639195	5.655335	
Ni_mgkg_ICPar	23.83327	250.5704	15.82942	0.550661	0.819468	
P_mgkg_ICPar	846.0988	133456.7	365.3172	0.820626	2.97741	
S_mgkg_ICPar	1407.96	1762627	1327.64	1.888017	4.279955	
Sr_mgkg_ICPar	30.7402	1081.536	32.88671	6.028225	60.39281	
Ti_mgkg_ICPar	54.47076	2981.128	54.59971	7.989398	118.5132	
V_mgkg_ICPar	27.17912	263.2057	16.22361	0.379919	0.654514	
Zn_mgkg_ICPar	75.12399	21810.49	147.6838	55.77953	3410.741	
Zr_mgkg_ICPar	2.044299	1.930596	1.389459	0.45649	-0.03571	
Ag_mgkg_ICPar	0.092918	0.002351	0.048492	1.96427	14.40929	
As_mgkg_ICPar	9.156474	62.10599	7.880735	5.672476	61.71711	
Be_mgkg_ICPar	0.60504	0.215318	0.464024	11.54916	387.2972	
Bi_mgkg_ICPar	0.128533	0.065018	0.254987	53.84426	3243.677	
Cd_mgkg_ICPar	0.975805	0.68581	0.828137	3.301074	23.1531	
Ce_mgkg_ICPar	25.85664	257.9745	16.06158	1.827203	22.49816	
Co_mgkg_ICPar	6.584149	19.17033	4.378394	0.552693	1.473653	
Cs_mgkg_ICPar	0.726242	0.584798	0.764721	13.50948	382.1651	
Ga_mgkg_ICPar	3.028185	3.737538	1.933271	0.743792	1.36927	
Ge_mgkg_ICPar	0.048462	0.000616	0.02481	2.779386	20.46345	

Hf_mgkg_ICPar	0.060497	0.001834	0.042831	0.462709	-0.08893	
Hg_mgkg_ICPar	0.12237	0.024626	0.156928	48.16831	2787.493	
In_mgkg_ICPar	0.019149	0.000147	0.012113	7.01641	142.2199	
La_mgkg_ICPar	13.19149	66.80901	8.173678	1.145882	9.550463	
Mo_mgkg_ICPar	1.388849	2.982059	1.726864	15.12847	437.6588	
Nb_mgkg_ICPar	0.321048	0.079802	0.282493	5.108419	57.85452	
Pb_mgkg_ICPar	26.6733	533.4029	23.09552	10.17009	189.7051	
Rb_mgkg_ICPar	11.13725	58.86767	7.672527	0.433595	-0.16528	
Sb_mgkg_ICPar	0.504086	0.197917	0.444879	9.19362	166.9385	
Sc_mgkg_ICPar	2.208147	2.066003	1.43736	0.451862	0.033523	
Se_mgkg_ICPar	1.425132	3.491065	1.868439	6.447675	72.05779	
Sn_mgkg_ICPar	0.837092	0.557988	0.746986	8.636526	134.1327	
Ta_mgkg_ICPar	0.002704	4.00E-06	0.00206	32.66896	1338.599	
Te_mgkg_ICPar	0.019515	0.001255	0.035425	37.76352	1782.056	
Th_mgkg_ICPar	0.992706	0.585513	0.765188	4.569341	101.7435	
Tl_mgkg_ICPar	0.185596	0.016268	0.127547	3.638654	57.77457	
U_mgkg_ICPar	1.773371	11.8906	3.448275	16.53825	430.5707	
W_mgkg_ICPar	0.119511	0.24207	0.492006	22.93134	625.2796	
Y_mgkg_ICPar	13.21152	106.9455	10.34145	1.634059	8.30295	
Au_mgkg_ICPar	0.002118	0.00057	0.023873	47.60156	2363.869	
Pd_mgkg_ICPar	0.001725	6.00E-05	0.007747	21.09326	554.0816	
Pt_mgkg_ICPar	0.007613	0.001437	0.037907	16.61179	419.9599	
Re_mgkg_ICPar	0.001365	1.40E-05	0.003722	10.66353	189.1378	

7.2.3 (Table) Simplified R^2, Spearman r and Pearson r for ilr-transformed shallow topsoil geochemistry Castleisland, Co. Kerry

Table 7.2.3 Shallow topsoil geochemistry coefficient of determination (R2), Spearman r and Pearson correlation coefficients for Castleisland Co. Kerry dataset.

Element	Spearman log10SGRn	Element	r2 log10SGRn	Element	Pearson log10SGRn
log10RnConc	1	**log10RnConc**	1	**log10RnConc**	1
U	0.6	**U**	0.39	**U**	0.62
Sr	0.57	**Sr**	0.47	**Sr**	0.69
Cu	0.54	**Cu**	0.3	**Cu**	0.55
V	0.54	**V**	0.43	**V**	0.65
P	0.54	**P**	0.49	**P**	0.7
Ba	0.51	**Ba**	0.45	**Ba**	0.67
Sb	0.48	**Sb**	0.13	**Sb**	0.35
Mo	0.46	**Mo**	0.4	**Mo**	0.63
La	0.43	**La**	0.27	**La**	0.52
Cr	0.4	**Cr**	0.21	**Cr**	0.46
Hg	0.31	**Hg**	0.06	**Hg**	0.24
Pb	0.24	**Pb**	0.04	**Pb**	0.21
K	0.24	**K**	0.12	**K**	0.34
Th	0.21	**Th**	0.08	**Th**	0.27
As	0.18	**As**	0.14	**As**	0.37
Ca	0.18	**Ca**	0.01	**Ca**	0.09
Na	0.17	**Na**	0.05	**Na**	0.23
Zn	0.12	**Zn**	0.02	**Zn**	0.14
Al	0.1	**Al**	0.03	**Al**	0.18
Ga	0.03	**Ga**	0.02	**Ga**	0.13
Sc	-0.03	**Sc**	0.003	**Sc**	-0.06
Mn	-0.14	**Mn**	0.002	**Mn**	-0.05
Ni	-0.18	**Ni**	0.03	**Ni**	-0.18
Mg	-0.19	**Mg**	0.08	**Mg**	-0.27
Co	-0.22	**Co**	0.05	**Co**	-0.22
Fe	-0.29	**Fe**	0.14	**Fe**	-0.37

7.2.4 (Table) R^2 of Castleisland, Co. Kerry shallow topsoil geochemistry ilr-transformed.

File name: CLR_ShallowTopsoil_r2Table_Castleisland_Co.Kerry

Table 7.2.4 R2 coefficient of determination tabulation for Castleisland, Co. Kerry topsoil data (isometric log ratio transformed).

r2	Mo	Cu	Pb	Zn	Ni	Co	Mn	Fe	As	U	Th	Sr	Sb	V	Ca	P	La	Cr	Mg	Ba	Al	Na	K	Hg	Sc	Ga	log10RnC
Mo	1	0.13	0.002	0.001	0.053	0.09	0.002	0.018	0.348	0.632	0.052	0.368	0.497	0.392	0.0002	0.512	0.15	0.058	0.119	0.344	0.003	0.001	0.048	0.0003	0.052	0.004	0.395
Cu	0.13	1	0.173	0.342	0.006	0.109	0.024	0.259	0.001	0.178	0.066	0.442	0.155	0.588	0.038	0.492	0.48	0.547	0.031	0.636	0.048	0.202	0.313	0.083	0.0001	0.118	0.3
Pb	0.002	0.173	1	0.005	0.047	0.147	0.047	0.446	0.004	0.052	0.003	0.124	0.128	0.261	0.097	0.213	0.256	0.506	0.089	0.215	0.233	0.327	0.176	0.593	0.021	0.309	0.043
Zn	0.001	0.342	0.005	1	0.246	0.097	0.073	0.036	0.00E+00	0.002	0.014	0.046	0.01	0.047	0.017	0.045	0.147	0.047	0.036	0.087	0.005	1.00E-04	0.039	0.013	0.03	0.003	0.019
Ni	0.053	0.006	0.047	0.246	1	0.659	0.412	1.00E-04	0.005	0.067	3.00E-05	0.039	0.006	0.121	0.024	0.079	0.0005	0.091	0.166	0.078	0.041	0.131	0.059	0.049	0.202	0.143	0.034
Co	0.09	0.109	0.147	0.097	0.659	1	0.572	0.091	0.031	0.125	0.011	0.146	0.049	0.321	0.001	0.238	0.079	0.286	0.135	0.229	0.129	0.289	0.21	0.142	0.095	0.298	0.049
Mn	0.002	0.024	0.047	0.073	0.412	0.572	1	0.019	0.188	0.06	0.022	0.017	0.003	0.053	0.0004	0.032	0.006	0.106	0.005	0.034	0.086	0.157	0.041	0.064	0.044	0.11	0.002
Fe	0.018	0.259	0.446	0.036	0	0.091	0.019	1	0.053	0.145	0.008	0.244	0.045	0.406	0.392	0.392	0.497	0.517	0.019	0.38	0.244	0.434	0.286	0.505	0.117	0.222	0.137
As	0.348	0.001	0.004	0.00E+00	0.005	0.031	0.188	0.053	1	0.112	0.006	0.044	0.225	0.017	0.019	0.057	0.008	0.017	0.155	0.012	0.073	0.116	0.015	0.016	0.035	0.081	0.136
U	0.632	0.178	0.052	0.002	0.067	0.125	0.06	0.145	0.112	1	0.008	0.446	0.324	0.422	0.041	0.597	0.166	0.157	0.123	0.451	0.015	0.003	0.02	0.069	0.007	0.0004	0.391
Th	0.052	0.066	0.003	0.014	3.00E-05	0.011	0.022	0.008	0.006	0.008	1	0.043	0.034	0.079	0.104	0.013	0.105	0.054	0.14	0.101	0.132	0.099	0.282	0.085	0.248	0.094	0.075
Sr	0.368	0.442	0.124	0.046	0.039	0.146	0.017	0.244	0.044	0.446	0.043	1	0.282	0.664	0.013	0.742	0.548	0.395	0.113	0.805	0.082	0.088	0.209	0.042	0.018	0.074	0.47
Sb	0.497	0.155	0.128	0.01	0.006	0.049	0.003	0.045	0.225	0.324	0.034	0.282	1	0.274	0.0002	0.316	0.16	0.144	0.047	0.244	0.01	0.005	0.053	0.026	0.002	0.006	0.125
V	0.392	0.588	0.261	0.047	0.121	0.321	0.053	0.406	0.017	0.422	0.079	0.664	0.274	1	0.026	0.814	0.715	0.664	0.125	0.85	0.171	0.348	0.493	0.123	0.0002	0.253	0.428
Ca	0.0002	0.038	0.097	0.017	0.024	0.001	0.0004	0.392	0.019	0.041	0.104	0.013	0.0002	0.026	1	0.077	0.024	0.008	0.044	0.011	0.104	0.007	0.008	0.377	0.001	0.054	0.009
P	0.512	0.492	0.213	0.045	0.079	0.238	0.032	0.392	0.057	0.597	0.013	0.742	0.316	0.814	0.077	1	0.524	0.548	0.191	0.813	0.069	0.142	0.22	0.155	0.015	0.086	0.492
La	0.15	0.48	0.256	0.147	0.0005	0.079	0.006	0.497	0.008	0.166	0.105	0.548	0.16	0.715	0.024	0.524	1	0.537	0.051	0.704	0.255	0.317	0.612	0.066	0.089	0.32	0.271
Cr	0.058	0.547	0.506	0.047	0.091	0.286	0.106	0.517	0.017	0.157	0.054	0.395	0.144	0.664	0.008	0.548	0.537	1	0.025	0.639	0.46	0.556	0.491	0.287	0.014	0.546	0.211
Mg	0.119	0.031	0.089	0.036	0.166	0.135	0.005	0.019	0.155	0.123	0.14	0.113	0.047	0.125	0.044	0.191	0.051	0.025	1	0.1	0.004	0.0004	0.001	0.126	0.093	0.0001	0.075
Ba	0.344	0.636	0.215	0.087	0.078	0.229	0.034	0.38	0.012	0.451	0.101	0.805	0.244	0.85	0.011	0.813	0.704	0.639	0.1	1	0.196	0.258	0.412	0.083	0.001	0.216	0.454
Al	0.003	0.048	0.233	0.005	0.041	0.129	0.086	0.244	0.073	0.015	0.132	0.082	0.01	0.171	0.104	0.069	0.255	0.46	0.004	0.196	1	0.481	0.37	0.072	0.173	0.678	0.032
Na	0.001	0.202	0.327	1.00E-04	0.131	0.289	0.157	0.434	0.116	0.003	0.099	0.088	0.005	0.348	0.007	0.142	0.317	0.556	0.0004	0.258	0.481	1	0.664	0.223	0.051	0.682	0.052
K	0.048	0.313	0.176	0.039	0.059	0.21	0.041	0.286	0.015	0.02	0.282	0.209	0.053	0.493	0.008	0.22	0.612	0.491	0.001	0.412	0.37	0.664	1	0.022	0.066	0.648	0.118
Hg	0.0003	0.083	0.593	0.013	0.049	0.142	0.064	0.505	0.016	0.069	0.085	0.042	0.026	0.123	0.377	0.155	0.066	0.287	0.126	0.083	0.072	0.223	0.022	1	0.002	0.11	0.057
Sc	0.052	0.0001	0.021	0.03	0.202	0.095	0.044	0.117	0.035	0.007	0.248	0.018	0.002	0.0002	0.001	0.015	0.089	0.014	0.093	0.001	0.173	0.051	0.066	0.002	1	0.052	0.003
Ga	0.004	0.118	0.309	0.003	0.143	0.298	0.11	0.222	0.081	0.0004	0.094	0.074	0.006	0.253	0.054	0.086	0.32	0.546	0.0001	0.216	0.678	0.682	0.648	0.11	0.052	1	0.017
log10RnC	0.395	0.3	0.043	0.019	0.034	0.049	0.002	0.137	0.136	0.391	0.075	0.47	0.125	0.428	0.009	0.492	0.271	0.211	0.075	0.454	0.032	0.052	0.118	0.057	0.003	0.017	1

7.2.5 (Table) Coefficient of determination (R^2) of Castleisland, Co. Kerry deeper topsoil geochemistry ilr-transformed.

File name: 5. ILR_DeeperTopsoil_r2Table_CastleislandCoKerry

Log10SG	Mo	Cu	Pb	Zn	Ni	Co	Mn	Fe	As	U	Th	Sr	Sb	V	Ca	P	La	Cr	Mg	Ba	Al	Na	K	Hg	Sc	Ga
Mo	1	0.22	0.12	0.003	0.05	0.02	0.02	0.08	0.1	0.0004	0.11	0.03	0.48	0.23	0.12	1.00E-05	0.16	0.08	0.06	0.12	0.004	0.12	0.05	0.08	0.01	0.08
Cu	0.22	1	0.2	0.06	0.01	0.05	0.06	0.22	0.03	0.3	0.23	0.03	0.17	0.62	0.35	0.01	0.22	0.23	0.01	0.02	0.05	0.01	0.02	0.0002	0.14	0.001
Pb	0.12	0.2	1	0.07	0.003	0.01	0.05	0.29	0.01	0.01	0.43	0.01	0.21	0.1	0.07	0.23	0.48	0.08	0.02	0.01	0.07	0.00E+00	0.07	5.00E-05	0.15	0.01
Zn	0	0.06	0.07	1	0.12	0.1	0.04	0.59	0.05	0.03	0.05	0.46	0.04	0.08	0.34	0.34	0.02	0.62	0.46	0.24	0.59	0.46	0.48	0.52	0.3	0.35
Ni	0.05	0.01	0.003	0.12	1	0.79	0.6	0.17	0.14	0.05	0.002	0.3	0.07	0.01	0.02	0.06	0.08	1.00E-04	0.44	0.76	0.08	0.44	0.28	0.16	0.13	0.4
Co	0.02	0.05	0.01	0.1	0.79	1	0.71	0.15	0.04	0.002	0.01	0.22	0.02	0.001	0.01	0.02	0.13	0.001	0.36	0.78	0.06	0.39	0.15	0.14	0.01	0.26
Mn	0.02	0.06	0.05	0.04	0.6	0.71	1	0.04	0.05	0.02	0.0003	0.2	0.13	0.03	0.05	0.03	0.27	0.01	0.23	0.57	0.06	0.29	0.14	0.05	0.01	0.32
Fe	0.08	0.22	0.29	0.59	0.17	0.15	0.04	1	0.07	0.13	0.19	0.41	0.32	0.24	0.55	0.26	0.16	0.58	0.43	0.19	0.69	0.36	0.39	0.34	0.35	0.33
As	0.1	0.03	0.01	0.05	0.14	0.04	0.05	0.07	1	0.65	0.02	0.43	0.1	0.0004	0.03	0.001	0.01	1.00E-06	0.51	0.17	0.07	0.38	0.16	0.28	0.19	0.35
U	0.0004	0.3	0.01	0.03	0.05	0.002	0.02	0.13	0.65	1	0.04	0.24	0.005	0.07	0.12	0.01	0.01	0.04	0.22	0.03	0.06	0.1	0.1	0.08	0.21	0.21
Th	0.11	0.23	0.43	0.05	0.002	0.01	0.0003	0.19	0.02	0.04	1	0.04	0.1	0.01	0.07	0.33	0.19	0.08	3.00E-05	0.01	0.11	0.0004	0.23	0.01	0.19	0.1
Sr	0.03	0.03	0.01	0.46	0.3	0.22	0.2	0.41	0.43	0.24	0.04	1	0.01	0.02	0.09	0.26	0.02	0.23	0.81	0.42	0.43	0.78	0.56	0.54	0.39	0.82
Sb	0.48	0.17	0.21	0.04	0.07	0.02	0.13	0.32	0.1	0.00481	0.1	0.01	1	0.36	0.39	0.005	0.46	0.3	0.02	0.08	0.13	0.03	0.01	0.0001	0.01	0.05
V	0.23	0.62	0.1	0.08	0.01	0.001	0.03	0.24	0.0004	0.07	0.01	0.02	0.36	1	0.38	0.01	0.16	0.31	0.02	0.002	0.02	0.004	0.02	0.002	0.01	0.02
Ca	0.12	0.35	0.07	0.34	0.02	0.01	0.05	0.55	0.03	0.12	0.07	0.09	0.39	0.38	1	0.04	0.17	0.61	0.11	0.001	0.36	0.06	0.07	0.16	0.1	0.03
P	0.00E+00	0.01	0.23	0.34	0.06	0.02	0.03	0.26	0.001	0.01	0.33	0.26	0.005	0.01	0.04	1	0.03	0.19	0.14	0.06	0.31	0.21	0.45	0.08	0.38	0.37
La	0.1613	0.22	0.48	0.02	0.08	0.13	0.27	0.16	0.01	0.01	0.19	0.02	0.46	0.16	0.17	0.03	1	0.06	0.01	0.16	0.03	0.03	0.001	1.00E-08	0.08	0.03
Cr	0.08	0.23	0.08	0.62	1.00E-04	0.001	0.01	0.58	1.00E-06	0.04	0.08	0.23	0.3	0.31	0.61	0.19	0.06	1	0.14	0.01	0.53	0.11	0.17	0.25	0.18	0.12
Mg	0.06	0.01	0.02	0.46	0.44	0.36	0.23	0.43	0.51	0.22	3.00E-05	0.81	0.02	0.02	0.11	0.14	0.01	0.14	1	0.59	0.33	0.87	0.49	0.65	0.27	0.63
Ba	0.12	0.02	0.01	0.24	0.76	0.78	0.57	0.19	0.17	0.03	0.01	0.42	0.08	0.002	0.001	0.06	0.16	0.01	0.59	1	0.14	0.62	0.31	0.31	0.08	0.45
Al	0.004	0.05	0.07	0.59	0.08	0.06	0.06	0.69	0.07	0.06	0.11	0.43	0.13	0.02	0.36	0.31	0.03	0.53	0.33	0.14	1	0.42	0.51	0.41	0.35	0.47
Na	0.12	0.01	2.00E-05	0.46	0.44	0.39	0.29	0.36	0.38	0.1	0.0004	0.78	0.03	0.004	0.06	0.21	0.03	0.11	0.87	0.62	0.42	1	0.61	0.73	0.26	0.71
K	0.05	0.02	0.07	0.48	0.28	0.15	0.14	0.39	0.16	0.1	0.23	0.56	0.01	0.02	0.07	0.45	0.001	0.17	0.49	0.31	0.51	0.61	1	0.53	0.38	0.69
Hg	0.08	0.0002	5.00E-05	0.52	0.16	0.14	0.05	0.34	0.28	0.08	0.01	0.54	0.0001	0.002	0.16	0.08	1.00E-08	0.25	0.65	0.31	0.41	0.73	0.53	1	0.22	0.39
Sc	0.01	0.14	0.15	0.3	0.13	0.01	0.01	0.35	0.19	0.21	0.19	0.39	0.01	0.01	0.1	0.38	0.08	0.18	0.27	0.08	0.35	0.26	0.38	0.22	1	0.39
Ga	0.08	0.001	0.01	0.35	0.4	0.26	0.32	0.33	0.35	0.21	0.1	0.82	0.05	0.02	0.03	0.37	0.03	0.12	0.63	0.45	0.47	0.71	0.69	0.39	0.39	1

7.2.6 (Table) Correlation coefficient (Pearson r) of Castleisland, Co. Kerry shallow topsoil geochemistry Clr-transformed.
File name: ILR_Shallow_Topsoil__PearsonsCorrplot_Castleisland_Co.Kerry

Table 7.2.6a Pearson correlation table of Castleisland, Co. Kerry, shallow topsoil geochemistry (ilr transformed) and log10 soil-gas radon

Shallow_T	Mo	Cu	Pb	Zn	Ni	Co	Mn	Fe	As	U	Th	Sr	Sb	V	Ca	P	La	Cr	Mg	Ba	Al	Na	K	Hg	Sc	Ga	log10RnC
Mo	1	0.36	0.05	0.03	-0.23	-0.3	-0.04	-0.13	0.59	0.79	0.23	0.61	0.71	0.63	0.01	0.72	0.39	0.24	-0.35	0.59	-0.06	-0.03	0.22	-0.02	-0.23	-0.06	0.63
Cu	0.36	1	0.42	0.58	-0.08	-0.33	-0.16	-0.51	0.03	0.42	0.26	0.66	0.39	0.77	0.2	0.7	0.69	0.74	-0.18	0.8	0.22	0.45	0.56	0.29	0.01	0.34	0.55
Pb	0.05	0.42	1	0.07	-0.22	-0.38	-0.22	-0.67	-0.06	0.23	-0.05	0.35	0.36	0.51	0.31	0.46	0.51	0.71	-0.3	0.46	0.48	0.57	0.42	0.77	0.14	0.56	0.21
Zn	0.03	0.58	0.07	1	0.5	0.31	0.27	-0.19	-0.002	-0.04	0.12	0.21	0.1	0.22	0.13	0.21	0.38	0.22	0.19	0.29	-0.07	-0.01	0.2	-0.11	0.17	-0.06	0.14
Ni	-0.23	-0.08	-0.22	0.5	1	0.81	0.64	-0.01	0.07	-0.26	-0.01	-0.2	-0.07	-0.35	0.15	-0.28	0.02	-0.3	0.41	-0.28	-0.2	-0.36	-0.24	-0.22	0.45	-0.38	-0.18
Co	-0.3	-0.33	-0.38	0.31	0.81	1	0.76	0.3	0.18	-0.35	-0.1	-0.38	-0.22	-0.57	-0.02	-0.49	-0.28	-0.54	0.37	-0.48	-0.36	-0.54	-0.46	-0.38	0.31	-0.55	-0.22
Mn	-0.04	-0.16	-0.22	0.27	0.64	0.76	1	0.14	0.43	-0.25	-0.15	-0.13	-0.06	-0.23	0.02	-0.18	0.08	-0.33	-0.07	-0.18	-0.29	-0.4	-0.2	-0.25	0.21	-0.33	-0.05
Fe	-0.13	-0.51	-0.67	-0.19	-0.01	0.3	0.14	1	0.23	-0.38	-0.09	-0.49	-0.21	-0.64	-0.63	-0.63	-0.71	-0.72	0.14	-0.62	-0.49	-0.66	-0.53	-0.71	-0.34	-0.47	-0.37
As	0.59	0.03	-0.06	-0.002	0.07	0.18	0.43	0.23	1	0.33	-0.07	0.21	0.47	0.13	-0.14	0.24	0.09	-0.13	-0.39	0.11	-0.27	-0.34	-0.12	-0.13	-0.19	-0.29	0.37
U	0.79	0.42	0.23	-0.04	-0.26	-0.35	-0.25	-0.38	0.33	1	0.09	0.67	0.57	0.65	0.2	0.77	0.41	0.4	-0.35	0.67	0.12	0.05	0.14	0.26	-0.08	-0.02	0.62
Th	0.23	0.26	-0.05	0.12	-0.01	-0.1	-0.15	-0.09	-0.07	0.09	1	0.21	0.18	0.28	-0.32	0.11	0.32	0.23	0.37	0.32	0.36	0.32	0.53	-0.29	0.5	0.31	0.27
Sr	0.61	0.66	0.35	0.21	-0.2	-0.38	-0.13	-0.49	0.21	0.67	0.21	1	0.53	0.81	0.11	0.86	0.74	0.63	-0.34	0.9	0.29	0.3	0.46	0.21	-0.14	0.27	0.69
Sb	0.71	0.39	0.36	0.1	-0.07	-0.22	-0.06	-0.21	0.47	0.57	0.18	0.53	1	0.52	0.01	0.56	0.4	0.38	-0.22	0.49	0.1	0.07	0.23	0.16	-0.04	0.08	0.35
V	0.63	0.77	0.51	0.22	-0.35	-0.57	-0.23	-0.64	0.13	0.65	0.28	0.81	0.52	1	0.16	0.9	0.85	0.82	-0.35	0.92	0.41	0.59	0.7	0.35	-0.01	0.5	0.65
Ca	0.01	0.2	0.31	0.13	0.15	-0.02	0.02	-0.63	-0.14	0.2	-0.32	0.11	0.01	0.16	1	0.28	0.15	0.09	-0.21	0.11	-0.32	0.08	-0.09	0.61	0.03	-0.23	0.09
P	0.72	0.7	0.46	0.21	-0.28	-0.49	-0.18	-0.63	0.24	0.77	0.11	0.86	0.56	0.9	0.28	1	0.72	0.74	-0.44	0.9	0.26	0.38	0.47	0.39	-0.12	0.29	0.7
La	0.39	0.69	0.51	0.38	0.02	-0.28	0.08	-0.71	0.09	0.41	0.32	0.74	0.4	0.85	0.15	0.72	1	0.73	-0.23	0.84	0.51	0.56	0.78	0.26	0.3	0.57	0.52
Cr	0.24	0.74	0.71	0.22	-0.3	-0.54	-0.33	-0.72	-0.13	0.4	0.23	0.63	0.38	0.82	0.09	0.74	0.73	1	-0.16	0.8	0.68	0.75	0.7	0.54	0.12	0.74	0.46
Mg	-0.35	-0.18	-0.3	0.19	0.41	0.37	-0.07	0.14	-0.39	-0.35	0.37	-0.34	-0.22	-0.35	-0.21	-0.44	-0.23	-0.16	1	-0.32	0.06	0.02	0.03	-0.36	0.3	-0.01	-0.27
Ba	0.59	0.8	0.46	0.29	-0.28	-0.48	-0.18	-0.62	0.11	0.67	0.32	0.9	0.49	0.92	0.11	0.9	0.84	0.8	-0.32	1	0.44	0.51	0.64	0.29	0.03	0.46	0.67
Al	-0.06	0.22	0.48	-0.07	-0.2	-0.36	-0.29	-0.49	-0.27	0.12	0.36	0.29	0.1	0.41	-0.32	0.26	0.51	0.68	0.06	0.44	1	0.69	0.61	0.27	0.42	0.82	0.18
Na	-0.03	0.45	0.57	-0.01	-0.36	-0.54	-0.4	-0.66	-0.34	0.05	0.32	0.3	0.07	0.59	0.08	0.38	0.56	0.75	0.02	0.51	0.69	1	0.81	0.47	0.23	0.83	0.23
K	0.22	0.56	0.42	0.2	-0.24	-0.46	-0.2	-0.53	-0.12	0.14	0.53	0.46	0.23	0.7	-0.09	0.47	0.78	0.7	0.03	0.64	0.61	0.81	1	0.15	0.26	0.8	0.34
Hg	-0.02	0.29	0.77	-0.11	-0.22	-0.38	-0.25	-0.71	-0.13	0.26	-0.29	0.21	0.16	0.35	0.61	0.39	0.26	0.54	-0.36	0.29	0.27	0.47	0.15	1	0.04	0.33	0.24
Sc	-0.23	0.01	0.14	0.17	0.45	0.31	0.21	-0.34	-0.19	-0.08	0.5	-0.14	-0.04	-0.01	0.03	-0.12	0.3	0.12	0.3	0.03	0.42	0.23	0.26	0.04	1	0.23	-0.06
Ga	-0.06	0.34	0.56	-0.06	-0.38	-0.55	-0.33	-0.47	-0.29	-0.02	0.31	0.27	0.08	0.5	-0.23	0.29	0.57	0.74	-0.01	0.46	0.82	0.83	0.8	0.33	0.23	1	0.13
log10RnC	0.63	0.55	0.21	0.14	-0.18	-0.22	-0.05	-0.37	0.37	0.62	0.27	0.69	0.35	0.65	0.09	0.7	0.52	0.46	-0.27	0.67	0.18	0.23	0.34	0.24	-0.06	0.13	1

Table 7.2.6b Pearson correlation table of Castleisland, Co. Kerry, deeper topsoil geochemistry (ilr transformed) and log10 soil-gas radon

Appendix A

Deeper_T	Log10SGl	Mo	Cu	Pb	Zn	Ni	Co	Mn	Fe	As	U	Th	Sr
Log10SGl	1	0.47	0.35	-0.05	-0.22	-0.15	-0.15	-0.29	-0.32	0.02	0.33	-0.18	0.69
Mo	0.47	1	0.45	0.25	-0.11	-0.22	-0.24	-0.47	0.18	0.55	0.48	0.17	0.42
Cu	0.35	0.45	1	0.26	0.05	-0.09	-0.22	-0.53	-0.09	0.09	0.65	0.12	0.46
Pb	-0.05	0.25	0.26	1	0.35	0.31	0.19	-0.77	0.21	0.17	0.22	0.68	0.21
Zn	-0.22	-0.11	0.05	0.35	1	0.89	0.77	-0.41	0.37	0.22	0.04	0.55	-0.27
Ni	-0.15	-0.22	-0.09	0.31	0.89	1	0.84	-0.38	0.21	0.05	-0.1	0.47	-0.15
Co	-0.15	-0.24	-0.22	0.19	0.77	0.84	1	-0.21	0.23	0.13	-0.02	0.45	-0.36
Mn	-0.29	-0.47	-0.53	-0.77	-0.41	-0.38	-0.21	1	-0.27	-0.36	-0.44	-0.64	-0.56
Fe	-0.32	0.18	-0.09	0.21	0.37	0.21	0.23	-0.27	1	0.8	-0.13	0.66	-0.32
As	0.02	0.55	0.09	0.17	0.22	0.05	0.13	-0.36	0.8	1	0.19	0.49	-0.07
U	0.33	0.48	0.65	0.22	0.04	-0.1	-0.02	-0.44	-0.13	0.19	1	0.19	0.31
Th	-0.18	0.17	0.12	0.68	0.55	0.47	0.45	-0.64	0.66	0.49	0.19	1	-0.11
Sr	0.69	0.42	0.46	0.21	-0.27	-0.15	-0.36	-0.56	-0.32	-0.07	0.31	-0.11	1
Sb	0.48	0.79	0.31	0.28	-0.1	-0.02	-0.19	-0.49	0.02	0.27	0.11	0.12	0.6
V	0.35	0.59	0.27	0.59	-0.13	-0.08	-0.22	-0.74	0.16	0.35	0.26	0.3	0.63
Ca	0.003	0.11	0.48	0.58	0.25	0.15	0.16	-0.51	0.03	0.07	0.57	0.51	0.07
P	0.4	0.47	0.69	0.12	-0.28	-0.36	-0.52	-0.4	-0.07	0.11	0.44	-0.13	0.68
La	0.28	0.48	0.29	0.78	-0.01	0.04	-0.08	-0.76	-0.001	0.19	0.29	0.48	0.55
Cr	-0.25	0.11	0.15	0.68	0.66	0.6	0.48	-0.66	0.71	0.47	0.01	0.9	-0.14
Mg	-0.34	-0.16	-0.11	0.49	0.87	0.88	0.75	-0.43	0.41	0.17	-0.1	0.65	-0.29
Ba	0.06	0.23	0.26	0.77	0.29	0.24	0.24	-0.83	0.26	0.24	0.33	0.66	0.36
Al	-0.35	-0.08	0.004	0.68	0.66	0.63	0.54	-0.6	0.62	0.32	-0.02	0.88	-0.18
Na	-0.23	0.13	0.27	0.69	0.53	0.38	0.37	-0.63	0.4	0.32	0.48	0.75	-0.1
K	-0.28	0.01	-0.01	0.72	0.4	0.38	0.21	-0.58	0.53	0.29	-0.1	0.74	-0.01
Hg	0.11	0.37	0.38	0.54	0.36	0.1	0.1	-0.59	0.44	0.46	0.44	0.63	0.1
Sc	-0.28	0.03	0.12	0.59	0.63	0.51	0.57	-0.57	0.59	0.46	0.32	0.91	-0.22
Ga	-0.39	-0.08	-0.02	0.71	0.49	0.44	0.37	-0.55	0.63	0.35	-0.09	0.83	-0.16

Deeper_T	Sb	V	Ca	P	La	Cr	Mg	Ba	Al	Na	K	Hg	Sc	Ga
Log10SGl	0.48	0.35	0	0.4	0.28	-0.25	-0.34	0.06	-0.35	-0.23	-0.28	0.11	-0.28	-0.39
Mo	0.79	0.59	0.11	0.47	0.48	0.11	-0.16	0.23	-0.08	0.13	0.01	0.37	0.03	-0.08
Cu	0.31	0.27	0.48	0.69	0.29	0.15	-0.11	0.26	0.004	0.27	-0.01	0.38	0.12	-0.02
Pb	0.28	0.59	0.58	0.12	0.78	0.68	0.49	0.77	0.68	0.69	0.72	0.54	0.59	0.71
Zn	-0.1	-0.13	0.25	-0.28	-0.01	0.66	0.87	0.29	0.66	0.53	0.4	0.36	0.63	0.49
Ni	-0.02	-0.08	0.15	-0.36	0.04	0.6	0.88	0.24	0.63	0.38	0.38	0.1	0.51	0.44
Co	-0.19	-0.22	0.16	-0.52	-0.08	0.48	0.75	0.24	0.54	0.37	0.21	0.1	0.57	0.37
Mn	-0.49	-0.74	-0.51	-0.4	-0.76	-0.66	-0.43	-0.83	-0.6	-0.63	-0.58	-0.59	-0.57	-0.55
Fe	0.02	0.16	0.03	-0.07	-0.001	0.71	0.41	0.26	0.62	0.4	0.53	0.44	0.59	0.63
As	0.27	0.35	0.07	0.11	0.19	0.47	0.17	0.24	0.32	0.32	0.29	0.46	0.46	0.35
U	0.11	0.26	0.57	0.44	0.29	0.01	-0.1	0.33	-0.02	0.48	-0.1	0.44	0.32	-0.09
Th	0.12	0.3	0.51	-0.13	0.48	0.9	0.65	0.66	0.88	0.75	0.74	0.63	0.91	0.83
Sr	0.6	0.63	0.07	0.68	0.55	-0.14	-0.29	0.36	-0.18	-0.1	-0.01	0.1	-0.22	-0.16
Sb	1	0.61	-0.08	0.4	0.55	0.14	-0.05	0.15	-0.06	-0.14	0.04	0.1	-0.15	-0.06
V	0.61	1	0.2	0.41	0.78	0.33	0.04	0.6	0.24	0.26	0.4	0.31	0.16	0.29
Ca	-0.08	0.2	1	0.18	0.43	0.37	0.24	0.56	0.46	0.67	0.29	0.61	0.61	0.43
P	0.4	0.41	0.18	1	0.25	-0.08	-0.4	0.16	-0.18	0.03	8.23E-05	0.28	-0.18	-0.13
La	0.55	0.78	0.43	0.25	1	0.37	0.11	0.73	0.34	0.41	0.5	0.42	0.35	0.4
Cr	0.14	0.33	0.37	-0.08	0.37	1	0.77	0.57	0.93	0.7	0.81	0.52	0.8	0.87
Mg	-0.05	0.04	0.24	-0.4	0.11	0.77	1	0.38	0.79	0.55	0.56	0.27	0.67	0.65
Ba	0.15	0.6	0.56	0.16	0.73	0.57	0.38	1	0.65	0.71	0.64	0.6	0.68	0.66
Al	-0.06	0.24	0.46	-0.18	0.34	0.93	0.79	0.65	1	0.78	0.86	0.51	0.84	0.95
Na	-0.14	0.26	0.67	0.03	0.41	0.7	0.55	0.71	0.78	1	0.73	0.62	0.83	0.76
K	0.04	0.4	0.29	0	0.5	0.81	0.56	0.64	0.86	0.73	1	0.47	0.62	0.91
Hg	0.1	0.31	0.61	0.28	0.42	0.52	0.27	0.6	0.51	0.62	0.47	1	0.62	0.47
Sc	-0.15	0.16	0.61	-0.18	0.35	0.8	0.67	0.68	0.84	0.83	0.62	0.62	1	0.75
Ga	-0.06	0.29	0.43	-0.13	0.4	0.87	0.65	0.66	0.95	0.76	0.91	0.47	0.75	1

Deeper_Topsoil	Log10SGR n	Mo	Cu	Pb	Zn
Log10SGRn	1	0.47	0.35	-0.05	-0.22
Mo	0.47	1	0.45	0.25	-0.11
Cu	0.35	0.45	1	0.26	0.05
Pb	-0.05	0.25	0.26	1	0.35
Zn	-0.22	-0.11	0.05	0.35	1
Ni	-0.15	-0.22	-0.09	0.31	0.89

Co	**-0.15**	**-0.24**	**-0.22**	**0.19**	**0.77**
Mn	**-0.29**	**-0.47**	**-0.53**	**-0.77**	**-0.41**
Fe	**-0.32**	**0.18**	**-0.09**	**0.21**	**0.37**
As	**0.02**	**0.55**	**0.09**	**0.17**	**0.22**
U	**0.33**	**0.48**	**0.65**	**0.22**	**0.04**
Th	**-0.18**	**0.17**	**0.12**	**0.68**	**0.55**
Sr	**0.69**	**0.42**	**0.46**	**0.21**	**-0.27**
Sb	**0.48**	**0.79**	**0.31**	**0.28**	**-0.1**
V	**0.35**	**0.59**	**0.27**	**0.59**	**-0.13**
Ca	**0.003**	**0.11**	**0.48**	**0.58**	**0.25**
P	**0.4**	**0.47**	**0.69**	**0.12**	**-0.28**
La	**0.28**	**0.48**	**0.29**	**0.78**	**-0.01**
Cr	**-0.25**	**0.11**	**0.15**	**0.68**	**0.66**

Mg	**-0.34**	**-0.16**	**-0.11**	**0.49**	**0.87**
Ba	**0.06**	**0.23**	**0.26**	**0.77**	**0.29**
Al	**-0.35**	**-0.08**	**0.004**	**0.68**	**0.66**
Na	**-0.23**	**0.13**	**0.27**	**0.69**	**0.53**
K	**-0.28**	**0.01**	**-0.01**	**0.72**	**0.4**
Hg	**0.11**	**0.37**	**0.38**	**0.54**	**0.36**
Sc	**-0.28**	**0.03**	**0.12**	**0.59**	**0.63**
Ga	**-0.39**	**-0.08**	**-0.02**	**0.71**	**0.49**

table

Variable	Mo	Cu	Pb	Zn	Ni	Co	Mn	Fe	As	U	Th	Sr	Sb	V	Ca	P	La	Cr	Mg	Ba	Al	Na	K	Hg	Sc	Ga	log10RnConc
Mo	1	0.48	0.09	0.26	0.03	0.02	0.2	0.26	0.61	0.55	0.19	0.58	0.66	0.69	-0.04	0.64	0.45	0.35	0	0.57	0.11	-0.06	0.28	0.03	0.03	0.03	0.46
Cu	0.48	1	0.2	0.28	-0.01	-0.12	-0.01	-0.18	0.09	0.61	-0.02	0.75	0.56	0.68	0.26	0.67	0.52	0.33	-0.15	0.64	-0.09	-0.11	0.09	0.21	-0.13	-0.2	0.61
Pb	0.09	0.2	1	0.19	0.09	0.1	0.1	0.01	0.18	0.22	-0.13	0.08	0.25	0.18	0.17	0.26	0.15	0.2	-0.07	0.23	0.08	0.02	-0.15	0.59	0.06	-0.02	0

Zn	0.26	0.28	0.19	1	0.85	0.79	0.72	0.71	0.61	-0.04	0.65	-0.06	0.03	0.01	0.14	0.17	0.45	0.71	0.77	0.41	0.66	0.45	0.54	-0.1	0.75	0.43	-0.14
Ni	0.03	-0.01	0.09	0.85	1	0.95	0.76	0.75	0.63	-0.16	0.63	-0.28	-0.05	-0.3	0.14	-0.1	0.25	0.57	0.86	0.13	0.68	0.39	0.39	-0.1	0.84	0.34	-0.32
Co	0.02	-0.12	0.1	0.79	0.95	1	0.81	0.82	0.67	-0.17	0.61	-0.35	-0.1	-0.36	0.07	-0.15	0.11	0.55	0.84	0.06	0.68	0.4	0.32	-0.1	0.83	0.36	-0.35
Mn	0.2	-0.01	0.1	0.72	0.76	0.81	1	0.63	0.62	-0.25	0.45	-0.15	0	-0.13	0.09	0.05	0.31	0.42	0.54	0.15	0.44	0.15	0.3	-0.13	0.61	0.24	-0.22
Fe	0.26	-0.18	0.01	0.71	0.75	0.82	0.63	1	0.79	-0.15	0.72	-0.35	-0.1	-0.22	-0.15	-0.1	0.03	0.64	0.83	0.16	0.78	0.53	0.48	-0.22	0.81	0.57	-0.35
As	0.61	0.09	0.18	0.61	0.63	0.67	0.62	0.79	1	0.23	0.57	0.07	0.33	0.17	0.02	0.29	0.37	0.59	0.53	0.4	0.61	0.26	0.4	0	0.66	0.34	0.01
U	0.55	0.61	0.22	-0.04	-0.16	-0.17	-0.25	-0.15	0.23	1	-0.17	0.7	0.58	0.71	0.3	0.72	0.28	0.24	-0.25	0.55	-0.08	-0.18	-0.19	0.43	-0.16	-0.31	0.62
Variable	Mo	Cu	Pb	Zn	Ni	Co	Mn	Fe	As	U	Th	Sr	Sb	V	Ca	P	La	Cr	Mg	Ba	Al	Na	K	Hg	Sc	Ga	log10RnConc
Th	0.19	-0.02	-0.13	0.65	0.63	0.61	0.45	0.72	0.57	-0.17	1	-0.18	0.04	-0.08	-0.19	-0.11	0.35	0.64	0.79	0.35	0.79	0.59	0.79	-0.42	0.85	0.61	-0.07
Sr	0.58	0.75	0.08	-0.06	-0.28	-0.35	-0.15	-0.35	0.07	0.7	-0.18	1	0.66	0.85	0.18	0.8	0.58	0.11	-0.45	0.65	-0.25	-0.24	0.01	0.18	-0.35	-0.33	0.78
Sb	0.66	0.56	0.25	0.03	-0.05	-0.1	0	-0.1	0.33	0.58	0.04	0.66	1	0.61	0.06	0.55	0.43	0.14	-0.22	0.41	-0.15	-0.31	0.02	0.07	-0.12	-0.34	0.47
V	0.69	0.68	0.18	0.01	-0.3	-0.36	-0.13	-0.22	0.17	0.71	-0.08	0.85	0.61	1	0.09	0.87	0.61	0.32	-0.38	0.75	-0.06	-0.06	0.13	0.21	-0.24	-0.09	0.66

Ca	-0.04	0.26	0.17	0.14	0.14	0.07	0.09	-0.15	0.02	0.3	-0.19	0.18	0.06	0.09	1	0.31	0.15	-0.12	-0.08	0.06	-0.21	-0.23	-0.33	0.54	0.02	-0.48	0.07
P	0.64	0.67	0.26	0.17	-0.1	-0.15	0.05	-0.1	0.29	0.72	-0.11	0.8	0.55	0.87	0.31	1	0.55	0.4	-0.28	0.72	-0.03	-0.09	0.04	0.34	-0.14	-0.16	0.6
La	0.45	0.52	0.15	0.45	0.25	0.11	0.31	0.03	0.37	0.28	0.35	0.58	0.43	0.61	0.15	0.55	1	0.41	0.05	0.73	0.32	0.09	0.55	-0.05	0.31	0.19	0.4
Cr	0.35	0.33	0.2	0.71	0.57	0.55	0.42	0.64	0.59	0.24	0.64	0.11	0.14	0.32	-0.12	0.4	0.41	1	0.61	0.67	0.82	0.59	0.57	-0.03	0.66	0.62	0.05
Mg	0	-0.15	-0.07	0.77	0.86	0.84	0.54	0.83	0.53	-0.25	0.79	-0.45	-0.22	-0.38	-0.08	-0.28	0.05	0.61	1	0.07	0.78	0.59	0.55	-0.29	0.85	0.56	-0.37
Ba	0.57	0.64	0.23	0.41	0.13	0.06	0.15	0.16	0.4	0.55	0.35	0.65	0.41	0.75	0.06	0.72	0.73	0.67	0.07	1	0.42	0.34	0.47	0.14	0.25	0.29	0.53
Al	0.11	-0.09	0.08	0.66	0.68	0.68	0.44	0.78	0.61	-0.08	0.79	-0.25	-0.15	-0.06	-0.21	-0.03	0.32	0.82	0.78	0.42	1	0.71	0.68	-0.17	0.86	0.82	-0.22
Na	-0.06	-0.11	0.02	0.45	0.39	0.4	0.15	0.53	0.26	-0.18	0.59	-0.24	-0.31	-0.06	-0.23	-0.09	0.09	0.59	0.59	0.34	0.71	1	0.62	-0.11	0.58	0.68	-0.18
Variable	**Mo**	**Cu**	**Pb**	**Zn**	**Ni**	**Co**	**Mn**	**Fe**	**As**	**U**	**Th**	**Sr**	**Sb**	**V**	**Ca**	**P**	**La**	**Cr**	**Mg**	**Ba**	**Al**	**Na**	**K**	**Hg**	**Sc**	**Ga**	**log10RnConc**
K	0.28	0.09	-0.15	0.54	0.39	0.32	0.3	0.48	0.4	-0.19	0.79	0.01	0.02	0.13	-0.33	0.04	0.55	0.57	0.55	0.47	0.68	0.62	1	-0.48	0.59	0.72	0
Hg	0.03	0.21	0.59	-0.1	-0.1	-0.1	-0.13	-0.22	0	0.43	-0.42	0.18	0.07	0.21	0.54	0.34	-0.05	-0.03	-0.29	0.14	-0.17	-0.11	-0.48	1	-0.15	-0.29	0.18
Sc	0.03	-0.13	0.06	0.75	0.84	0.83	0.61	0.81	0.66	-0.16	0.85	-0.35	-0.12	-0.24	0.02	-0.14	0.31	0.66	0.85	0.25	0.86	0.58	0.59	-0.15	1	0.58	-0.29
Ga	0.03	-0.2	-0.02	0.43	0.34	0.36	0.24	0.57	0.34	-0.31	0.61	-0.33	-0.34	-0.09	-0.48	-0.16	0.19	0.62	0.56	0.29	0.82	0.68	0.72	-0.29	0.58	1	-0.28

log10RnConc	**0.46**	**0.61**	**0**	**-0.14**	**-0.32**	**-0.35**	**-0.22**	**-0.35**	**0.01**	**0.62**	**-0.07**	**0.78**	**0.47**	**0.66**	**0.07**	**0.6**	**0.4**	**0.05**	**-0.37**	**0.53**	**-0.22**	**-0.18**	**0**	**0.18**	**-0.29**	**-0.28**	**1**

7.2.7 (Table) PCA Summary of Castleisland, Co. Kerry deeper topsoil geochemistry Clr-transformed.
File name: CLR_DeeperTopsoil_PCASummary_Castleisland_Co.Kerry

Variable	PC1	PC2	PC3	PC4	PC5	PC6	PC7	PC8	PC9	PC10	PC11	PC12	PC13	PC14	PC15	PC16	PC17	PC18	PC19	PC20	PC21	PC22	PC23	PC24	PC25	PC26
rotation.Sr	-0.04	0.42	-0.06	0.17	-0.44	0.02	-0.14	0.17	-0.3	0.11	0.06	-0.29	0.04	0.07	0.33	-0.29	-0.14	-0.08	-0.01	-0.07	-0.13	0.04	0.25	0.12	0.08	0.16
rotation.Ca	-0.11	0.25	0	-0.2	0.13	0.16	-0.35	0.51	0.45	-0.05	0.38	-0.1	0.08	0.14	-0.1	0.13	0.02	0.05	-0.03	-0.11	0.12	0.05	-0.03	0.02	0.05	-0.02
rotation.U	-0.04	0.06	-0.01	-0.1	0.09	0.08	0.05	-0.04	-0.04	0.14	-0.04	-0.37	-0.15	-0.3	-0.43	-0.44	-0.31	-0.06	-0.17	-0.14	0.2	0.04	-0.36	0.04	0	0.01
rotation.Hg	-0.31	0	0.12	0.04	0.12	0.01	-0.18	0.06	-0.13	-0.02	0.04	0.02	-0.01	-0.15	0.07	-0.26	0.07	0.26	0.61	0.28	-0.13	0.28	-0.19	-0.25	0.05	-0.07
rotation.V	-0.3	-0.04	0.11	0.26	0.33	-0.04	-0.1	0.03	-0.19	-0.1	0.1	-0.01	0.26	-0.02	-0.01	0.06	-0.25	-0.26	0.05	0.02	-0.17	-0.43	-0.04	0.31	0.19	-0.31
rotation.La	-0.37	-0.09	0.2	0.2	0.16	-0.23	-0.15	0.08	-0.2	0.06	0	0.26	0.02	0.23	0.01	-0.28	0.27	0.1	-0.44	-0.14	0.26	0.17	0	0.03	-0.15	0.08

rotation.Sb	**-0.56**	**0.05**	**-0.15**	**-0.47**	**-0.01**	**-0.37**	**0.28**	**-0.06**	**0.02**	**0**	**-0.09**	**-0.28**	**-0.02**	**0.11**	**0.17**	**0.19**	**-0.06**	**0.02**	**0.06**	**0.04**	**0.13**	**-0.12**	**0.02**	**0**	**-0.06**	**0.11**
rotation.Mo	**-0.32**	**-0.01**	**-0.03**	**0.18**	**-0.33**	**0.28**	**-0.05**	**-0.18**	**0.03**	**-0.06**	**0.17**	**0.24**	**-0.4**	**-0.06**	**0.1**	**0.17**	**-0.05**	**-0.05**	**0.17**	**-0.44**	**0.09**	**-0.18**	**-0.26**	**-0.01**	**-0.14**	**0.01**
rotation.Pb	**-0.25**	**0.18**	**0**	**0.15**	**-0.46**	**-0.04**	**0.12**	**-0.16**	**0.05**	**-0.06**	**0.2**	**0.17**	**0.36**	**-0.13**	**-0.49**	**0.14**	**-0.09**	**0.12**	**-0.13**	**0.26**	**0.05**	**0.08**	**0.11**	**-0.13**	**0.04**	**-0.06**
rotation.Na	**0.07**	**0.38**	**0.55**	**0.18**	**-0.06**	**-0.19**	**0.27**	**0.14**	**0.17**	**0.21**	**-0.29**	**-0.04**	**-0.07**	**0.27**	**-0.14**	**0.12**	**0.04**	**-0.06**	**0.14**	**-0.09**	**-0.14**	**-0.05**	**-0.22**	**-0.08**	**-0.08**	**-0.1**
rotation.Ba	**-0.08**	**-0.04**	**0.05**	**0.15**	**0**	**0.03**	**0.03**	**0**	**0.38**	**-0.21**	**-0.24**	**0.03**	**-0.04**	**-0.05**	**0.28**	**-0.11**	**-0.49**	**0.07**	**-0.08**	**0.07**	**0.13**	**0.27**	**0.22**	**0.06**	**-0.3**	**-0.36**
rotation.Th	**0.1**	**0.41**	**0**	**0.09**	**0.4**	**0.09**	**0.21**	**0.06**	**-0.31**	**-0.15**	**0.11**	**0.2**	**-0.12**	**-0.05**	**-0.06**	**0.2**	**-0.28**	**0.07**	**0.13**	**0.05**	**0.31**	**0.04**	**0.18**	**-0.02**	**-0.14**	**0.33**
rotation.K	**-0.03**	**0.35**	**-0.42**	**0.29**	**0.23**	**-0.1**	**-0.27**	**-0.37**	**0.28**	**0.15**	**-0.28**	**-0.03**	**0.06**	**0.04**	**0**	**0.01**	**0.07**	**0.32**	**-0.02**	**-0.07**	**-0.03**	**-0.13**	**-0.07**	**0.02**	**0.13**	**0.09**
rotation.Ga	**0.01**	**0.24**	**-0.08**	**0.13**	**0.06**	**0.19**	**0.27**	**-0.15**	**0.03**	**0.12**	**0.2**	**-0.13**	**0**	**-0.07**	**0.31**	**0.04**	**0.37**	**-0.25**	**-0.09**	**0.28**	**0.36**	**0.16**	**-0.22**	**0.08**	**0.11**	**-0.32**

rotation.Cu	**0.08**	**0.06**	**0.5**	**-0.25**	**0.1**	**0.03**	**-0.21**	**-0.58**	**0.03**	**0.15**	**0.32**	**-0.1**	**0.2**	**-0.02**	**0.19**	**0.06**	**-0.13**	**0.08**	**-0.06**	**-0.12**	**-0.05**	**0.09**	**0.05**	**0**	**-0.06**	**0.09**
rotation.P	**-0.12**	**0.36**	**-0.07**	**-0.48**	**0.04**	**0.21**	**-0.18**	**-0.07**	**-0.15**	**0.11**	**-0.27**	**0.4**	**-0.13**	**-0.04**	**-0.11**	**-0.06**	**0.05**	**-0.25**	**-0.11**	**0.04**	**-0.23**	**0.08**	**0.11**	**0.01**	**-0.03**	**-0.28**
rotation.Cr	**-0.01**	**0.15**	**-0.08**	**0.02**	**0.14**	**-0.12**	**0.26**	**-0.03**	**0.18**	**-0.24**	**0.13**	**-0.02**	**0.26**	**-0.3**	**-0.02**	**-0.29**	**0.32**	**-0.2**	**0.15**	**-0.43**	**-0.17**	**-0.02**	**0.22**	**-0.12**	**-0.26**	**-0.02**
rotation.Al	**-0.13**	**0**	**0.01**	**0.09**	**0.05**	**0.23**	**-0.04**	**-0.04**	**0.18**	**0**	**0.06**	**-0.09**	**-0.08**	**0.07**	**-0.02**	**-0.11**	**0.08**	**-0.18**	**-0.12**	**0.49**	**-0.27**	**-0.24**	**-0.08**	**0.04**	**-0.54**	**0.36**
rotation.Sc	**-0.22**	**-0.12**	**0.06**	**0.22**	**0.14**	**0.17**	**-0.1**	**0.04**	**-0.11**	**0.2**	**-0.14**	**-0.4**	**-0.18**	**-0.25**	**-0.15**	**0.44**	**0.16**	**-0.06**	**-0.1**	**-0.11**	**-0.14**	**0.27**	**0.35**	**-0.1**	**-0.05**	**-0.02**
rotation.Mg	**-0.07**	**0.1**	**0.12**	**-0.04**	**0.08**	**0.14**	**0.36**	**0.06**	**0.02**	**-0.14**	**0.18**	**0**	**-0.3**	**-0.12**	**0.1**	**-0.09**	**0.07**	**0.54**	**-0.32**	**0.03**	**-0.38**	**-0.13**	**0.06**	**0.1**	**0.22**	**-0.11**
rotation.As	**-0.13**	**-0.07**	**0.07**	**0.05**	**0.11**	**0.26**	**0.1**	**-0.08**	**0.14**	**-0.02**	**-0.04**	**-0.01**	**-0.03**	**0.25**	**0.06**	**-0.2**	**-0.12**	**-0.22**	**-0.09**	**0**	**0.09**	**-0.19**	**0.21**	**-0.67**	**0.38**	**0.09**
rotation.Ni	**-0.05**	**-0.06**	**0.17**	**-0.08**	**-0.06**	**0.26**	**0.05**	**0.22**	**0.06**	**0.42**	**-0.24**	**0.14**	**0.29**	**-0.39**	**0.16**	**-0.04**	**0.07**	**0.23**	**0.06**	**0**	**0.29**	**-0.38**	**0.14**	**0.05**	**-0.06**	**0.06**

rotation.Zn	**-0.08**	**-0.05**	**-0.16**	**-0.03**	**0.07**	**0.38**	**0.23**	**0.09**	**-0.15**	**-0.01**	**-0.15**	**0**	**0.5**	**0.17**	**0.14**	**0.14**	**-0.13**	**0.09**	**-0.14**	**-0.21**	**-0.24**	**0.28**	**-0.39**	**-0.07**	**-0.08**	**0.11**
rotation.Fe	**0.02**	**0.12**	**0.23**	**-0.08**	**-0.12**	**0.19**	**-0.21**	**-0.07**	**-0.14**	**-0.67**	**-0.36**	**-0.26**	**0.08**	**-0.01**	**-0.03**	**0.05**	**0.24**	**0.1**	**-0.05**	**0.02**	**0.21**	**-0.15**	**-0.07**	**0.01**	**0.02**	**0**
rotation.Co	**-0.16**	**-0.03**	**0.17**	**0.02**	**-0.01**	**0.01**	**0.08**	**-0.01**	**0.3**	**-0.11**	**-0.17**	**0.19**	**-0.01**	**-0.21**	**0.05**	**-0.02**	**0.01**	**-0.26**	**0.03**	**0.03**	**-0.05**	**0.29**	**-0.01**	**0.37**	**0.44**	**0.48**
rotation.Mn	**-0.08**	**-0.11**	**-0.02**	**-0.03**	**0.01**	**0.35**	**0.19**	**-0.17**	**0.03**	**0.08**	**0**	**-0.09**	**0.02**	**0.48**	**-0.29**	**-0.2**	**0.11**	**0.13**	**0.33**	**-0.08**	**0.1**	**0.06**	**0.31**	**0.41**	**-0.01**	**-0.07**
Standard deviation	**0.66**	**0.64**	**0.38**	**0.3**	**0.29**	**0.25**	**0.2**	**0.16**	**0.13**	**0.12**	**0.11**	**0.1**	**0.09**	**0.08**	**0.06**	**0.06**	**0.05**	**0.04**	**0.04**	**0.03**	**0.03**	**0.03**	**0.02**	**0.02**	**0.01**	**0.01**
Proportion of Variance	**0.32**	**0.3**	**0.1**	**0.07**	**0.06**	**0.04**	**0.03**	**0.02**	**0.01**	**0.01**	**0.01**	**0.01**	**0.01**	**0**	**0**	**0**	**0**	**0**	**0**	**0**	**0**	**0**	**0**	**0**	**0**	**0**
Cumulative Proportion	**0.32**	**0.62**	**0.72**	**0.79**	**0.85**	**0.89**	**0.92**	**0.94**	**0.95**	**0.96**	**0.97**	**0.98**	**0.98**	**0.99**	**0.99**	**0.99**	**0.99**	**1**	**1**	**1**	**1**	**1**	**1**	**1**	**1**	**1**

7.2.8 (Figures) PC3 to PC5 score maps of Castleisland, Co. Kerry topsoil geochemistry Clr-transformed.

File name: PC3 to PC5 Score maps of shallow topsoil Castleisland, Co, Kerry, Ireland

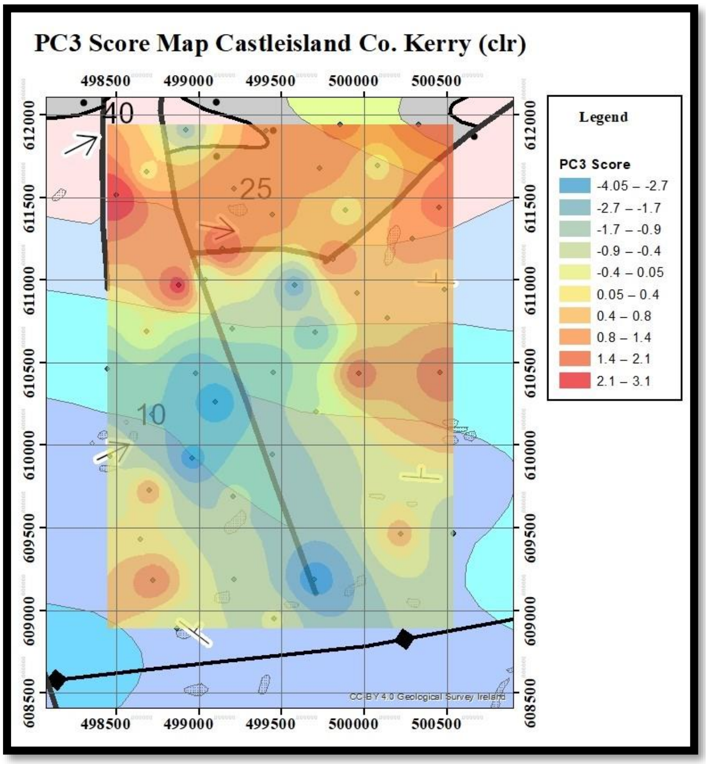

Figure 7.2.8.1 PC3 Score map of Castleisland, Co. Kerry topsoil geochemistry clr and centred.

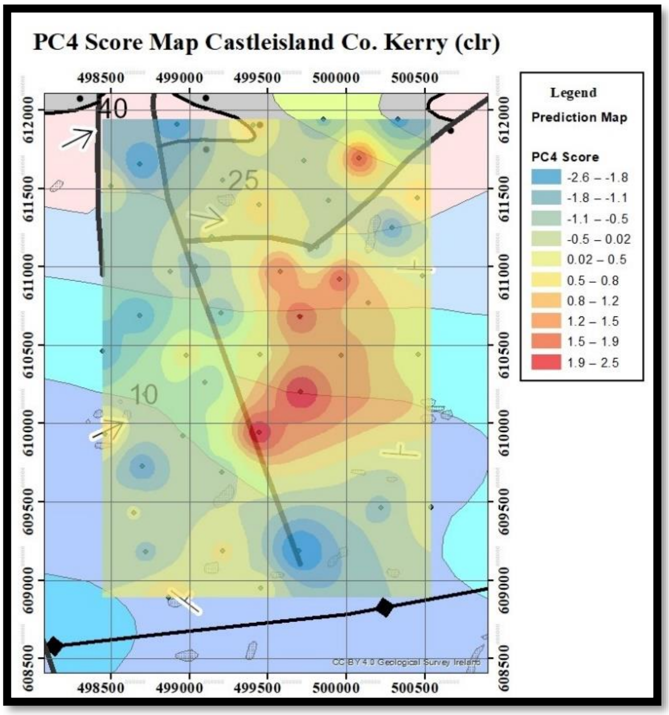

Figure 7.2.8.2 PC4 Score map of Castleisland, Co. Kerry topsoil geochemistry clr and centred.

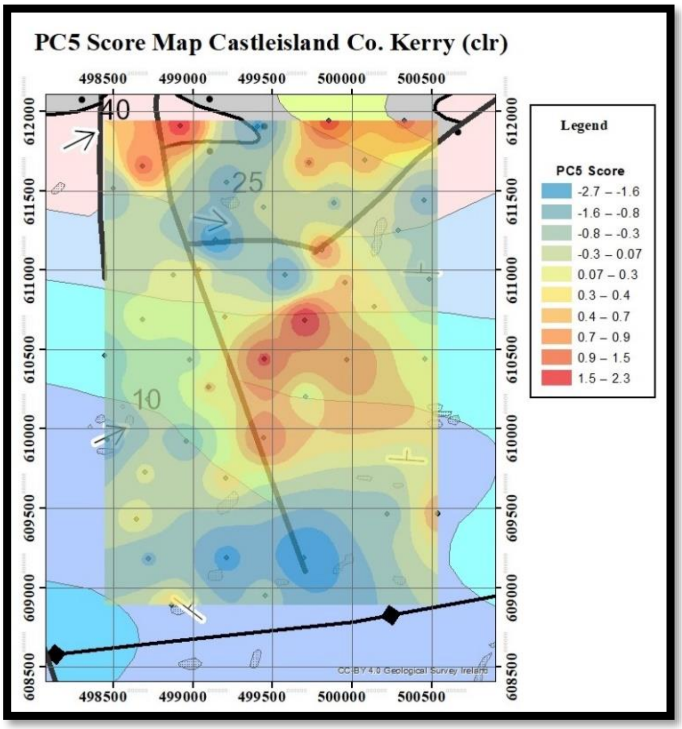

Figure.2.8.3 PC5 Score map of Castleisland, Co. Kerry topsoil geochemistry clr and centred.

7.2.9 (Figure) (A) PC1 vs PC2 biplot and (B) Cluster analysis of deeper topsoil geochemistry Clr-transformed Castleisland, Co. Kerry.

File name: PCA biplot and cluster analysis of deeper topsoil geochemistry, Castleisland, Co. Kerry.

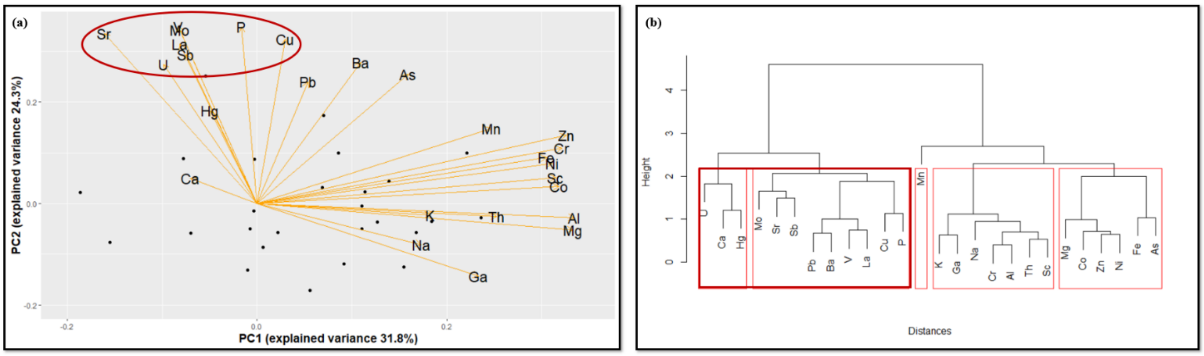

Figure-2 7.2.9 (a) PC1 vs PC2 biplot and (b) cluster analysis of deeper topsoil geochemistry from Castleisland Co. Kerry.

7.2.10 (Table) ANOVA of shallow topsoil geochemistry from TELLUS Midlands ilr-transformed.

File name:

ANOVA_TELLUS_Midlands_ShallowTopsoilElementsvsGeogenicRadonClass

Table 7.2.10 ANOVA of shallow topsoil geochemistry from TELLUS Midlands (ilr-transformed) versus Radon Potnential boinary class (eta squared value).

Element	Eta squared	p value	Significance code	Element	Eta squared	p value	Significance code
S	0.29	<2e-16	***	**Pb**	0.04	<2e-16	***
Na	0.24	<2e-16	***	**Ca**	0.04	<2e-16	***
Sr	0.22	<2e-16	***	**Sn**	0.03	<2e-16	***
Cr	0.18	<2e-16	***	**Cs**	0.03	<2e-16	***
Ni	0.18	<2e-16	***	**K**	0.03	<2e-16	***
Co	0.18	<2e-16	***	**Sb**	0.02	<2e-16	***
Al	0.15	<2e-16	***	**Pt**	0.02	<2e-16	***
V	0.15	<2e-16	***	**Nb**	0.02	<2e-16	***
Sc	0.15	<2e-16	***	**Bi**	0.02	<2e-16	***
Zr	0.15	<2e-16	***	**In**	0.02	<2e-16	***
Se	0.14	<2e-16	***	**Re**	0.01	<2e-16	***
Y	0.14	<2e-16	***	**P**	0.01	2.60E-12	***
Fe	0.14	<2e-16	***	**Cd**	0.01	3.57E-06	***
La	0.13	<2e-16	***	**Ti**	0.004	2.03E-05	***
Hf	0.13	<2e-16	***	**Ba**	0.003	0.00053	***
Rb	0.12	<2e-16	***	**Cu**	0.003	0.00061	***
Li	0.12	<2e-16	***	**Mo**	0.002	0.002	**
Ce	0.12	<2e-16	***	**Zn**	0.002	0.00323	**
Mg	0.11	<2e-16	***	**As**	0.002	0.00468	**

Tl	0.11	<2e-16	***	**Ag**	0.001	0.0132	*
Be	0.1	<2e-16	***	**U**	0.001	0.0625	
Hg	0.1	<2e-16	***	**Au**	0.001	0.1	
Th	0.09	<2e-16	***	**Pd**	0.0004	0.209	
Ga	0.08	<2e-16	***	**W**	0.0003	0.271	
Ta	0.08	<2e-16	***	**Te**	0.0002	0.381	
Mn	0.07	<2e-16	***	**log10SGRn**	1	<2e-16	***
Ge	0.04	<2e-16	***				

7.2.11 (Figures) Tukey-boxplots comparing shallow topsoil geochemistry with (a) geogenic radon potential as derived from Elío et al 2020 *, and (b) main lithologies Geological Survey Ireland bedrock geology map 1:500 k.

File name: TukeyBoxplots_ShallowTopsoil_vs_(a) Bedrock_and_(b) GeogenicRadonClass_TELLUSMidlands

*Elío, J., Crowley, Q., Scanlon, R., Hodgson, J., Long, S., Cooper, M. and Gallagher, V., 2020. Application of airborne radiometric surveys for large-scale geogenic radon potential classification. *Journal of the European Radon Association*, *1*.

Prepared using ‘R studio’ version 4.0.2, ggplot2

Appendix A

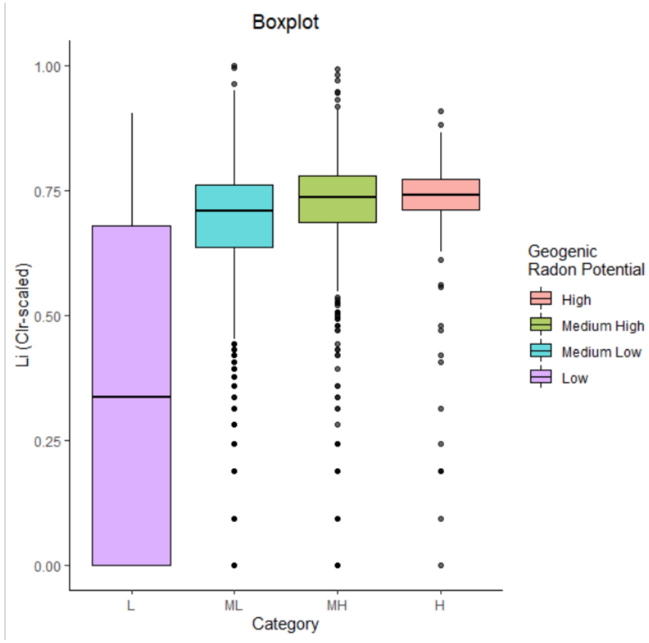
Boxplot
Li (Clr-scaled)
1.00
0.75
0.50
0.25
0.00
L
ML
MH
H
Category
Geogenic Radon Potential
High
Medium High
Medium Low
Low

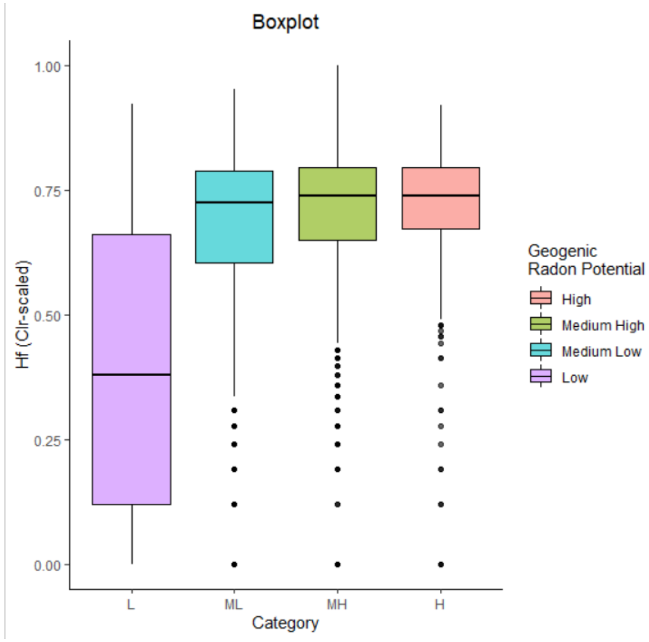
Boxplot
Hf (Clr-scaled)
1.00
0.75
0.50
0.25
0.00
L
ML
MH
H
Category
Geogenic Radon Potential
High
Medium High
Medium Low
Low

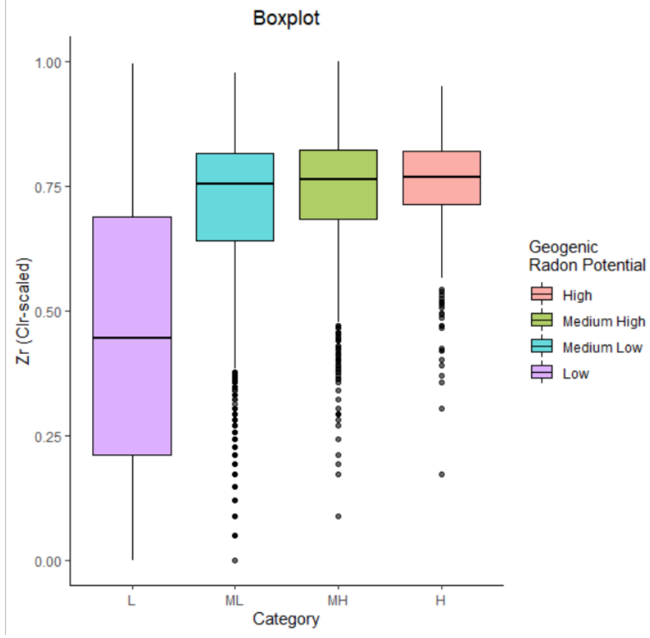
Boxplot
Zr (Clr-scaled)
1.00
0.75
0.50
0.25
0.00
L
ML
MH
H
Category
Geogenic Radon Potential
High
Medium High
Medium Low
Low

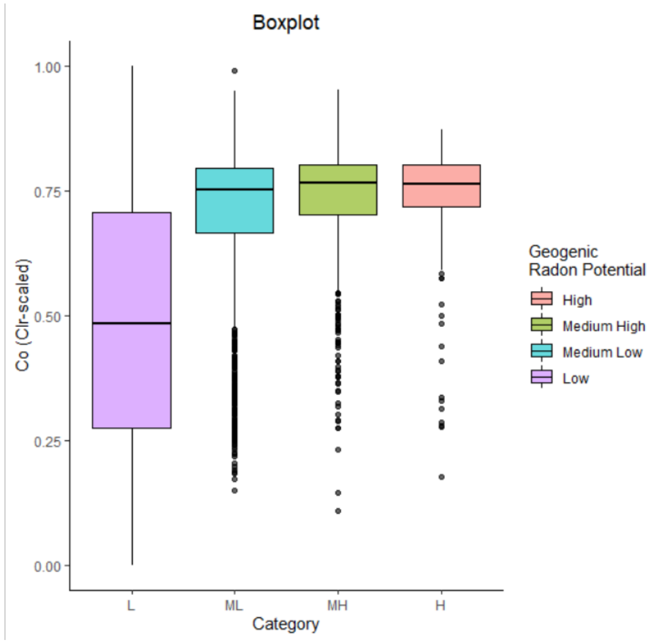
Boxplot
Co (Clr-scaled)
1.00
0.75
0.50
0.25
0.00
L
ML
MH
H
Category
Geogenic Radon Potential
High
Medium High
Medium Low
Low

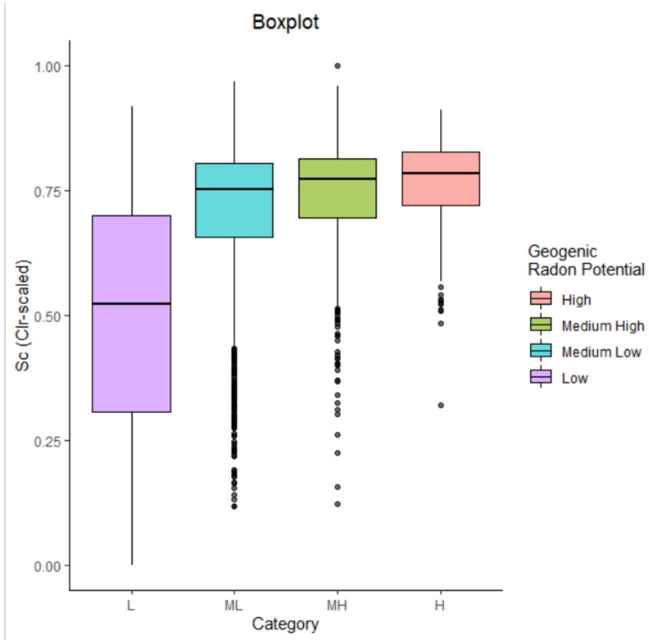
Boxplot
Sc (Clr-scaled)
1.00
0.75
0.50
0.25
0.00
L
ML
MH
H
Category
Geogenic Radon Potential
High
Medium High
Medium Low
Low

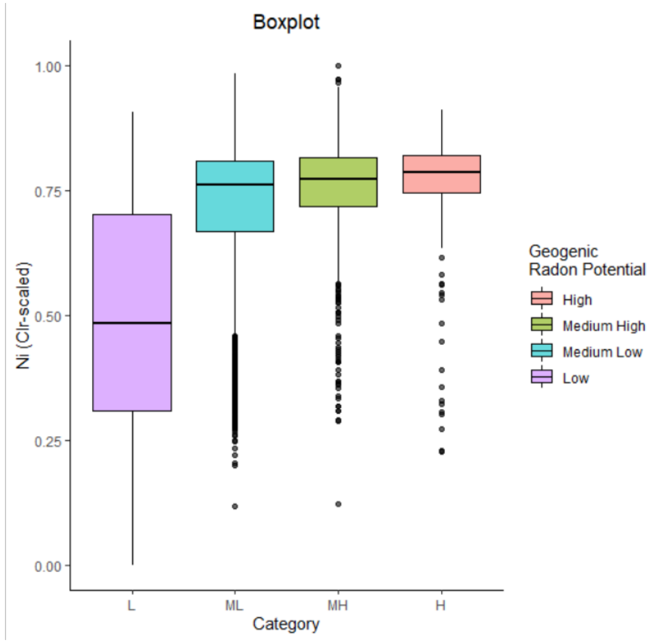
Boxplot
Ni (Clr-scaled)
1.00
0.75
0.50
0.25
0.00
L
ML
MH
H
Category
Geogenic Radon Potential
High
Medium High
Medium Low
Low

Appendix A

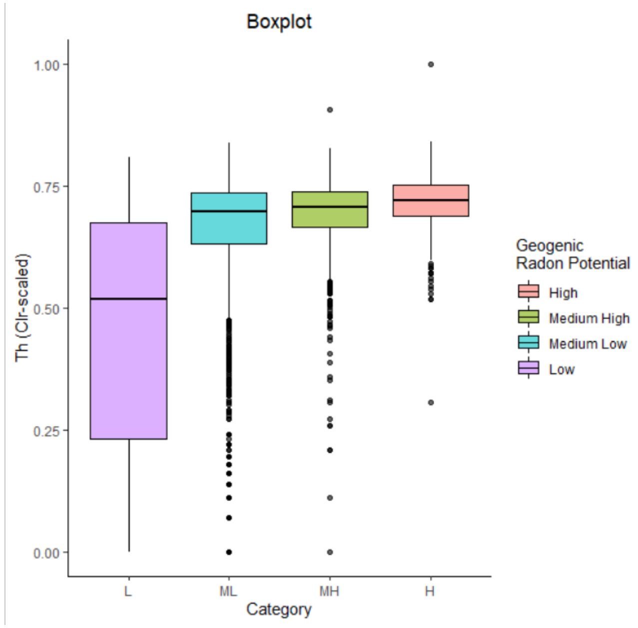

Boxplot
1.00
0.75
0.50
0.25
0.00
Th (Clr-scaled)
L
ML
MH
H
Category
Geogenic
Radon Potential
High
Medium High
Medium Low
Low

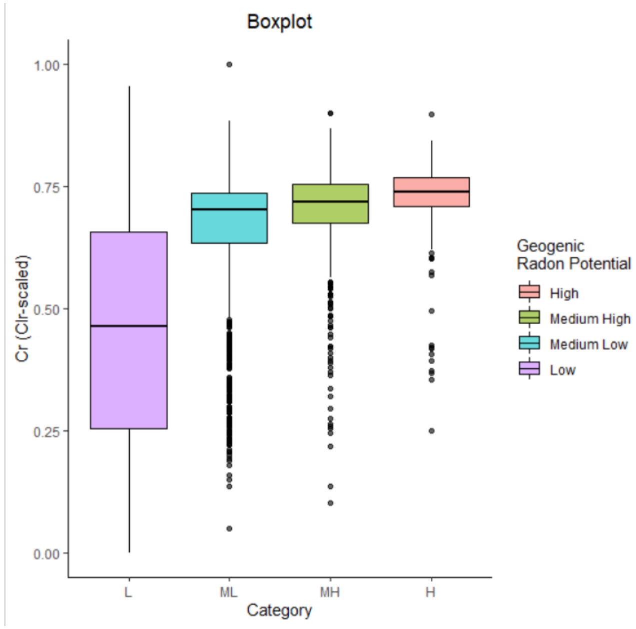

Boxplot
1.00
0.75
0.50
0.25
0.00
Cr (Clr-scaled)
L
ML
MH
H
Category
Geogenic
Radon Potential
High
Medium High
Medium Low
Low

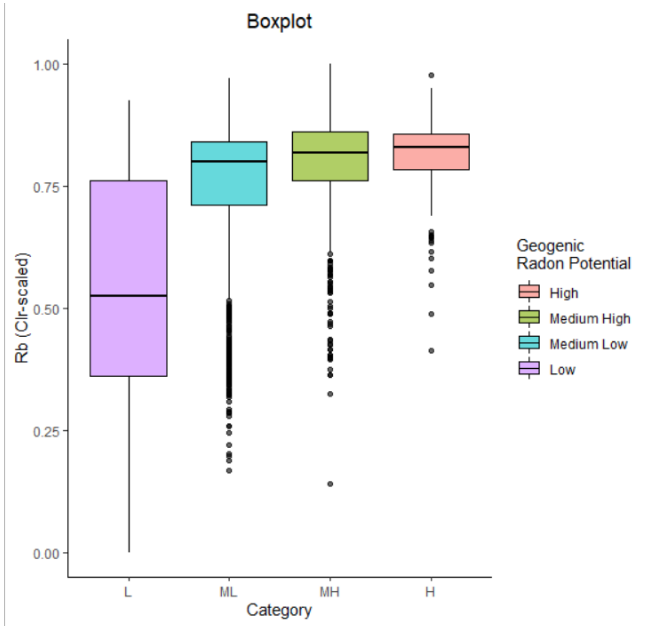

Boxplot
1.00
0.75
0.50
0.25
0.00
Rb (Clr-scaled)
L
ML
MH
H
Category
Geogenic
Radon Potential
High
Medium High
Medium Low
Low

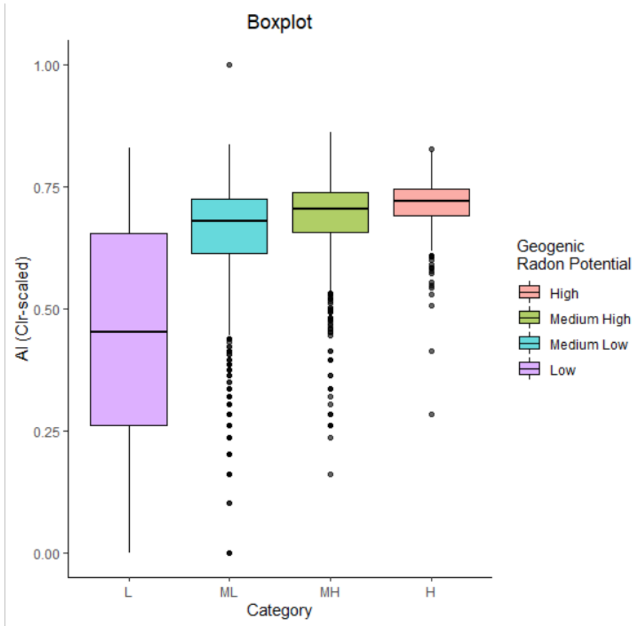

Boxplot
1.00
0.75
0.50
0.25
0.00
Al (Clr-scaled)
L
ML
MH
H
Category
Geogenic
Radon Potential
High
Medium High
Medium Low
Low

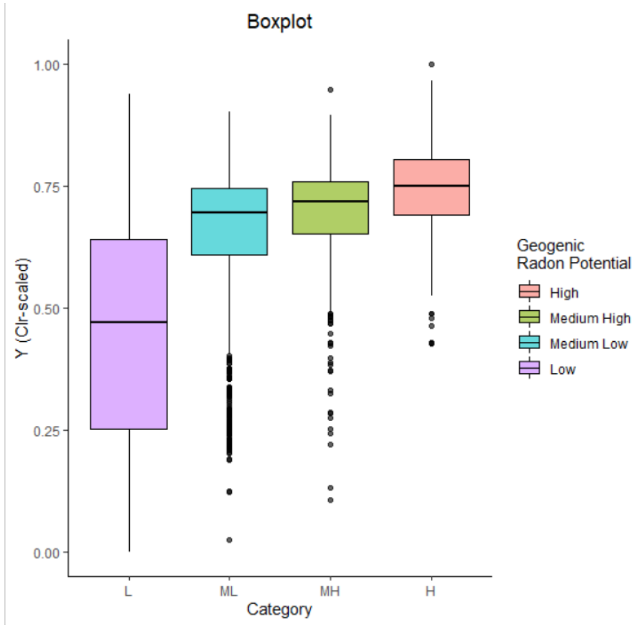

Boxplot
1.00
0.75
0.50
0.25
0.00
Y (Clr-scaled)
L
ML
MH
H
Category
Geogenic
Radon Potential
High
Medium High
Medium Low
Low

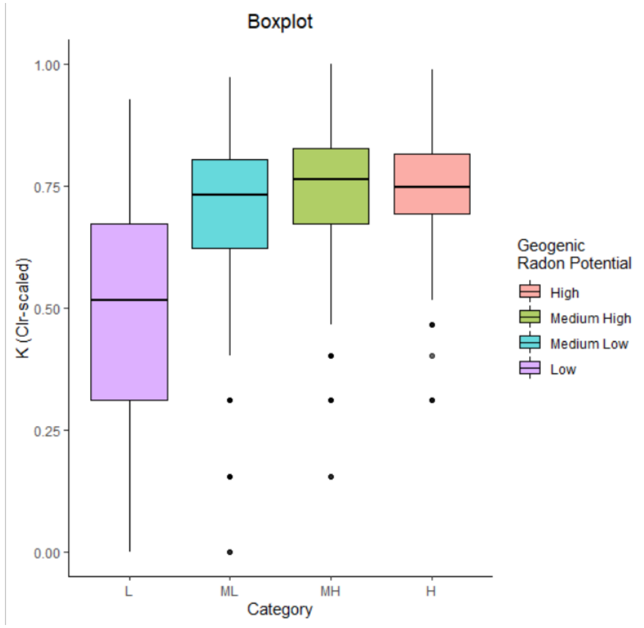

Boxplot
1.00
0.75
0.50
0.25
0.00
K (Clr-scaled)
L
ML
MH
H
Category
Geogenic
Radon Potential
High
Medium High
Medium Low
Low

Appendix A

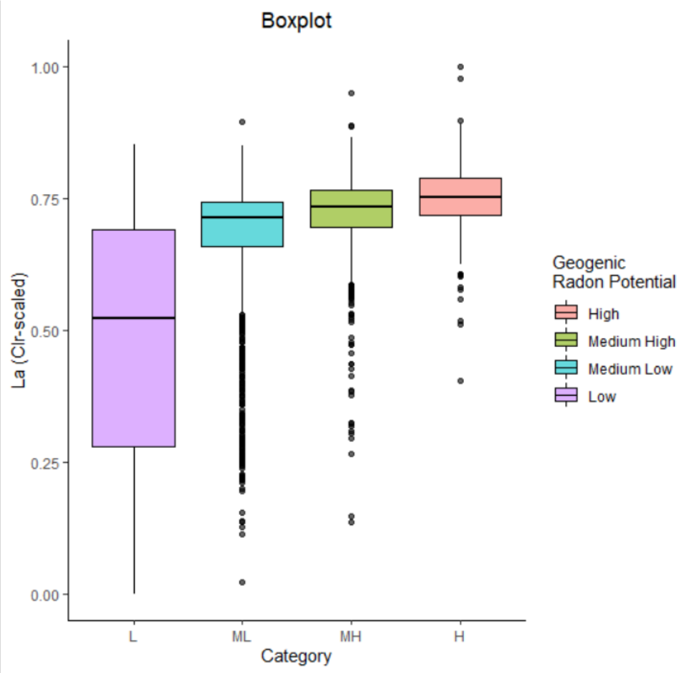

Boxplot
La (Clr-scaled)
1.00
0.75
0.50
0.25
0.00
L
ML
MH
H
Category
Geogenic Radon Potential
High
Medium High
Medium Low
Low

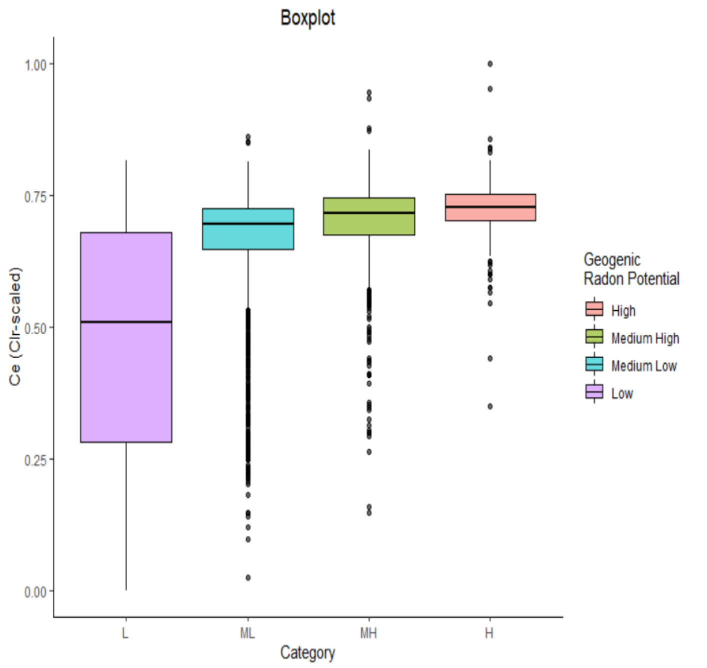

Boxplot
Ce (Clr-scaled)
1.00
0.75
0.50
0.25
0.00
L
ML
MH
H
Category
Geogenic Radon Potential
High
Medium High
Medium Low
Low

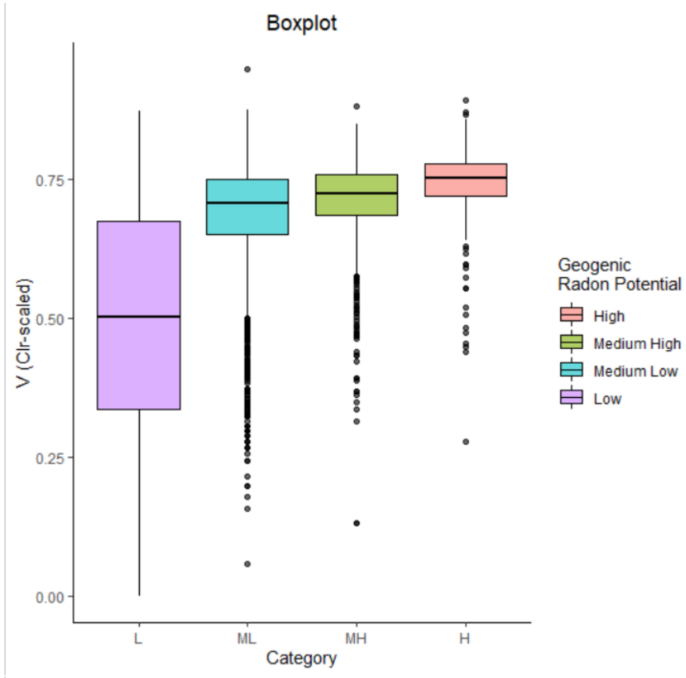

Boxplot
V (Clr-scaled)
0.75
0.50
0.25
0.00
L
ML
MH
H
Category
Geogenic Radon Potential
High
Medium High
Medium Low
Low

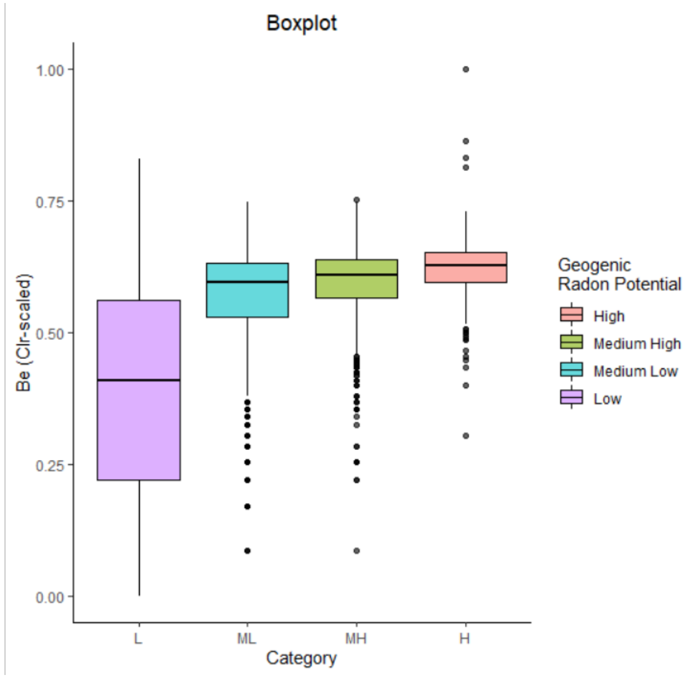

Boxplot
Be (Clr-scaled)
1.00
0.75
0.50
0.25
0.00
L
ML
MH
H
Category
Geogenic Radon Potential
High
Medium High
Medium Low
Low

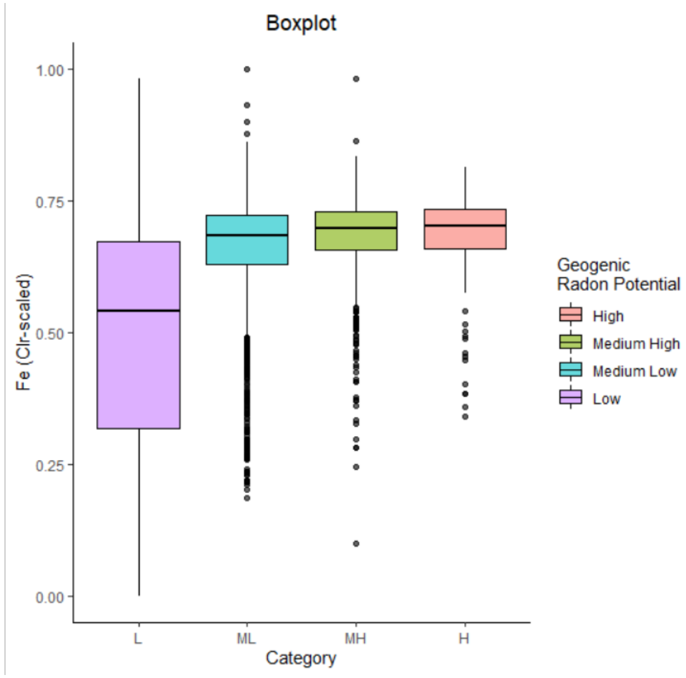

Boxplot
Fe (Clr-scaled)
1.00
0.75
0.50
0.25
0.00
L
ML
MH
H
Category
Geogenic Radon Potential
High
Medium High
Medium Low
Low

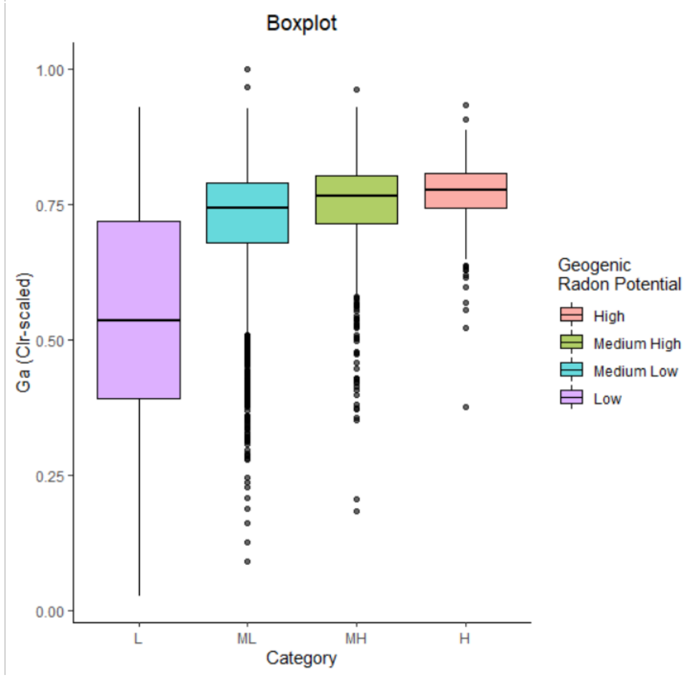

Boxplot
Ga (Clr-scaled)
1.00
0.75
0.50
0.25
0.00
L
ML
MH
H
Category
Geogenic Radon Potential
High
Medium High
Medium Low
Low

Appendix A

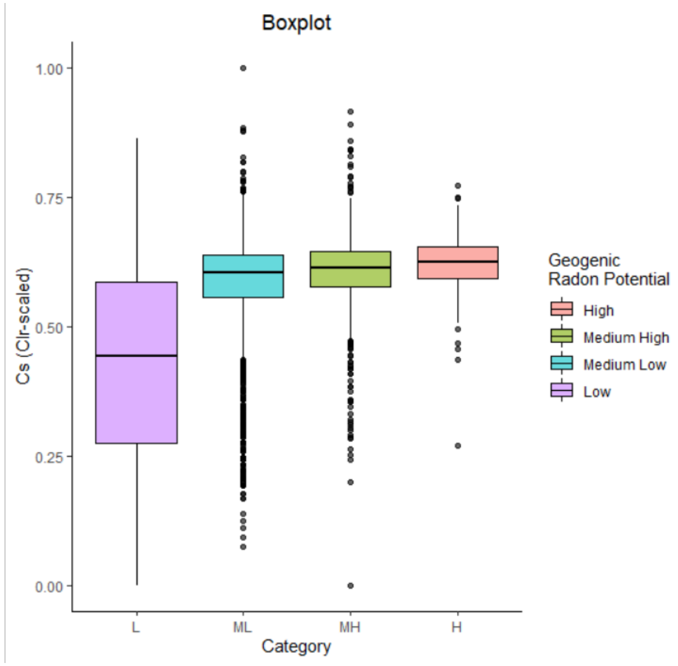
Boxplot
Cs (Clr-scaled)
1.00
0.75
0.50
0.25
0.00
L
ML
MH
H
Category
Geogenic Radon Potential
High
Medium High
Medium Low
Low

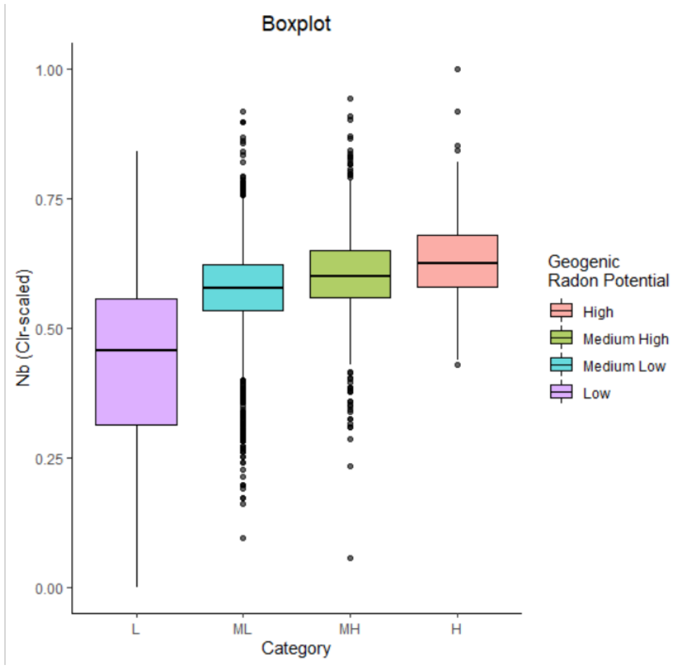
Boxplot
Nb (Clr-scaled)
1.00
0.75
0.50
0.25
0.00
L
ML
MH
H
Category
Geogenic Radon Potential
High
Medium High
Medium Low
Low

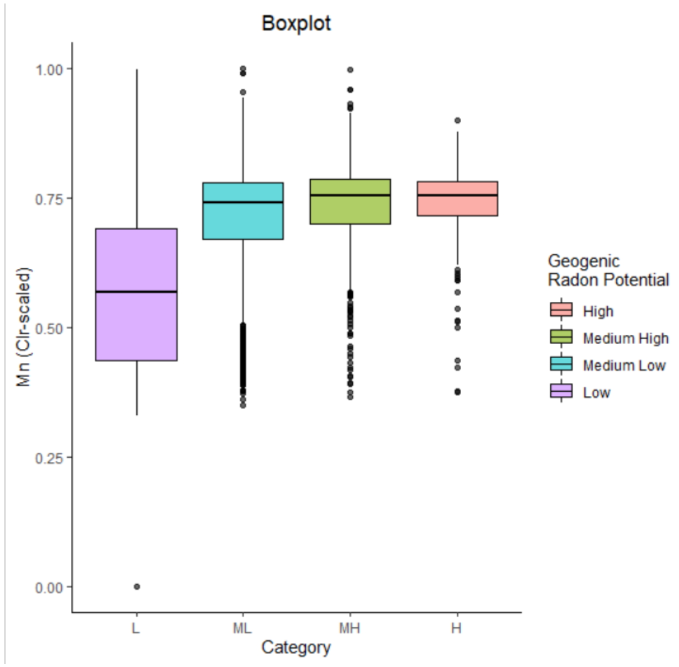
Boxplot
Mn (Clr-scaled)
1.00
0.75
0.50
0.25
0.00
L
ML
MH
H
Category
Geogenic Radon Potential
High
Medium High
Medium Low
Low

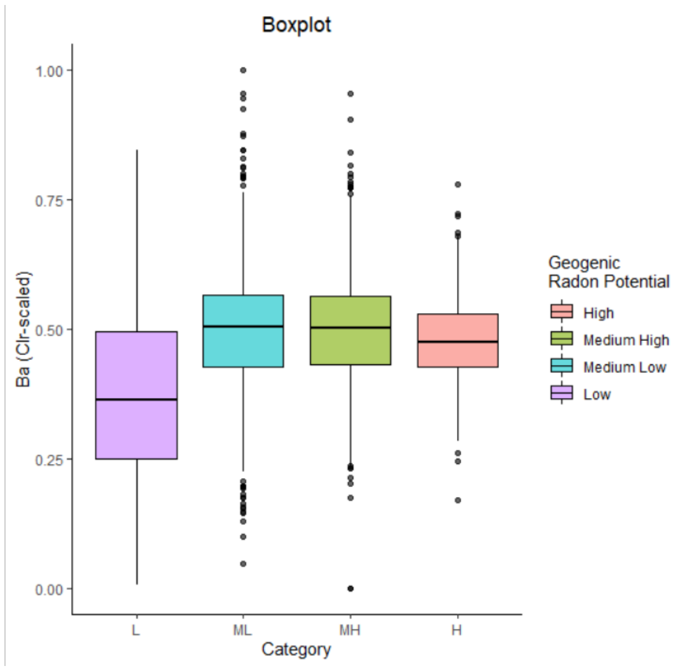
Boxplot
Ba (Clr-scaled)
1.00
0.75
0.50
0.25
0.00
L
ML
MH
H
Category
Geogenic Radon Potential
High
Medium High
Medium Low
Low

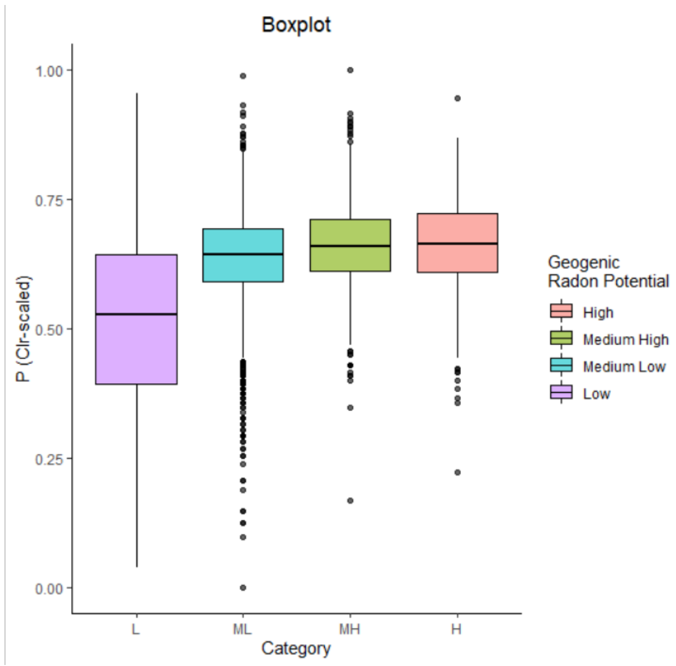
Boxplot
P (Clr-scaled)
1.00
0.75
0.50
0.25
0.00
L
ML
MH
H
Category
Geogenic Radon Potential
High
Medium High
Medium Low
Low

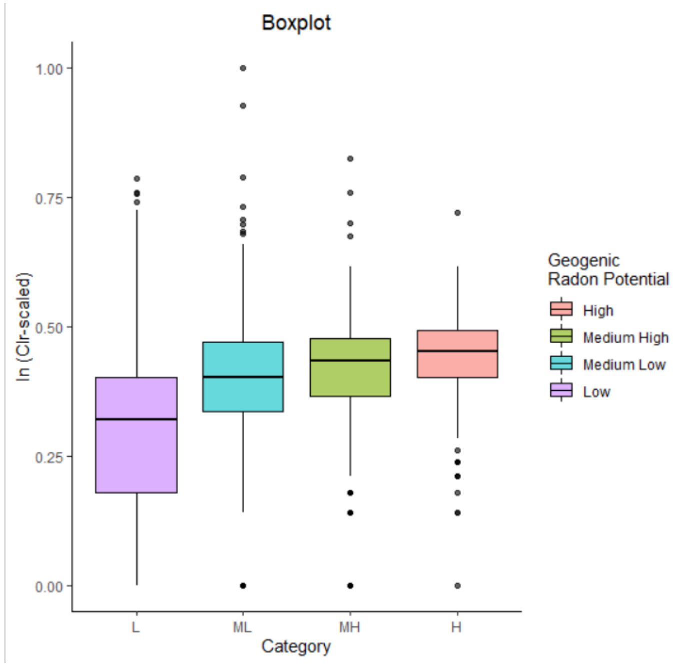
Boxplot
In (Clr-scaled)
1.00
0.75
0.50
0.25
0.00
L
ML
MH
H
Category
Geogenic Radon Potential
High
Medium High
Medium Low
Low

Appendix A

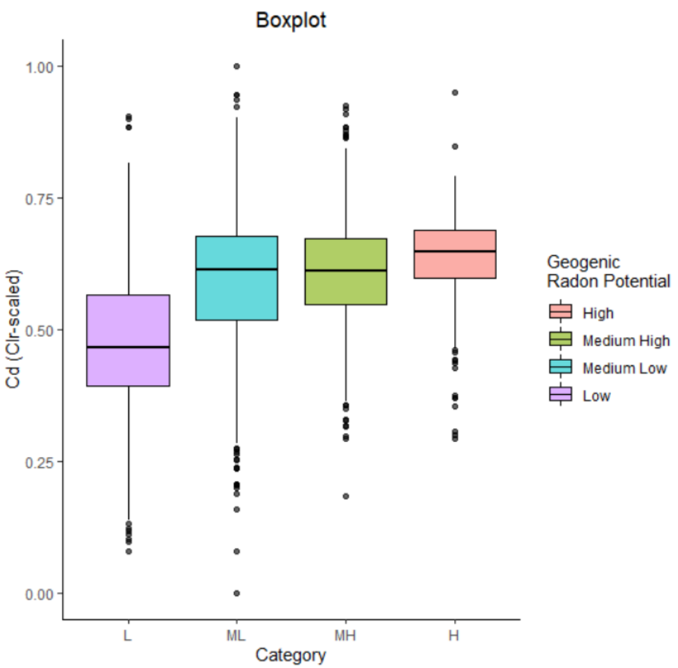
Boxplot
Cd (Clr-scaled)
1.00
0.75
0.50
0.25
0.00
L
ML
MH
H
Category
Geogenic Radon Potential
High
Medium High
Medium Low
Low

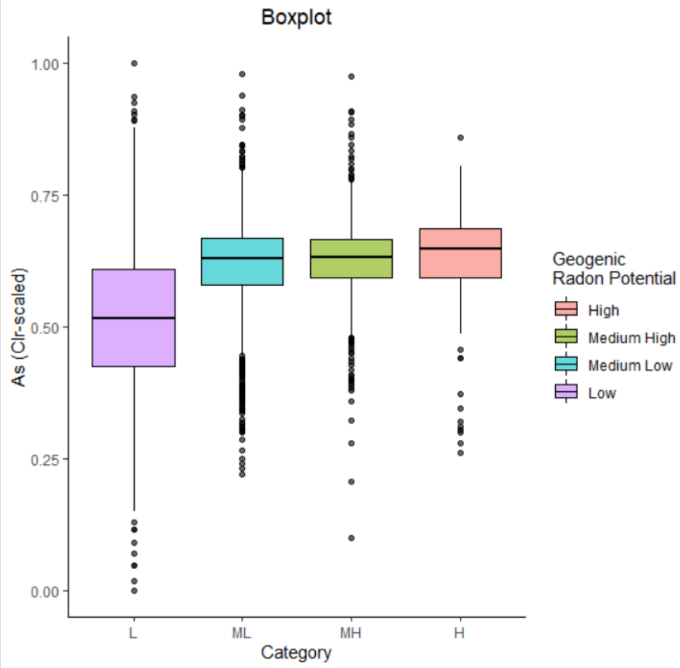
Boxplot
As (Clr-scaled)
1.00
0.75
0.50
0.25
0.00
L
ML
MH
H
Category
Geogenic Radon Potential
High
Medium High
Medium Low
Low

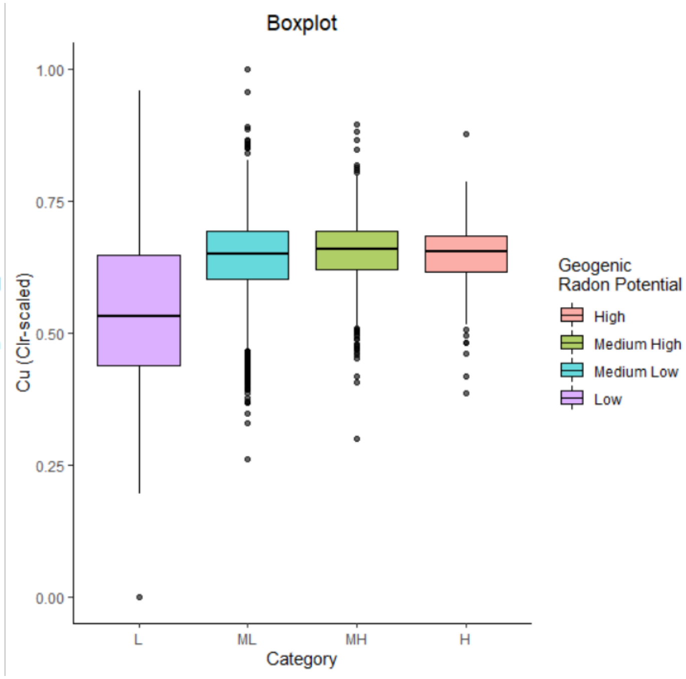
Boxplot
Cu (Clr-scaled)
1.00
0.75
0.50
0.25
0.00
L
ML
MH
H
Category
Geogenic Radon Potential
High
Medium High
Medium Low
Low

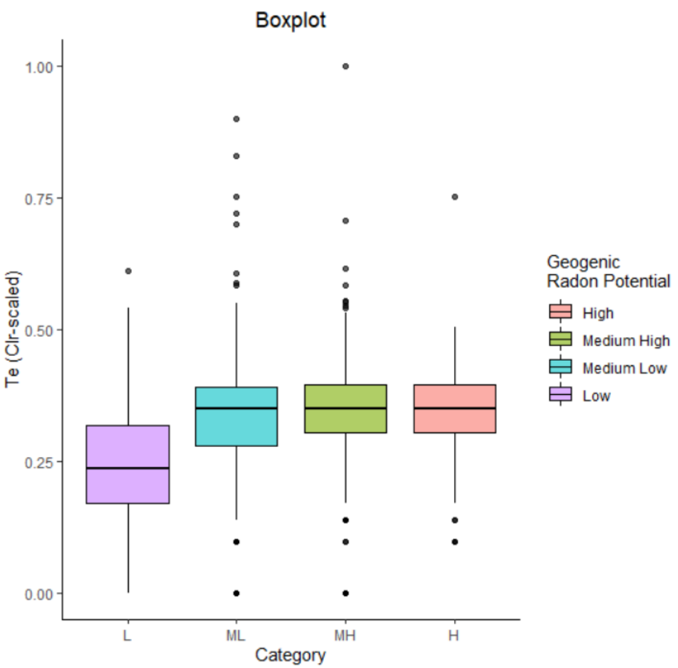
Boxplot
Te (Clr-scaled)
1.00
0.75
0.50
0.25
0.00
L
ML
MH
H
Category
Geogenic Radon Potential
High
Medium High
Medium Low
Low

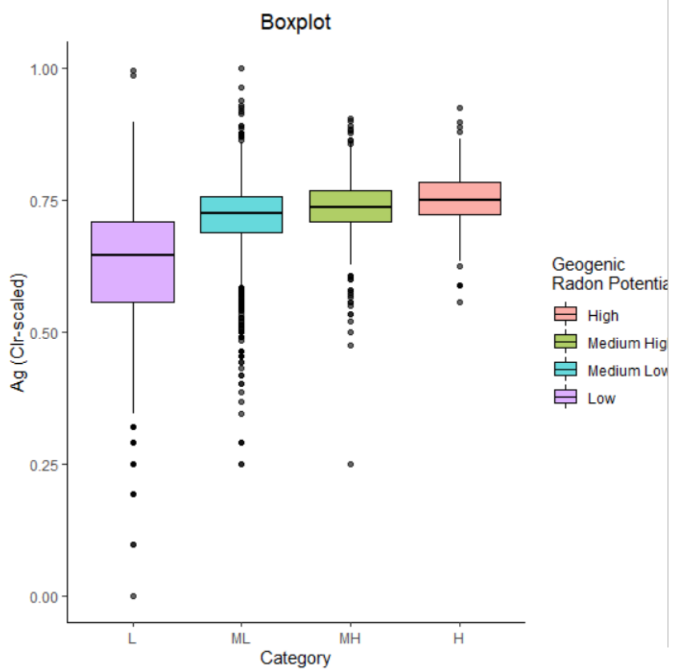
Boxplot
Ag (Clr-scaled)
1.00
0.75
0.50
0.25
0.00
L
ML
MH
H
Category
High
Low

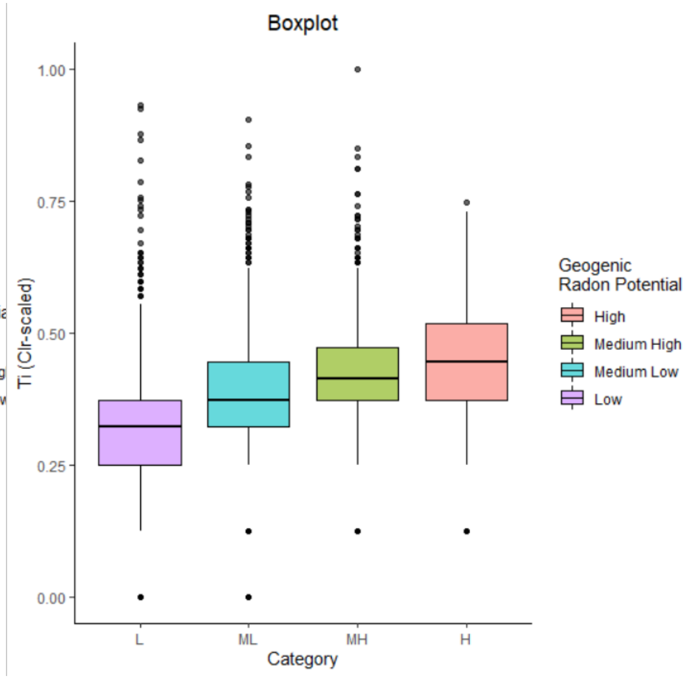
Boxplot
Ti (Clr-scaled)
1.00
0.75
0.50
0.25
0.00
L
ML
MH
H
Category
Geogenic Radon Potential
High
Medium High
Medium Low
Low

Appendix A

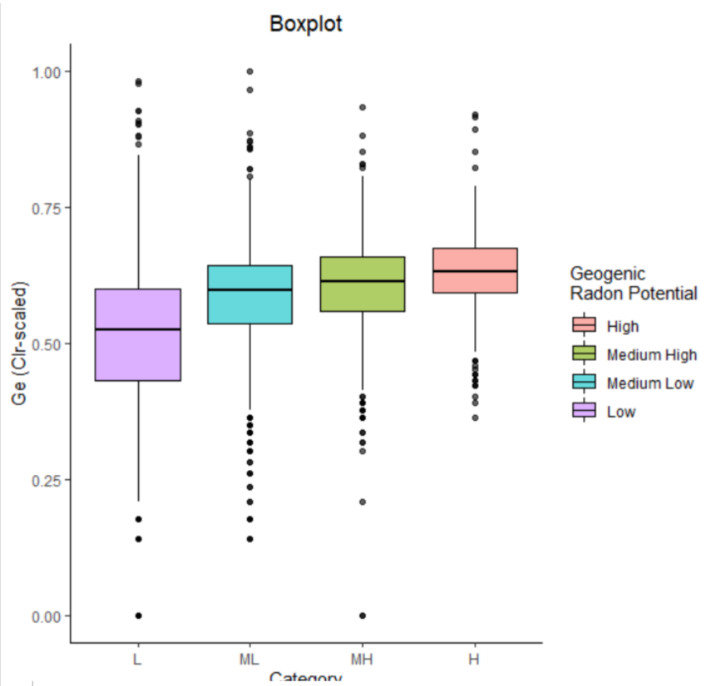
Boxplot
Ge (Clr-scaled)
1.00
0.75
0.50
0.25
0.00
L
ML
MH
H
Category
Geogenic Radon Potential
High
Medium High
Medium Low
Low

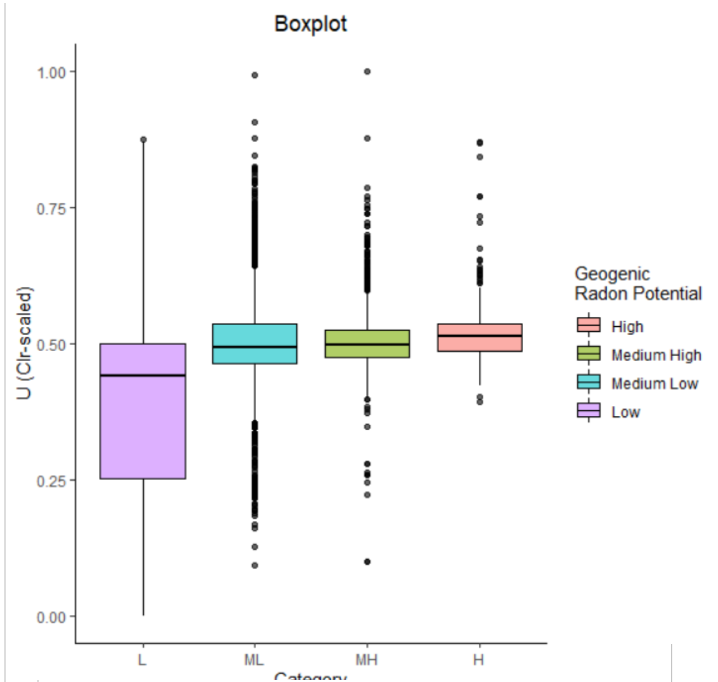
Boxplot
U (Clr-scaled)
1.00
0.75
0.50
0.25
0.00
L
ML
MH
H
Category
Geogenic Radon Potential
High
Medium High
Medium Low
Low

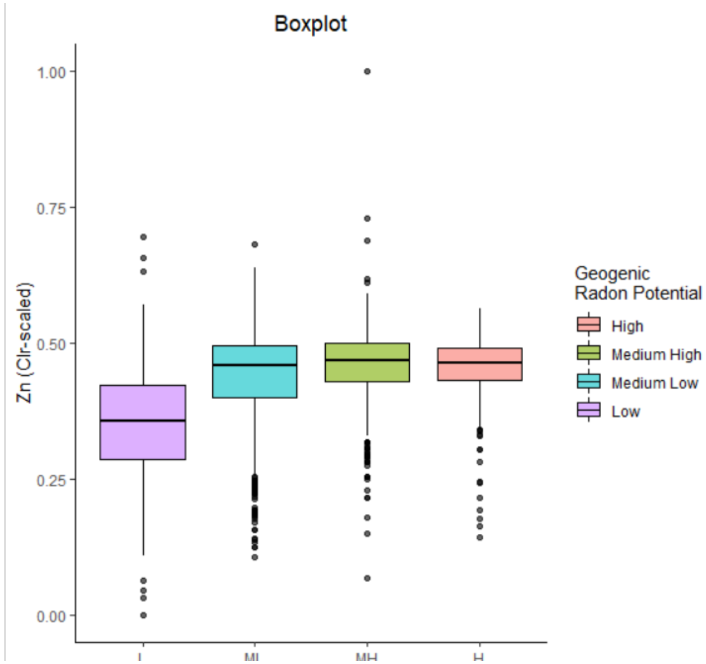
Boxplot
Zn (Clr-scaled)
1.00
0.75
0.50
0.25
0.00
Geogenic Radon Potential
High
Medium High
Medium Low
Low

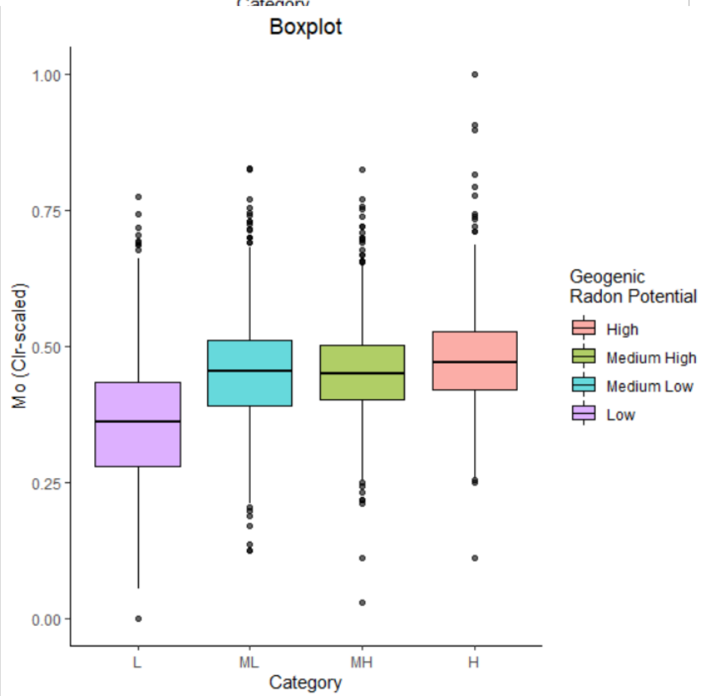
Boxplot
Mo (Clr-scaled)
1.00
0.75
0.50
0.25
0.00
L
ML
MH
H
Category
Geogenic Radon Potential
High
Medium High
Medium Low
Low

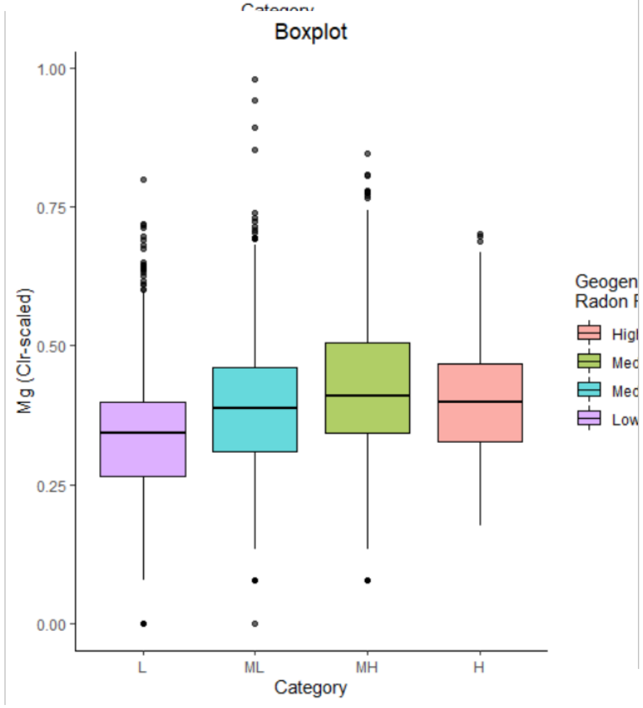
Boxplot
Mg (Clr-scaled)
1.00
0.75
0.50
0.25
0.00
L
ML
MH
H
Category

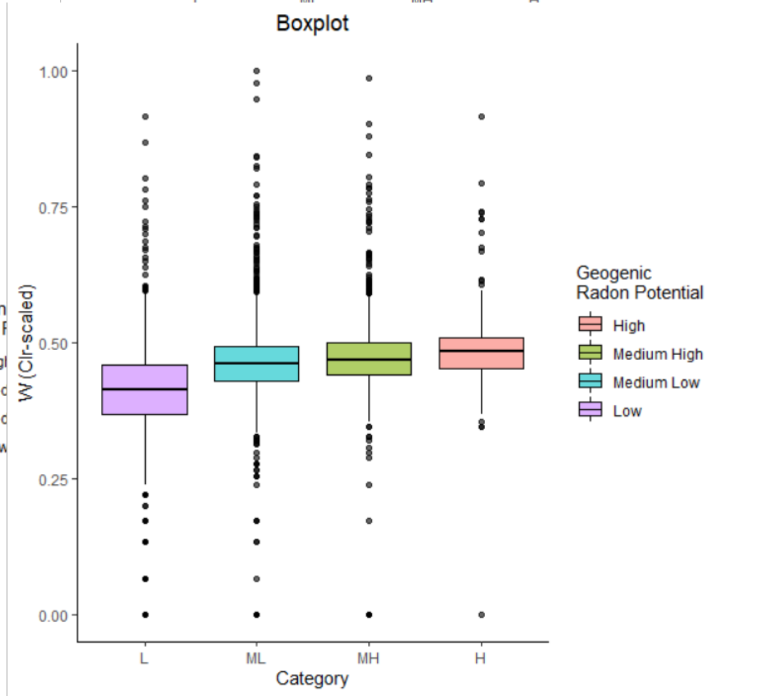
Boxplot
W (Clr-scaled)
1.00
0.75
0.50
0.25
0.00
L
ML
MH
H
Category
Geogenic Radon Potential
High
Medium High
Medium Low
Low

Appendix A

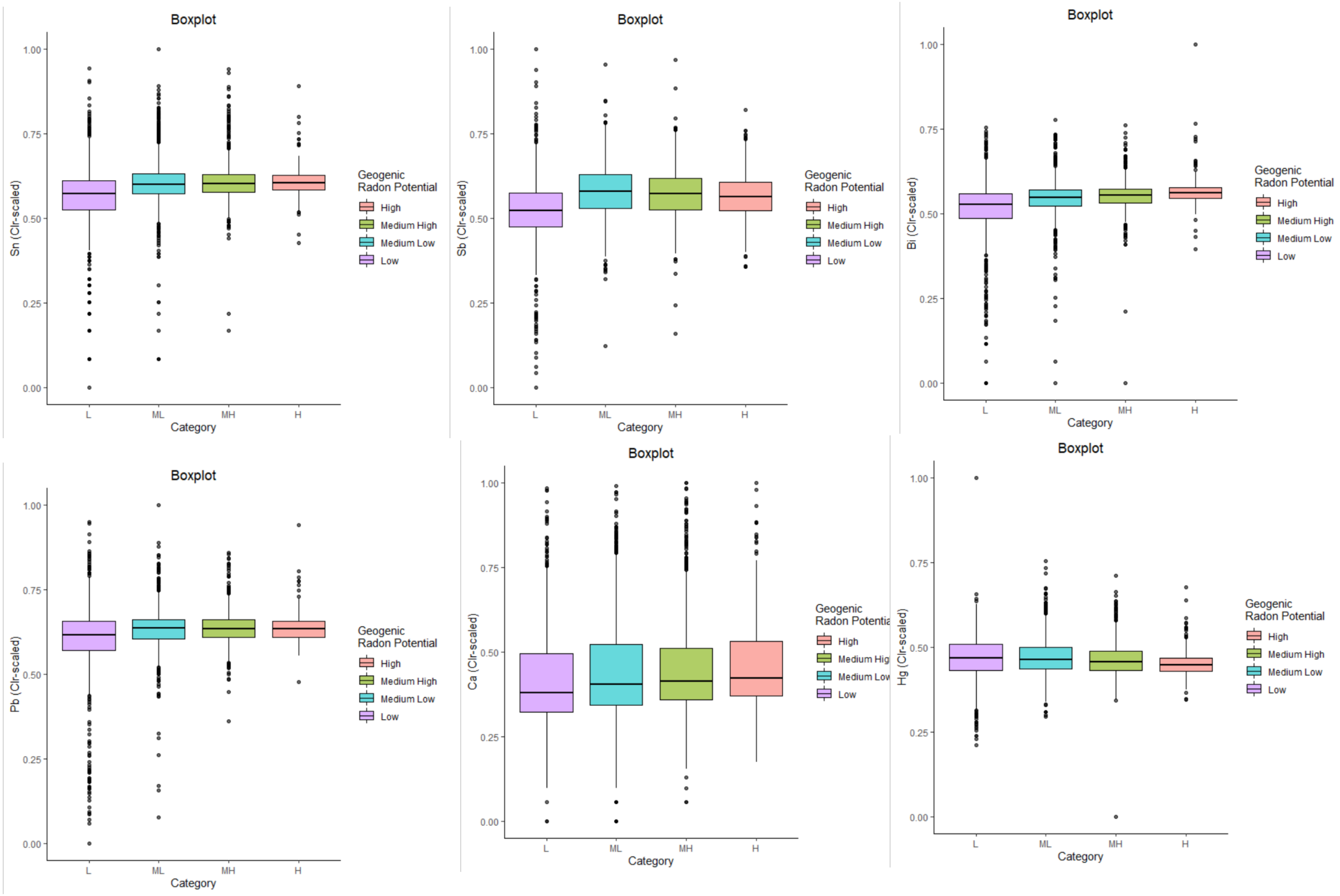
Boxplot
Sn (Clr-scaled)
1.00
0.75
0.50
0.25
0.00
L
ML
MH
H
Category
Geogenic Radon Potential
High
Medium High
Medium Low
Low
Boxplot
Sb (Clr-scaled)
Category
Geogenic Radon Potential
High
Medium High
Medium Low
Low
Boxplot
Bi (Clr-scaled)
Category
Geogenic Radon Potential
High
Medium High
Medium Low
Low
Boxplot
Pb (Clr-scaled)
Category
Geogenic Radon Potential
High
Medium High
Medium Low
Low
Boxplot
Ca (Clr-scaled)
Category
Boxplot
Hg (Clr-scaled)
Category
Geogenic Radon Potential
High
Medium High
Medium Low
Low

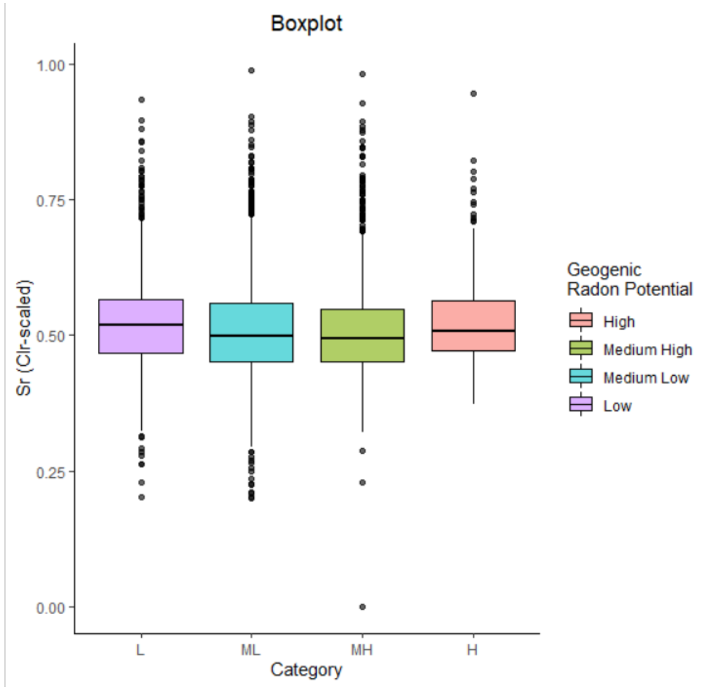
Boxplot
1.00
0.75
0.50
0.25
0.00
Sr (Clr-scaled)
L
ML
MH
H
Category
Geogenic Radon Potential
High
Medium High
Medium Low
Low

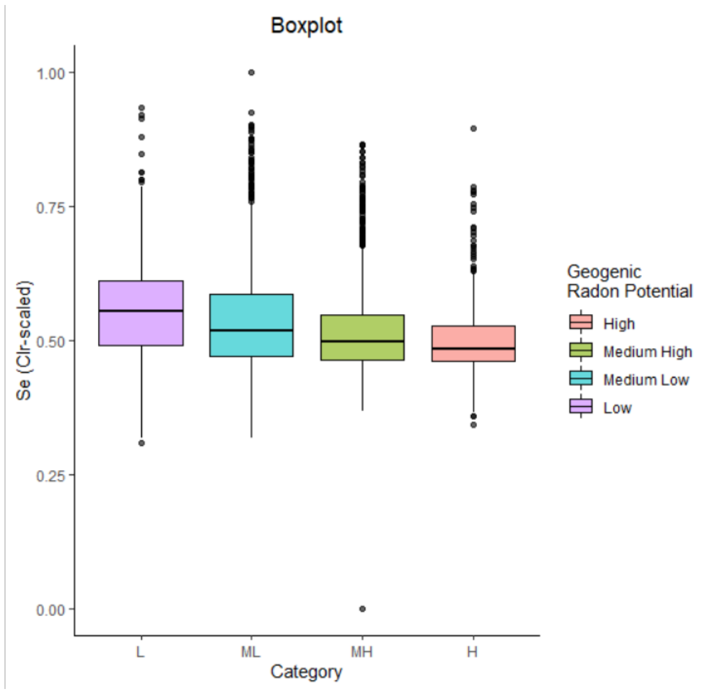
Boxplot
1.00
0.75
0.50
0.25
0.00
Se (Clr-scaled)
L
ML
MH
H
Category
Geogenic Radon Potential
High
Medium High
Medium Low
Low

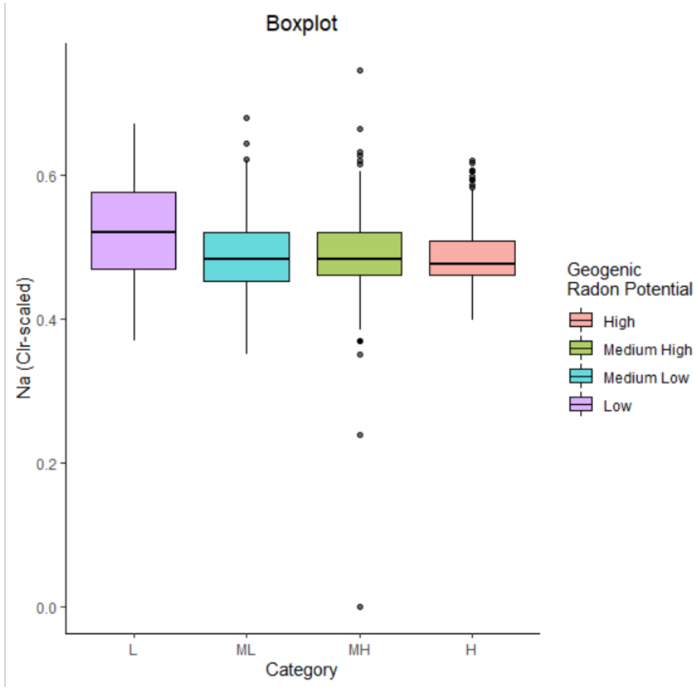
Boxplot
0.6
0.4
0.2
0.0
Na (Clr-scaled)
L
ML
MH
H
Category
Geogenic Radon Potential
High
Medium High
Medium Low
Low

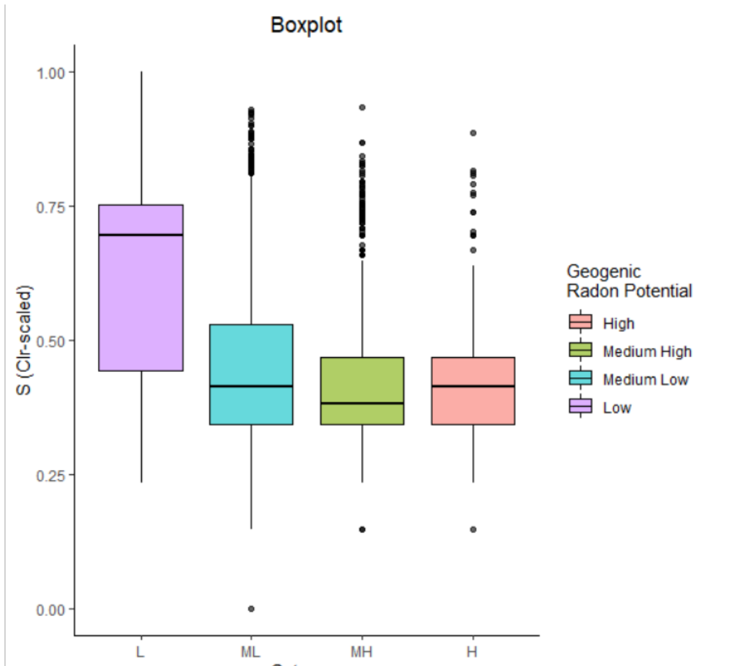
Boxplot
1.00
0.75
0.50
0.25
0.00
S (Clr-scaled)
L
ML
MH
H
Geogenic Radon Potential
High
Medium High
Medium Low
Low

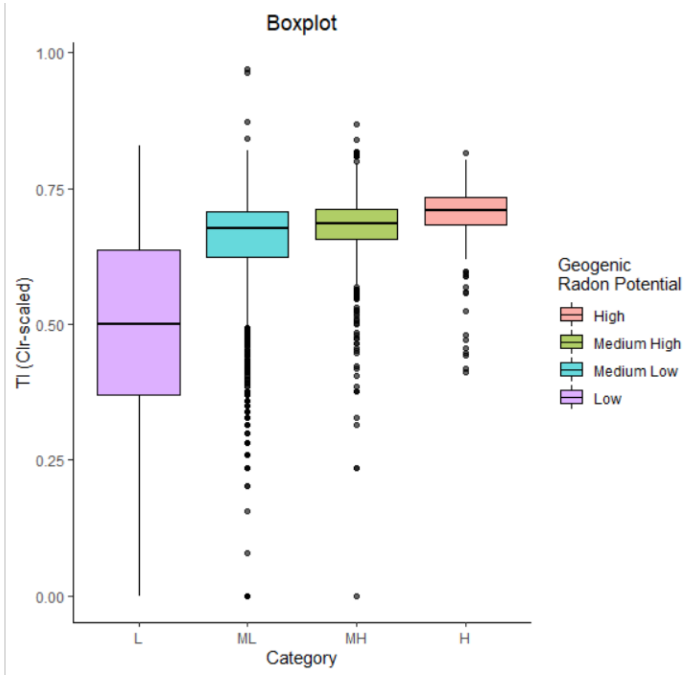
Boxplot
1.00
0.75
0.50
0.25
0.00
Tl (Clr-scaled)
L
ML
MH
H
Category
Geogenic Radon Potential
High
Medium High
Medium Low
Low

Appendix A

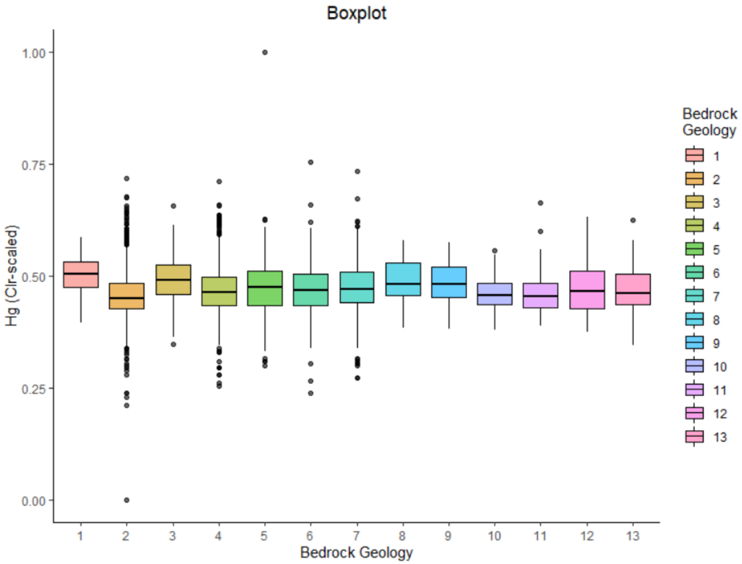

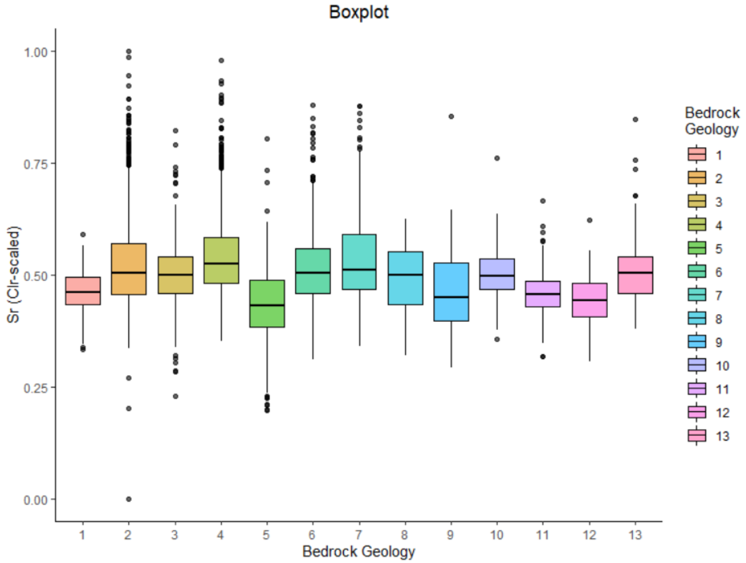

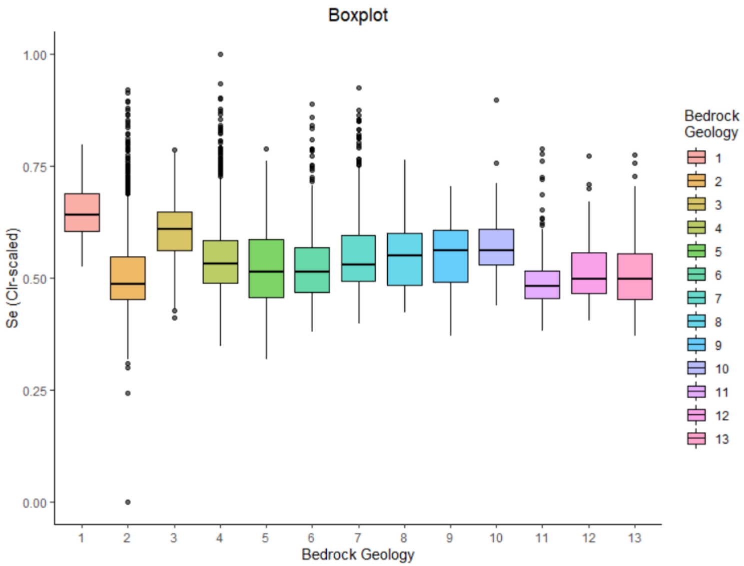

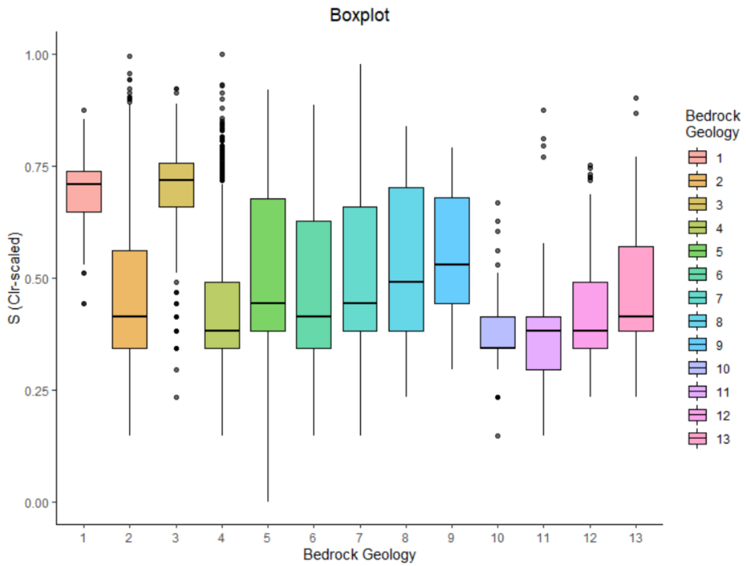

Legend

1. **27, Argyll Group; Psammitic & pelitic schist, marble, amphibolite, diamictite**
2. **64, Marine shelf facies; Limestone & calcareous shale**
3. **8, Granite, granodiorite**
4. **65, Marine basinal facies (Tobercolleen & Lucan Fms - "Calp"); Dark-grey argillaceous & cherty limestone & shale**
5. **59, Shallow marine & coastal plain (basal clastics); Sandstone, mudstone & conglomerate**
6. **61, Marine shelf & ramp facies; Argillaceous dark-grey bioclastic limestone, subsidiary shale**
7. **62, Waulsortian mudbank; Pale-grey massive limestone**
8. **56, Basalt, trachyte, syenite & tuff 5, Gabbro, dolerite & diorite**
9. **52, Continental redbed facies; Sandstone, siltstone & mudstone (base of Dingle Group is in the Upper Silurian)**
10. **71, Fluvio-deltaic & basinal marine (Turbiditic); Shale, sandstone, siltstone & coal**
11. **49, Deep marine turbidite sequence; Mudstone, greywacke & conglomerate**
12. **32, Marine; Greywacke & shale 42, "Moffat shale" facies (Ordovician - Silurian); Shale & greywacke 39, Deep marine; Slate, shale, minor sandstone & siltstone**
13. **60, Shallow & marginal marine (Navan Group); Dark-grey limestone, mudstone, sandstone, minor evaporite**

Appendix A

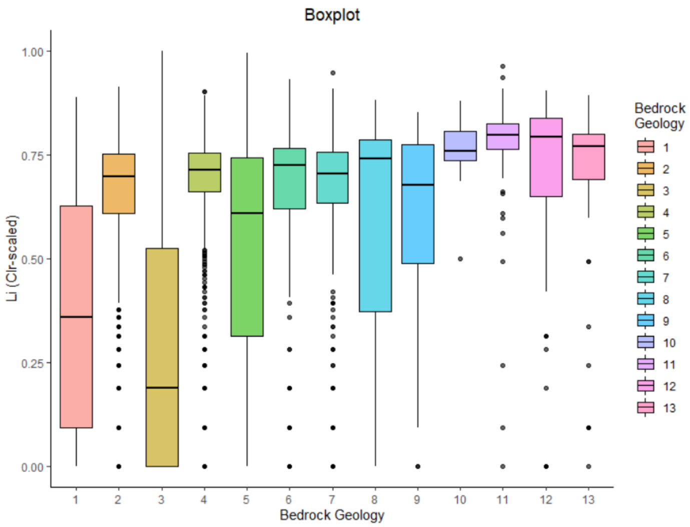
Boxplot
Li (Clr-scaled)
Bedrock Geology
Bedrock Geology
1
2
3
4
5
6
7
8
9
10
11
12
13

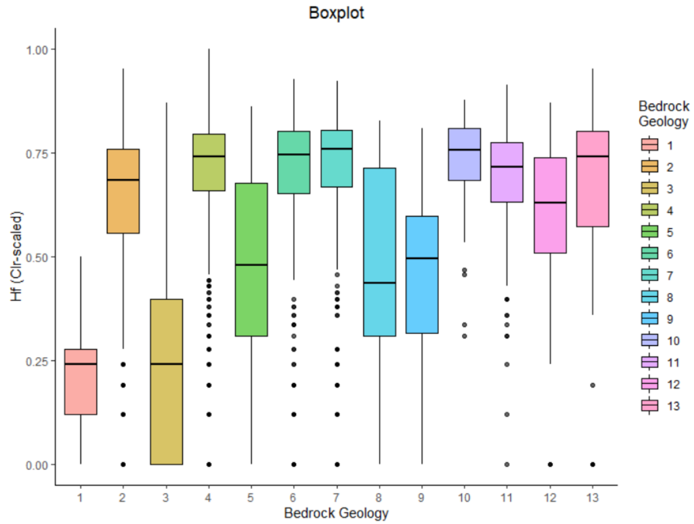
Boxplot
Hf (Clr-scaled)
Bedrock Geology
Bedrock Geology

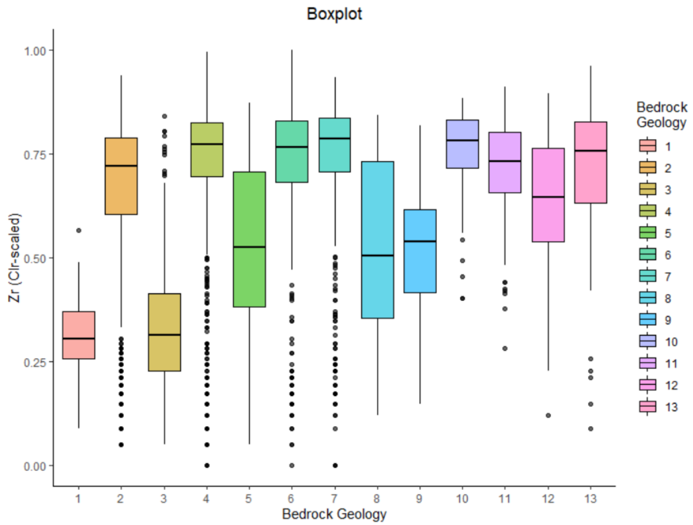
Boxplot
Zr (Clr-scaled)
Bedrock Geology
Bedrock Geology

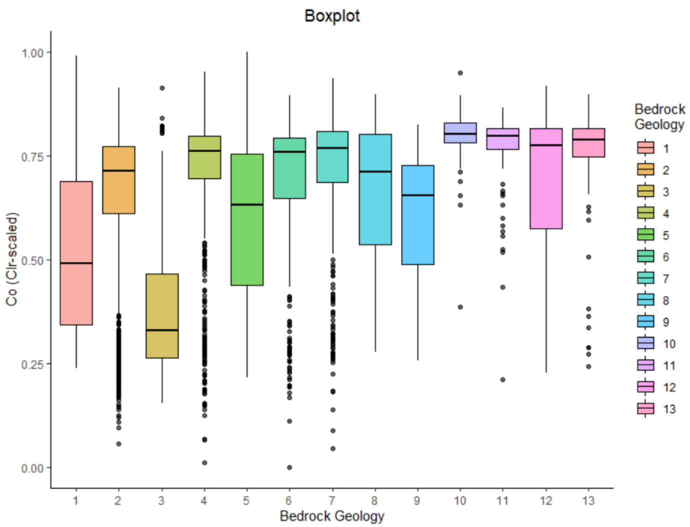
Boxplot
Co (Clr-scaled)
Bedrock Geology
Bedrock Geology

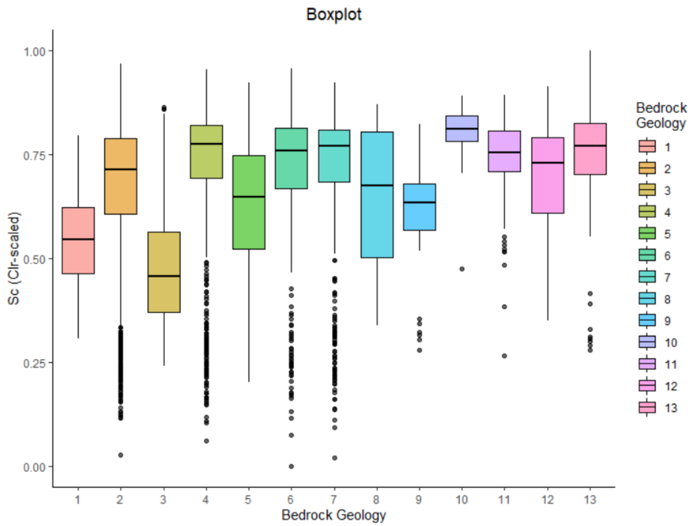
Boxplot
Sc (Clr-scaled)
Bedrock Geology
Bedrock Geology

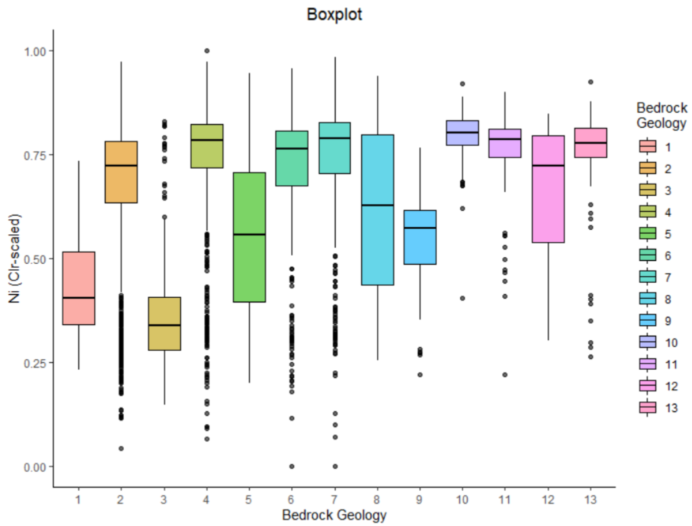
Boxplot
Ni (Clr-scaled)
Bedrock Geology
Bedrock Geology

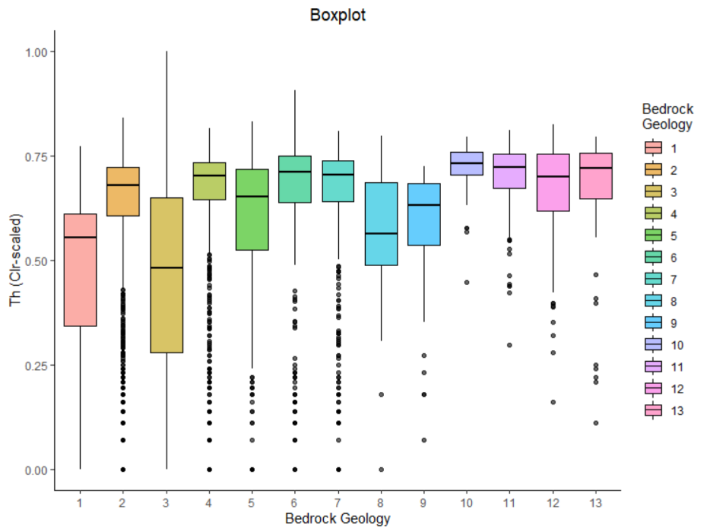
Boxplot
Th (Clr-scaled)
Bedrock Geology
Bedrock Geology
1 2 3 4 5 6 7 8 9 10 11 12 13

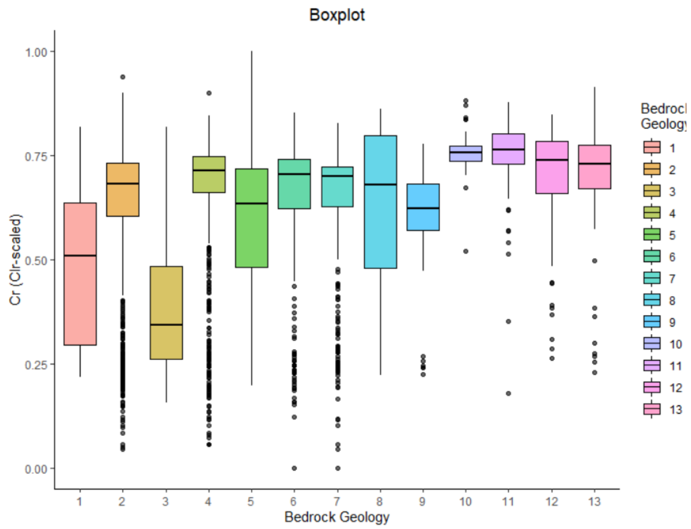
Boxplot
Cr (Clr-scaled)
Bedrock Geology
1 2 3 4 5 6 7 8 9 10 11 12 13

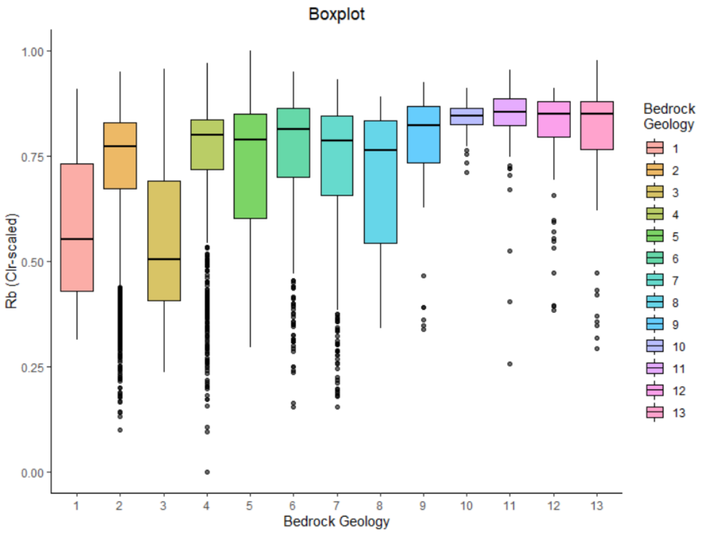
Boxplot
Rb (Clr-scaled)
Bedrock Geology
Bedrock Geology
1 2 3 4 5 6 7 8 9 10 11 12 13

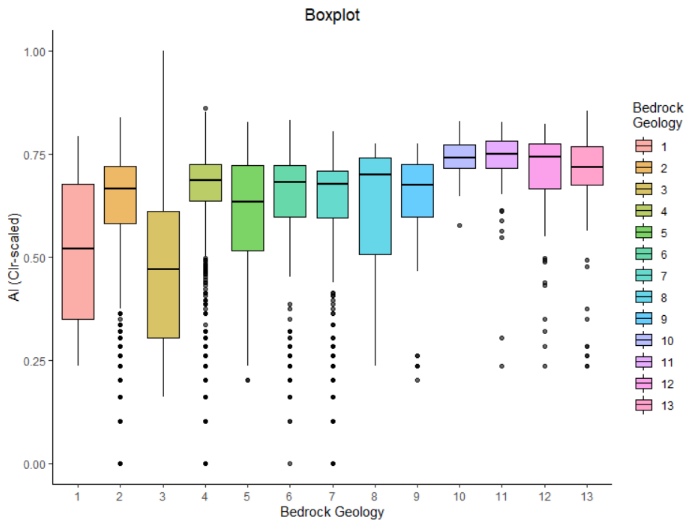
Boxplot
Al (Clr-scaled)
Bedrock Geology
Bedrock Geology
1 2 3 4 5 6 7 8 9 10 11 12 13

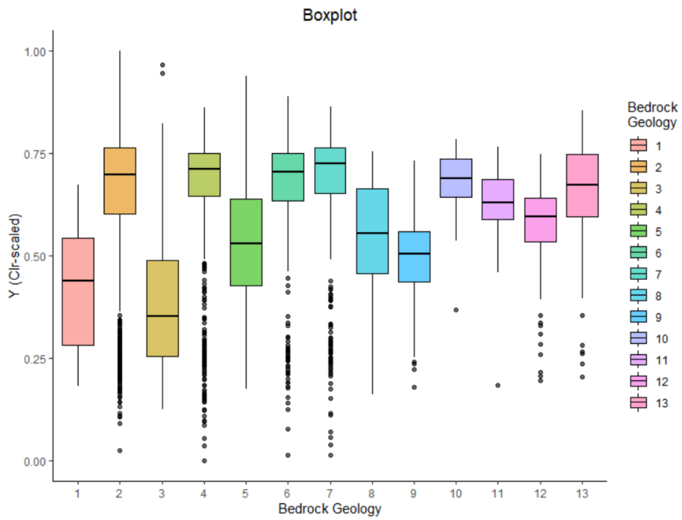
Boxplot
Y (Clr-scaled)
Bedrock Geology
Bedrock Geology
1 2 3 4 5 6 7 8 9 10 11 12 13

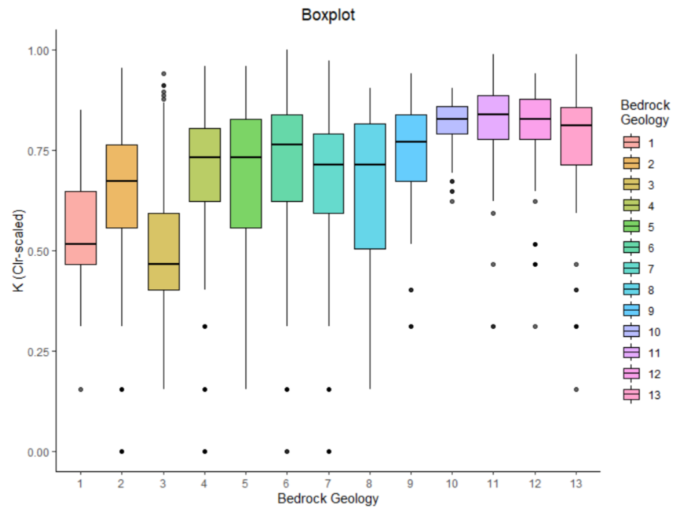
Boxplot
K (Clr-scaled)
Bedrock Geology
Bedrock Geology
1 2 3 4 5 6 7 8 9 10 11 12 13

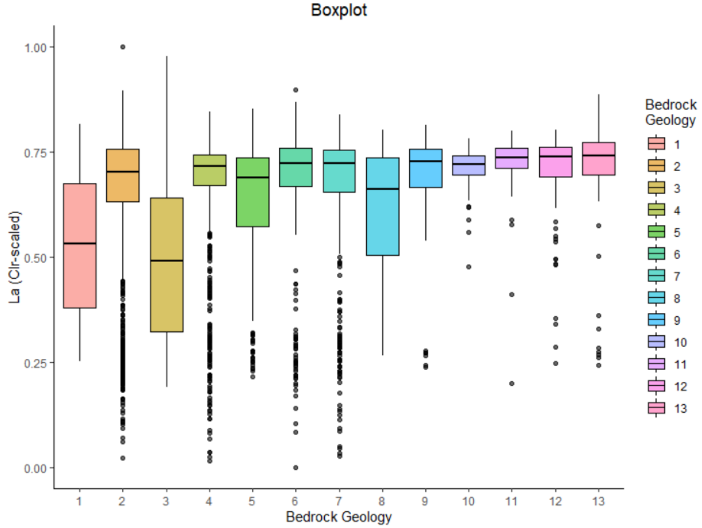
Boxplot
La (Clr-scaled)
Bedrock Geology
Bedrock Geology
1
2
3
4
5
6
7
8
9
10
11
12
13

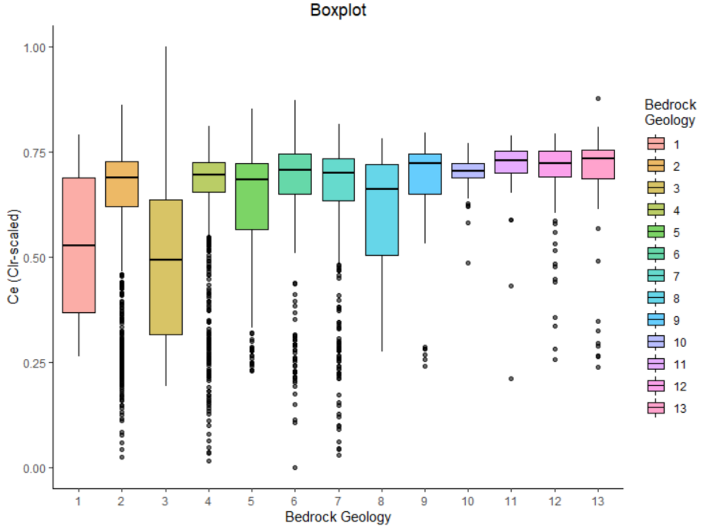
Boxplot
Ce (Clr-scaled)
Bedrock Geology
Bedrock Geology
1
2
3
4
5
6
7
8
9
10
11
12
13

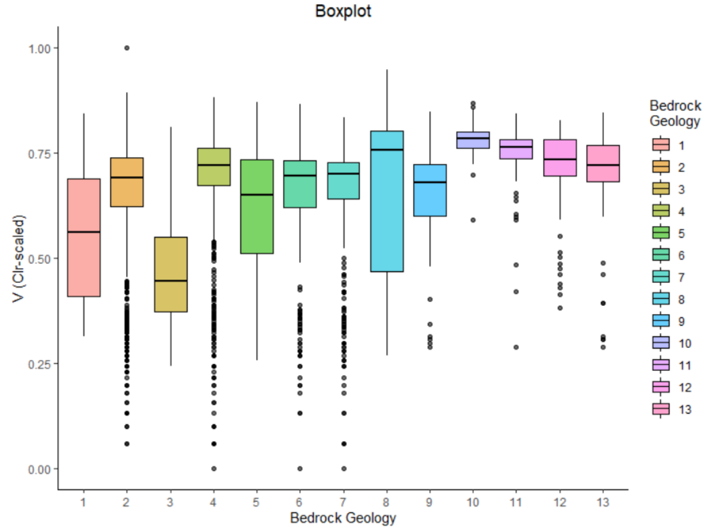
Boxplot
V (Clr-scaled)
Bedrock Geology
Bedrock Geology
1
2
3
4
5
6
7
8
9
10
11
12
13

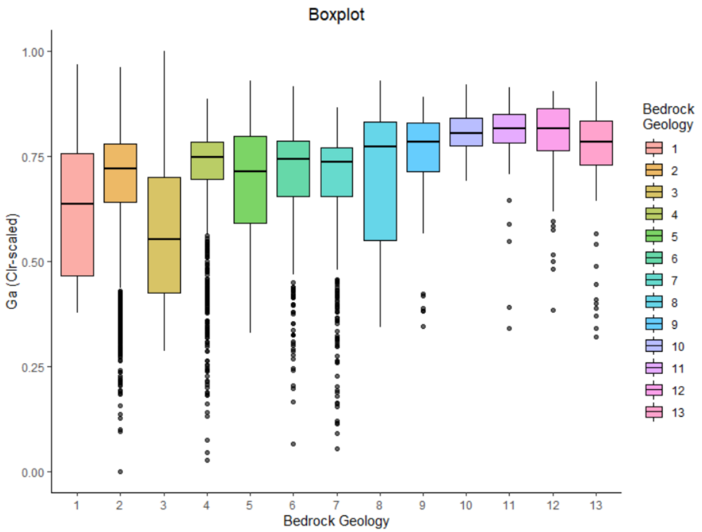
Boxplot
Ga (Clr-scaled)
Bedrock Geology
Bedrock Geology
1
2
3
4
5
6
7
8
9
10
11
12
13

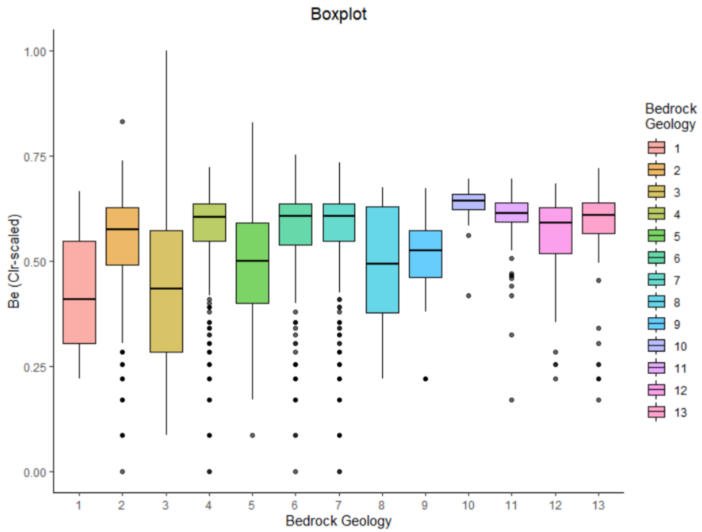
Boxplot
Be (Clr-scaled)
Bedrock Geology
Bedrock Geology
1
2
3
4
5
6
7
8
9
10
11
12
13

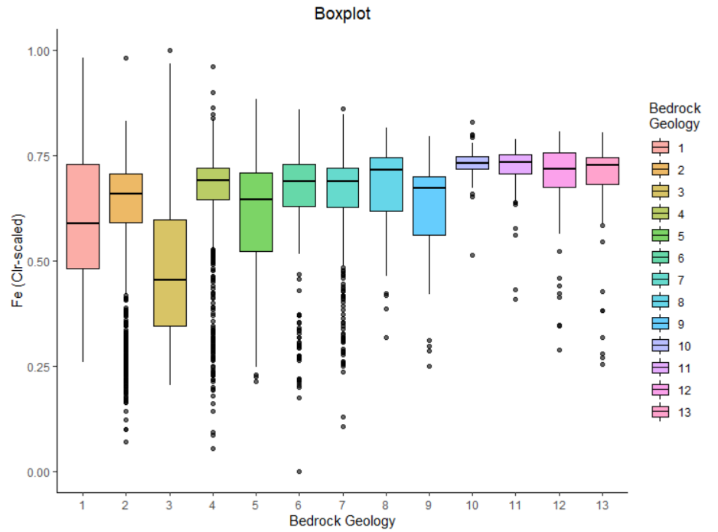
Boxplot
Fe (Clr-scaled)
Bedrock Geology
Bedrock Geology
1
2
3
4
5
6
7
8
9
10
11
12
13

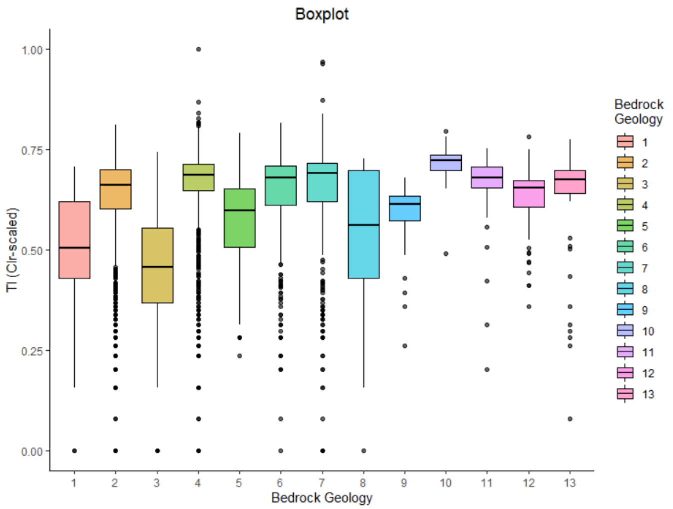
Boxplot
Tl (Clr-scaled)
Bedrock Geology
Bedrock Geology
1 2 3 4 5 6 7 8 9 10 11 12 13

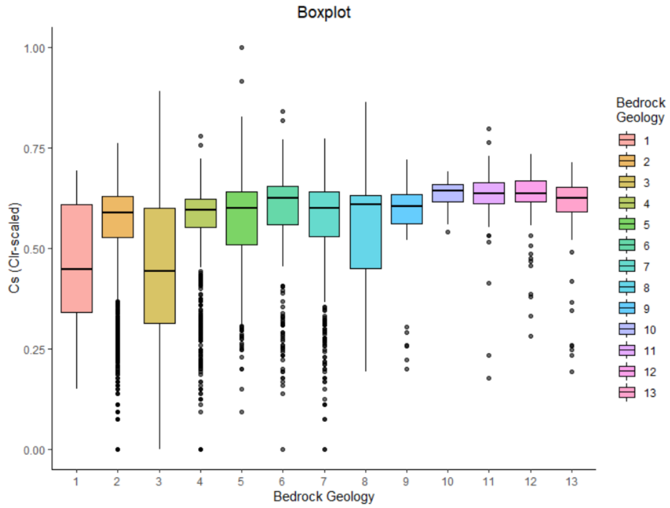
Boxplot
Cs (Clr-scaled)
Bedrock Geology
Bedrock Geology
1 2 3 4 5 6 7 8 9 10 11 12 13

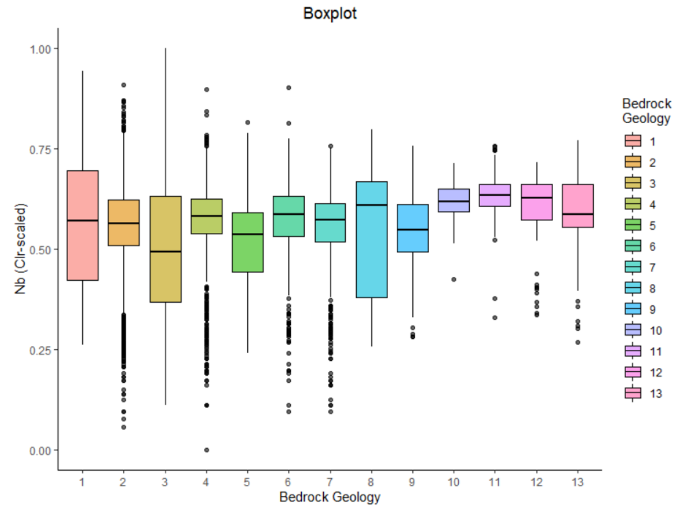
Boxplot
Nb (Clr-scaled)
Bedrock Geology
Bedrock Geology
1 2 3 4 5 6 7 8 9 10 11 12 13

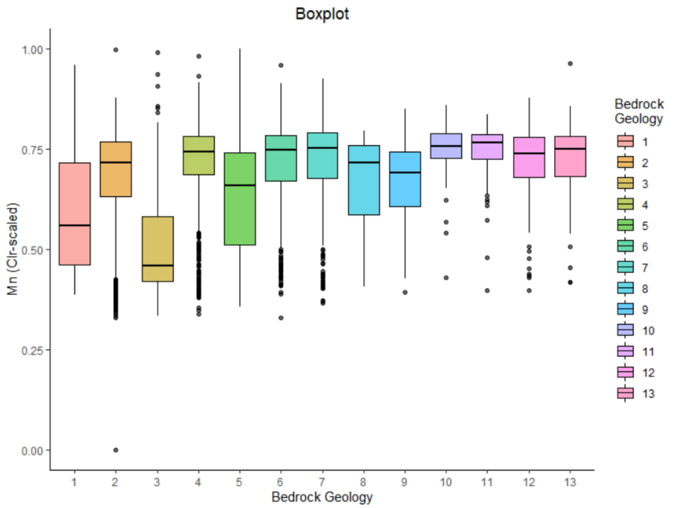
Boxplot
Mn (Clr-scaled)
Bedrock Geology
Bedrock Geology
1 2 3 4 5 6 7 8 9 10 11 12 13

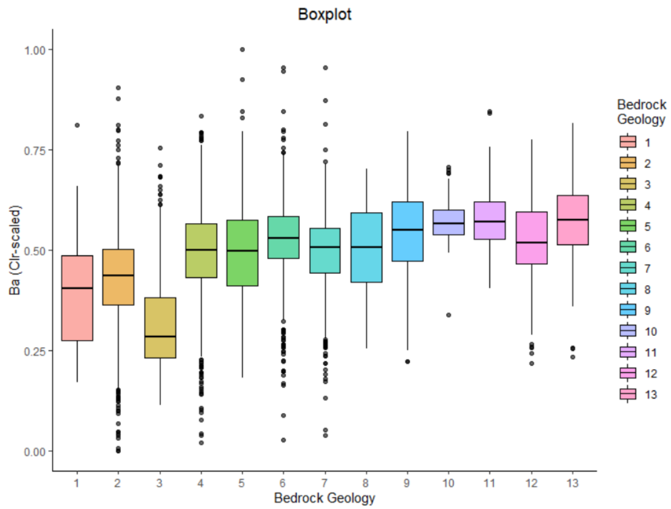
Boxplot
Ba (Clr-scaled)
Bedrock Geology
Bedrock Geology
1 2 3 4 5 6 7 8 9 10 11 12 13

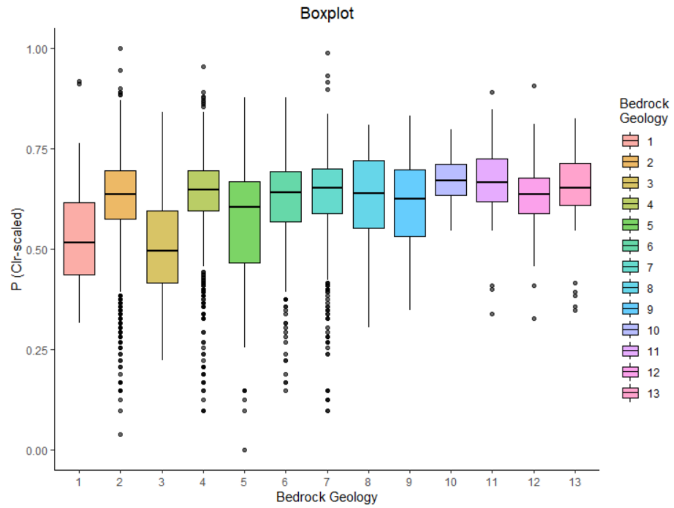
Boxplot
P (Clr-scaled)
Bedrock Geology
Bedrock Geology
1 2 3 4 5 6 7 8 9 10 11 12 13

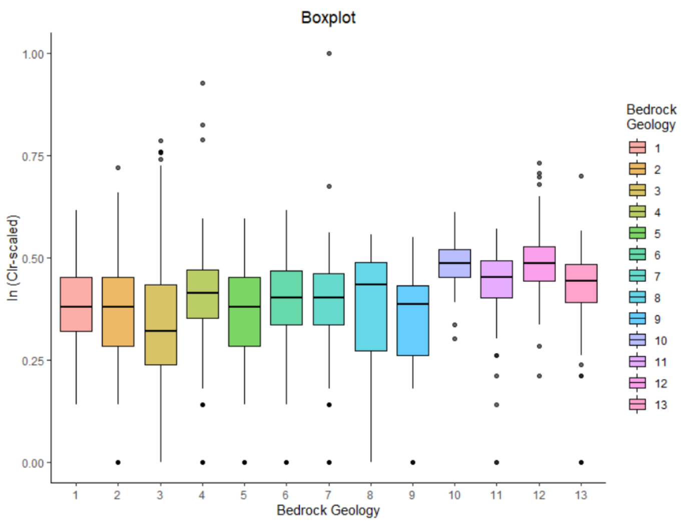
Boxplot
In (Clr-scaled)
0.00
0.25
0.50
0.75
1.00
1 2 3 4 5 6 7 8 9 10 11 12 13
Bedrock Geology
Bedrock Geology
1
2
3
4
5
6
7
8
9
10
11
12
13

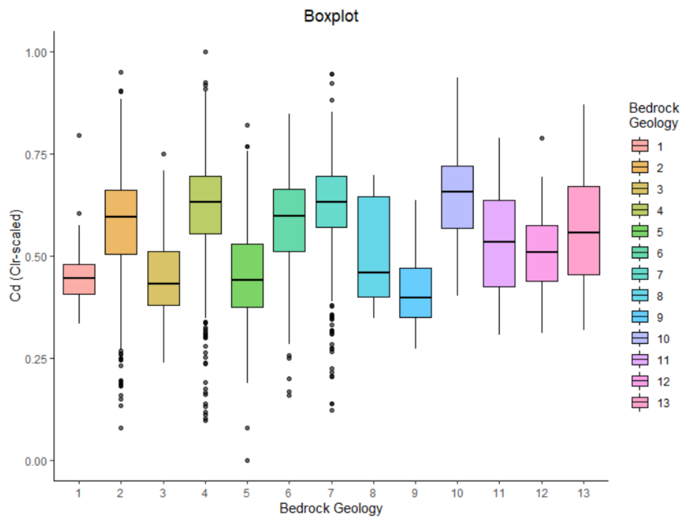
Boxplot
Cd (Clr-scaled)
0.00
0.25
0.50
0.75
1.00
1 2 3 4 5 6 7 8 9 10 11 12 13
Bedrock Geology
Bedrock Geology
1
2
3
4
5
6
7
8
9
10
11
12
13

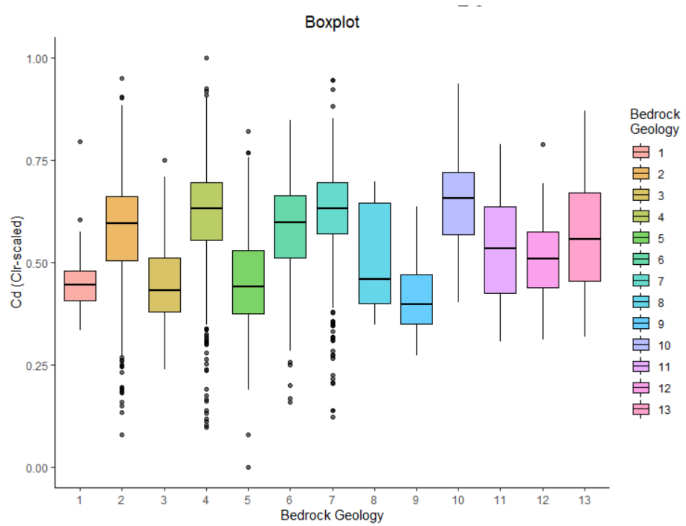
Boxplot
Cd (Clr-scaled)
0.00
0.25
0.50
0.75
1.00
1 2 3 4 5 6 7 8 9 10 11 12 13
Bedrock Geology
Bedrock Geology
1
2
3
4
5
6
7
8
9
10
11
12
13

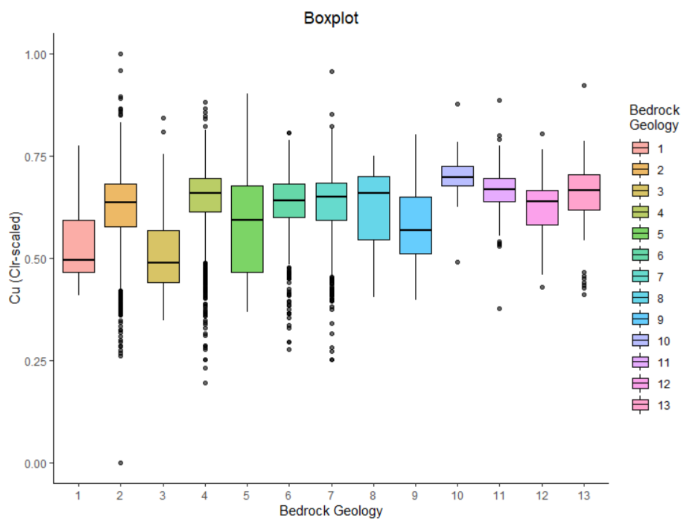
Boxplot
Cu (Clr-scaled)
0.00
0.25
0.50
0.75
1.00
1 2 3 4 5 6 7 8 9 10 11 12 13
Bedrock Geology
Bedrock Geology
1
2
3
4
5
6
7
8
9
10
11
12
13

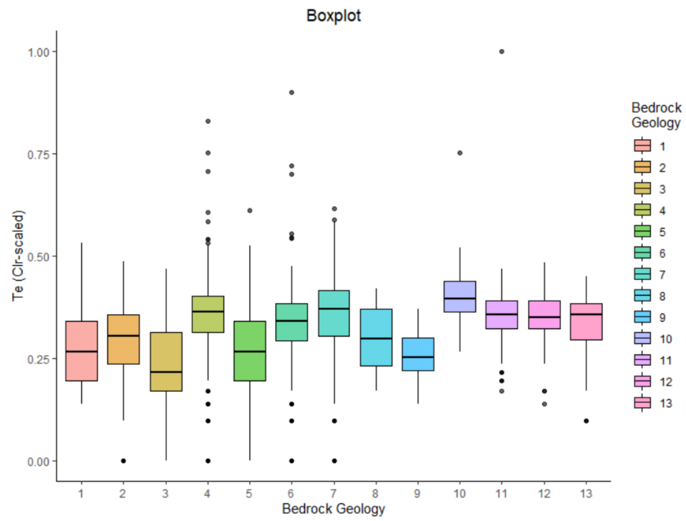
Boxplot
Te (Clr-scaled)
0.00
0.25
0.50
0.75
1.00
1 2 3 4 5 6 7 8 9 10 11 12 13
Bedrock Geology
Bedrock Geology
1
2
3
4
5
6
7
8
9
10
11
12
13

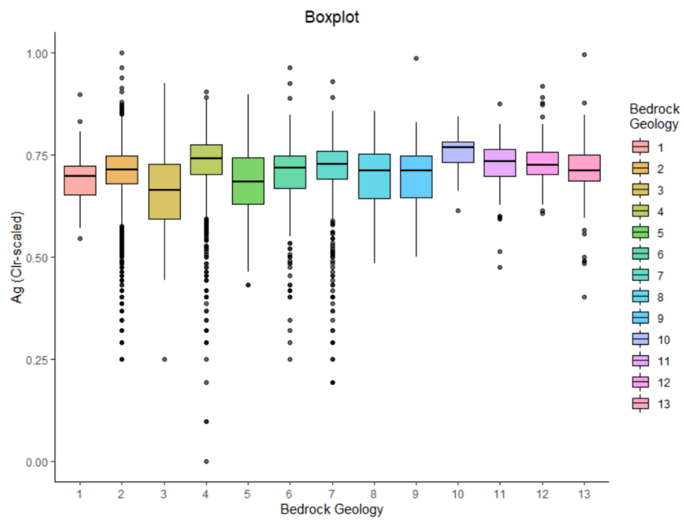
Boxplot
Ag (Clr-scaled)
0.00
0.25
0.50
0.75
1.00
1 2 3 4 5 6 7 8 9 10 11 12 13
Bedrock Geology
Bedrock Geology
1
2
3
4
5
6
7
8
9
10
11
12
13

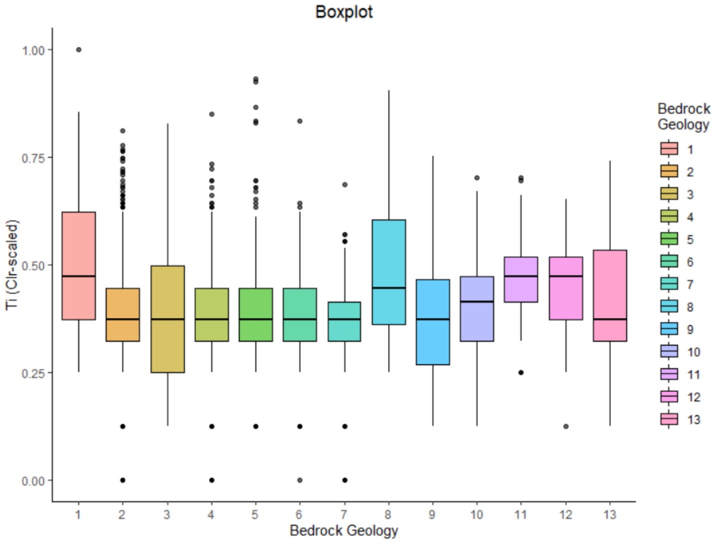
Boxplot
Ti (Clr-scaled)
0.00
0.25
0.50
0.75
1.00
1 2 3 4 5 6 7 8 9 10 11 12 13
Bedrock Geology
Bedrock Geology
1 2 3 4 5 6 7 8 9 10 11 12 13

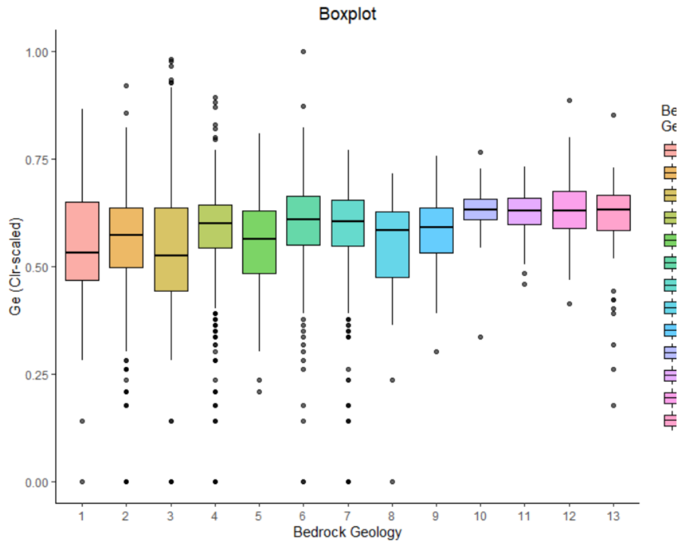
Boxplot
Ge (Clr-scaled)
0.00
0.25
0.50
0.75
1.00
1 2 3 4 5 6 7 8 9 10 11 12 13
Bedrock Geology

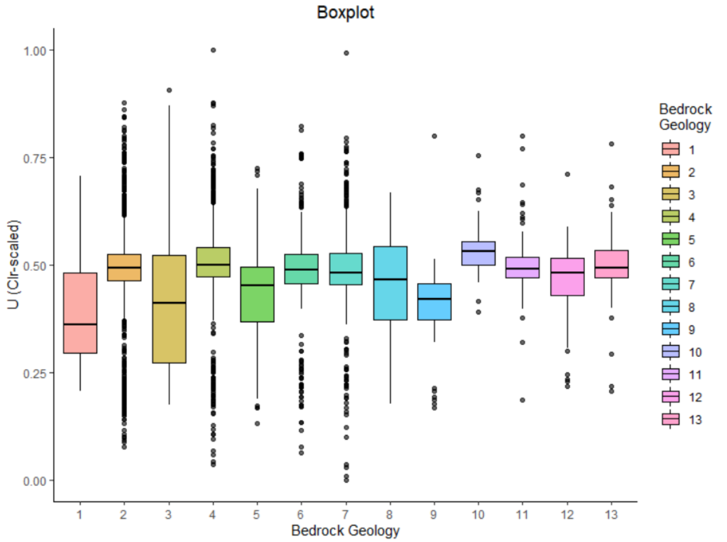
Boxplot
U (Clr-scaled)
0.00
0.25
0.50
0.75
1.00
1 2 3 4 5 6 7 8 9 10 11 12 13
Bedrock Geology
Bedrock Geology
1 2 3 4 5 6 7 8 9 10 11 12 13

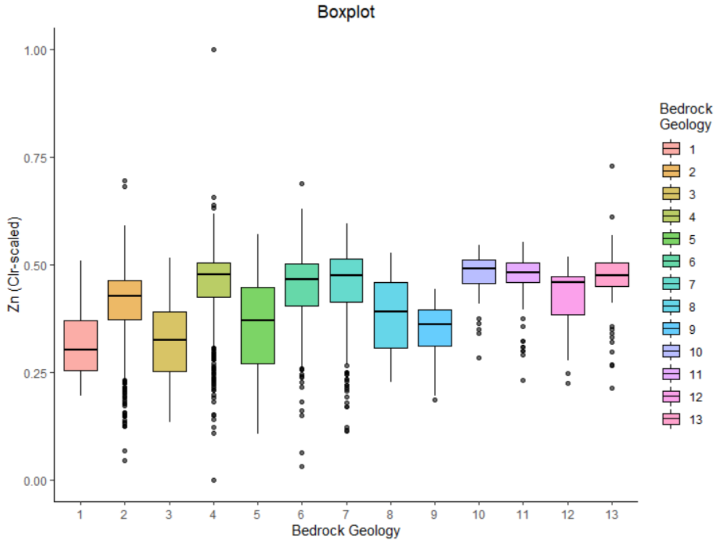
Boxplot
Zn (Clr-scaled)
0.00
0.25
0.50
0.75
1.00
1 2 3 4 5 6 7 8 9 10 11 12 13
Bedrock Geology
Bedrock Geology
1 2 3 4 5 6 7 8 9 10 11 12 13

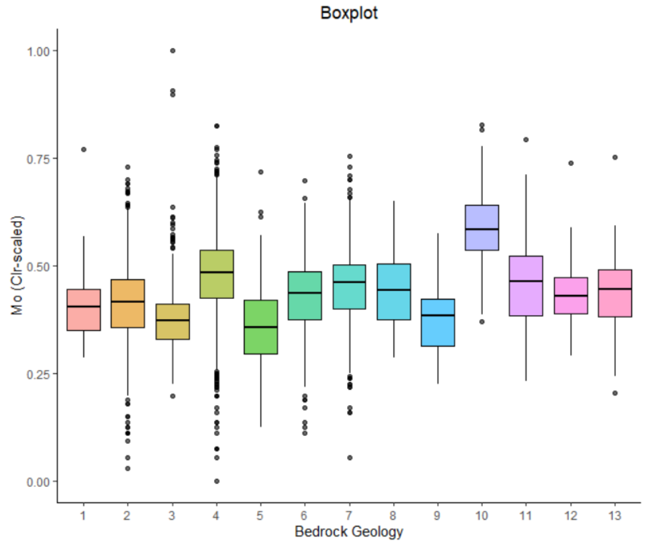
Boxplot
Mo (Clr-scaled)
0.00
0.25
0.50
0.75
1.00
1 2 3 4 5 6 7 8 9 10 11 12 13
Bedrock Geology

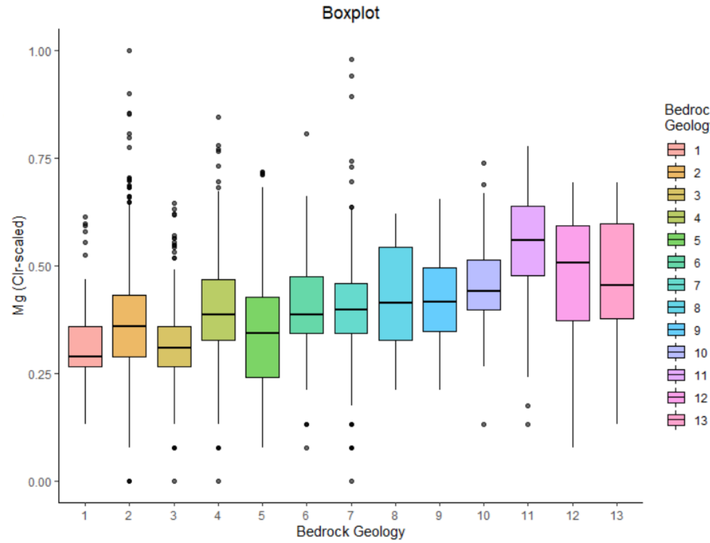
Boxplot
Mg (Clr-scaled)
0.00
0.25
0.50
0.75
1.00
1 2 3 4 5 6 7 8 9 10 11 12 13
Bedrock Geology
1 2 3 4 5 6 7 8 9 10 11 12 13

Appendix A

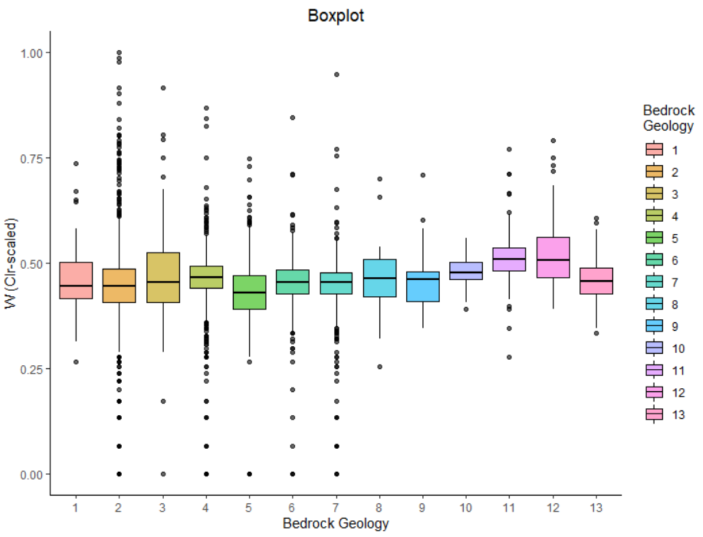
Boxplot
W (Clr-scaled)
Bedrock Geology
Bedrock Geology

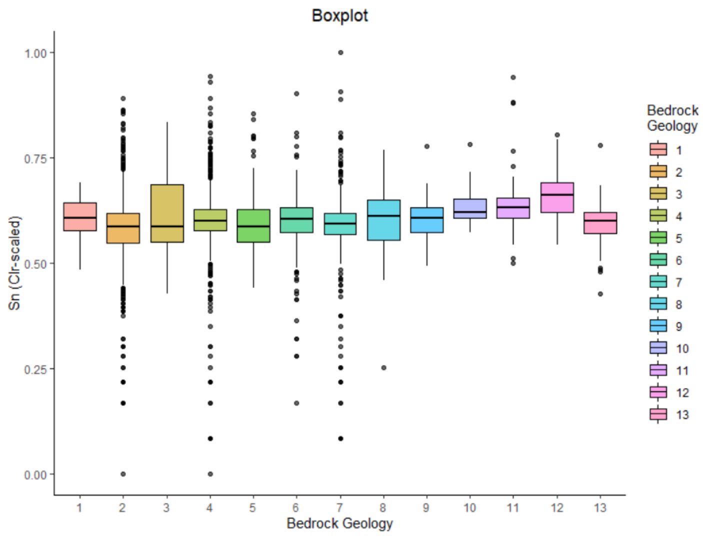
Boxplot
Sn (Clr-scaled)
Bedrock Geology
Bedrock Geology

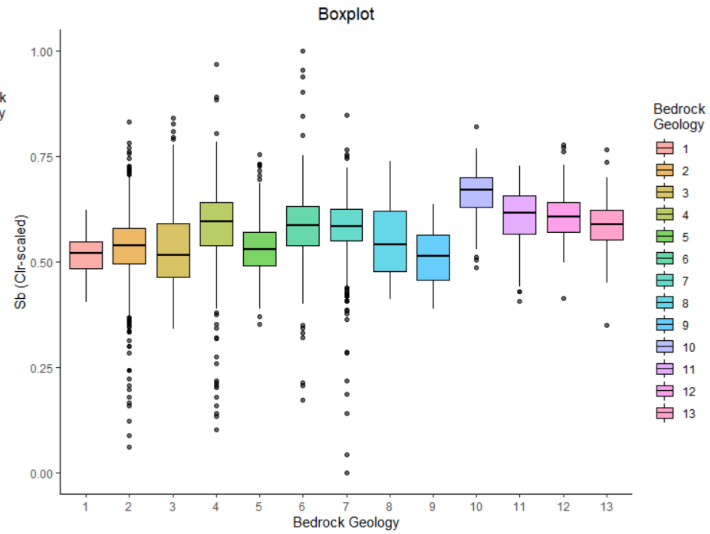
Boxplot
Sb (Clr-scaled)
Bedrock Geology
Bedrock Geology

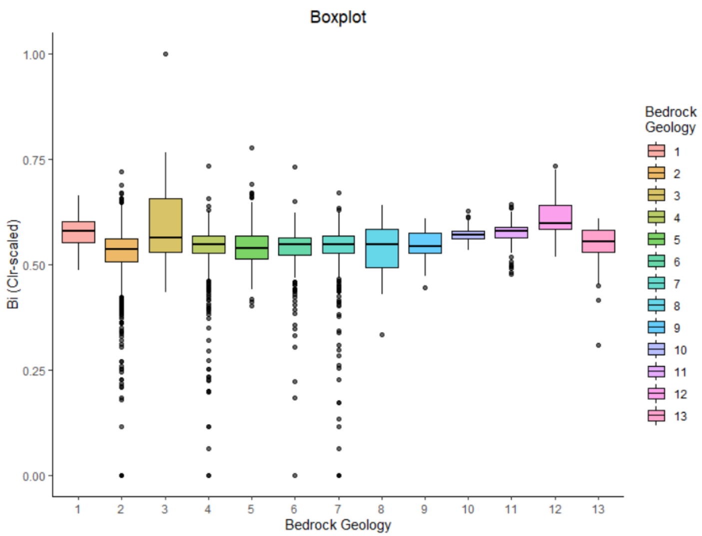
Boxplot
Bi (Clr-scaled)
Bedrock Geology
Bedrock Geology

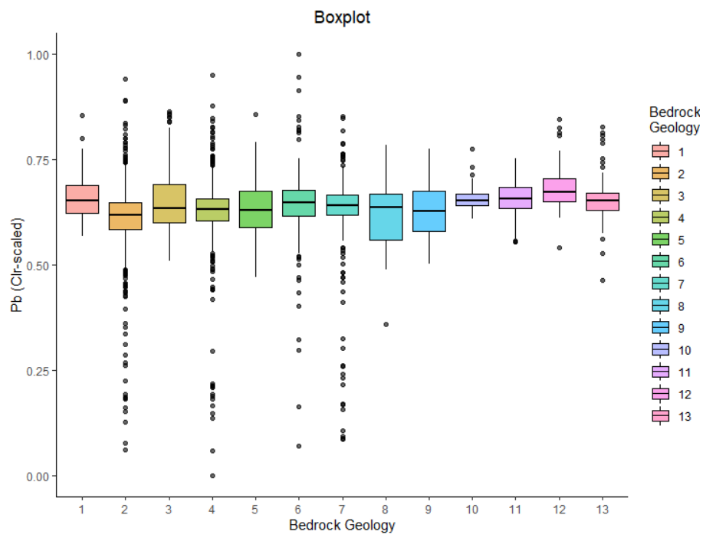
Boxplot
Pb (Clr-scaled)
Bedrock Geology
Bedrock Geology

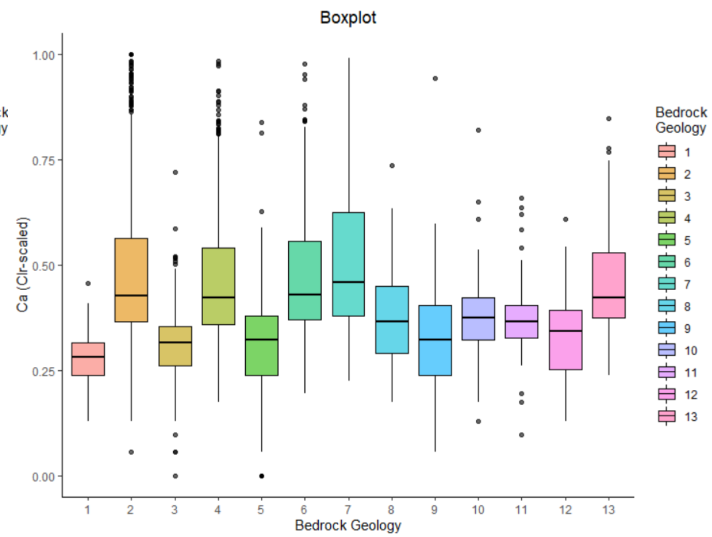
Boxplot
Ca (Clr-scaled)
Bedrock Geology
Bedrock Geology

7.2.12 (Figures) PC1 to PC4 score maps of TELLUS Midlands Clr-transformed topsoil geochemistry.

File name: PC1_4_ScoreMaps_TELLUSMidlands

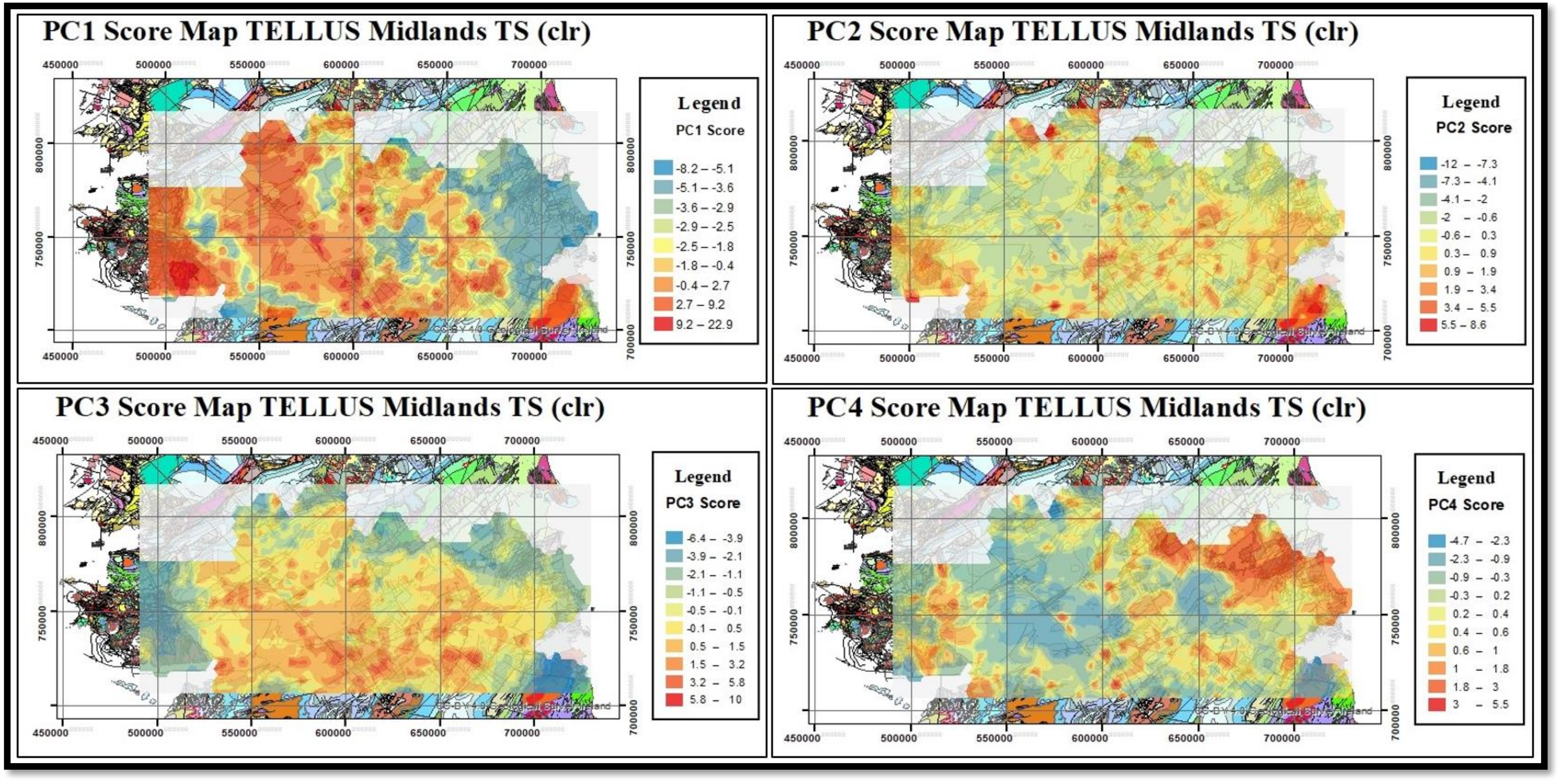

Figure 7.2.12 (Figures) PC1 to PC4 score maps of TELLUS Midlands Clr-transformed topsoil geochemistry.

7.2.13 (Figure) Cluster analysis dendrogram TELLUS Midlands Clr-transformed shallow topsoil geochemistry.

File name: 13. Cluster analysis dendrogram TELLUS Midlands

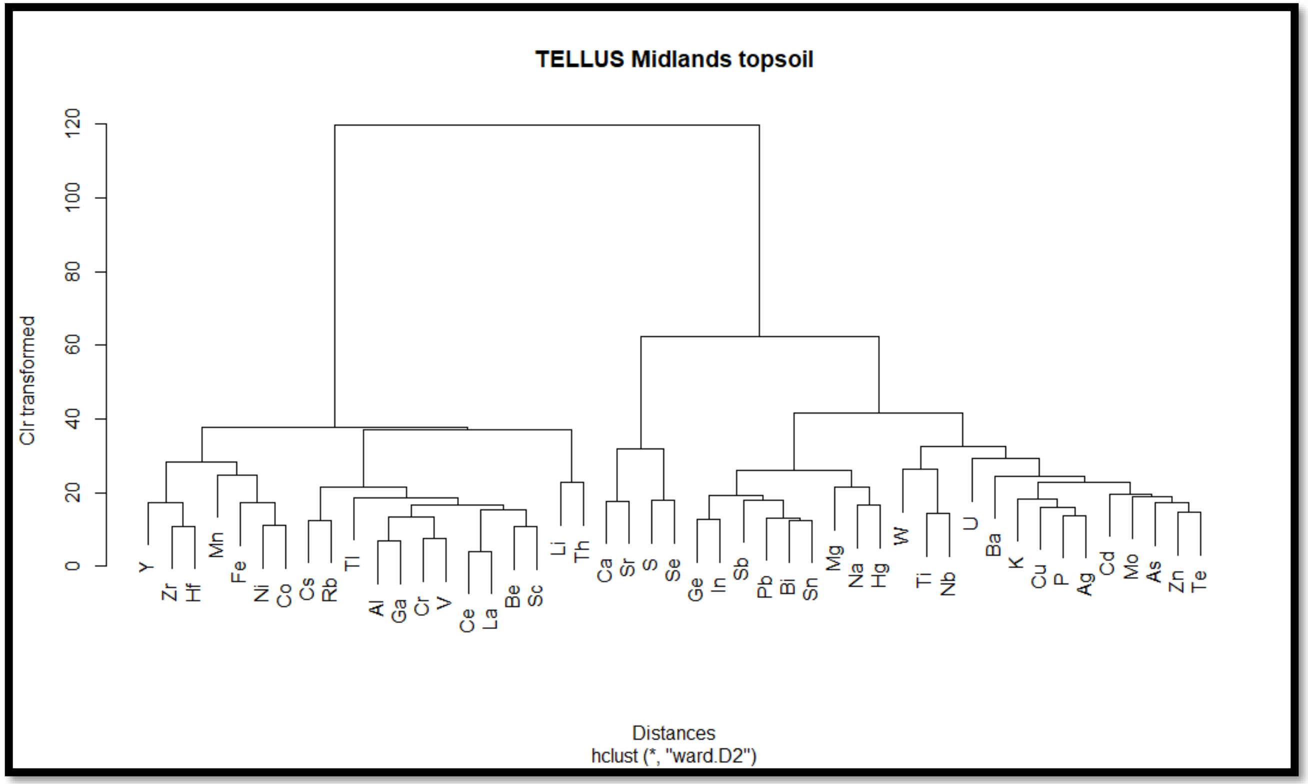

Figure 7.2.13 Cluster analysis dendrogram TELLUS Midlands Clr-transformed shallow topsoil geochemistry

7.2.14 ransformed shallow topsoil TELLUS Midlands.

File name: 14. ANOVA PCA_vs_(a)Geogenicradon_(b)Bedrocklithology

Table 7.2.14 ANOVA results of PC1-PC4 vs (a) Geogenic radon potential and (b) bedrock lithology (1:100k) of Clr-transformed shallow topsoil TELLUS Midlands Ireland.

Principle component	GRP ANOVA	F-value	Pr (>F)	Principle component	Bedrock (1:100k) ANOVA	F-value	Pr (>F)
PC1	33.1%	698	<0.05	PC1	14%	18	<0.05
PC2	1.1%	15	<0.05	PC2	9%	12	<0.05
PC3	0.5%	6	<0.05	PC3	30%	52	<0.05
PC4	0.7%	11	<0.05	PC4	11%	15	<0.05

7.2.15 (Figures) Receiving Operator Characteristic and Area Under Curve graphs for (a) Random forest, (b) logistic regression, (c) Gaussian process regress and (d) control models using clr-transformed shallow topsoil TELLUS Midlands. As well as ROC-AUC graphs for (a) logistic regression and (b) Gaussian process regress using clr-transformed shallow topsoil geochemistry TELLUS Midlands limited to elements present in Castleisland.

File name: 15. Receiving Operator Characteristic (ROC_AUC) for machine learning models using Clr-transformed shallow topsoil geochemistry TELLUS Midlands

Receiving Operator Characteristic (ROC_AUC) for machine learning models using Clr-transformed shallow topsoil geochemistry TELLUS Midlands

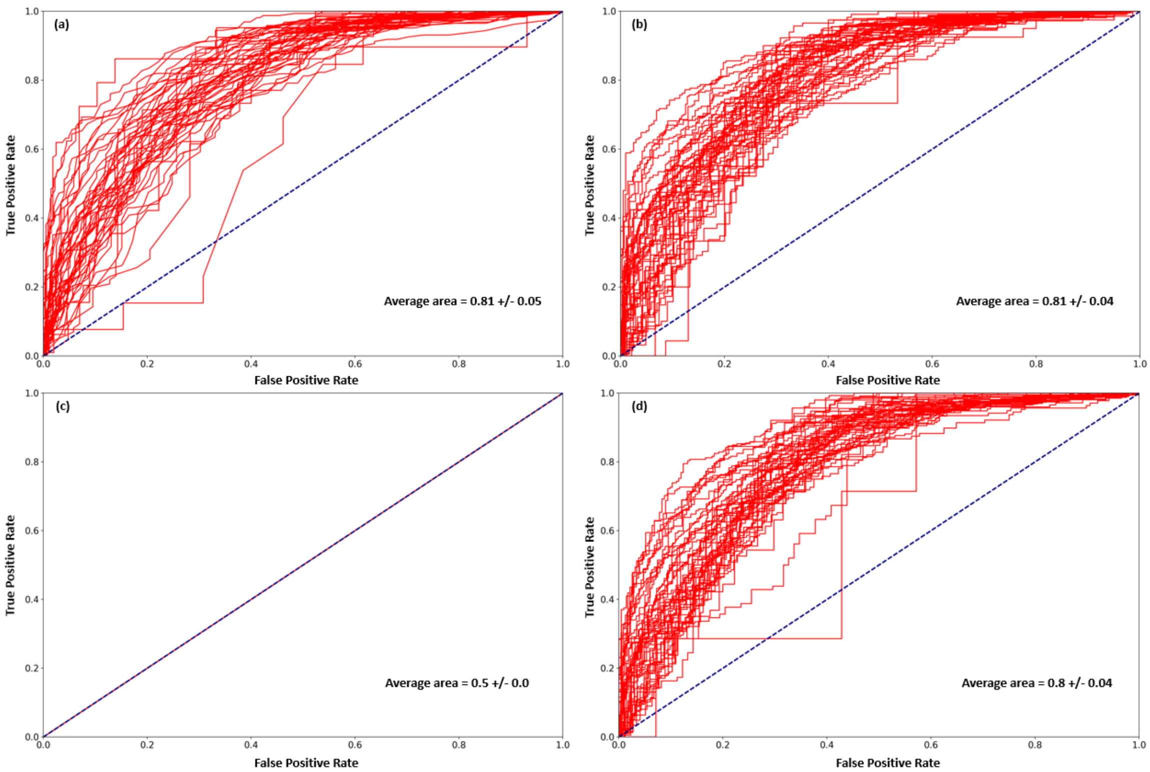

Figure 7.2.15a Receiving Operator Characteristic (ROC) for the GRP class 1 vs GRP group 2+3+4 classes. (a) Random Forest, (b) Gaussian Process Regression, (c) Control model and (d) Logistic Regression.

Receiving Operator Characteristic (ROC) for the GRP class 1 vs GRP group 2+3+4 classes. (a) Random Forest, (b) Gaussian Process Regression, (c) Control model and (d) Logistic Regression.

Receiving Operator Characteristic (ROC_AUC) for LR and GPR using Clr-transformed shallow topsoil geochemistry TELLUS Midlands limited to Castleisland elements

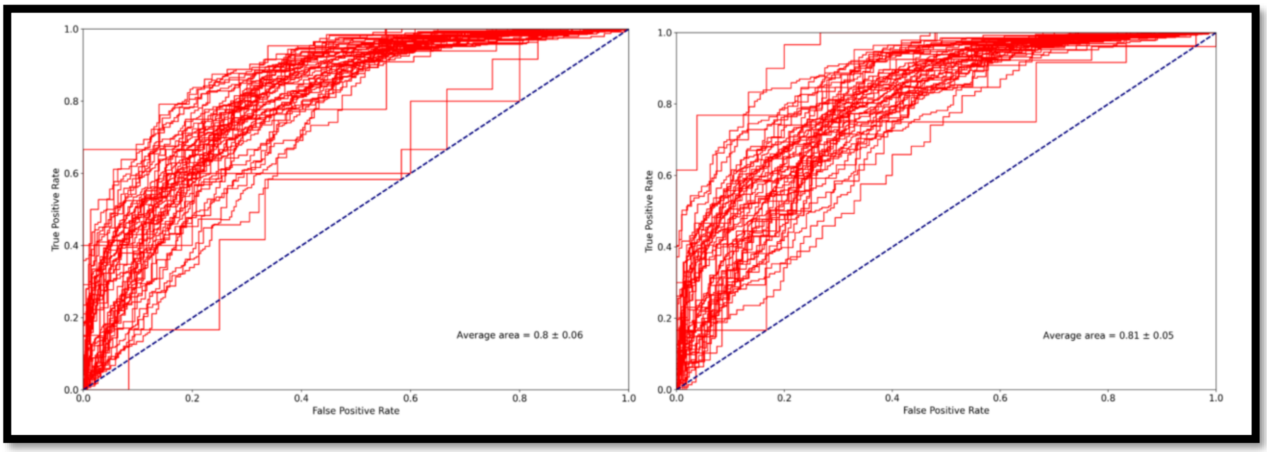

Figure 7.1.15b ROC-AUC for (left) Logistic regression and (right) Gaussian process regression. Models spatially cross validated and trained using range of elements present in Castleisland Co. Kerry topsoil geochemistry dataset.

7.2.16 (Figure) Gaussian process regression model verification (model trained on Midlands TELLUS data and tested on Castleisland data). Boxplot average soil-gas radon of (a) predicted low geogenic radon and (b) predicted high geogenic radon class

File name: 16. Boxplot average soil-gas radon of (a) predicted low geogenic radon and (b) predicted high geogenic radon class

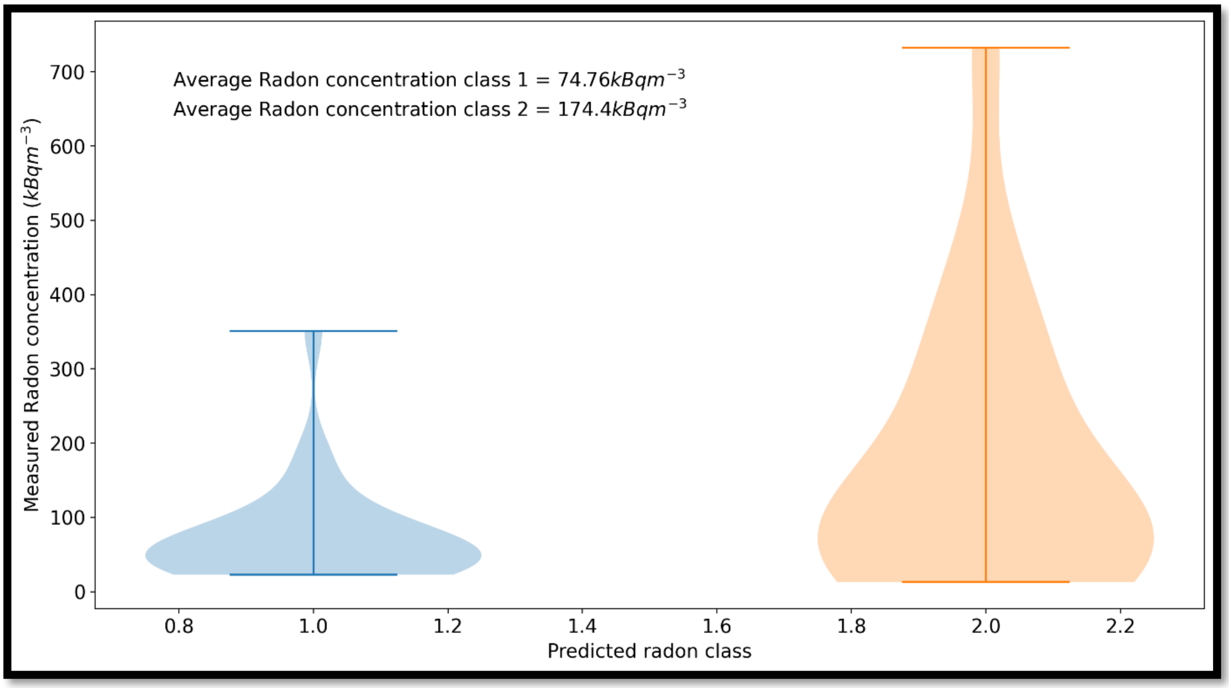

Figure 7.2.16 Gaussian process regression model verification (model trained on Midlands TELLUS data and tested on Castleisland data). Boxplot average soil-gas radon of (a) predicted low geogenic radon and (b) predicted high geogenic radon class

7.2.17 (Figure) Complete canonical heatmap(s) of isometric log ratio transformed TELLUS midlands data.

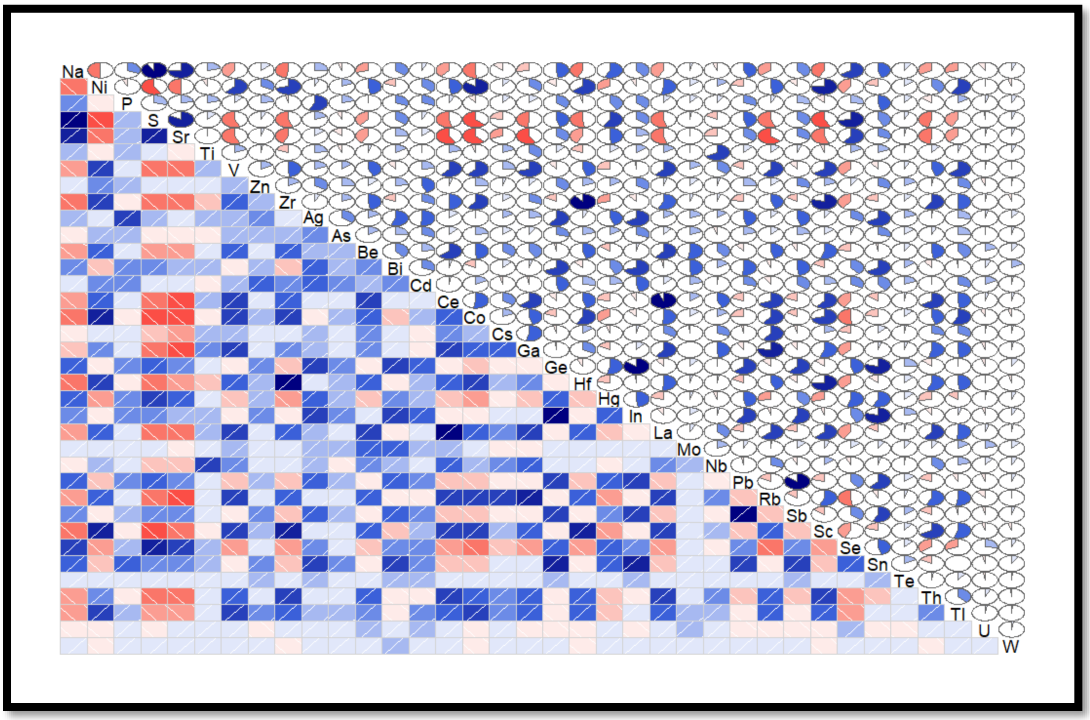

Figure 7.2.17a Canonical heatmap-1 of ilr-transformed shallow topsoil geochemistry from the TELLUS Midlands

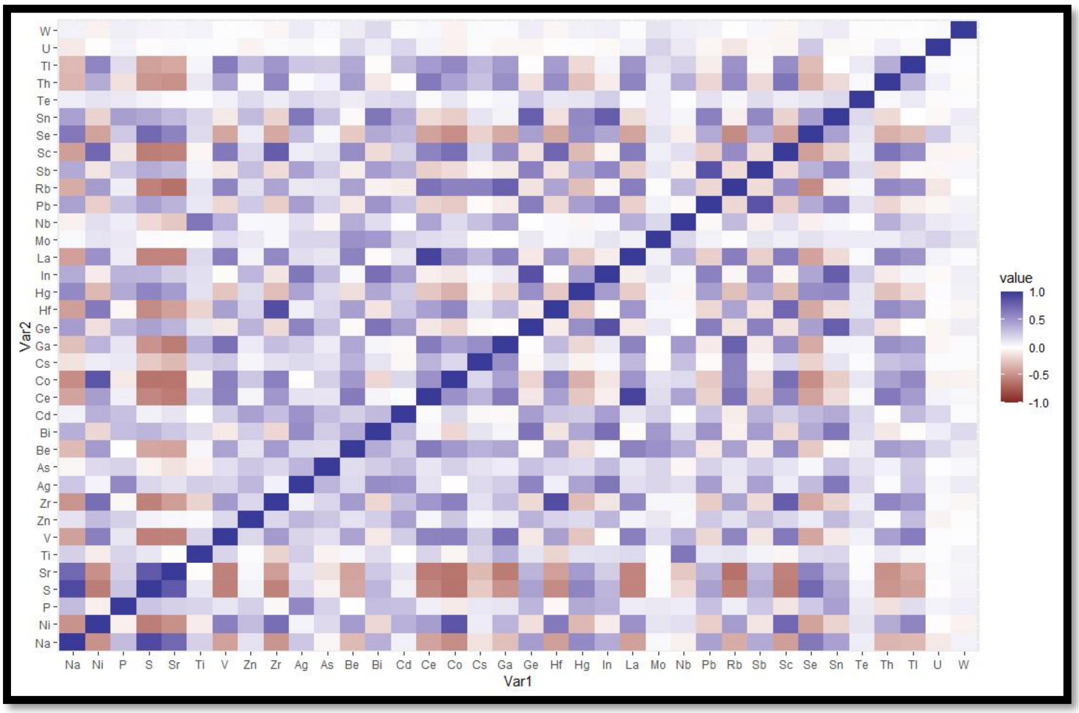

Figure 7.2.17b Canonical heatmap-2 of ilr-transformed shallow topsoil geochemistry from the TELLUS Midlands

7.2.18 Canonical heatmap(s) of isometric log ratio transformed shallow topsoil elements from Castleisland, Co. Kerry, SW Ireland.

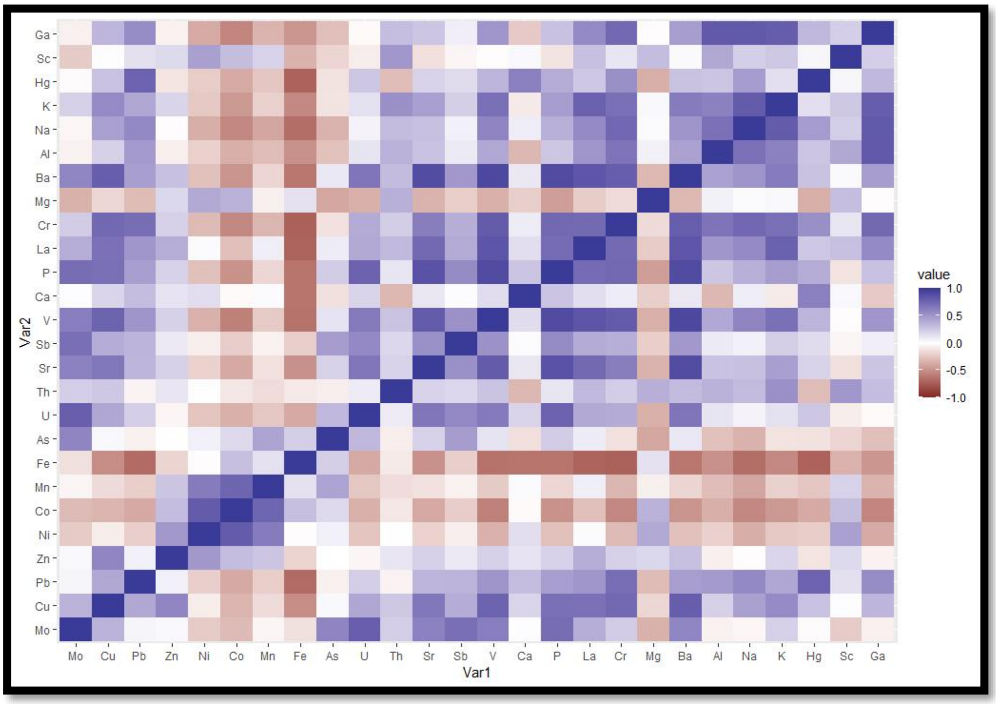

Figure 7.2.18a Canonical heatmap-1 of ilr-transformed shallow topsoil geochemistry from Castleisland case study area.

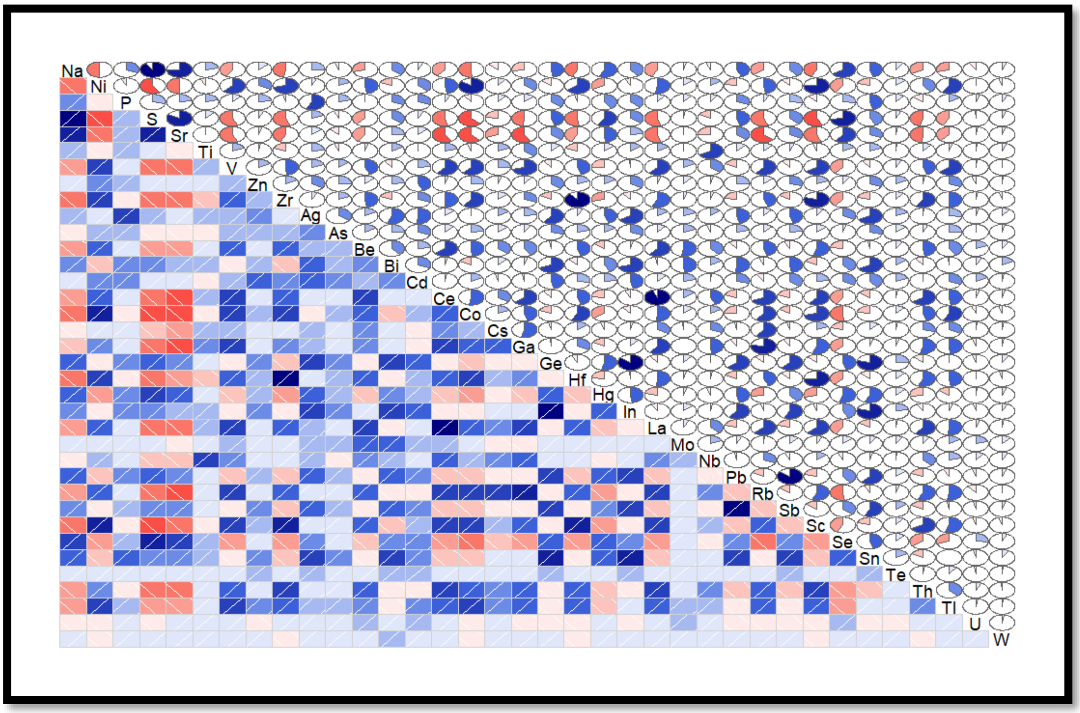

Figure 7.2.18b Canonical heatmap-2 of ilr-transformed shallow topsoil geochemistry from Castleisland case study area.

Appendix A

Pearson correlation coefficient Tellus Midlands topsoil geochemistry

Pearson c	Al_mgkg_	Ba_mgkg_	Ca_mgkg_	Cr_mgkg_	Cu_mgkg_	Fe_mgkg_	K_mgkg_	Li_mgkg_	Mg_mgkg	Mn_mgkg	Na_mgkg_	Ni_mgkg_	P_mgkg_	S_mgkg_	Sr_mgkg_	Ti_mgkg_	V_mgkg_	Zn_mgkg_	Zr_mgkg_	Ag_mgkg_	As_mgkg_	Be_mgkg_	Bi_mgkg_	Cd_mgkg_	Ce_mgkg_	Co_mgkg_
Al_mgkg_	1	0.157519	-0.76795	0.823901	0.183438	0.635251	0.616577	0.744847	-0.25478	0.240833	-0.43627	0.542897	0.033932	-0.63315	-0.71229	0.204431	0.778192	0.095394	0.490615	0.141302	0.076191	0.548516	-0.07528	-0.01272	0.745664	0.619266
Ba_mgkg_	0.157519	1	-0.1795	0.092104	0.062558	0.154393	0.179881	0.073611	-0.06934	0.210468	-0.07129	0.005792	-0.04326	-0.10426	-0.18225	-0.01015	0.066158	0.02297	0.075905	0.053577	0.059019	0.097195	-0.03574	-0.00385	0.129405	0.088995
Ca_mgkg_	-0.76795	-0.1795	1	-0.6183	-0.17759	-0.74661	-0.63975	-0.537	-0.04624	-0.32283	0.040281	-0.421	-0.19998	0.246908	0.514887	-0.28294	-0.62721	-0.21365	-0.29283	-0.24945	-0.26119	-0.41753	-0.0761	-0.03647	-0.57631	-0.56318
Cr_mgkg_	0.823901	0.092104	-0.6183	1	0.204364	0.611023	0.425283	0.609002	-0.23961	0.260395	-0.50329	0.709467	1.94E-05	-0.65157	-0.64711	0.153573	0.857881	0.172304	0.527245	0.086444	0.08069	0.437433	-0.17865	0.126268	0.632179	0.678858
Cu_mgkg_	0.183438	0.062558	-0.17759	0.204364	1	0.148677	0.163839	0.086274	-0.14021	0.079074	-0.08615	0.213302	0.35841	-0.12041	-0.07647	0.040229	0.24666	0.146081	0.192833	0.256268	0.224788	0.139025	0.080561	0.236417	0.198311	0.186686
Fe_mgkg_	0.635251	0.154393	-0.74661	0.611023	0.148677	1	0.350296	0.492167	-0.4541	0.445189	-0.55484	0.549972	-0.09681	-0.67007	-0.78244	0.042163	0.602646	0.062548	0.440279	-0.02441	0.310298	0.40026	-0.18104	-0.01653	0.53509	0.686827
K_mgkg_	0.616577	0.179881	-0.63975	0.425283	0.163839	0.350296	1	0.450421	0.028459	0.151619	0.00329	0.257949	0.279619	-0.23016	-0.35564	0.250422	0.434367	0.168174	0.261193	0.275163	0.112625	0.291818	0.085498	-0.00712	0.570963	0.351056
Li_mgkg_	0.744847	0.073611	-0.537	0.609002	0.086274	0.492167	0.450421	1	-0.16941	0.229396	-0.40497	0.429925	-0.06431	-0.56282	-0.60057	0.078427	0.519685	0.068725	0.373936	-0.01669	0.116082	0.473584	-0.07138	-0.08698	0.506882	0.514544
Mg_mgkg	-0.25478	-0.06934	-0.04624	-0.23961	-0.14021	-0.4541	0.028459	-0.16941	1	-0.26326	0.749762	-0.30286	0.097746	0.665057	0.528052	0.132248	-0.29588	0.119137	-0.40666	0.054738	-0.15363	-0.27545	0.21539	-0.07326	-0.32155	-0.31417
Mn_mgkg	0.240833	0.210468	-0.32283	0.260395	0.079074	0.445189	0.151619	0.229396	-0.26326	1	-0.30348	0.420583	-0.08172	-0.36269	-0.38941	-0.02656	0.249385	0.162485	0.310738	-0.02348	0.168001	0.256762	-0.10511	0.099309	0.271503	0.58153
Na_mgkg_	-0.43627	-0.07129	0.040281	-0.50329	-0.08615	-0.55484	0.00329	-0.40497	0.749762	-0.30348	1	-0.49003	0.317391	0.905955	0.738787	0.219459	-0.41888	0.132902	-0.47856	0.267078	-0.04065	-0.30186	0.372951	0.070589	-0.40533	-0.50943
Ni_mgkg_	0.542897	0.005792	-0.421	0.709467	0.213302	0.549972	0.257949	0.429925	-0.30286	0.420583	-0.49003	1	-0.06945	-0.58453	-0.49573	-0.08299	0.621611	0.315421	0.71189	0.053168	0.176894	0.480479	-0.17702	0.372008	0.467735	0.848
P_mgkg_	0.033932	-0.04326	-0.19998	1.94E-05	0.35841	-0.09681	0.279619	-0.06431	0.097746	-0.08172	0.317391	-0.06945	1	0.277125	0.225078	0.203175	0.114364	0.220608	-0.03585	0.574643	0.210058	0.00673	0.304509	0.296337	0.077142	-0.09203
S_mgkg_	-0.63315	-0.10426	0.246908	-0.65157	-0.12041	-0.67007	-0.23016	-0.56282	0.665057	-0.36269	**0.905955**	-0.58453	0.277125	1	**0.826471**	0.110334	-0.56969	0.061249	-0.56177	0.190453	-0.05604	-0.39217	0.350937	0.0663	-0.54319	-0.628
Sr_mgkg_	-0.71229	-0.18225	0.514887	-0.64711	-0.07647	-0.78244	-0.35564	-0.60057	0.528052	-0.38941	0.738787	-0.49573	0.225078	0.826471	1	-0.01045	-0.56331	0.038839	-0.43663	0.138116	-0.1289	-0.40881	0.258002	0.12381	-0.58861	-0.62317
Ti_mgkg_	0.204431	-0.01015	-0.28294	0.153573	0.040229	0.042163	0.250422	0.078427	0.132248	-0.02656	0.219459	-0.08299	0.203175	0.110334	-0.01045	1	0.197681	0.020744	-0.19517	0.23456	-0.0573	0.041879	0.163903	-0.00646	0.20278	-0.04829
V_mgkg_	0.778192	0.066158	-0.62721	0.857881	0.24666	0.602646	0.434367	0.519685	-0.29588	0.249385	-0.41888	0.621611	0.114364	-0.56969	-0.56331	0.197681	1	0.179096	0.485115	0.201646	0.147948	0.43723	-0.09467	0.236284	0.599413	0.616625
Zn_mgkg_	0.095394	0.02297	-0.21365	0.172304	0.146081	0.062548	0.168174	0.068725	0.119137	0.162485	0.132902	0.315421	0.220608	0.061249	0.038839	0.020744	0.179096	1	0.185782	0.341687	0.264211	0.136465	0.234313	0.44771	0.046934	0.265034
Zr_mgkg_	0.490615	0.075905	-0.29283	0.527245	0.192833	0.440279	0.261193	0.373936	-0.40666	0.310738	-0.47856	0.71189	-0.03585	-0.56177	-0.43663	-0.19517	0.485115	0.185782	1	0.069501	0.190273	0.479004	-0.17893	0.307259	0.500045	0.611346
Ag_mgkg_	0.141302	0.053577	-0.24945	0.086444	0.256268	-0.02441	0.275163	-0.01669	0.054738	-0.02348	0.267078	0.053168	0.574643	0.190453	0.138116	0.23456	0.201646	0.341687	0.069501	1	0.349119	0.172526	0.555181	0.520306	0.134427	-0.00407
As_mgkg_	0.076191	0.059019	-0.26119	0.08069	0.224788	0.310298	0.112625	0.116082	-0.15363	0.168001	-0.04065	0.176894	0.210058	-0.05604	-0.1289	-0.0573	0.147948	0.264211	0.190273	0.349119	1	0.158997	0.240705	0.309861	0.118632	0.220457
Be_mgkg_	0.548516	0.097195	-0.41753	0.437433	0.139025	0.40026	0.291818	0.473584	-0.27545	0.256762	-0.30186	0.480479	0.00673	-0.39217	-0.40881	0.041879	0.43723	0.136465	0.479004	0.172526	0.158997	1	0.391314	0.229978	0.640114	0.49216
Bi_mgkg_	-0.07528	-0.03574	-0.0761	-0.17865	0.080561	-0.18104	0.085498	-0.07138	0.21539	-0.10511	0.372951	-0.17702	0.304509	0.350937	0.258002	0.163903	-0.09467	0.234313	-0.17893	0.555181	0.240705	0.391314	1	0.320809	0.044664	-0.17873
Cd_mgkg_	-0.01272	-0.00385	-0.03647	0.126268	0.236417	-0.01653	-0.00712	-0.08698	-0.07326	0.099309	0.070589	0.372008	0.296337	0.0663	0.12381	-0.00646	0.236284	0.44771	0.307259	0.520306	0.309861	0.229978	0.320809	1	0.021837	0.183093
Ce_mgkg_	0.745664	0.129405	-0.57631	0.632179	0.198311	0.53509	0.570963	0.506882	-0.32155	0.271503	-0.40533	0.467735	0.077142	-0.54319	-0.58861	0.20278	0.599413	0.046934	0.500045	0.134427	0.118632	0.640114	0.044664	0.021837	1	0.523236
Co_mgkg_	0.619266	0.088995	-0.56318	0.678858	0.186686	0.686827	0.351056	0.514544	-0.31417	0.58153	-0.50943	0.848	-0.09203	-0.628	-0.62317	-0.04829	0.616625	0.265034	0.611346	-0.00407	0.220457	0.49216	-0.17873	0.183093	0.523236	1
Cs_mgkg_	0.439523	0.125801	-0.34037	0.243	0.048489	0.223619	0.46801	0.623393	-0.15682	0.15855	-0.1241	0.090086	0.108749	-0.23513	-0.30846	0.200226	0.257265	0.047818	0.137902	0.172315	0.133236	0.365136	0.119795	-0.0357	0.35492	0.187797
Ga_mgkg_	0.90041	0.139211	-0.72984	0.720335	0.168659	0.521862	0.656447	0.732333	-0.1353	0.156434	-0.2814	0.356162	0.123033	-0.48511	-0.59133	0.370602	0.702452	0.096427	0.304181	0.234297	0.092131	0.419636	0.04663	-0.0304	0.644098	0.45178
Ge_mgkg_	-0.14721	-0.03072	-0.07655	-0.17113	0.08916	-0.23039	0.089378	-0.17972	0.354428	-0.12316	0.472628	-0.14083	0.348558	0.446043	0.355885	0.127623	-0.09615	0.361009	-0.16238	0.598551	0.292754	-0.0267	0.678083	0.465689	-0.10399	-0.18583
Hf_mgkg_	0.48715	0.090951	-0.3167	0.500302	0.161067	0.425178	0.266501	0.386899	-0.3301	0.295489	-0.42894	0.650144	-0.03402	-0.51893	-0.42772	-0.18902	0.449134	0.207413	0.892678	0.078622	0.199883	0.453399	-0.11888	0.275177	0.451601	0.580822
Hg_mgkg_	-0.30211	0.024659	0.046656	-0.33902	0.043809	-0.34868	-0.02612	-0.3146	0.346258	-0.20428	0.565891	-0.31543	0.406732	0.588329	0.481475	0.141716	-0.25664	0.16797	-0.28835	0.4396	0.17026	-0.14405	0.418199	0.245057	-0.24933	-0.349
In_mgkg_	-0.03219	-0.01606	-0.15964	-0.09354	0.108064	-0.13137	0.142147	-0.09139	0.263572	-0.09722	0.397028	-0.08115	0.360896	0.351723	0.234207	0.151081	-0.01451	0.346383	-0.11469	0.669247	0.317031	0.029385	0.703676	0.461721	-0.07369	-0.11108
La_mgkg_	0.710445	0.102429	-0.49974	0.653833	0.194434	0.482641	0.502143	0.480901	-0.35463	0.269193	-0.42774	0.523076	0.091395	-0.55104	-0.55398	0.174767	0.62012	0.056268	0.570208	0.154229	0.115172	0.602036	-0.01975	0.118327	0.94142	0.51055
Mo_mgkg	0.036313	-0.0079	-0.17123	0.025433	0.132164	0.1802	0.045488	-0.05301	-0.09028	0.076728	0.032594	0.121046	0.10822	0.019772	-0.00755	0.007476	0.166704	0.108455	0.042055	0.194332	0.197222	0.527237	0.487782	0.220811	0.160203	0.138686
Nb_mgkg_	0.411872	0.018135	-0.35929	0.341264	0.051598	0.22559	0.269684	0.278141	-0.06113	0.075075	-0.05982	0.147055	0.089786	-0.16516	-0.24545	0.667875	0.365556	0.036796	0.042526	0.146612	-0.04119	0.385905	0.161467	0.011349	0.433007	0.169151
Pb_mgkg_	-0.20951	-0.0135	0.003352	-0.24053	0.041676	-0.26903	0.022972	-0.20571	0.315534	-0.13002	0.443984	-0.21468	0.295777	0.450185	0.358706	0.111232	-0.17526	0.251254	-0.22247	0.466208	0.211989	-0.10167	0.513712	0.294054	-0.19952	-0.23356
Rb_mgkg_	0.797235	0.128536	-0.67718	0.633368	0.1593	0.582284	0.792678	0.730972	-0.211	0.337251	-0.36776	0.470304	0.084214	-0.56356	-0.64194	0.129776	0.592078	0.141534	0.435118	0.104589	0.11688	0.449405	-0.06016	-0.07945	0.683088	0.602068
Sb_mgkg_	-0.19491	-0.00283	-0.01015	-0.19231	0.076145	-0.21631	0.048344	-0.20214	0.289047	-0.09527	0.404775	-0.11484	0.262124	0.38963	0.328106	0.057168	-0.10839	0.29994	-0.15705	0.452402	0.23425	-0.07735	0.472726	0.361218	-0.20687	-0.15337
Sc_mgkg_	0.718731	0.140304	-0.55575	0.695809	0.142096	0.583341	0.418315	0.502674	-0.30881	0.31203	-0.42902	0.749867	-0.11615	-0.58466	-0.56157	-0.03886	0.654106	0.19162	0.802894	0.08897	0.131103	0.543864	-0.16153	0.230069	0.594944	0.707898
Se_mgkg_	-0.49069	-0.01335	0.190003	-0.48462	-0.02166	-0.45367	-0.22105	-0.49521	0.36047	-0.29966	0.659641	-0.41325	0.254674	0.739067	0.60072	0.170241	-0.39767	0.093867	-0.38802	0.318819	0.042318	-0.2336	0.402107	0.328654	-0.41577	-0.50692
Sn_mgkg_	-0.11867	-0.02342	-0.07339	-0.19087	0.148607	-0.22713	0.134521	-0.09875	0.271794	-0.14268	0.453108	-0.19474	0.453844	0.416114	0.320722	0.191418	-0.09176	0.320416	-0.19192	0.664353	0.293392	-0.02423	0.669684	0.404354	-0.15408	-0.22193
Ta_mgkg_	-0.19177	-0.07242	-0.00376	-0.29115	0.004122	-0.32507	0.037344	-0.25267	0.35947	-0.20268	0.545171	-0.30794	0.280667	0.52653	0.432055	0.249567	-0.21554	0.076363	-0.24757	0.277783	0.010479	-0.0081	0.37726	0.076066	-0.09589	-0.32011
Te_mgkg_	0.046362	-0.00638	-0.12819	0.041245	0.061415	0.046856	0.082807	0.029658	0.06065	0.065007	0.082096	0.12462	0.100015	0.058705	0.023383	0.014324	0.069696	0.168313	0.08733	0.187138	0.142327	0.086326	0.15744	0.188579	0.024501	0.110791
Th_mgkg_	0.625314	0.126445	-0.46826	0.471463	0.077954	0.459768	0.494831	0.417231	-0.28552	0.212239	-0.33068	0.39544	-0.13563	-0.4728	-0.49649	0.107897	0.451067	0.027606	0.584775	0.021521	0.068209	0.470667	-0.10082	-0.00799	0.651824	0.441514
Tl_mgkg_	0.561888	0.01776	-0.43671	0.582357	0.209457	0.412108	0.367165	0.436208	-0.29231	0.299488	-0.30595	0.591959	0.159661	-0.41997	-0.38926	0.04706	0.634085	0.315309	0.506592	0.267021	0.249902	0.414209	-0.01505	0.321676	0.477523	0.573197
U_mgkg_	-0.03069	0.056617	0.089138	-0.01351	0.127561	-0.02154	-0.12851	-0.05872	-0.2009	-0.01533	-0.09	-0.00766	0.056838	-0.01213	0.026046	0.015425	0.013937	-0.05023	0.025891	0.042042	0.009076	0.19376	0.082895	0.185566	0.055893	-0.05899
W_mgkg_	0.000362	-0.01397	-0.02381	-0.01976	0.02496	-0.01974	0.029397	-0.0188	0.014591	-0.03242	0.062471	-0.0561	0.078648	0.054079	0.047958	0.056811	0.006899	0.013722	-0.04245	0.093812	0.035243	0.087154	0.175975	0.02373	0.03844	-0.05323
Y_mgkg_	0.42826	-0.01376	-0.22416	0.520651	0.160292	0.360847	0.09574	0.288736	-0.41114	0.325286	-0.44481	0.65857	0.008945	-0.48755	-0.38746	-0.07668	0.499588	0.137851	0.709745	0.10124	0.159547	0.583515	-0.07688	0.376577	0.60446	0.544952
Au_mgkg_	-0.01536	-0.00844	-0.00215	-0.01744	-0.00104	0.005745	-0.00383	-0.02309	-0.01117	-0.01952	0.006133	-0.01575	0.031573	0.017789	0.013129	0.003873	-0.0143	-0.01039	-0.01415	0.182591	0.022743	-0.01591	0.008635	-0.00284	-0.00544	-0.01866
Pd_mgkg_	-0.01903	-0.01212	0.001012	-0.01652	-0.00237	-0.0571	-0.00192	-0.02982	0.063454	-0.02699	0.076932	-0.02034	0.050443	0.072083	0.06538	0.033832	-0.00961	0.050565	-0.0114	0.093601	0.046195	0.00933	0.096019	0.093594	-0.02639	-0.04053
Pt_mgkg_	-0.1827	-0.04747	0.066774	-0.17967	-0.04195	-0.20967	-0.04003	-0.15147	0.265781	-0.09985	0.300326	-0.15481	0.065197	0.287537	0.267539	0.003924	-0.16063	0.03172	-0.15676	0.044424	-0.02664	-0.12938	0.080621	0.019458	-0.17007	-0.16628
Re_mgkg_	-0.28047	0.002103	0.25145	-0.18883	-0.0108	-0.1966	-0.23389	-0.21231	-0.02219	-0.11756	0.064894	-0.11301	-0.02982	0.190104	0.192002	-0.07641	-0.1923	0.038052	-0.12184	0.035387	0.073661	-0.13274	0.109071	0.163695	-0.24256	-0.18178

Pearson c	Cs_mgkg_	Ga_mgkg_	Ge_mgkg_	Hf_mgkg_	Hg_mgkg_	In_mgkg_	La_mgkg_	Mo_mgkg	Nb_mgkg_	Pb_mgkg_	Rb_mgkg_	Sb_mgkg_	Sc_mgkg_	Se_mgkg_	Sn_mgkg_	Ta_mgkg_	Te_mgkg_	Th_mgkg_	Tl_mgkg_	U_mgkg_	W_mgkg_	Y_mgkg_	Au_mgkg_	Pd_mgkg_	Pt_mgkg_	Re_mgkg_
Al_mgkg_	0.439523	0.90041	-0.14721	0.48715	-0.30211	-0.03219	0.710445	0.036313	0.411872	-0.20951	0.797235	-0.19491	0.718731	-0.49069	-0.11867	-0.19177	0.046362	0.625314	0.561888	-0.03069	0.000362	0.42826	-0.01536	-0.01903	-0.1827	-0.28047
Ba_mgkg_	0.125801	0.139211	-0.03072	0.090951	0.024659	-0.01606	0.102429	-0.0079	0.018135	-0.0135	0.128536	-0.00283	0.140304	-0.01335	-0.02342	-0.07242	-0.00638	0.126445	0.01776	0.056617	-0.01397	-0.01376	-0.00844	-0.01212	-0.04747	0.002103
Ca_mgkg_	-0.34037	-0.72984	-0.07655	-0.3167	0.046656	-0.15964	-0.49974	-0.17123	-0.35929	0.003352	-0.67718	-0.01015	-0.55575	0.190003	-0.07339	-0.00376	-0.12819	-0.46826	-0.43671	0.089138	-0.02381	-0.22416	-0.00215	0.001012	0.066774	0.25145
Cr_mgkg_	0.243	0.720335	-0.17113	0.500302	-0.33902	-0.09354	0.653833	0.025433	0.341264	-0.24053	0.633368	-0.19231	0.695809	-0.48462	-0.19087	-0.29115	0.041245	0.471463	0.582357	-0.01351	-0.01976	0.520651	-0.01744	-0.01652	-0.17967	-0.18883
Cu_mgkg_	0.048489	0.168659	0.08916	0.161067	0.043809	0.108064	0.194434	0.132164	0.051598	0.041676	0.1593	0.076145	0.142096	-0.02166	0.148607	0.004122	0.061415	0.077954	0.209457	0.127561	0.02496	0.160292	-0.00104	-0.00237	-0.04195	-0.0108
Fe_mgkg_	0.223619	0.521862	-0.23039	0.425178	-0.34868	-0.13137	0.482641	0.1802	0.22559	-0.26903	0.582284	-0.21631	0.583341	-0.45367	-0.22713	-0.32507	0.046856	0.459768	0.412108	-0.02154	-0.01974	0.360847	0.005745	-0.0571	-0.20967	-0.1966
K_mgkg_	0.46801	0.656447	0.089378	0.266501	-0.02612	0.142147	0.502143	0.045488	0.269684	0.022972	0.792678	0.048344	0.418315	-0.22105	0.134521	0.037344	0.082807	0.494831	0.367165	-0.12851	0.029397	0.09574	-0.00383	-0.00192	-0.04003	-0.23389
Li_mgkg_	0.623393	0.732333	-0.17972	0.386899	-0.3146	-0.09139	0.480901	-0.05301	0.278141	-0.20571	0.730972	-0.20214	0.502674	-0.49521	-0.09875	-0.25267	0.029658	0.417231	0.436208	-0.05872	-0.0188	0.288736	-0.02309	-0.02982	-0.15147	-0.21231
Mg_mgkg	-0.15682	-0.1353	0.354428	-0.3301	0.346258	0.263572	-0.35463	-0.09028	-0.06113	0.315534	-0.211	0.289047	-0.30881	0.36047	0.271794	0.35947	0.06065	-0.28552	-0.29231	-0.2009	0.014591	-0.41114	-0.01117	0.063454	0.265781	-0.02219
Mn_mgkg	0.15855	0.156434	-0.12316	0.295489	-0.20428	-0.09722	0.269193	0.076728	0.075075	-0.13002	0.337251	-0.09527	0.31203	-0.29966	-0.14268	-0.20268	0.065007	0.212239	0.299488	-0.01533	-0.03242	0.325286	-0.01952	-0.02699	-0.09985	-0.11756
Na_mgkg_	-0.1241	-0.2814	0.472628	-0.42894	0.565891	0.397028	-0.42774	0.032594	-0.05982	0.443984	-0.36776	0.404775	-0.42902	0.659641	0.453108	0.545171	0.082096	-0.33068	-0.30595	-0.09	0.062471	-0.44481	0.006133	0.076932	0.300326	0.064894
Ni_mgkg_	0.090086	0.356162	-0.14083	0.650144	-0.31543	-0.08115	0.523076	0.121046	0.147055	-0.21468	0.470304	-0.11484	0.749867	-0.41325	-0.19474	-0.30794	0.12462	0.39544	0.591959	-0.00766	-0.0561	0.65857	-0.01575	-0.02034	-0.15481	-0.11301
P_mgkg_	0.108749	0.123033	0.348558	-0.03402	0.406732	0.360896	0.091395	0.10822	0.089786	0.295777	0.084214	0.262124	-0.11615	0.254674	0.453844	0.280667	0.100015	-0.13563	0.159661	0.056838	0.078648	0.008945	0.031573	0.050443	0.065197	-0.02982
S_mgkg_	-0.23513	-0.48511	0.446043	-0.51893	**0.588329**	0.351723	-0.55104	0.019772	-0.16516	0.450185	-0.56356	0.38963	-0.58466	**0.739067**	0.416114	0.52653	0.058705	-0.4728	-0.41997	-0.01213	0.054079	-0.48755	0.017789	0.072083	0.287537	0.190104
Sr_mgkg_	-0.30846	-0.59133	0.355885	-0.42772	0.481475	0.234207	-0.55398	-0.00755	-0.24545	0.358706	-0.64194	0.328106	-0.56157	0.60072	0.320722	0.432055	0.023383	-0.49649	-0.38926	0.026046	0.047958	-0.38746	0.013129	0.06538	0.267539	0.192002
Ti_mgkg_	0.200226	0.370602	0.127623	-0.18902	0.141716	0.151081	0.174767	0.007476	0.667875	0.111232	0.129776	0.057168	-0.03886	0.170241	0.191418	0.249567	0.014324	0.107897	0.04706	0.015425	0.056811	-0.07668	0.003873	0.033832	0.003924	-0.07641
V_mgkg_	0.257265	0.702452	-0.09615	0.449134	-0.25664	-0.01451	0.62012	0.166704	0.365556	-0.17526	0.592078	-0.10839	0.654106	-0.39767	-0.09176	-0.21554	0.069696	0.451067	0.634085	0.013937	0.006899	0.499588	-0.0143	-0.00961	-0.16063	-0.1923
Zn_mgkg_	0.047818	0.096427	0.361009	0.207413	0.16797	0.346383	0.056268	0.108455	0.036796	0.251254	0.141534	0.29994	0.19162	0.093867	0.320416	0.076363	0.168313	0.027606	0.315309	-0.05023	0.013722	0.137851	-0.01039	0.050565	0.03172	0.038052
Zr_mgkg_	0.137902	0.304181	-0.16238	0.892678	-0.28835	-0.11469	0.570208	0.042055	0.042526	-0.22247	0.435118	-0.15705	0.802894	-0.38802	-0.19192	-0.24757	0.08733	0.584775	0.506592	0.025891	-0.04245	0.709745	-0.01415	-0.0114	-0.15676	-0.12184
Ag_mgkg_	0.172315	0.234297	0.598551	0.078622	0.4396	0.669247	0.154229	0.194332	0.146612	0.466208	0.104589	0.452402	0.08897	0.318819	0.664353	0.277783	0.187138	0.021521	0.267021	0.042042	0.093812	0.10124	0.182591	0.093601	0.044424	0.035387
As_mgkg_	0.133236	0.092131	0.292754	0.199883	0.17026	0.317031	0.115172	0.197222	-0.04119	0.211989	0.11688	0.23425	0.131103	0.042318	0.293392	0.010479	0.142327	0.068209	0.249902	0.009076	0.035243	0.159547	0.022743	0.046195	-0.02664	0.073661
Be_mgkg_	0.365136	0.419636	-0.0267	0.453399	-0.14405	0.029385	0.602036	0.527237	0.385905	-0.10167	0.449405	-0.07735	0.543864	-0.2336	-0.02423	-0.0081	0.086326	0.470667	0.414209	0.19376	0.087154	0.583515	-0.01591	0.00933	-0.12938	-0.13274
Bi_mgkg_	0.119795	0.04663	0.678083	-0.11888	0.418199	0.703676	-0.01975	0.487782	0.161467	0.513712	-0.06016	0.472726	-0.16153	0.402107	0.669684	0.37726	0.15744	-0.10082	-0.01505	0.082895	0.175975	-0.07688	0.008635	0.096019	0.080621	0.109071
Cd_mgkg_	-0.0357	-0.0304	0.465689	0.275177	0.245057	0.461721	0.118327	0.220811	0.011349	0.294054	-0.07945	0.361218	0.230069	0.328654	0.404354	0.076066	0.188579	-0.00799	0.321676	0.185566	0.02373	0.376577	-0.00284	0.093594	0.019458	0.163695
Ce_mgkg_	0.35492	0.644098	-0.10399	0.451601	-0.24933	-0.07369	0.94142	0.160203	0.433007	-0.19952	0.683088	-0.20687	0.594944	-0.41577	-0.15408	-0.09589	0.024501	0.651824	0.477523	0.055893	0.03844	0.60446	-0.00544	-0.02639	-0.17007	-0.24256
Co_mgkg_	0.187797	0.45178	-0.18583	0.580822	-0.349	-0.11108	0.51055	0.138686	0.169151	-0.23356	0.602068	-0.15337	0.707898	-0.50692	-0.22193	-0.32011	0.110791	0.441514	0.573197	-0.05899	-0.05323	0.544952	-0.01866	-0.04053	-0.16628	-0.18178
Cs_mgkg_	1	0.53988	-0.03047	0.146392	-0.05092	0.037479	0.329214	-0.01179	0.296576	-0.02234	0.606048	-0.03864	0.188939	-0.19723	0.12178	-0.00175	0.021451	0.292033	0.32884	0.022101	0.020316	0.103565	-0.00314	0.004755	-0.06818	-0.12481
Ga_mgkg_	0.53988	1	-0.01171	0.324358	-0.17409	0.100581	0.60328	-0.00177	0.484229	-0.08552	0.777169	-0.09235	0.552951	-0.37556	0.055899	-0.08681	0.052955	0.534191	0.486368	-0.04229	0.020712	0.227808	-0.01059	-0.00236	-0.13951	-0.23981
Ge_mgkg_	-0.03047	-0.01171	1	-0.08411	0.534016	0.866257	-0.10216	0.10522	0.004814	0.62963	-0.1219	0.616565	-0.1329	0.454379	0.791054	0.353756	0.24632	-0.13082	-0.00395	-0.04284	0.081135	-0.10528	0.010479	0.177438	0.1356	0.185695
Hf_mgkg_	0.146392	0.324358	-0.08411	1	-0.23718	-0.0166	0.503554	0.032746	0.030437	-0.17311	0.435979	-0.11672	0.755046	-0.38008	-0.13194	-0.07799	0.111715	0.555101	0.474791	-0.0079	-0.04144	0.615927	-0.00635	0.231347	-0.11828	0.052633
Hg_mgkg_	-0.05092	-0.17409	0.534016	-0.23718	1	0.474839	-0.22319	0.052001	-0.04093	0.464263	-0.28619	0.411261	-0.30302	0.545702	0.571416	0.388937	0.119317	-0.26964	-0.16157	0.013798	0.063882	-0.17666	0.026466	0.148183	0.20759	0.142118
In_mgkg_	0.037479	0.100581	0.866257	-0.0166	0.474839	1	-0.0789	0.119331	0.032479	0.607451	-0.03717	0.578103	-0.04839	0.423632	0.803245	0.302553	0.226966	-0.08094	0.045534	-0.02665	0.080878	-0.10266	0.014385	0.211413	0.083643	0.169632
La_mgkg_	0.329214	0.60328	-0.10216	0.503554	-0.22319	-0.0789	1	0.066051	0.377652	-0.20759	0.623974	-0.20862	0.637532	-0.40768	-0.15913	-0.14798	0.023893	0.596535	0.515677	0.05679	0.021784	0.7421	-0.0066	-0.01226	-0.17211	-0.22652
Mo_mgkg	-0.01179	-0.00177	0.10522	0.032746	0.052001	0.119331	0.066051	1	0.183089	0.060736	0.016604	0.117319	0.076772	0.141413	0.092494	0.201283	0.092997	0.088931	0.154497	0.212029	0.126027	0.120025	0.003345	0.008896	-0.01299	0.089222
Nb_mgkg_	0.296576	0.484229	0.004814	0.030437	-0.04093	0.032479	0.377652	0.183089	1	-0.03021	0.3202	-0.06108	0.149893	-0.06793	0.045764	0.340025	0.010557	0.38195	0.214959	0.102235	0.076792	0.208363	-0.00841	4.97E-05	-0.07468	-0.12468
Pb_mgkg_	-0.02234	-0.08552	0.62963	-0.17311	0.464263	0.607451	-0.20759	0.060736	-0.03021	1	-0.17072	0.859081	-0.21554	0.403531	0.615633	0.298312	0.139848	-0.1866	-0.0765	-0.04323	0.05868	-0.20466	0.010379	0.075878	0.156821	0.112644
Rb_mgkg_	0.606048	0.777169	-0.1219	0.435979	-0.28619	-0.03717	0.623974	0.016604	0.3202	-0.17072	1	-0.1513	0.55774	-0.51922	-0.0684	-0.1671	0.043378	0.568327	0.527983	-0.10719	0.004848	0.305224	-0.0184	-0.03299	-0.15201	-0.26917
Sb_mgkg_	-0.03864	-0.09235	0.616565	-0.11672	0.411261	0.578103	-0.20862	0.117319	-0.06108	0.859081	-0.1513	1	-0.14754	0.366181	0.57645	0.251436	0.157497	-0.16888	-0.02872	-0.03519	0.043095	-0.16267	0.006617	0.076326	0.129148	0.119927
Sc_mgkg_	0.188939	0.552951	-0.1329	0.755046	-0.30302	-0.04839	0.637532	0.076772	0.149893	-0.21554	0.55774	-0.14754	1	-0.42491	-0.1921	-0.26149	0.087509	0.681368	0.54935	-0.04845	-0.04504	0.660113	-0.00853	-0.01339	-0.17327	-0.20587
Se_mgkg_	-0.19723	-0.37556	0.454379	-0.38008	0.545702	0.423632	-0.40768	0.141413	-0.06793	0.403531	-0.51922	0.366181	-0.42491	1	0.447777	0.422992	0.121183	-0.35045	-0.29867	0.254371	0.064158	-0.35064	0.015777	0.064227	0.183149	0.305913
Sn_mgkg_	0.12178	0.055899	0.791054	-0.13194	0.571416	0.803245	-0.15913	0.092494	0.045764	0.615633	-0.0684	0.57645	-0.1921	0.447777	1	0.340477	0.17495	-0.1643	0.001858	-0.03257	0.09163	-0.1998	0.025632	0.116518	0.110545	0.122486
Ta_mgkg_	-0.00175	-0.08681	0.353756	-0.07799	0.388937	0.302553	-0.14798	0.201283	0.340025	0.298312	-0.1671	0.251436	-0.26149	0.422992	0.340477	1	0.065654	0.039807	-0.12792	0.052222	0.091207	-0.17263	0.042744	0.288385	0.183244	0.280326
Te_mgkg_	0.021451	0.052955	0.24632	0.111715	0.119317	0.226966	0.023893	0.092997	0.010557	0.139848	0.043378	0.157497	0.087509	0.121183	0.17495	0.065654	1	0.033544	0.098779	-0.01882	0.014815	0.044415	0.008713	0.192364	0.025718	0.081626
Th_mgkg_	0.292033	0.534191	-0.13082	0.555101	-0.26964	-0.08094	0.596535	0.088931	0.38195	-0.1866	0.568327	-0.16888	0.681368	-0.35045	-0.1643	0.039807	0.033544	1	0.38319	0.072115	-0.0145	0.429319	-0.01621	-0.01292	-0.14625	-0.18484
Tl_mgkg_	0.32884	0.486368	-0.00395	0.474791	-0.16157	0.045534	0.515677	0.154497	0.214959	-0.0765	0.527983	-0.02872	0.54935	-0.29867	0.001858	-0.12792	0.098779	0.38319	1	0.028308	0.008987	0.508865	-0.01261	0.007855	-0.11126	-0.11252
U_mgkg_	0.022101	-0.04229	-0.04284	-0.0079	0.013798	-0.02665	0.05679	0.212029	0.102235	-0.04323	-0.10719	-0.03519	-0.04845	0.254371	-0.03257	0.052222	-0.01882	0.072115	0.028308	1	0.023708	0.083223	0.008644	0.015058	-0.04092	0.265749
W_mgkg_	0.020316	0.020712	0.081135	-0.04144	0.063882	0.080878	0.021784	0.126027	0.076792	0.05868	0.004848	0.043095	-0.04504	0.064158	0.09163	0.091207	0.014815	-0.0145	0.008987	0.023708	1	-0.01425	0.032888	0.014245	0.003608	-0.00065
Y_mgkg_	0.103565	0.227808	-0.10528	0.615927	-0.17666	-0.10266	0.7421	0.120025	0.208363	-0.20466	0.305224	-0.16267	0.660113	-0.35064	-0.1998	-0.17263	0.044415	0.429319	0.508865	0.083223	-0.01425	1	-0.01672	0.011242	-0.14358	-0.13105
Au_mgkg_	-0.00314	-0.01059	0.010479	-0.00635	0.026466	0.014385	-0.0066	0.003345	-0.00841	0.010379	-0.0184	0.006617	-0.00853	0.015777	0.025632	0.042744	0.008713	-0.01621	-0.01261	0.008644	0.032888	-0.01672	1	0.034847	0.008009	0.039543
Pd_mgkg_	0.004755	-0.00236	0.177438	0.231347	0.148183	0.211413	-0.01226	0.008896	4.97E-05	0.075878	-0.03299	0.076326	-0.01339	0.064227	0.116518	0.288385	0.192364	-0.01292	0.007855	0.015058	0.014245	0.011242	0.034847	1	0.075397	0.365378
Pt_mgkg_	-0.06818	-0.13951	0.1356	-0.11828	0.20759	0.083643	-0.17211	-0.01299	-0.07468	0.156821	-0.15201	0.129148	-0.17327	0.183149	0.110545	0.183244	0.025718	-0.14625	-0.11126	-0.04092	0.003608	-0.14358	0.008009	0.075397	1	0.073212
Re_mgkg_	-0.12481	-0.23981	0.185695	0.052633	0.142118	0.169632	-0.22652	0.089222	-0.12468	0.112644	-0.26917	0.119927	-0.20587	0.305913	0.122486	0.280326	0.081626	-0.18484	-0.11252	0.265749	-0.00065	-0.13105	0.039543	0.365378	0.073212	1

7.2.20 Cluster dendrogram of ilr-transformed topsoil data from Castleisland, Co. Kerry study area

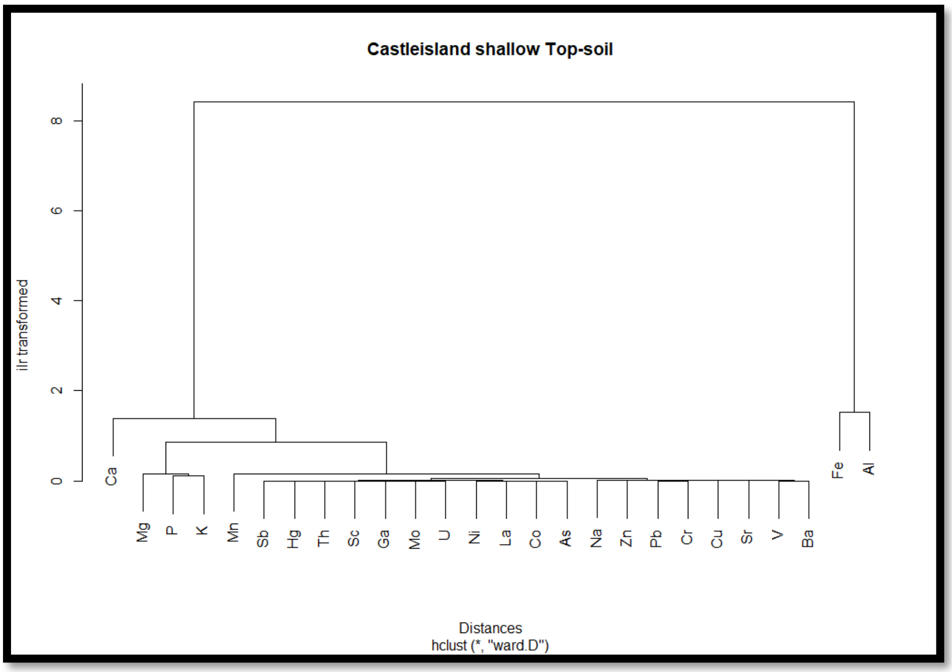

Figure 2.2.20 Cluster dendrogram of ilr-transformed topsoil data from Castleisland, Co. Kerry study area

Appendix A